Minimally invasive smart glaucoma implants

Minimally invasive smart glaucoma implants

A catalogue record is available from the Eindhoven University of Technology Library

ISBN: 978-90-386-5790-5

Printed by: Ridderprint

Cover design: Inês Pereira

This thesis was financially supported by Chemelot Institute for Science & Technology (InSciTe) under grant agreement BM3.03 SEAMS: Smart, Easy and Accurate Minimally invasive Glaucoma Surgery.

Minimally invasive smart glaucoma implants

PROEFSCHRIFT

ter verkrijging van de graad van doctor aan de Technische Universiteit Eindhoven, op gezag van de rector magnificus prof.dr. S.K. Lenaerts, voor een commissie aangewezen door het College voor Promoties, in het openbaar te verdedigen op woensdag 5 juli 2023 om 16:00 uur.

door

Inês Carolina Figueiredo Pereira

Geboren te Viseu, Portugal

Dit proefschrift is goedgekeurd door de promotoren en de samenstelling van de promotiecommissie is als volgt:

Voorzitter	prof.dr.ir. P.D. Anderson	
1e promotor	prof.dr.ir. J.M.J. den Toonder	
2e promotor	prof.dr. H.J.M. Beckers	
copromotor:	dr. H.M. Wyss	
leden:	prof.dr.ir. R. Dekker	(Technische Universiteit Delft)
	prof.dr.ir. S. Le Gac	(Universiteit Twente)
	prof.dr. J. de Boer	
	prof.dr. L. Pinchuk	(University of Miami)
	prof.dr. A.P.H.J. Schenning	

Het onderzoek of ontwerp dat in dit proefschrift wordt beschreven is uitgevoerd in overeenstemming met de TU/e Gedragscode Wetenschapsbeoefening.

Summary

Glaucoma is a group of eye conditions that damage the optic nerve, the health of which is vital for vision. The degeneration of the optic nerve leads to characteristic and progressive visual field loss. The key risk factor for the development and progression of this disease is increased intraocular pressure (IOP), which may lead to severe visual impairment or blindness if it is not properly controlled. Glaucoma drainage devices that are implanted in the eye have been developed to reduce IOP and thus stop disease progression. These include the traditional, bleb-forming aqueous shunts and the new minimally invasive glaucoma surgery (MIGS) devices.

In this thesis, we start with reviewing the existing glaucoma drainage devices and the recent scientific and technological developments in this growing field. We describe each implant in detail and provide an evidence-based comparison between devices, with focus on their efficacy in reducing disease progression and safety profile. Following this, we provide a survey of recent scientific and technological developments that aim to address prevailing unmet needs and unsolved problems. From this literature review, we conclude that a common drawback of most aqueous shunts currently used in clinical practice is that they are passive and do not allow for postsurgical IOP control, which may result in possible serious complications such as persistent hypotony (too low IOP) that can only be partly avoided at the serious cost of additional invasions. This clearly indicates that there is a need for glaucoma implants with a hydrodynamic resistance that can be adjusted after implantation.

To study the possibility of controlling the IOP in glaucoma patients by using a glaucoma implant with an adjustable hydrodynamic resistance, we first developed a numerical model describing the fluid removal from the eye through a glaucoma drainage device, its drainage into a filtering bleb and absorption by the subconjunctival vasculature. To obtain insight into the adjustments in the implant's hydrodynamic resistance that are required for IOP control when the two most common postoperative complications following glaucoma filtration surgery take place, hypotony and bleb scarring, we have simulated the flow through a microshunt with an adjustable lumen diameter. Our findings show that increasing the hydrodynamic resistance of the microshunt can effectively help to prevent hypotony. However, decreasing the hydrodynamic resistance of the implant will not sufficiently decrease the IOP to acceptable levels when the bleb is already encapsulated and fibrosed. The results reported herein may provide guidelines to support the design of future glaucoma implants with adjustable hydrodynamic resistances.

Using the numerical model described above, we developed a novel miniature magnetically adjustable glaucoma implant for non-invasively regulating IOP after implantation. Our implant has an innovative microfluidic design resulting in a small device size. An advantage of the small size is that the implantation requires less operating time and a reduced learning curve for surgeons, and is probably safer because of less tissue dissection necessary for the implantation of the device in the eye. Moreover, our

implant is comprised of a material, poly(styrene-*block*-isobutylene-*block*-styrene) (SIBS), that evokes minimal tissue reaction, which in combination with the small size might reduce inflammation and the resultant incidence of postoperative complications. The postoperative adjustment of IOP is achieved by integrating a magnetic micro-pencil shaped plug into the implant, which opens or closes fluidic channels using a simple external magnet. The micro-plug is made from the biocompatible SIBS containing iron microparticles. The complete implant consists of a SIBS drainage tube and a housing element containing the microvalve, fabricated with hot embossing using femtosecond laser-machined fused silica glass molds. With this implant, the ophthalmologist will be able to adjust the IOP precisely and actively to a desired, healthy range to successfully stop the progression of visual field loss from glaucoma. *In vitro* and *ex vivo* microfluidic experiments performed on the fabricated implant show that, when closed, the microvalve can provide sufficient hydrodynamic resistance to prevent hypotony. Furthermore, our findings demonstrate that the valve function is repeatable and stable over time. The new microfabrication technique, based upon replica molding using hot embossing and femtosecond laser-machined glass molds, represents a potentially advantageous process for mass production of microdevices containing three-dimensional structures requiring a few micrometers resolution, high accuracy and complexity. Furthermore, the new proposed valving system can be suitable for other microfluidic applications, such as in lab-on-chip and organ-on-chip systems, and in controlled drug delivery devices, amongst others.

Next to our magnetically actuated glaucoma drainage device, we also developed a new bioresorbable and minimally invasive glaucoma implant. This implant works by increasing the outflow of aqueous humor from the anterior chamber directly into Schlemm's canal, thus bypassing the trabecular meshwork which is traditionally considered the major site of aqueous humor outflow resistance in open-angle glaucoma. MIGS devices using this approach to reduce IOP already exist on the market, but they are made of metallic materials. Our device, on the other hand, is a non-metallic and non-permanent implant that will be naturally absorbed into the body. The slow degradation of the device should offer enough time for a proper and sufficient remodeling of the trabecular meshwork to occur around the implant. When degradation is finished, the extra outflow site created by the implant should remain patent, thus creating a long-term modification of the trabecular meshwork without the need for a permanent implant that may further scar and lose effectiveness. The cytotoxicity of the biodegradable polycarbonate bisamide (PC-BA) polymer from which our implant is made was investigated, and the results confirm that it is non-cytotoxic. Preliminary *in vitro* degradation experiments were performed, and while the observed mass loss and changes in molecular weight were not significant under the experimental conditions used, we hypothesize that the PC-BA is a slow-degradation polymer that might require up to a few years to fully degrade. By employing the new replica molding technique described before, using hot embossing and a femtosecond laser-machined glass mold, our biodegradable implants were successfully fabricated. An injector device was used to implant the fabricated implants into the eye of a *post-mortem* rabbit. The result from this experiment is very promising, since it proves that our implants can be successfully delivered into the trabecular meshwork.

In summary, two different types of glaucoma drainage devices were successfully developed. Both devices aim at overcoming major downsides of currently available glaucoma implants

by reducing the rate of postoperative complications and enhancing the safety profile, while providing a sufficient IOP-lowering effect that will prevent further damage to the optic nerve. First, our magnetically actuated glaucoma implant represents a possible alternative to the available passive aqueous shunts. By switching between two hydrodynamic resistances, we expect that our device will prevent hypotony from occurring in the early period after surgery and allow for maximum outflow capacity at a later stage to effectively reduce IOP. Hence, we believe that our device is suitable for the whole spectrum of glaucoma patients, from mild-to-severe. Second, our biodegradable MIGS implant has the unique feature of being comprised of a biodegradable material that will slowly degrade over time possibly leaving a permanent outflow site for the aqueous humor to effectively exit the anterior chamber to reduce IOP. We believe that this implant can offer similar positive outcomes as other MIGS implants, but with the benefit of being a non-metallic and non-permanent implant that will be naturally absorbed into the body.

Table of contents

List of Abbreviations

^{1}H-NMR	Proton Nuclear Magnetic Resonance
ABC	Ahmed Baerveldt Comparison
ATR	Attenuated Total Reflectance
AVB	Ahmed Versus Baerveldt
CIP	Carbonyl Iron Powder
CPVC	Critical Particle Volume Concentration
DCM	Dichloromethane
DI	De-Ionized
DiC	N,N'-diisopropylcarbodiimide
DIPEA	N,N-Diisopropylethylamine
DMAP	4-Dimethylaminopyridine
DMEM	Dulbecco's Modified Eagle Medium
DMF	Dimethylformamide
DSC	Differential Scanning Calorimetry
FBS	Fetal Bovine Serum
FDA	Food and Drug Administration
FEM	Finite Element Method
FT-IR	Fourier-Transform Infrared Spectroscopy
GPC	Gel Permeation Chromatography
ID	Inner Diameter
IOP	Intraocular Pressure
KOH	Potassium Hydroxide
LDH	Lactate Dehydrogenase
M_n	Number average molecular weight
M_w	Weight averaged molecular weight
MIGS	Minimally Invasive Glaucoma Surgery
MMC	Mitomycin C
MRI	Magnetic Resonance Imaging
NA	Numerical Aperture
OCT	Optical Coherence Tomography
OD	Outer Diameter
PBS	Phosphate-Buffered Saline
PC-BA	Polycarbonate Bisamide
POAG	Primary Open-Angle Glaucoma
RMA	Relative Metabolic Activity
RNFL	Retinal Nerve Fibre Layer
SA	Surface Area
SD	Standard Deviation
SIBS	Poly(styrene-*block*-isobutylene-*block*-styrene)
T_{cc}	Cold crystallization temperature
T_g	Glass transition temperature
T_m	Melting temperature
TGA	Thermogravimetric Analysis
THF	Tetrahydrofuran
WGA	World Glaucoma Association

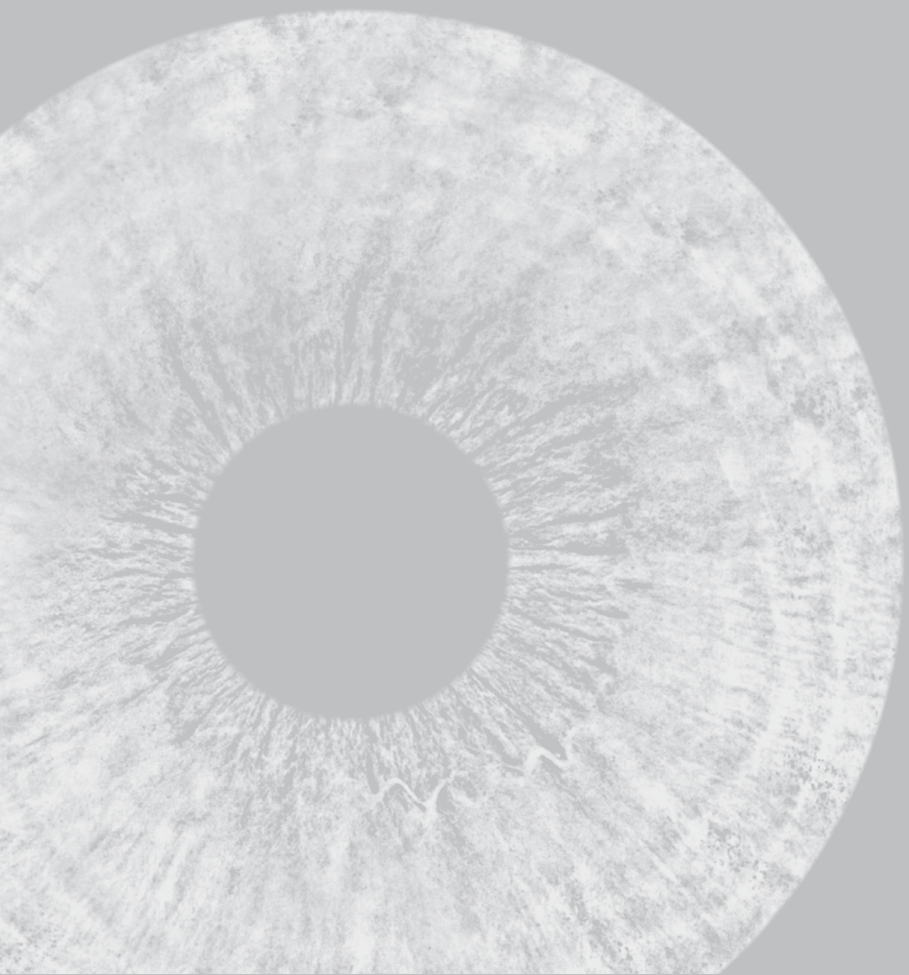

CHAPTER 1

Introduction

Glaucoma is a disease of the optic nerve and a leading worldwide cause of irreversible vision loss and blindness. In 2020, over 70 million people suffered from glaucoma, and this number is expected to increase to more than 100 million people by 2040 [1]. Patients suffering from glaucoma are often asymptomatic until later stages, when significant and irreversible visual impairment has already taken place [2]. For this reason, this disease is often called the "silent thief of sight" [3]. Amongst several risk factors, including increasing age, genetics, ethnics and structural ocular variations, elevated intraocular pressure (IOP) is considered the major contributor for the development and progression of primary open-angle glaucoma [4]. The IOP is normally maintained by the equilibrium between the production and drainage of aqueous humor, the clear fluid that circulates inside the anterior and posterior chambers of the eye [5]. The aqueous humor is produced and secreted by the ciliary body at the posterior chamber, and then flows anteriorly around the lens and through the pupil, filling the anterior chamber [6]. From there, the aqueous humor drains out of the eye through two distinct pathways – the trabecular and the non-trabecular pathways [7]. As aqueous humor inflow rate is relatively constant, IOP is mainly determined by the resistance to aqueous humor outflow [8]. In a glaucomatous eye, there is an abnormal increase of resistance to aqueous outflow, which leads to an accumulation of fluid in the eye that results in high IOP [9].

Current treatment options for glaucoma aim to lower the IOP with the goal of preventing additional optic nerve damage and thus stop the progression of glaucoma. Ophthalmologists use a variety of approaches to lower IOP, including pharmacological medication, laser procedures, and incisional surgeries [10]. In the traditional paradigm, topical ocular hypotensive drugs in the form of eye drops represent the first-line treatment option for glaucoma. However, fundamental challenges to pharmacological therapy continue to exist which may turn their administration unappealing, including the frequently reported local and systemic adverse effects as well as poor patient compliance [11]. Laser-therapy is considered when the visual field continues to deteriorate despite maximum use of topical medication, and if still unsuccessful, incisional surgery is considered [12]. Conventional filtration surgeries include trabeculectomy and implantation of glaucoma drainage devices. Both procedures are based upon the same principle: creating an alternative drainage route that allows the excess aqueous humor to escape from the anterior chamber of the eye, thereby helping to reduce IOP [13]. Although highly effective at lowering IOP, these strategies are associated with possible serious postsurgical complications, require substantial postoperative management, and have been reported to have high failure rates [14, 15]. In order to provide a safer and less invasive way of reducing IOP, a new class of glaucoma drainage devices has recently emerged, termed minimally invasive glaucoma surgery (MIGS) devices [16]. MIGS devices help to reduce the IOP with minimal tissue

manipulation/destruction, and are associated with a relatively high safety profile, short surgery time, simple instrumentation and rapid recovery [17]. To date, most of the available MIGS devices offer a more modest IOP-lowering effect than traditional incisional surgeries, but with the benefit of a safer risk profile [18]. Therefore, these devices are currently targeted at patients with mild-to-moderate glaucoma, whereas trabeculectomy and conventional aqueous shunts are generally preferred for patients with more advanced and severe glaucoma [19].

In this thesis, we first explore the existing glaucoma drainage devices and provide an evidence-based comparison between devices in **Chapter 2**. Following this, we provide a survey of recent scientific and technological developments that aim to address the prevailing unmet needs and unsolved problems. From this literature review, we concluded that one of those unmet needs is for glaucoma implants which are not passive, but instead have a hydrodynamic resistance that can be adjusted even after implantation. To determine the ideal hydrodynamic resistance that a glaucoma implant must have to maintain the IOP within acceptable levels and overcome the two most common postoperative complications following glaucoma filtration surgery – bleb scarring and hypotony – we developed a new numerical model, described in **Chapter 3**. The results reported in this study provided valuable insights that supported the design of the magnetically adjustable glaucoma implant presented in **Chapter 4**. This implant will allow for non-invasively regulating IOP after implantation, achieved by integrating a magnetic micro-pencil shaped plug into the implant which opens or closes fluidic channels using a simple external magnet. *In vitro* microfluidic experiments were performed which demonstrated that the valve can provide sufficient hydrodynamic resistance to overcome hypotony, and which showed that the valve function is repeatable and stable over time under static or dynamic conditions, in either open or closed states. Additionally, *ex vivo* experiments were carried out to better understand the performance of our magnetically actuated implant in a real eye. In **Chapter 5**, we turn our attention towards even less invasive drainage devices for glaucoma and we introduce a new MIGS implant with approximately the same size of the world's smallest medical device known to be implanted in the human body. Unlike the currently available fully-metallic MIGS implants, the main novelty of our device is that it is made of a biodegradable and flexible polymer which will slowly degrade in the body and may leave a patent outflow site for the aqueous humor to continue draining out of the anterior chamber to reduce IOP. We performed cytotoxic, mechanical and degradation experiments to characterize the biodegradable polymer used to fabricate the implants. Moreover, we carried out a preliminary *post-mortem* experiment which confirmed that our device can be easily and successfully implanted into the trabecular meshwork of the eye. Finally, **Chapter 6** discusses the advantages and limitations of the technologies presented in this thesis, and which potential aspects should be explored further to prove their efficacy in stopping the glaucoma disease progression and related visual field loss, and improve the quality of life of glaucoma patients.

Bibliography

1. Tham, Y. C. *et al.* Global Prevalence of Glaucoma and Projections of Glaucoma Burden through 2040: A Systematic Review and Meta-Analysis. *Ophthalmology* **121,** 2081–2090 (2014).
2. Khouri, A. S. & Fechtner, R. D. *Primary Open-Angle Glaucoma.* in *Glaucoma* (eds Shaarawy, T. M., Sherwood, M. B., Hitchings, R. A. & Crowston, J. G.) 2nd ed., 333–345 (W.B. Saunders, London, England, UK, 2015).
3. Greco, A. *et al.* Emerging Concepts in Glaucoma and Review of the Literature. *American Journal of Medicine* **129,** 1000.e7–1000.e13 (2016).
4. Cardigos, J. *et al.* Nanotechnology-Ocular Devices for Glaucoma Treatment: A Literature Review. *Current Eye Research* **44,** 111–117 (2019).
5. Meier-Gibbons, F. & Töteberg-Harms, M. *Aqueous Humor Dynamics and Its Influence on Glaucoma.* in *Ocular Fluid Dynamics* (eds Guidoboni, G., Harris, A. & Sacco, R.) 191–214 (Birkhäuser, Basel, Switzerland, 2019).
6. Goel, M., Picciani, R. G., Lee, R. K. & Bhattacharya, S. K. Aqueous Humor Dynamics: A Review. *The Open Ophthalmology Journal* **4,** 52–59 (2010).
7. Andrew, N. H., Akkach, S. & Casson, R. J. A review of aqueous outflow resistance and its relevance to microinvasive glaucoma surgery. *Survey of Ophthalmology* **65,** 18–31. ISSN: 18793304 (2020).
8. Acott, T. S. *et al.* Intraocular Pressure Homeostasis: Maintaining Balance in a High-Pressure Environment. *Journal of Ocular Pharmacology and Therapeutics* **30,** 94–101 (2014).
9. Stamer, W. D. & Acott, T. S. Current understanding of conventional outflow dysfunction in glaucoma. *Current Opinion in Ophthalmology* **23,** 135–143 (2012).
10. Weinreb, R. N., Aung, T. & Medeiros, F. A. The Pathophysiology and Treatment of Glaucoma: A Review. *JAMA* **311,** 1901–1911 (2014).
11. Quigley, H. A. 21st century glaucoma care. *Eye* **33,** 254–260 (2019).
12. Conlon, R., Saheb, H. & Ahmed, I. I. K. Glaucoma treatment trends: a review. *Canadian Journal of Ophthalmology* **52,** 114–124 (2017).
13. Gedde, S. J., Parrish, R. K., Budenz, D. L. & Heuer, D. K. Update on aqueous shunts. *Experimental Eye Research* **93,** 284–290 (2011).
14. Gedde, S. J. *et al.* Treatment Outcomes in the Tube Versus Trabeculectomy (TVT) Study After Five Years of Follow-up. *American Journal of Ophthalmology* **153,** 789–803.e2 (2012).
15. Christakis, P. G. *et al.* Five-Year Pooled Data Analysis of the Ahmed Baerveldt Comparison Study and the Ahmed Versus Baerveldt Study. *American Journal of Ophthalmology* **176,** 118–126 (2017).
16. Bloom, P. & Au, L. "Minimally Invasive Glaucoma Surgery (MIGS) Is a Poor Substitute for Trabeculectomy"—The Great Debate. *Ophthalmology and Therapy* **7,** 203–210 (2018).

17. Bar-David, L. & Blumenthal, E. Z. Evolution of Glaucoma Surgery in the Last 25 Years. *Rambam Maimonides Medical Journal* **9,** e0024 (2018).

18. Richter, G. M. & Coleman, A. L. Minimally invasive glaucoma surgery: Current status and future prospects. *Clinical Ophthalmology* **10,** 189–206 (2016).

19. Ansari, E. An Update on Implants for Minimally Invasive Glaucoma Surgery (MIGS). *Ophthalmology and Therapy* **6,** 233–241 (2017).

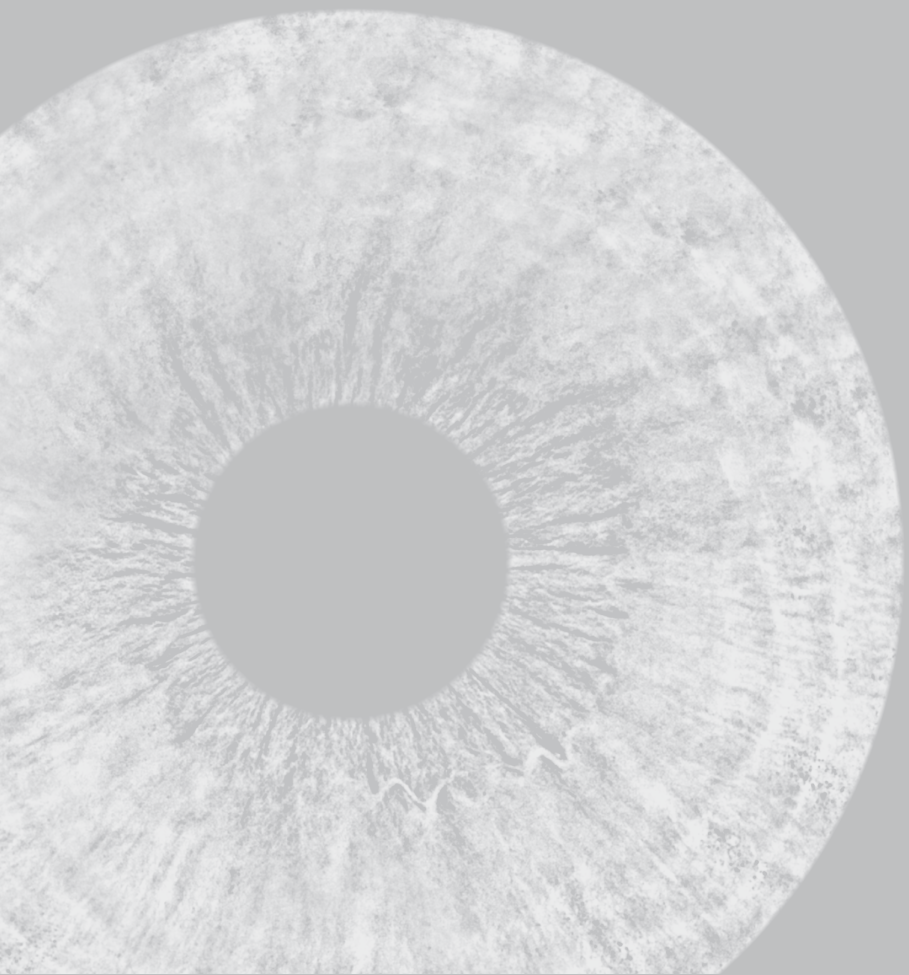

CHAPTER 2

Conventional glaucoma implants and the new MIGS devices: current options and future directions

Glaucoma is a progressive optic neuropathy that is the second leading cause of preventable blindness worldwide, after cataract formation. A rise in the intraocular pressure (IOP) is considered to be a major risk factor for glaucoma and is associated with an abnormal increase of resistance to aqueous humor outflow from the anterior chamber. Glaucoma drainage devices have been developed to provide an alternative pathway through which aqueous humor can effectively exit the anterior chamber, thereby reducing IOP. These devices include the traditional aqueous shunts with tube-plate design, as well as more recent implants, such as the trabeculectomy-modifying EX-PRESS® implant and the new minimally invasive glaucoma surgery (MIGS) devices. In this Chapter, we will describe each implant in detail, focusing on their efficacy in reducing IOP and safety profile. Additionally, a critical and evidence-based comparison between these implants will be provided. Finally, we will propose potential developments that may help to improve the performance of current devices.

This Chapter is based on:
Conventional glaucoma implants and the new MIGS devices: a comprehensive review of current options and future directions, **Inês C.F. Pereira**, Rosanne van de Wijdeven, Hans M. Wyss, Henny J.M. Beckers, Jaap M.J. den Toonder, *Eye*, **35**, 2021.

2.1 Introduction

Glaucoma is a progressive optic neuropathy characterized by optic nerve damage and visual field loss [1]. It is the leading cause of irreversible blindness in the world, with over 70 million people affected and 10% being bilaterally blind [2]. Patients suffering from this disease are asymptomatic until later stages, when significant and irreversible visual impairment has already taken place [3, 4]. Elevated intraocular pressure (IOP, above 21 mmHg) is the most important known risk factor for the development and progression of patients with ocular hypertension and primary open-angle glaucoma. It results from an unbalance between production and drainage of aqueous humor, the fluid that circulates inside the anterior and posterior chambers of the eye [5, 6]. Aqueous humor is produced by the ciliary processes within the posterior chamber, and then flows anteriorly around the lens and through the pupil, filling the anterior chamber (see Figure 2.1a, b [7–10]). From there, aqueous humor drains at the iridocorneal angle via two routes: the trabecular and the non-trabecular pathways [11]. The trabecular outflow pathway is considered to be the major site of aqueous humor outflow, and is anatomically comprised of the trabecular meshwork (subdivided into uveal, corneoscleral, and juxtacanalicular meshworks), Schlemm's canal, collector channels and the episcleral veins, as represented in Figure 2.1b [8, 11]. Within this pathway, the juxtacanalicular meshwork and the inner wall of Schlemm's canal have been shown to be the key source of outflow resistance that leads to increased IOP [12, 13]. A minor fraction of the aqueous humor also drains through an alternative route, the non-trabecular outflow pathway (indicated in Figure 2.1b) [11, 14–16]. In this route, the aqueous humor passes through the ciliary muscle from the anterior chamber and enters the suprachoroidal space. From there, it is drained through the sclera and ultimately reenters the systemic circulation via the blood vessels within the eye's orbit.

Current treatment options for glaucoma are focused on lowering IOP, which remains the only proven treatment for stopping vision loss progression up to now. This can be achieved by different methods, including pharmacological medication, laser treatment and surgery [17, 18]. Surgical intervention is required when there is progressive optic neuropathy as indicated by worsening disc/retinal nerve fibre layer (RNFL) parameters and/or visual fields changes, or indeed in the case of very high IOPs without significant disc damage, despite prior pharmacological and/or laser treatment [19]. Conventional filtration surgeries include trabeculectomy and implantation of glaucoma drainage devices, also known as aqueous shunts. Both surgical procedures are based on the same principle: bypassing the eye's natural outflow pathways to provide an alternative route for aqueous humor to effectively exit the anterior chamber, thereby reducing IOP [18, 20]. In trabeculectomy, a fistula is created into the anterior chamber from underneath a scleral flap (*ab externo* approach), which allows the aqueous humor to drain from the anterior chamber into the sub-Tenon's space (space formed between the Tenon's capsule and sclera, see Figure 2.1b), forming a subconjunctival reservoir of aqueous humor referred to as filtering bleb [21]. Conventional aqueous shunts drain aqueous humor via a tube inserted into the anterior chamber to a sub-Tenon's end plate, creating a more posteriorly located bleb [20]. While these devices were traditionally reserved for high-risk patients or after trabeculectomy had failed, they are increasingly used as a primary procedure [2, 22]. However, despite being efficacious at lowering IOP, these incisional surgeries are associated with possible serious

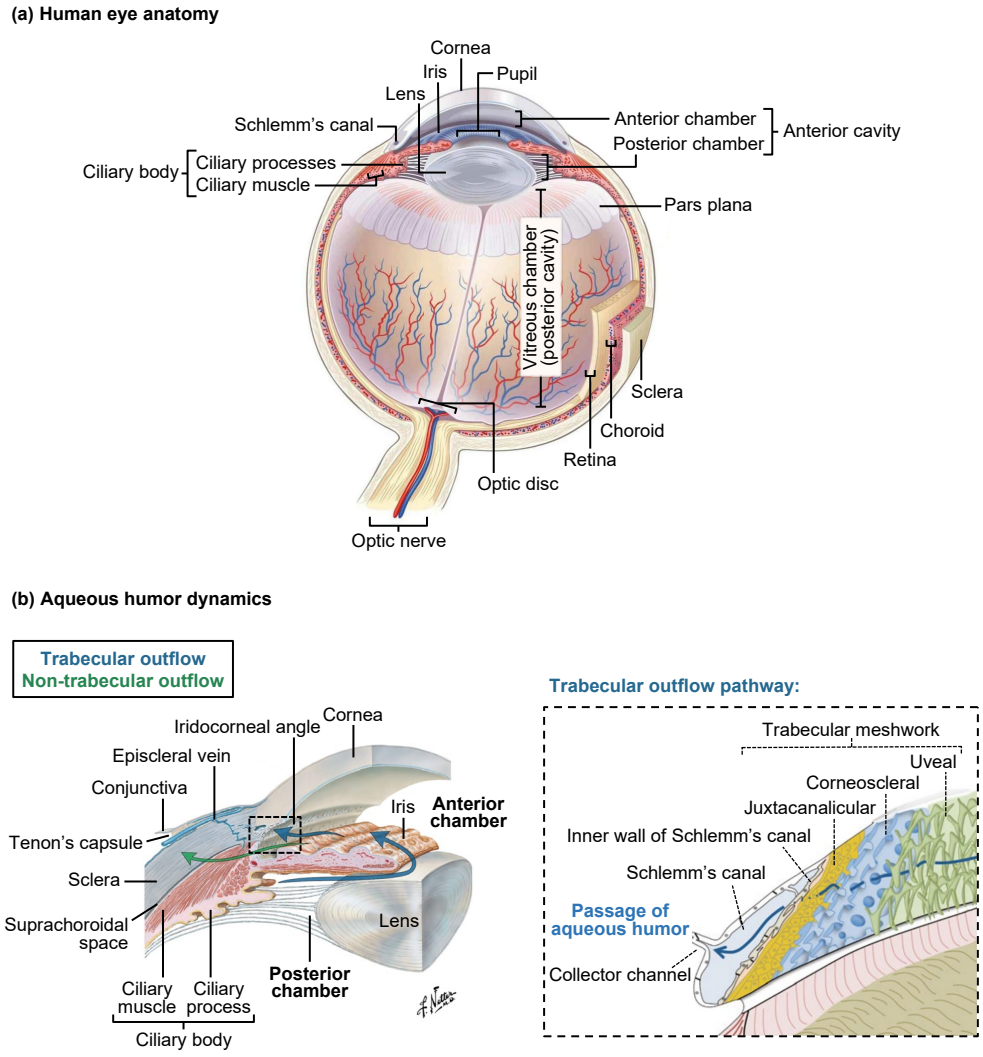

Figure 2.1: Anatomy of the human eye and aqueous humor dynamics. (**a**) Schematic representation of the anatomy of the human eye [9]. (**b**) Schematic representation of the aqueous humor dynamics inside the anterior cavity of the eye, where the blue arrows represent both the production/secretion of aqueous humor and its drainage via the trabecular outflow pathway, whereas the green arrow represents the non-trabecular outflow pathway; the anatomical structures involved in the trabecular outflow pathway, including the trabecular meshwork, Schlemm's canal and collector channel, are represented in the figure on the right; images reproduced with permission from [8] and [10].

postsurgical complications and require substantial postoperative management. Thus, in order to provide a safer and less invasive method of reducing IOP, a new class of glaucoma drainage devices and procedures has recently emerged, termed minimally- or micro- invasive glaucoma surgery (MIGS) [18, 23, 24]. Regardless of the procedure or

device used, the overall goal of surgical treatment is to reduce IOP to a level that will prevent further damage of the optic nerve, typically around 10 mmHg [25].

This review will focus on several of the currently available glaucoma drainage devices, including conventional aqueous shunts (tube-plate design) and more recent implants, such as the EX-PRESS® Glaucoma Filtration Device and the new MIGS devices. We will describe each implant in detail, highlighting their efficacy in reducing IOP and their safety profile (see Table 2.1 [26–36]). A critical and evidence-based comparison of the devices will then be provided. Finally, we will provide our opinion about the future directions of this growing field.

2.2 Conventional glaucoma drainage devices

Conventional glaucoma implants fall into two categories: valved or non-valved devices, depending on whether a valve mechanism is present to help prevent hypotony, usually in the early postoperative phase [25]. Hypotony is defined as an IOP of 5 mmHg or less, and it may lead to vision loss in up to 20% of patients. It can be accompanied by a shallow anterior chamber, hyphema (collection of blood inside the anterior chamber), but it may also lead to more devastating complications (e.g. choroidal effusions/hemorrhage) [39]. A detailed description of each commercially available aqueous shunt, including the Molteno®, Baerveldt®, and PAUL® implants, Ahmed® Glaucoma Valve and Ahmed® ClearPath, will be given below. These implants are shown in Figure 2.2 [25, 37, 40] and Figure 2.3 [41, 42].

2.2.1 Molteno® Glaucoma Drainage Device

The original Molteno implant (Molteno Ophthalmic Limited, Dunedin, New Zealand), shown in Figure 2.2a-i, consists of a long silicone tube (inner diameter (ID) = 0.34 mm; outer diameter (OD) = 0.64 mm) connected to a large 133 mm^2 polypropylene end plate [43–45]. A double plate version is also available, as demonstrated in Figure 2.2a-ii, which allows for a greater IOP reduction due to the increased available space for aqueous absorption in the subconjunctival/sub-Tenon's space [1, 44, 46, 47]. Although acceptable long-term outcomes were obtained with these early devices, severe postoperative hypotony and hypotony-related complications were often reported as a result of overfiltration [45, 48]. Thus, techniques to address this problem were soon explored, including ligating the tube externally with an absorbable ligature (which degrades after $\sim$6 weeks). This enables the formation of a tissue-capsule over the plate, which then offers some resistance to aqueous humor outflow [1, 25, 49]. Later on, Molteno additionally introduced the Molteno implant with a pressure ridge (see Figure 2.2a-iii, iv), designed to further reduce the risk of postoperative hypotony [46]. In this device, the top portion of the (main) plate is divided into two separate chambers, with the help of a thin V-shaped ring, which limits the initial available area for drainage of fluid [44]. The smaller V-chamber, when covered by Tenon's capsule, serves as a pressure-sensitive valve that regulates the fluid flow into the bleb cavity [1, 46]. Aqueous humor in the V-chamber must therefore overcome the resistance imposed by the tension of the overlying Tenon's capsule to flow further, which presumably delays fluid drainage thereby preventing severe postoperative hypotony [44]. A new larger single plate Molteno implant with pressure ridge, called Molteno3® S-series, is

Table 2.1: Conventional glaucoma drainage devices, the trabeculectomy-modifying EX-PRESS® device and the new MIGS devices – summary of the current regulatory status, advantages and disadvantages of each group of devices (aqueous shunts – valved and non-valved; MIGS devices – Schlemm's canal, suprachoroidal and subconjunctival devices), and effectiveness of each device in reducing IOP, as reported in selected studies.

Type of device	Site of anatomical intervention	Device (Manufacturer)	Regulatory status	Advantages	Disadvantages	% IOP reduction at follow-up (Study type)
Conventional glaucoma drainage devices	Subconjunctival space	Molteno® Glaucoma Drainage device (Molteno Ophthalmic Limited)	CE mark, FDA approval	Larger surface area of end plate provides greater long-term IOP reduction	Delayed functioning until encapsulation of plate occurs (high IOP in the postoperative period); Greater risk of postoperative hypotony and hypotony-related complications	53.4% at 2 years (Prospective, randomized clinical trial) [26]
		Baerveldt® Glaucoma Implant (Johnson & Johnson Vision)	CE mark, FDA approval			57.4% at 5 years (Prospective, randomized clinical trial) [29]
		PAUL® Glaucoma Implant (Advanced Ophthalmic Innovations)	CE mark granted in 2017	Smaller tube diameter occupies less space in the anterior chamber angle	Complications reported so far: shallow anterior chamber, tube occlusion and exposure, hypotony requiring intervention and endophthalmitis	42.9% at 1 year (Prospective, single-arm clinical trial) [37]
		Ahmed® Glaucoma Valve (New World Medical, Inc.)	CE mark, FDA approval	Valve minimizes risk of postoperative hypotony and hypotony-related complications; Allows immediate IOP reduction	Higher rate of bleb encapsulation and smaller surface area of end plate may decrease IOP-reducing efficacy; Valve malfunction can result in hypotony and hypotony-related complications	46.6% at 5 years (Prospective, randomized clinical trial) [29]
		Ahmed® ClearPath Glaucoma Drainage Device (New World Medical, Inc.)	CE mark, FDA approved since 2019	Equivalent to Baerveldt implant	Equivalent to Baerveldt implant	Equivalent to Baerveldt implant

Type of device	Site of anatomical intervention	Device (Manufacturer)	Regulatory status	Advantages	Disadvantages	% IOP reduction at follow-up (Study type)
Trabeculectomy-modifying device	Subconjunctival space	EX-PRESS® Glaucoma Filtration Device (Alcon Laboratories, Inc.)	CE mark, FDA approved since 2002	High efficacy in reducing IOP; More predictable than trabeculectomy, with less IOP fluctuations during the early postoperative period; Complications are less frequent when compared to trabeculectomy	Risk of failure as a consequence of subconjunctival fibrosis and bleb-related complications; hypotony is commonly reported, as well as erosion, displacement, and blockage of the implant	41.4% at 2 years (Prospective, randomized clinical trial) [31]
Minimally invasive glaucoma surgery (MIGS) devices	Schlemm's canal	iStent® (Glaukos Corporation)	CE mark granted in 2004, FDA approved since 2012	Lower risk of hypotony and hypotony-related complications; Favorable safety profile	High risk of fibrosis that may lead to device obstruction; Modest IOP reduction, which makes these devices only suitable for patients with mild-to-moderate glaucoma; Not suitable for patients with high episcleral venous pressure	33.7% at 1 year (Prospective, randomized clinical trial) [32]
		iStent *inject*® (Glaukos Corporation)	CE mark granted in 2010			31.0% at 2 years* (Prospective, randomized clinical trial) [33]
		iStent *inject*® W (Glaukos Corporation)	FDA approval since 2020			No published studies
		Hydrus® Microstent (Ivantis, Inc.)	CE mark granted in 2011, FDA approved since 2018			37.1% at 1 year (Prospective, randomized clinical trial) [32]
	Suprachoroidal space	CyPass® Micro-Stent (Alcon Laboratories, Inc.)	Withdrawn from the global market in 2018	More effective at reducing IOP as compared with Schlemm's canal MIGS devices	High risk of fibrosis that may lead to device obstruction; Unpredictable IOP spikes; Higher risk for (transient) hypotony	34.3% at 5 years* (Prospective, randomized clinical trial) [34]

*In combination with cataract surgery.

Table 2.1: (continued)

Type of device	Site of anatomical intervention	Device (Manufacturer)	Regulatory status	Advantages	Disadvantages	% IOP reduction at follow-up (Study type)
Minimally invasive glaucoma surgery (MIGS) devices	Suprachoroidal space	iStent SUPRA® (Glaukos Corporation)	CE mark granted in 2010, under FDA review	More effective at reducing IOP as compared with Schlemm's canal MIGS devices	High risk of fibrosis that may lead to device obstruction; Unpredictable IOP spikes; Higher risk for (transient) hypotony	No published studies
		SOLX® gold shunt (SOLX, Inc.)	CE mark granted, approved in Canada			35.8% at 5 years (Prospective, randomized clinical trial) [35]
		STARflo™ Glaucoma Implant (iSTAR Medical)	CE mark granted in 2012			38.5% at 2 years (Prospective study) [36]
		MINIject™ (iSTAR Medical)	Application for CE marking expected in 2020			39.1% at 6 months (Prospective, single-arm clinical trial) [27]
	Subconjunctival space	XEN® Gel Stent (Allergan, Inc.)	CE mark granted in 2013, FDA approval since 2016	High efficacy in reducing IOP, making these devices suitable for patients with more severe glaucoma; Possibility of applying antifibrotic agents in the subconjunctival space optimizes the fibrotic response; Modulating bleb encapsulation is possible with techniques such as bleb massage or bleb needling	Risk of failure as a consequence of subconjunctival fibrosis and bleb-related complications	36.3% at 1 year (Prospective, single-arm clinical trial) [28]
		PRESERFLO™ MicroShunt (Santen)	CE mark granted in 2012, under FDA review			46.7% at 5 years (Prospective, nonrandomized, single-arm clinical trial) [38]

nowadays preferably used over previous devices. It has a thinner and more flexible episcleral plate which is available in two sizes: 185 mm^2 and 245 mm^2, represented in Figure 2.2a-v [49, 50]. Other variations of the Molteno implant include a paediatric/microphthalmic implant shown in Figure 2.2a-vi, which is a mini version of the original single plate implant designed to fit a microphthalmic globe (abnormally small eye) [46].

2.2.2 Baerveldt® Glaucoma Implant

The Baerveldt implant (Johnson & Johnson Vision, California, USA) contains a single plate with a larger surface area than any Molteno device [53]. Baerveldt designed this implant in an attempt to provide an easy placement of a large end plate, that should offer greater long-term IOP control, in a single quadrant of the eye. This is not possible with the double plate Molteno devices that require two-quadrant dissection. The Baerveldt implant is comprised of a soft silicone tube (ID = 0.305 mm; OD = 0.635 mm) connected to a soft, pliable, barium-impregnated silicone end plate [44]. The end plate is available in two sizes: 350 mm^2 that is usually sufficient to manage adult glaucomas (see Figure 2.2b-i), and 250 mm^2 used for individuals with small eyes or when the larger plate cannot be placed (see Figure 2.2b-ii) [25]. The plate is additionally equipped with small fenestrations, allowing the growth of fibrous bands through the plate thereby riveting the bleb to the sclera and thus reducing bleb height [44]. The implantation procedure is similar to the Molteno implant, with both devices requiring special techniques to temporarily obstruct flow in the early postoperative period [25]. Despite the use of flow restricting techniques, severe hypotony is still frequently associated with the Baerveldt implant [44]. More recently, another version of the Baerveldt implant was introduced: the Hoffman-elbowed pars plana Baerveldt implant, shown in Figure 2.2b-iii. This implant was designed to be inserted into the vitreous cavity, with the distal end of the tube specially modified with an additional small silicone plate (Hoffman elbow) for this purpose [54]. Tube insertion through the pars plana (the posterior part of the ciliary body, represented in Figure 2.1a) is indicated in pseudophakic eyes with prior pars plana vitrectomy (procedure where vitreous humor is removed), patients with very shallow anterior chambers, or in patients that underwent corneal transplantation [25, 44, 55].

2.2.3 PAUL® Glaucoma Implant

The PAUL Glaucoma Implant (Advanced Ophthalmic Innovations, Singapore, Republic of Singapore) is a novel shunt manufactured from medical-grade silicone that differentiates from other aqueous shunts by its smaller lumen diameter (ID = 0.127 mm; OD = 0.467 mm). This device is also comprised of a large surface area end plate for aqueous absorption (342 mm^2), as shown in Figure 2.2c. A recent 12-month follow-up study revealed that the PAUL implant has comparable efficacy with other currently available implants, with almost three quarters of the patients enrolled in the study achieving complete surgical success after 1 year. The most significant postoperative complications included shallow anterior chamber, tube occlusion and exposure, hypotony requiring intervention and endophthalmitis-purulent inflammation (inflammation of the intraocular fluids usually due to infection) [37]. As it is a relatively recent implant, more studies are necessary to confirm its long-term efficacy in reducing IOP and its safety profile.

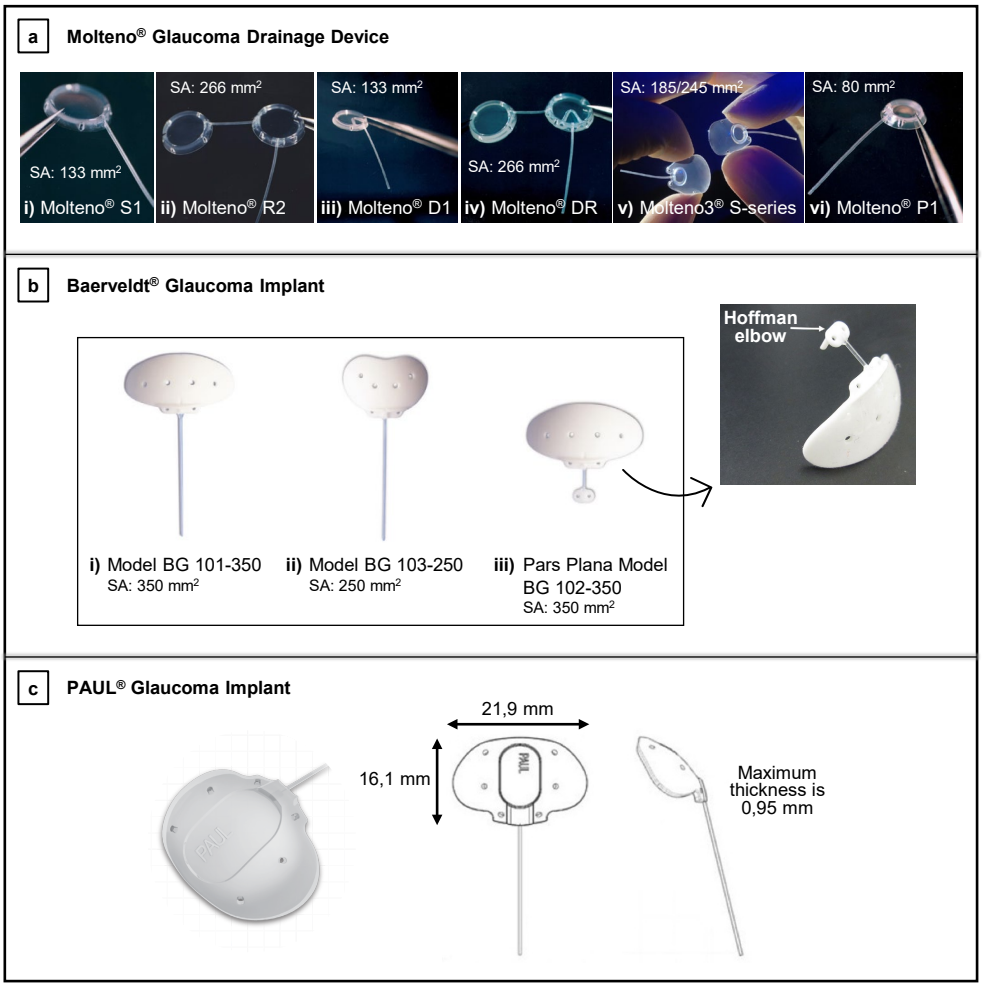

Figure 2.2: Molteno, Baerveldt and PAUL implants. (**a**) The Molteno® implants: (i) Molteno® single plate implant S1, the original Molteno® glaucoma implant; (ii) Molteno® double plate implant, available in right eye (R2) and left eye (L2) configurations; (iii) Molteno® pressure ridge single plate implant D1; (iv) Molteno® pressure ridge double plate implant, available in right eye (DR) and left eye (DL) configurations; (v) Molteno3® S-series, with the end plate available in two different sizes: 185 mm^2 (SS, left side) and 245 mm^2 (SL, right side); and (vi) Molteno® microphthalmic implant P1 [40]; images courtesy of Molteno Ophthalmic Ltd. (**b**) The Baerveldt® implants: (i) Baerveldt® BG 101-350; (ii) Baerveldt® BG 103-250; and (iii) Baerveldt® Pars Plana BG 102-350, showing its Hoffman elbow that allows positioning the tube into the vitreous cavity; images reproduced with permission from [25] and [51]. (**c**) The PAUL® Glaucoma Implant, showing the dimensions of the end plate [37, 52]; left image courtesy of Advanced Ophthalmic Innovations, and right image reproduced with permission from [37]. "SA" stands for surface area of the end plate.

2.2.4 Ahmed® Glaucoma Valve

The Ahmed implant (New World Medical, Inc., California, USA) is comprised of three parts, represented in Figure 2.3a-1: an oblong-shaped end plate, a drainage tube (ID = 0.30 mm; OD = 0.63 mm) and a valve mechanism [41, 50]. The restricting valve is located on the end plate and is comprised of two opposed deformable silicone elastomer membranes pinned together along their edges [56]. These membranes are pretensioned to open at an IOP threshold of 8 mmHg, and to remain closed below this value to reduce risk of hypotony [41]. To reduce internal friction within the valve system, the Ahmed valve utilizes a specially designed, tapered trapezoidal chamber which, according to the manufacturer, creates a Venturi effect that helps aqueous flow through the device. In this Venturi-shaped chamber the inlet cross-section is wider than the outlet, which generates a pressure differential across the chamber. As demonstrated by Bernoulli's principle [57], the velocity of aqueous entering the larger port of the Venturi chamber (Section A in Figure 2.3a-1) increases significantly towards the smaller outlet port (Section B in Figure 2.3a-1). This increased exit velocity facilitates the evacuation of aqueous humor from the valve, thereby helping to reduce internal valve friction [41]. Although this outflow restriction mechanism embedded in the Ahmed valve appears to decrease to some extent the risk of postoperative hypotony, this is still a very serious complication that affects a significant proportion of patients. This might be associated with valve malfunctioning, as *in vitro* studies have shown a high variability of the opening and closing pressures [58, 59]. Different models of the Ahmed valve are available, varying in size, shape and number of end plates [48]. All tubes are made of silicone, and the end plates are made of polypropylene or silicone. Figure 2.3a-2 shows the silicone models, which have been shown to offer improved IOP reduction, as well as a lower incidence of excessive encapsulation when compared to the polypropylene models [60, 61]. A newer design of the Ahmed valve made of porous high-density polyethylene polymer is also available, whose pores are believed to allow for tissue integration and vascular ingrowth resulting in thinner and more vascular bleb capsules. Studies comparing this concept with the prior silicone models did not find significant differences in final IOP outcomes, although less "hypertensive spikes", which usually occur several months after surgery, were observed with the newer porous polyethylene Ahmed valve [62].

2.2.5 Ahmed® ClearPath Glaucoma Drainage Device

New World Medical has recently launched a new valveless glaucoma drainage device: the Ahmed® ClearPath. This implant consists of a medical-grade silicone tube (ID = 0.305 mm; OD = 0.635 mm) secured to a flexible, barium-impregnated silicone episcleral plate that conforms to the natural shape of the globe. Two models CP250 and CP350 are available, shown in Figure 2.3b, covering surface areas of approximately 250 mm^2 and 350 mm^2. The CP350 model is positioned more posteriorly to avoid muscle attachment points, while the CP250 model is a single quadrant implant that fits between the muscles. Suture fixation points are positioned more anteriorly on the ClearPath than on other valveless drainage devices, making it easier to secure the implant to the eye. The device is supplied with a polypropylene ripcord (pre-loaded in the lumen of the tube) to prevent early hypotony, and a 23-gauge needle. The Ahmed ClearPath received clearance from Food and

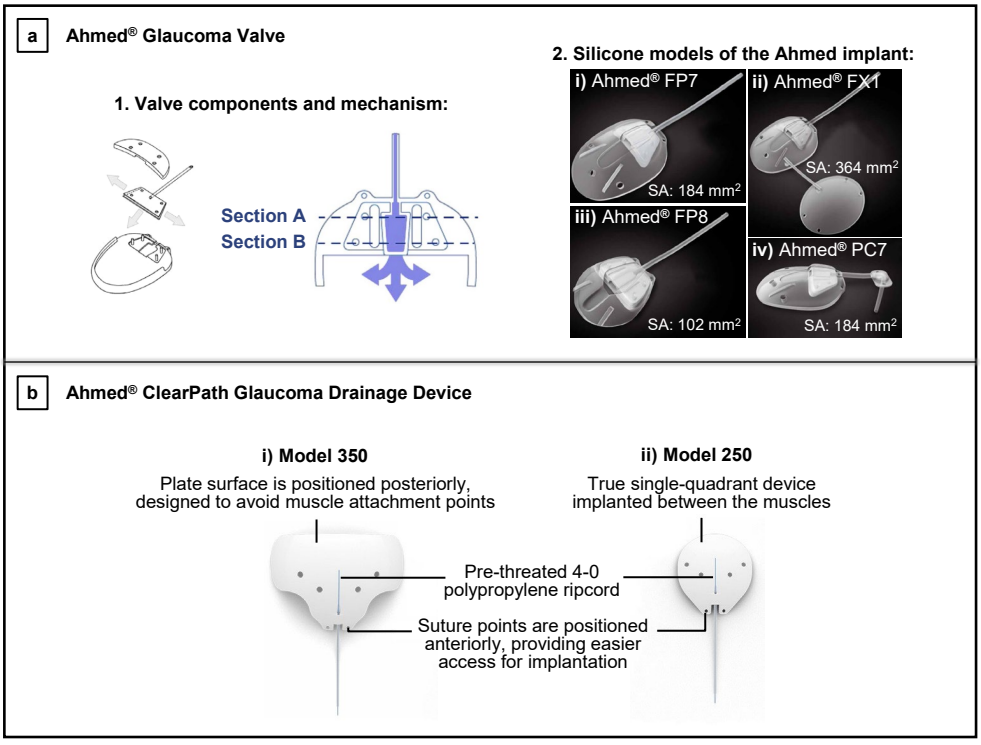

Figure 2.3: Ahmed implants. (**a**-1) The Ahmed® Glaucoma Valve showing its components and valve mechanism, where Section A represents the larger inlet port of the integrated Venturi chamber, and Section B represents the smaller outlet port of the Venturi chamber [41]. (**a**-2) Silicone models of the Ahmed® Glaucoma Valve: (2i) Ahmed® Glaucoma Valve Model FP7; (2ii) Ahmed® Glaucoma Valve Model FX1; (2iii) Ahmed® Glaucoma Valve Model FP8; and (2iv) Ahmed® Glaucoma Valve Model PC7 – Ahmed® FP7 with Pars Plana Clip [42]. (**b**) The Ahmed® ClearPath Glaucoma Drainage Device: (i) model CP350; and (ii) model CP250 [63]. "SA" stands for surface area of the end plate.

Drug Administration (FDA) in 2019 via the 510(k) pathway with the Baerveldt Glaucoma Implant as predicate device. When comparing both devices in terms of pressure/flow properties and effectiveness of tube occlusion utilizing a ripcord, the results establish that the Ahmed ClearPath and Baerveldt implant are equivalent [64, 65].

2.3 Trabeculectomy-modifying device – EX-PRESS®

The EX-PRESS Glaucoma Filtration Device (Alcon Laboratories, Inc., Texas, USA) is a miniature, tube-like implant made of medical-grade stainless steel (316LVM) that was designed with the intention of offering a simple and safe alternative to the classic trabeculectomy [66, 67]. Overall, glaucoma surgery with the EX-PRESS device achieves IOP reduction similar to that of trabeculectomy, but the EX-PRESS procedure is more predictable with less variance of IOP during the early postoperative period [21, 67]. However, complications such as erosion, displacement, and blockage of the implant, as well as hypotony-related complications are commonly reported [66, 67]. For this reason,

and due to the high cost of the device itself, trabeculectomy might still be preferred over this implant [68].

2.4 Minimally invasive glaucoma surgery (MIGS) devices

Although aqueous shunts have been proven to be effective at lowering IOP in glaucoma patients and in preventing disease progression, they have a long list of potential complications [22, 29, 69–71]. Hence, there is a clinical need for better designed devices which must have equivalent IOP-lowering capabilities as compared to traditional incisional surgeries but with an improved safety profile. To meet this clinical need, a number of procedures and devices have recently been developed labeled as either minimally invasive or micro-incisional glaucoma surgery (MIGS) [2, 72, 73]. For the current purpose, we will limit the discussion to implantable devices. The criteria for meeting the definition of a MIGS device are somewhat controversial. On one hand, FDA defines a MIGS device as "a type of IOP lowering device used to lower IOP using an outflow mechanism with either an *ab interno* or *ab externo* approach, associated with little or no scleral dissection and minimal or no conjunctival manipulation" [63]. On the other hand, the European Glaucoma Society Guidelines state that "only the *ab interno* non-bleb forming procedures can be defined as MIGS" [74]. The *ab interno* approach targets the trabecular meshwork or suprachoroidal space from within the anterior chamber, whereas in an *ab externo* procedure the trabecular meshwork is reached or a device is implanted into the anterior chamber from the outside of the eye, after a subconjunctival/sub-Tenon's or scleral flap is created [73]. In this review, we will follow the current FDA definition of a MIGS device, because in our opinion, irrespective of whether they are implanted through an *ab interno* or *ab externo* approach, the most important is the final outcome: IOP reduction with reduced tissue destruction, a relatively high safety profile, short surgery time, simple instrumentation, and rapid recovery [24]. MIGS devices can be classified into three main categories based on the site of anatomical intervention and augmentation: (i) Schlemm's canal MIGS devices, where trabecular outflow is increased by bypassing the trabecular meshwork and directing aqueous humor into Schlemm's canal; (ii) suprachoroidal MIGS devices, where uveoscleral outflow is increased via implantation of suprachoroidal shunts; and (iii) subconjunctival MIGS devices, where a drainage pathway is created into the sub-Tenon's space [23, 75].

2.4.1 Schlemm's canal MIGS devices

As the trabecular meshwork was originally considered the main site of resistance to aqueous humor outflow, bypassing this structure and directing aqueous flow from the anterior chamber directly into Schlemm's canal seemed to be a reasonable approach [13, 76]. Currently there are four Schlemm's canal MIGS devices available: the iStent®, iStent *inject*®, iStent *inject*® W and the Hydrus® Microstent [23]. These devices are shown in Figure 2.4 [72, 77–79]. They are all inserted via an *ab interno* approach, under gonioscopic view.

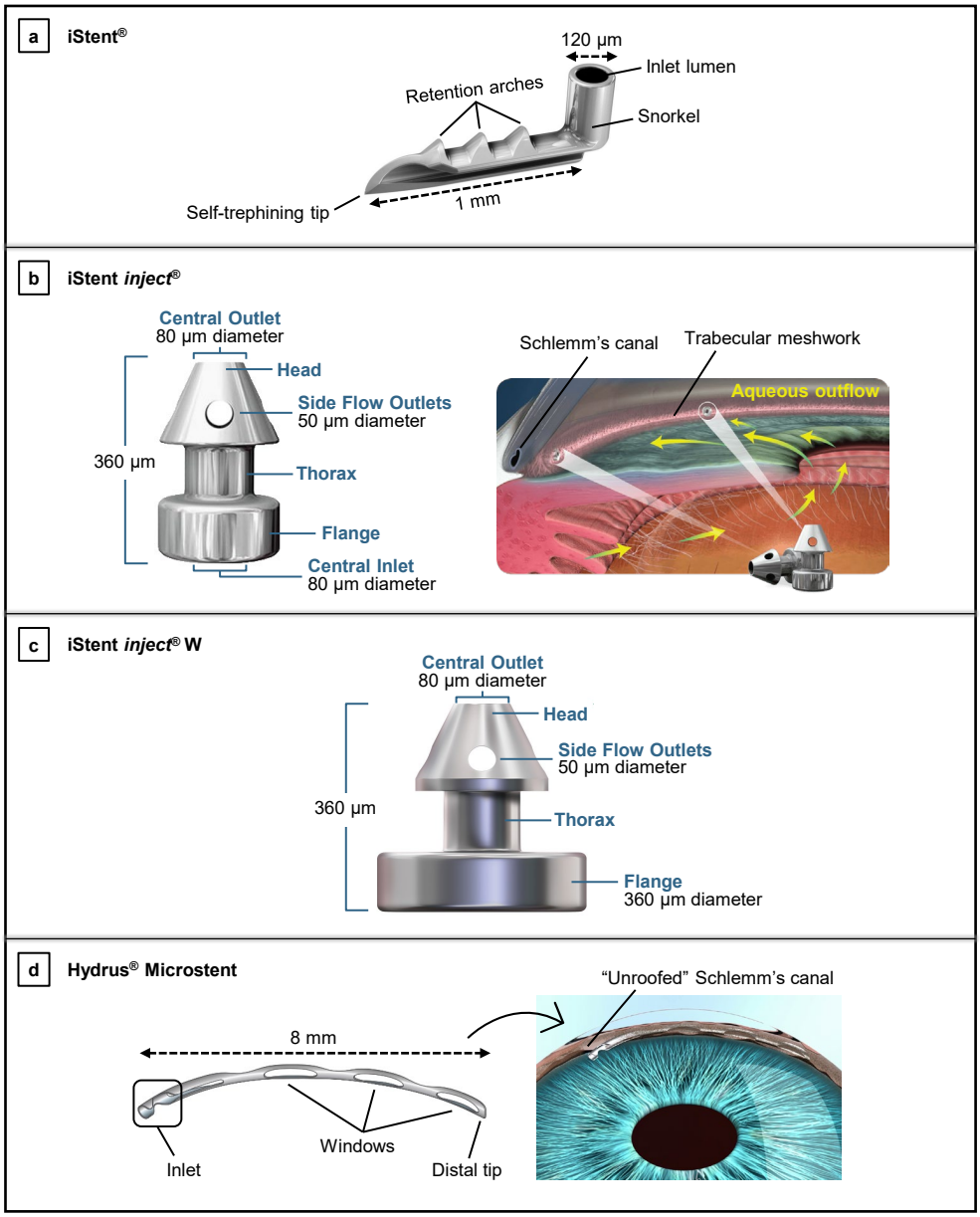

Figure 2.4: Schlemm's canal MIGS devices. (**a**) The first generation iStent®, showing its self-trephining tip that is inserted into Schlemm's canal via a sideways sliding technique, its retention arches which help maintaining the device in position, and its lumen that faces the anterior chamber [72]; image courtesy of Glaukos Corporation. (**b**) The second-generation iStent *inject*®, showing its head containing four side ports and designed to fit into Schlemm's canal, and its flange with an inlet lumen that faces the anterior chamber as illustrated in the figure on the right side [72, 77]; images courtesy of Glaukos Corporation. (**c**) The iStent *inject*® W, showing its larger flange diameter as compared with the previous version iStent *inject*® [80]; image courtesy of Glaukos Corporation. (**d**) The Hydrus® Microstent, showing its three open windows along its anterior surface and its placement in the eye (figure on the right) [78, 79]; images courtesy of Ivantis Inc.

The first-generation iStent (Glaukos Corporation, California, USA), represented in Figure 2.4a, is a heparin-coated titanium, "L"-shaped device which, via an *ab interno* incision and using a preloaded inserter, is placed through the trabecular meshwork into Schlemm's canal [78]. The canal portion of the iStent, designed to fit into Schlemm's canal, is an open half-pipe which contains a curved convex side that lies against the inner wall of the canal. Perpendicular to this portion, there is a tubular, small "snorkel" facing the anterior chamber, which serves as a conduit for aqueous to bypass the inner wall of Schlemm's canal and trabecular meshwork, thus increasing outflow [2, 78, 81]. In general, iStent implantation is associated with a good safety profile, with the most common complication being transient hyphema. Stent malposition and obstruction also occur, which is often resolved by laser intervention, or ultimately, by implant removal and replacement [72]. There are no reports yet of serious complications such as choroidal effusion, persistent hypotony, bleb formation, or endophthalmitis [82]. In addition, the placement of more than one iStent in the same eye was proven to have an additive effect in lowering IOP. Hence, a second-generation iStent was developed, called iStent *inject* (Glaukos Corporation, California, USA), shown in Figure 2.4b [24, 75, 81]. The iStent *inject* is smaller and is a conical-shaped device also made out of heparin-coated titanium [73, 82]. In contrast to the previous iStent, this device is administrated via auto-injection, where up to two devices can be delivered into Schlemm's canal with a single injector device. This allows the surgeon to inject two iStents while entering the eye only once, thus reducing surgical time and the risk of adverse events [72, 81]. More recently, a new version of the second-generation iStent *inject*, the iStent *inject* W, has been developed, featuring a wide flange at its base to optimize stent visualization and placement. The diameter of the flange was increased from 230 to 360 microns, as can be seen in Figure 2.4c. This device received FDA approval in 2020 [77]. The Hydrus Microstent (Ivantis, Inc., California, USA), illustrated in Figure 2.4d, is a scaffold-like implant inserted *ab interno* into the Schlemm's canal to maintain the canal open, thus enhancing trabecular outflow [83]. It is flexible in nature and is comprised of nitinol, a biocompatible nickel titanium alloy. It is open posteriorly along its length and has three open windows along its anterior surface. Using this device, Schlemm's canal can be dilated by up to four to five times the natural cross section of the canal, and along one fourth of its length thus targeting multiple collector channels. However, implantation of this device is also more difficult than other Schlemm's canal MIGS devices [2, 78]. The Hydrus implant is reported to be generally safe, and complications are infrequent. As with all other *ab interno* approaches, the most commonly reported complication is transient hyphema [81, 82]. A study comparing the Hydrus Microstent with two iStent *inject* implants revealed that, while the IOP results and the safety profile were similar between the two devices, the implantation of the Hydrus Microstent more often reduced the need for postoperative glaucoma medications. However, more studies are necessary to validate these results and further prove the efficacy of these implants [32].

2.4.2 Suprachoroidal MIGS

In contrast to the Schlemm's canal-based MIGS that aim to improve the trabecular outflow pathway, suprachoroidal MIGS devices aim to take advantage of the uveoscleral pathway to reduce IOP [75]. These devices, shown in Figure 2.5, include the CyPass® Micro-Stent,

iStent SUPRA®, SOLX® gold shunt, STARflo™ Glaucoma Implant and the MINIject™ [1, 27, 84, 85].

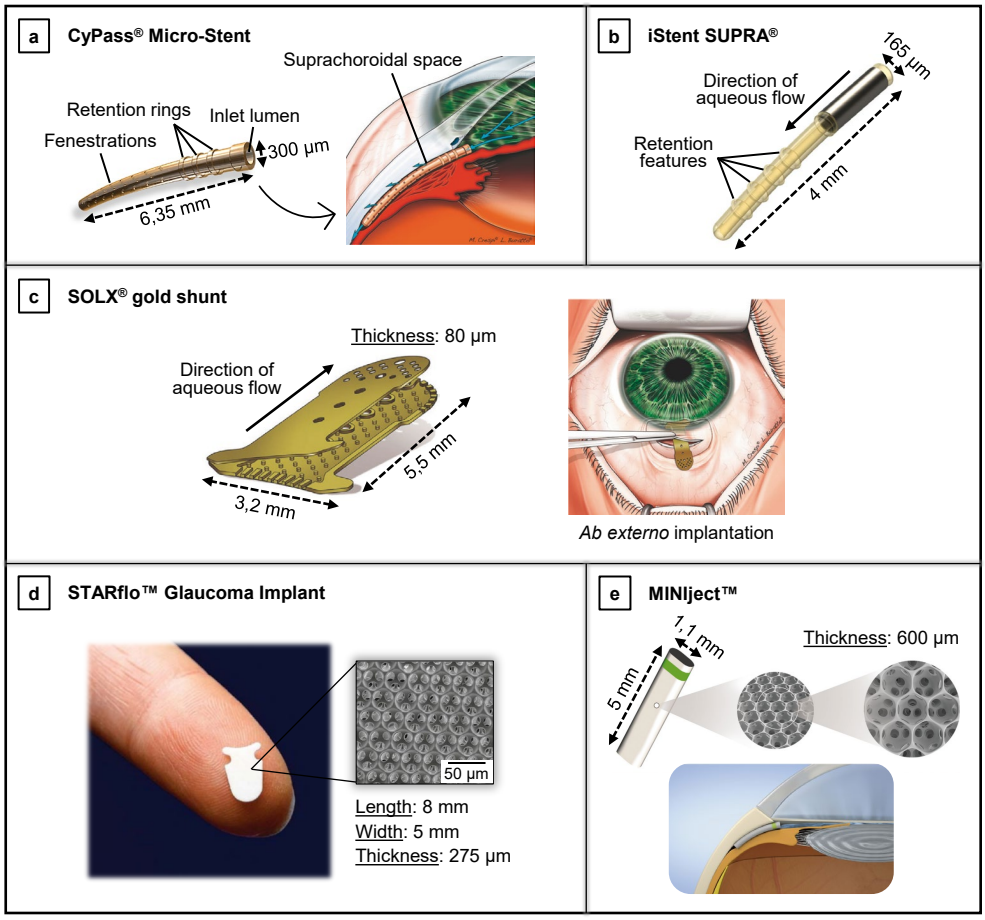

Figure 2.5: Suprachoroidal MIGS devices. (**a**) The CyPass® Micro-Stent showing its fenestrations through which aqueous humor flows into the suprachoroidal space, its retention rings which help anchoring the device, and its placement in the eye (figure on the right); image reproduced with permission from [84]. (**b**) The iStent SUPRA®, with its retention rings; image reproduced with permission from [1]. (**c**) The SOLX® gold shunt, showing its two gold plates and its implantation procedure performed through an *ab externo* incision (figure on the right); image reproduced with permission from [84]. (**d**) The STARflo™ Glaucoma Implant showing its anvil-like head designed to prevent extrusion from the anterior chamber, and its multi-porous geometry characterized by hollow spheres arranged in a regular network pattern [1, 85]; image reproduced with permission from [86]. (**e**) The MINIject™ device showing its multi-porous structure and its positioning in the eye [27].

The CyPass Micro-Stent (Alcon Laboratories, Inc., Texas, USA) is a device made of biocompatible polyimide [78]. It is fenestrated along its length as can be seen in Figure 2.5a, with pores of 76 µm in diameter which allow for aqueous outflow [2, 72]. The stent is threaded through a guidewire and applicator into the supraciliary space (via an *ab interno* procedure), where it is then anchored passively with molded-in retention rings

[72, 81]. Even though early clinical studies have shown that implantation of this device leads to slight reduction in IOP and glaucoma medications, in August 2018 the CyPass was withdrawn from the global market due to safety concerns about endothelial cell loss resulting from mispositioned devices [2, 18, 87, 88]. The iStent SUPRA (Glaukos Corporation, California, USA), shown in Figure 2.5b, is a different iteration of the two iStent Schlemm's canal MIGS devices discussed earlier. It is a small heparin-coated device composed of polyethersulfone and titanium, which is slightly curved to follow the curvature of the sclera and has ridges to improve implant retention [2, 75]. Like the CyPass microstent, the iStent SUPRA is inserted through an *ab interno* incision [72]. The SOLX gold shunt (SOLX, Inc., Massachusetts, USA) is a rectangular-shaped device made of 99.95% pure gold and its implantation procedure follows an *ab externo* approach, as shown in Figure 2.5c [89]. The device is composed of two gold plates welded together and containing 19 microchannels – initially 10 closed and 9 open [90, 91]. Holes at both ends of the device allow aqueous humor to flow through the channels from the anterior chamber into the suprachoroidal space [2]. The main novelty associated with this device was that it allows the surgeon to control aqueous humor outflow postoperatively if needed, by using a titanium-sapphire laser to open the channels [78]. Nevertheless, the SOLX microshunt never received FDA approval due to high rates of failure caused by significant fibrotic tissue formation both inside the shunt grid and around the device, which cannot be totally resolved by applying laser shots to increase outflow. Additionally, serious complications following implantation have been reported, such as retinal detachment, endophthalmitis and suprachoroidal hemorrhage [79, 92–95]. The STARflo (iStar Medical, Wavre, Belgium) is shown in Figure 2.5d, and is an innovative MIGS device made of a flexible silicone microporous material named "STAR" derived from NuSil med-6215 (a silicone elastomer). Its multi-porous geometry, comprised of a highly organized network of hollow spheres, was designed to promote biointegration from the surrounding tissues into the material, thereby maintaining the drainage efficiency on a long-term [86]. The device is composed of an anvil-like head designed to prevent extrusion from the anterior chamber, and a body that is positioned into the supraciliary space through an *ab externo* approach [90]. As the implant is relatively new, few clinical trials exist attesting its efficacy and safety [91]. However, a recent 24-month follow-up study revealed that the implant had failed to provide a safe and effective long-term alternative to conventional glaucoma surgeries, with unsatisfactory reduction in IOP [36]. The excessive fibrotic reaction and tissue ingrowth around the STARflo implant possibly reduced aqueous humor outflow through the suprachoroidal space, thus resulting in an insufficient reduction in IOP. Postoperative complications, such as corneal decompensation, hypotony, choroidal hemorrhage and unspecified macular changes have also been reported [36, 90]. The MINIject (iStar Medical, Wavre, Belgium) is another suprachoroidal MIGS device composed of the same STAR material and porous structure as the STARflo device, as illustrated in Figure 2.5e. It has a green ring on its surface which is used to confirm adequate implantation (*ab interno* approach). The results obtained from the first human trial indicated that the MINIject was able to reduce IOP in patients with mild-to-moderate glaucoma, and to maintain a stable IOP control without topical medication. No serious adverse events were reported, however, further studies are required to prove the long-term safety of this new device [27]. In general, although the suprachoroidal pathway is an interesting variant of MIGS devices, the results are not very

successful yet due to a high risk of fibrosis and/or possibly severe complications, such as corneal decompensation.

2.4.3 Subconjunctival MIGS

Contrarily to the MIGS strategies described above, the subconjunctival route is fundamentally non-physiological as aqueous humor does not naturally flow into the subconjunctival/sub-Tenon's space [75]. There are currently two subconjunctival MIGS devices, which are shown in Figure 2.6: the XEN® Gel Stent and the PRESERFLO™ MicroShunt [84, 96, 97]. The implantation of both devices is augmented with intraoperative application or injection of mitomycin C (MMC, antifibrotic agent) to reduce the risk of subconjunctival fibrosis.

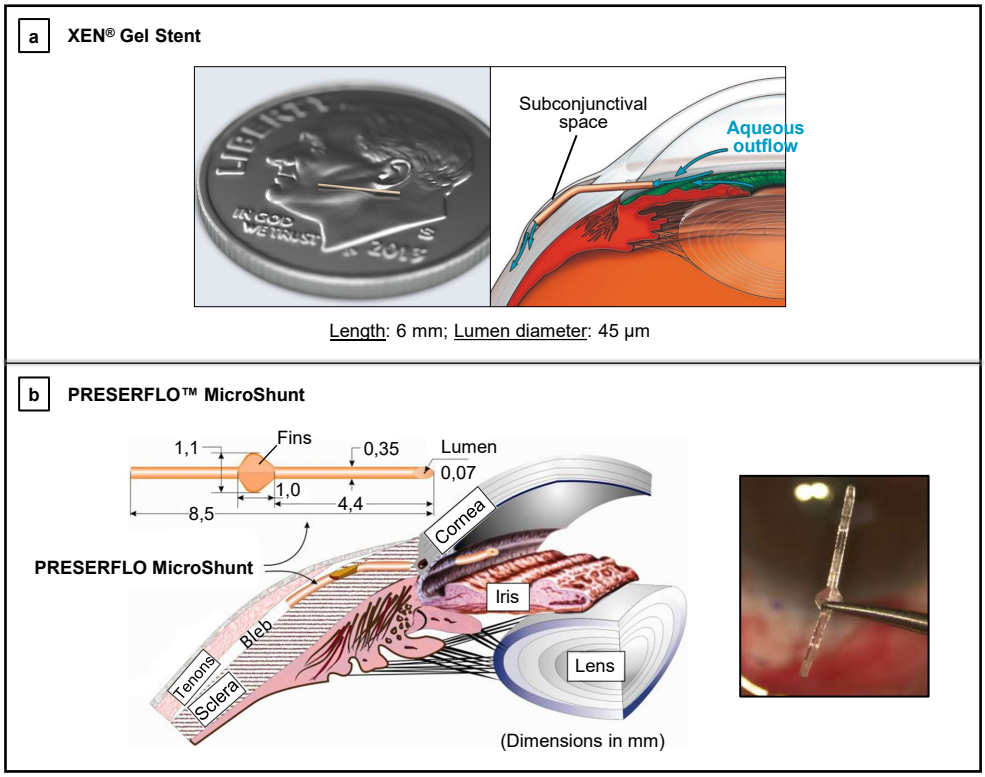

Figure 2.6: Subconjunctival MIGS devices. (**a**) The XEN® Gel Stent showing its small dimensions and its positioning in the subconjunctival space [84, 96]; image reproduced with permission from [84]. (**b**) The PRESERFLO™ MicroShunt showing its dimensions (mm) and placement in the eye [97].

The XEN gel stent (Allergan, Inc., Dublin, Ireland) targets the subconjunctival space for aqueous drainage via an *ab interno* approach, see Figure 2.6a [18]. The device is a hydrophilic tube made of porcine gelatin cross-linked with glutaraldehyde [2, 18]. According to the manufacturer, the XEN implant is designed to hydrate and swell in place during the implantation procedure, forming a soft and non-migrating drainage channel that

conforms to the surrounding tissue [78]. However, several studies have reported cases of implant migration into the anterior chamber [98–100]. The available evidence suggests that there is a reduction in IOP as well as in the number of postoperative glaucoma medications required, which presents a relatively good safety profile [101, 102]. However, a high need for postoperative bleb intervention (needling) after the implantation of this device is also commonly reported among studies [103]. The PRESERFLO MicroShunt (Santen, Osaka, Japan), formerly known as the InnFocus MicroShunt, is a flexible tube made from a highly biocompatible, bioinert material called poly(styrene-*block*-isobutylene-*block*-styrene), or SIBS (see Figure 2.6b) [97]. Located halfway down the microshunt is a 1.1 mm wingspan fin that sits within a shallow pocket in the sclera, which prevents migration of the device into the anterior chamber and also helps minimize aqueous leakage around the tube [78, 97, 104]. The SIBS material from which this implant is made is biostable and its inert nature evokes minimal inflammation and scar tissue formation. Initial studies in rabbit eyes comparing the tissue response to SIBS versus silicone tubes indicated that the silicone rubber stimulates inflammation and promotes development of a fibrotic capsule around the device that quickly becomes non-functional, while the SIBS tubes demonstrated minimal encapsulation with continuous aqueous outflow after one year [78, 105]. Subconjunctival inflammation induced by silicone has been reported in other studies [106]. Results from a recently completed clinical trial assessing the safety and effectiveness of the PRESERFLO MicroShunt indicate that the device is able to significantly reduce IOP in patients with mild-to-severe glaucoma, and to maintain healthy IOP levels in the long-term [30, 38]. Complications associated with this device are generally transient and self-limiting, and include early hypotony, shallow anterior chamber, choroidal effusion and hyphema. No cases of infections, migrations, erosions, or other serious bleb-related complications have been reported to date [30, 97, 107, 108].

2.5 Comparison between glaucoma implants

When comparing the different glaucoma implants, the most important factors to consider include short- and long-term IOP control, adjunctive use of glaucoma medications, and postoperative complications [109]. The degree of IOP reduction is a surrogate for successful glaucoma therapy, as IOP is the only known manageable risk factor for glaucoma progression. As such, it serves as an important measure of surgical success and is a good indicator of the effectiveness of a glaucoma drainage device [70].

Recent randomized clinical trials have compared the efficacy and safety of the three conventional glaucoma implants: Molteno, Baerveldt and Ahmed implants. The Ahmed Baerveldt Comparison (ABC) and Ahmed Versus Baerveldt (AVB) studies are two relevant multicenter, randomized trials comparing the most frequently used aqueous shunts: the Ahmed FP7 valve (see Figure 2.3a-2i) and the Baerveldt 101-350 implant (see Figure 2.2b-i) [29, 70, 106]. The effectiveness in reducing IOP reported for both devices in the AVB study is shown in Table 2.1. Overall, the success rate of IOP control was found to be very similar between these devices, with long-term percentage of reduction in IOP around 50% from the preoperative value. The Baerveldt implant produced slightly greater IOP reduction with fewer adjunctive medications as compared with the Ahmed valve during 5 years of follow-up, which can be explained by the larger end plate of the 350 mm^2 Baerveldt

implant: larger surface-area plates are associated with greater IOP reduction [20]. On the other hand, due to the built-in flow restriction valve of the Ahmed implant, complications associated with overfiltration and subsequent hypotony in the immediate postoperative period appear to occur less frequently [48]. However, ultimately most failures of glaucoma implants are the result of high IOP as opposed to low IOP. The Ahmed valve also showed greater IOP reduction in the early postoperative period as compared with the Baerveldt implant, although this is expected as the Baerveldt tube is occluded with a temporary suture during the first few weeks after surgery to prevent early hypotony. The most common postoperative complication was bleb encapsulation resulting in elevated IOP, although it was more frequently associated with the Ahmed valve. This may be explained by the early exposure of the Ahmed bleb to the mechanical stresses imposed by the aqueous outflow, as well as exposure to proinflammatory factors incited by surgery, which may produce more vigorous scarring of the fibrous capsule surrounding the end plate [29, 70]. This bleb encapsulation might additionally explain the lower IOP reduction achieved with the Ahmed valve in the long-term. In contrast, delaying flow may elicit less fibrous reaction, which potentially explains the lower incidence of bleb encapsulation with the Baerveldt implant [26, 29, 70, 106, 110].

The Ahmed valve was also compared to the single plate Molteno implant in a prospective randomized study, in which results are very similar to those reported in the AVB and ABC studies [26]. After 2-year follow-up, the Molteno implant showed significantly lower IOPs compared to the Ahmed valve, although it was associated with higher IOPs and mean number of antiglaucoma medications within the first postoperative month. On the other hand, the Ahmed valve was associated with higher rates of bleb encapsulation [26]. In summary, these findings suggest that the Molteno or Baerveldt implants may be a better choice for patients with a low long-term IOP target. However, patients need to be followed closely in the early postoperative period while the tube is ligated in the event a sudden increase in IOP occurs. The Ahmed implant may especially be an appropriate option for patients who need immediate postoperative IOP reduction and have moderate long-term IOP targets. Currently, the Ahmed and the Baerveldt implants are the most commonly used plated glaucoma shunts worldwide [26, 29, 70].

While conventional glaucoma implants are generally preferred for patients with more severe glaucoma, MIGS devices are currently considered when: (i) IOP reduction goals are more modest; (ii) the glaucoma disease is newly diagnosed; and/or (iii) the optic nerve damage is only mild to moderate [111]. The reason behind this is that IOP reduction tends to be less pronounced with the majority of MIGS devices as compared with more conventional implants and the trabeculectomy-modifying EX-PRESS device, as can be inferred from Table 2.1 [2]. A possible exception to this is the PRESERFLO MicroShunt, a subconjunctival MIGS device that seems to have the potential to be as effective as conventional implants in reducing IOP [30, 112]. However, this efficacy was found to be dependent on the concentration of MMC exposure during implantation. Two-year results from an international multicenter prospective trial presented at the World Glaucoma Congress revealed better IOP and medication outcomes in patients treated with 0.4 mg/mL MMC as compared to patients treated with 0.2 mg/mL MMC [108]. Similar findings were reported in other studies [113, 114]. Nevertheless, even when lower concentrations of MMC are used, the PRESERFLO MicroShunt appears to

perform better than other MIGS devices. In a recent study comparing the XEN Gel Stent and the PRESERFLO MicroShunt where the same concentration of MMC was applied (0.2 mg/mL), it was reported a reduction of IOP of 28.1% and 39.8% at two-years of follow-up for both devices, respectively [100]. This may indicate that the PRESERFLO MicroShunt is more effective in reducing IOP as compared with the XEN device. This finding may be associated with the high rate of bleb encapsulation that is frequently reported with the XEN device [100, 115]. The lower rate of bleb encapsulation with the PRESERFLO MicroShunt may be due to the biocompatibility of the SIBS material, which was designed specifically to be non-degradable, ultra-pure and therefore non-inflammatory thereby generating less tissue fibrosis [116]. Nonetheless, more robust data from long-term clinical trials is required to determine the relative efficacy and safety of these devices.

Although possibly more effective at lowering IOP, the subconjunctival MIGS devices, as bleb-forming procedures, carry risks of bleb-related complications. Regardless of their small luminal diameter, which provides increased resistance to prevent overfiltration, some cases of early hypotony have still been reported. In Schlemm's canal MIGS devices the risk of hypotony is significantly reduced, as postoperative IOP cannot fall below the episcleral venous pressure. This represents the main advantage of Schlemm's canal MIGS devices [117]. However, for the same reason, the Schlemm's canal devices should be avoided in glaucomatous eyes with raised episcleral venous pressure, as they yield disappointing outcomes in terms of IOP reduction [118]. Additionally, in case the IOP decreases below episcleral venous pressure, there is a high risk of blood reflux into the anterior chamber, causing hyphema, which represents the most common postoperative complication following Schlemm's canal procedures [111, 117]. Another important limitation of both Schlemm's canal and especially suprachoroidal MIGS devices is the fact that excessive wound healing can occur in the region of implantation, which may (and frequently) leads to device obstruction [79]. This results in increased IOP and potential need for additional interventions. One important reason behind the high rate of failure resultant from excessive fibrosis in these devices is that there is currently no approach to apply antifibrotic agents safely to the site of implantation without risk of intraocular toxicity [2, 119]. Device obstruction is an important limitation among all MIGS devices, most importantly due to their small lumen diameter. Despite being advantageous in decreasing the risk of hypotony, smaller lumens are at risk of blockage by sloughed endothelial cells, fibrin, iris pigment, blood, vitreous and/or lens fragments.

With regard to the current state of MIGS, limited data about the long-term efficacy and safety of these procedures are available until now. Additionally, lack of study standardization, randomized controlled trials and incomplete knowledge of ideal patient selection make it problematic to reach robust conclusions. Most evidence is derived from non-comparative studies and before-after studies. Furthermore, concomitant application of different therapies in clinical studies with MIGS implants, such as combination with cataract surgery, makes it difficult to do a proper evaluation and comparison of the results obtained. Thus, a standardization of future studies is urgently needed [117]. In March 2009, the World Glaucoma Association (WGA) has published guidelines for conducting clinical trials with recommendations regarding methodology, definition of success, ethical considerations, reporting of postoperative complications, economic evaluation, and statistical analysis. However, a study from Mathew et al. determining the extent of adherence

of MIGS trials to the WGA guidelines concluded that, from the studies evaluated, there was poor adherence (45.6%) to the WGA guidelines [120, 121]. There is additionally still limited evidence on the cost-effectiveness of MIGS. The downside of many of the MIGS devices is their high cost in comparison to both trabeculectomy and traditional devices – the cost of the MIGS is typically a factor of two higher than that of traditional devices (in the Netherlands approximately € 1200 versus € 650). It remains unclear whether the cost of using MIGS is outweighed by cost savings through decreased medication and reduced need for further interventions [122]. Recently published literature assessing the economic outcomes of MIGS devices/procedures concludes that most of the economic studies available so far do not consider indirect costs, costs related to postoperative complications and follow-up, and quality of life. These gross-costing studies use averages and assumptions, thereby decreasing the transparency and ability to deliver consistent estimates. Hence, future economic analyses of MIGS devices should be conducted through micro-costing studies, which include every input consumed in a patient's management. These studies will increase the precision and transparency in estimating costs and better reflect the use of resources. Another limitation of current economic evidence on MIGS, which is shared by most economic analyses, is that the reported findings may not be generalized between countries since the healthcare system and costs are different [121, 122]. To conclude, new and better designed cost-effectiveness studies are warranted to gain the MIGS devices a place within the total treatment armamentarium for glaucoma.

2.6 Future directions

For patients with mild to moderate glaucoma, Schlemm's canal or suprachoroidal MIGS devices are a promising treatment option. Since these procedures do not involve the formation of a filtering bleb, they avoid the bleb-related complications that the subconjunctival devices are susceptible to. Additionally, they preserve the conjunctiva in the event future incisional surgeries are required [91]. However, the longevity and success of these devices depend on the absence of excessive fibroblastic proliferation and scarring both within the devices or around them. Thus, the development of new methods of application of antifibrotic agents for these devices seems appropriate, especially for suprachoroidal devices. Alternatively, preventing excessive fibrosis may be achieved by using optimal biocompatible materials that induce minimal tissue reaction [2].

The ideal MIGS device for more severe cases of glaucoma would produce an IOP-lowering effect similar to trabeculectomy and conventional drainage devices, but with an improved safety profile. The newer subconjunctival, bleb-forming devices appear to be closer than other MIGS devices in achieving this goal. However, although the rate of hypotony and bleb-related complications seems to be lower with these devices as compared with more traditional surgeries, their occurrence is still significant [123].

To minimize the incidence of hypotony, valves have been incorporated in long-tube glaucoma implants, e.g. the Ahmed valve, in an attempt to increase the flow resistance and to provide better IOP control. Even though the Ahmed valve is associated with low rates of early postoperative hypotony, evidence suggests that hypotony continues to occur [124]. To overcome this, other innovative concepts of passive valves, as well as

active valves, have been proposed. In Figure 2.7 some of these proof-of-concept valve mechanisms are represented [125–129].

A number of passive flow-control mechanisms based on flaps, membranes or ferromagnetic substances have been described in the literature [125–127, 130, 131]. Park et al. proposed a novel polymeric micro-check valve for a glaucoma drainage device, which is comprised of three layers as shown in Figure 2.7a [125]. The intermediate layer is composed of a thin valve membrane resting on a pedestal, designed to lift upwards when the IOP is greater than the sum of the cracking pressure (the minimum upstream pressure required to open the valve) and external pressure on the outlet side. When the valve opens, a space is created between the valve and the pedestal, allowing the aqueous humor to flow further. Conversely, when the IOP is less than the sum of these pressures, the valve membrane returns to its original closed position, thereby avoiding postoperative hypotony. In this work, the pedestal was specially elevated by coating it with Parylene C, in order to induce a pre-stress in the valve membrane that allows for a precise opening pressure to be achieved (around 10 mmHg). Another micro-mechanical valve embodiment designed for a suprachoroidal implant was proposed by Siewert et al. [126]. The valve, represented in Figure 2.7b, exhibits a tongue-like shape and is located in the inflow area (anterior chamber), positioned in the wall of the drainage tube. The authors claimed that previous micro-check valves with direct contact between the valve membrane and the valve seat (pedestal) present high risk of stiction, and thus failure in IOP control, especially in a long-term application. Hence, they proposed this flap-like valve mechanism where no directly contacting components exist. Paschalis et al. proposed a quite different and innovative concept for a passive glaucoma valve, based on ferromagnetic nanoparticles, see Figure 2.7c [127]. A ferrofluid was used for the design of the valve, consisting of water-immiscible ferromagnetic nanoparticles that were dispersed in a fluorinated oil as a carrier liquid. Two permanent magnets were also part of the valve system: one placed next to the tube sub-section containing the ferrofluid droplet to hold it from moving with the flow, and the other was placed in the opposite side to adjust the pressure required to bend the droplet and initiate flow. *In vitro* tests proved that the ferromagnetic valve provided flow occlusion at a pressure of 7 mmHg and flow initiation at a pressure of 10 mmHg [127].

The main advantage of passive valves is that they are power-free, simple to operate, and generally easier to fabricate as compared to active valves. However, active valves allow for the ophthalmologist to precisely and actively adjust the resistance to the aqueous humor outflow to achieve the desired IOP. This allows for a non-invasive, patient-specific IOP management. An example of a device incorporating an active valve is the eyeWatch™ Implant (Rheon Medical SA, Lausanne, Switzerland), the world's first commercially available adjustable glaucoma implant that received CE mark in 2019. The eyeWatch system features the eyeWatch implant, acting as an adjustable faucet, and the eyeWatch Pen, used to tune the flow resistance of the implant by inducing variable compression of the drainage tube, see Figure 2.7d [128, 132]. This compression is achieved by rotating a magnetic disk present inside the implant, which enables the fluidic resistance to be adjusted in order to maintain the IOP within the optimal clinical-targeted range. This is possible by using the eyeWatch Pen, the external control unit containing a compass in one side, which measures the magnetic disk position, and a magnet in the other side,

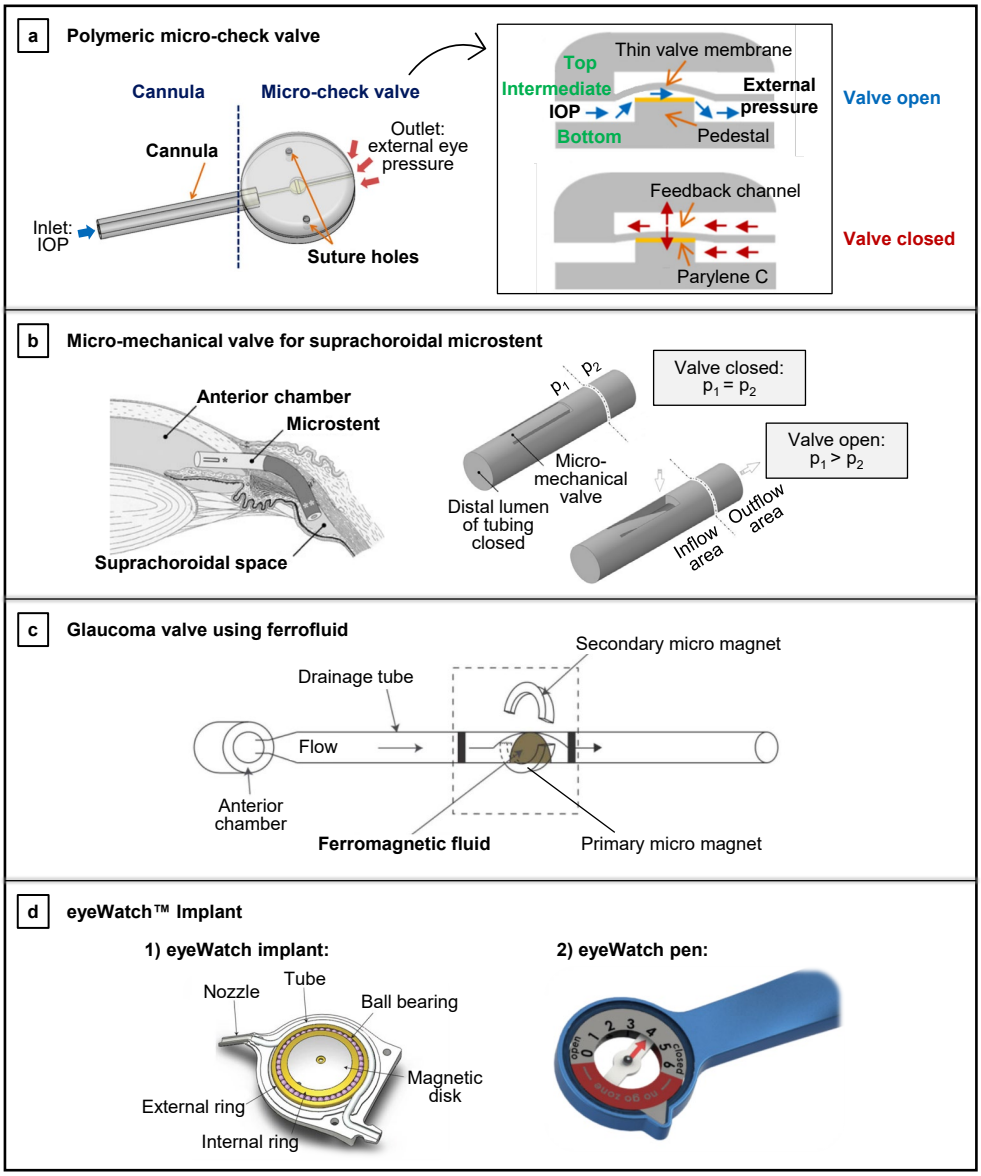

Figure 2.7: Proof-of-concept of innovative passive/active valve mechanisms for glaucoma drainage devices. (**a**) Illustration of a glaucoma drainage device consisting of a cannula (drainage tube) and a micro-check valve; the cross-sectional view of the valve and working principle are represented on the right; image reproduced with permission from [125]. (**b**) Concept of a microstent for drainage of aqueous humor into the suprachoroidal space, showing its flap-like micro-mechanical valve that opens when the pressure in the inflow area (p_1) is higher than the pressure in the outflow area (p_2); image reproduced with permission from [126]. (**c**), Representation of a ferrofluidic valve architecture for a glaucoma drainage device [127]. (**d**) The eyeWatch system, which is comprised of: (1) the eyeWatch implant, depicting details of its valve mechanism [128]; and (2) the eyeWatch pen, which is the control unit of the eyeWatch system [129]; images courtesy of Rheon Medical SA.

which adjusts the compression of the tube. A study comparing the efficacy and safety of the eyeWatch connected to a Baerveldt implant versus the Ahmed valve reported no cases of hypotony in the eyeWatch group as compared with the 33% of the patients implanted with the Ahmed valve where hypotony-related complications were observed [133]. Furthermore, initial clinical results with the eyeWatch suggests that it prevents IOP spikes from occurring by fine-tuning the flow resistance of the device when required, thus promoting smooth pressure transitions that may mitigate the tissue response. Within the 15 patients enrolled in this first clinical trial, 5 patients underwent a magnetic resonance imaging (MRI) for nonophthalmic reasons, and no cases of discomfort during imaging were reported. Moreover, the imaging artifacts created by the implant were not clinically significant. Patients did, however, require adjustment of the magnetic disk back to its previous position set before the MRI. Nonetheless, within this small number of patients ($n = 15$) enrolled in the study, 4 complications affecting 4 patients were reported in a relatively short follow-up time of 12 months: 2 cases of conjunctival wound leak and 2 cases of choroidal detachment. Conjunctival wound leak constitutes a very likely postoperative complication resulting from the implantation of the eyeWatch, which is currently inserted in the eye connected to the end plate of the Baerveldt implant. This combination results in a bulky device (6.5x5.8x0.8 mm for the eyeWatch plus the 250/350 mm^2 Baerveldt plate attached) that takes up too much space under the conjunctiva, which can lead to conjunctival erosion and other pathologies. Therefore, further studies involving a significant number of patients and longer follow-up times are necessary to support the long-term safety, efficacy and clinical relevance of this device in comparison with other implants, as well as its MRI-compatibility [134].

Concepts of temporary valves have also been described. Siewert et al. developed a biodegradable flow resisting polymer membrane designed to fit the inlet area of a glaucoma microstent [135]. The authors claimed that the biodegradable membrane would allow for controlled drainage in the early postoperative period and maximized flow capacity at 6 months when degradation is complete. Olson et al. proposed a similar flow restricting mechanism, using a semi-permeable membrane positioned at the tip of a drainage tube that can be ruptured with laser non-invasively after surgery [136]. Initially, the intact membrane will provide high resistance to aqueous humor outflow, to minimize hypotony. Then, when the ophthalmologist determines that the conjunctival wound is stable, the anterior surface of the membrane can be perforated using laser shots to increase fluid flow [136, 137]. The main disadvantage of these concepts is that flow control is only possible during a short-term period (i.e. temporarily).

To help improve the tissue response to MIGS devices implanted subconjunctivally, local drug delivery systems have also been developed. Antimetabolites such as MMC and 5-fluorouracil have been administrated to the subconjunctival space before and during surgery to delay the fibrotic response and improve long-term success [138, 139]. However, potential complications exist with over-administration of these drugs, such as blebitis/bleb related infection, endophthalmitis, bleb leakage, and conjunctival erosion. The incidence of these complications may be reduced with a sustained slow release of antimetabolites to the site of implantation. This can be achieved, for example, by impregnating the antimetabolite into a biodegradable film, which is then placed on the subconjunctival space at the time of device implantation. The biodegradable film will release the antimetabolite

in a controlled manner during the postoperative period, which may benefit the tissue response [140]. Another factor influencing the tissue reaction is the surface topography of the implant, as it constitutes the major site of interaction with the surrounding tissue. Thus, a proper adjustment of the topographic features as well as surface chemistry of the implant may additionally benefit the wound healing process [141].

2.7 Outlook

Glaucoma remains a leading cause of irreversible blindness in the world, and currently the only proven method to prevent disease progression is lowering IOP. For a large population of glaucoma patients, conventional treatments with pharmacological medication, laser treatment and surgery are not sufficiently effective and safe, and therefore we have witnessed over the last decades an acceleration in the variety of glaucoma drainage devices as alternative treatment approaches. In this review we have described and evaluated these devices, including conventional aqueous shunts, the trabeculectomy-modifying EX-PRESS® device, and the most recent MIGS devices. The ideal device to be used in more severe cases of glaucoma would be a MIGS device that produces an IOP-lowering effect similar to traditional incisional surgeries, such as trabeculectomy and conventional drainage devices, but with an improved safety profile. The newer subconjunctival, bleb-forming devices currently appear to be the best option in achieving this goal. However, longer term studies of these devices need to be performed, to confirm their efficacy in reducing IOP as compared to that of traditional incisional surgeries. For some patients, such as those with normal pressure glaucoma or very advanced glaucoma that need very low pressures (IOP of 6-10 mmHg), these subconjunctival devices, or any other MIGS devices, may not be sufficient.

Towards the future, reducing the rate of postoperative complications and enhancing the safety profile of current subconjunctival MIGS devices, while maintaining their IOP-lowering efficacy, may be achieved by: (i) integrating an active and non-invasive flow-control mechanism, which should allow for a very precise tuning of the IOP, adapted according to each patient's need – in particular to help avoid hypotony; (ii) using drug-delivery systems that release antifibrotic agents in a controlled manner, so that their effect on the implanted site is prolonged and beneficial for the tissue response; and (iii) optimizing the topography of the implant surface to modulate the fibroblast adhesion.

This thesis presents our contribution to this development of new and improved glaucoma drainage devices that are safer and more effective in reducing IOP, in halting glaucoma disease progression and related visual field loss, and enhancing the quality of life of glaucoma patients. Specifically, we have developed two types of devices that can be suitable for patients with varying degrees of glaucoma severity.

Our first proposed implant is a subconjunctival miniature and magnetically actuated device which contains a hydrodynamic resistance that can be adjusted even after implantation. With this implant, the ophthalmologist will be able to precisely and actively adjust a patient's IOP to a desired, healthy range postoperatively in a non-invasive and non-traumatic way. This is achieved by integrating a magnetic microvalve into the implant, which can open or close fluidic channels by using a simple external magnet. The outflow

of aqueous humor can be kept to a minimum in the immediate postoperative period, thus preventing hypotony, and can be increased to a maximum afterwards to further lower the IOP and stop the glaucoma disease progression. With this ability to change between hydrodynamic resistances, we believe that our device will have the same IOP-lowering capabilities as traditional incisional surgeries but with the benefit of being minimally invasive and thus having a safer risk profile. This minimally invasive nature of our device reduces operating time and tissue dissection required for implantation, which might reduce inflammation and the resultant incidence of postoperative complications.

Our second proposed glaucoma implant is an even less invasive device which might be more suitable for patients with mild glaucoma, where IOP reduction goals are more modest. The main innovation of this device is that, unlike other Schlemm's canal MIGS implants which are fully-metallic as presented earlier in this Chapter, this device is made of a biodegradable and flexible polymer which we expect to slowly degrade and be absorbed by the body over time, leaving behind a patent outflow site for the aqueous humor to continue draining out of the anterior chamber to reduce IOP. This will eliminate the need for a permanent implant which may further scar and lose effectiveness. This biodegradable glaucoma implant provides a promising new approach for restoring outflow in a more natural way.

Bibliography

1. *Surgical innovations in glaucoma* (eds Samples, J. R. & Ahmed, I. I. K.) (Springer, New York City, New York, USA, 2014).
2. Lee, R. M., Bouremel, Y., Eames, I., Brocchini, S. & Khaw, P. T. Translating Minimally Invasive Glaucoma Surgery Devices. *Clinical and Translational Science* **13,** 14–25 (2020).
3. Schellack, N., Schellack, G. & Bezuidenhout, S. Glaucoma: A brief review. *South African Pharmaceutical Journal* **82,** 18–22 (2015).
4. Khouri, A. S. & Fechtner, R. D. *Primary Open-Angle Glaucoma.* in *Glaucoma* (eds Shaarawy, T. M., Sherwood, M. B., Hitchings, R. A. & Crowston, J. G.) 2nd ed., 333–345 (W.B. Saunders, London, England, UK, 2015).
5. Goel, M., Picciani, R. G., Lee, R. K. & Bhattacharya, S. K. Aqueous Humor Dynamics: A Review. *The Open Ophthalmology Journal* **4,** 52–59 (2010).
6. Pitha, I. F. & Kass, M. A. *Ocular Hypertension.* in *Glaucoma* (eds Shaarawy, T. M., Sherwood, M. B., Hitchings, R. A. & Crowston, J. G.) 2nd ed., 325–332 (W.B. Saunders, London, England, UK, 2015).
7. Siggers, J. H. & Ethier, C. R. Fluid Mechanics of the Eye. *Annual Review of Fluid Mechanics* **44,** 347–372 (2012).
8. Skalicky, S. E. *The Ciliary Body and Aqueous Fluid Formation and Drainage.* in *Ocular and Visual Physiology: Clinical Application* 67–84 (Springer, Singapore, 2016).
9. Meshcer, A. L. *The Eye & Ear: Special Sense Organs* in *Junqueira's Basic Histology: Text and Atlas* 14th ed., 490–523 (McGraw-Hill Education, New York City, New York, USA, 2016).
10. Treuting, P. M., Wong, R., Tu, D. C. & Phan, I. *Special Senses: Eye.* in *Comparative Anatomy and Histology* (eds Treuting, P. M. & Dintzis, S. M.) 395–418 (Elsevier/Academic Press, London, England, UK, 2012).
11. Andrew, N. H., Akkach, S. & Casson, R. J. A review of aqueous outflow resistance and its relevance to microinvasive glaucoma surgery. *Survey of Ophthalmology* **65,** 18–31 (2020).
12. Swaminathan, S. S., Oh, D. J., Kang, M. H. & Rhee, D. J. Aqueous outflow: Segmental and distal flow. *Journal of Cataract and Refractive Surgery* **40,** 1263–1272 (2014).
13. Johnson, M. 'What controls aqueous humour outflow resistance?' *Experimental Eye Research* **82,** 545–557 (2006).
14. Meier-Gibbons, F. & Töteberg-Harms, M. *Aqueous Humor Dynamics and Its Influence on Glaucoma.* in *Ocular Fluid Dynamics* (eds Guidoboni, G., Harris, A. & Sacco, R.) 191–214 (Birkhäuser, Basel, Switzerland, 2019).
15. Johnson, M., McLaren, J. W. & Overby, D. R. Unconventional aqueous humor outflow: A review. *Experimental Eye Research* **158,** 94–111 (2017).

16. Johnson, M. & Erickson, K. *Mechanisms and routes of aqueous humor drainage.* in *Principles and Practice of Ophthalmology* (eds Albert, D. M. & Jakobiec, F. A.) 2577–2595 (W.B. Saunders, Philadelphia, Pennsylvania, USA, 2000).

17. Yadav, K. S., Rajpurohit, R. & Sharma, S. Glaucoma: Current treatment and impact of advanced drug delivery systems. *Life Sciences* **221,** 362–376 (2019).

18. Conlon, R., Saheb, H. & Ahmed, I. I. K. Glaucoma treatment trends: a review. *Canadian Journal of Ophthalmology* **52,** 114–124 (2017).

19. Lusthaus, J. & Goldberg, I. Current management of glaucoma. *The Medical Journal of Australia* **210,** 180–187 (2019).

20. Gedde, S. J., Parrish, R. K., Budenz, D. L. & Heuer, D. K. Update on aqueous shunts. *Experimental Eye Research* **93,** 284–290 (2011).

21. Shaarawy, T., Goldberg, I. & Fechtner, R. EX-PRESS glaucoma filtration device: Review of clinical experience and comparison with trabeculectomy. *Survey of Ophthalmology* **60,** 327–345 (2015).

22. Gedde, S. J. *et al.* Treatment Outcomes in the Tube Versus Trabeculectomy (TVT) Study After Five Years of Follow-up. *American Journal of Ophthalmology* **153,** 789–803.e2 (2012).

23. Richter, G. M. & Coleman, A. L. Minimally invasive glaucoma surgery: Current status and future prospects. *Clinical Ophthalmology* **10,** 189–206 (2016).

24. Bar-David, L. & Blumenthal, E. Z. Evolution of Glaucoma Surgery in the Last 25 Years. *Rambam Maimonides Medical Journal* **9,** e0024 (2018).

25. Stamper, R., Lieberman, M. & Drake, M. *Glaucoma outflow procedures*. in *Becker-Shaffer's Diagnosis and Therapy of the Glaucomas* 8th ed., 466–490 (Elsevier Inc., Edinburgh, Scotland, UK, 2009).

26. Nassiri, N. *et al.* Ahmed Glaucoma Valve and Single-Plate Molteno Implants in Treatment of Refractory Glaucoma: A Comparative Study. *American Journal of Ophthalmology* **149,** 893–902 (2010).

27. Denis, P. *et al.* A First-in-Human Study of the Efficacy and Safety of MINIject in Patients with Medically Uncontrolled Open-Angle Glaucoma (STAR-I). *Ophthalmology Glaucoma* **2,** 290–297 (2019).

28. Grover, D. S. *et al.* Performance and Safety of a New Ab Interno Gelatin Stent in Refractory Glaucoma at 12 Months. *American Journal of Ophthalmology* **183,** 25–36 (2017).

29. Christakis, P. G. *et al.* The Ahmed Versus Baerveldt Study: Five-Year Treatment Outcomes. *Ophthalmology* **123,** 2093–2102 (2016).

30. Batlle, J. F. *et al.* Three-Year Follow-up of a Novel Aqueous Humor MicroShunt. *Journal of Glaucoma* **25,** e58–65 (2016).

31. Netland, P. A. *et al.* Randomized, Prospective, Comparative Trial of EX-PRESS Glaucoma Filtration Device versus Trabeculectomy (XVT Study). *American Journal of Ophthalmology* **157,** 433–440.e3 (2014).

32. Ahmed, I. I. K. *et al.* A Prospective Randomized Trial Comparing Hydrus and iStent Microinvasive Glaucoma Surgery Implants for Standalone Treatment of Open-Angle Glaucoma: The COMPARE Study. *Ophthalmology* **127,** 52–61 (2020).

33. Samuelson, T. W. *et al.* Prospective, Randomized, Controlled Pivotal Trial of an Ab Interno Implanted Trabecular Micro-Bypass in Primary Open-Angle Glaucoma and Cataract: Two-Year Results. *Ophthalmology* **126,** 811–821 (2019).

34. Reiss, G. *et al.* Safety and Effectiveness of CyPass Supraciliary Micro-Stent in Primary Open-Angle Glaucoma: 5-Year Results from the COMPASS XT Study. *American Journal of Ophthalmology* **208,** 219–225 (2019).

35. Skaat, A. *et al.* Gold micro-shunt implants versus ahmed glaucoma valve: Long-term outcomes of a prospective randomized clinical trial. *Journal of Glaucoma* **25,** 155–161 (2016).

36. Fili, S., Janoud, L., Vastardis, I., Wölfelschneider, P. & Kohlhaas, M. The STARflo™ glaucoma implant: a single-centre experience at 24 months. *Graefe's Archive for Clinical and Experimental Ophthalmology* **257,** 2699–2706 (2019).

37. Koh, V., Chew, P., Triolo, G., Lim, K. S. & Barton, K. Treatment Outcomes Using the PAUL Glaucoma Implant to Control Intraocular Pressure in Eyes with Refractory Glaucoma. *Ophthalmology Glaucoma* **3,** 350–359 (2020).

38. Batlle, J. F., Corona, A. & Albuquerque, R. Long-term Results of the PRESERFLO MicroShunt in Patients with Primary Open-angle Glaucoma from a Single-center Nonrandomized Study. *Journal of Glaucoma* **30,** 281–286 (2021).

39. Sousa, D. C. & Pinto, L. A. Trabeculectomy - Prevention and Management of Complications. *European Ophthalmic Review* **12,** 98–101 (2018).

40. Molteno Ophthalmic Limited. *Molteno® and Molteno3® Glaucoma Drainage Devices.* https://glaucoma-molteno.com/. 2020.

41. Riva, I., Roberti, G., Oddone, F., Konstas, A. G. & Quaranta, L. Ahmed glaucoma valve implant: Surgical technique and complications. *Clinical Ophthalmology* **11,** 357–367 (2017).

42. New World Medical Inc. *The Ahmed Glaucoma Valve.* https://www.labtician.com/wp-content/uploads/2019/09/NWM_Product_Brochure_revE_50-0038.pdf. 2020.

43. Chaudhry, M., Grover, S., Baisakhiya, S., Bajaj, A. & Bhatia, M. S. Artificial drainage devices for glaucoma surgery: an overview. *Nepalese Journal of Ophthalmology* **4,** 295–302 (2012).

44. Ayyala, R. S., Duarte, J. L. & Sahiner, N. Glaucoma drainage devices: State of the art. *Expert Review of Medical Devices* **3,** 509–521 (2006).

45. Schmidt, W. *et al.* New Concepts for Glaucoma Implants - Controlled Aqueous Humor Drainage, Encapsulation Prevention and Local Drug Delivery. *Current Pharmaceutical Biotechnology* **14,** 98–111 (2013).

46. Thomas, R., Gieser, S. C. & Billson, F. Molteno implant surgery for advanced glaucoma. *Australian and New Zealand Journal of Ophthalmology* **23,** 9–15 (1995).

47. Molteno, A. C. The optimal design of drainage implants for glaucoma. *Transactions of the Ophthalmologic Society of New Zealand* **33,** 39–41 (1981).

48. Cullen, C. L. *Glaucoma drainage devices*. in *Visual Prosthesis and Ophthalmic Devices* (eds Tombran-Tink, J., Barnstable, C. J. & Rizzo, J. F.) 173–190 (Humana Press, Totowa, New Jersey, USA, 2007).

49. Thompson, A. M., Bevin, T. H. & Molteno, A. C. *Surgical Technique 1 (Molteno Glaucoma Implant).* in *Glaucoma* (eds Shaarawy, T. M., Sherwood, M. B., Hitchings, R. A. & Crowston, J. G.) 2nd ed., 1051–1063 (W.B. Saunders, London, England, UK, 2015).

50. Barton, K. & Heuer, D. K. *Aqueous Shunts: Choice of Implant*. in *Glaucoma* (eds Shaarawy, T. M., Sherwood, M. B., Hitchings, R. A. & Crowston, J. G.) 2nd ed., 1045–1050 (W.B. Saunders, London, England, UK, 2015).

51. Tojo, N., Ueda-Consolvo, T., Yanagisawa, S. & Hayashi, A. Baerveldt® glaucoma implant surgery with the double scleral flap technique to prevent Hoffman elbow exposure. *Graefe's Archive for Clinical and Experimental Ophthalmology* **255,** 2001–2008 (2017).

52. Advanced Ophthalmic Innovations. *PAUL® Glaucoma Implant.* https://aoi.sg/product/. 2021.

53. Lim, K. S. Control and optimisation of fluid flow in glaucoma drainage device surgery. *Eye* **32,** 230–234 (2018).

54. Brandt, J. D., Hammel, N., Fenerty, C. & Karaconji, T. *Glaucoma Drainage Devices*. in *Surgical Management of Childhood Glaucoma* (eds Grajewski, A. L., Bitrian, E., Papadopoulos, M. & Freedman, S. F.) 99–127 (Springer International Publishing, Cham, Switzerland, 2018).

55. Kolomeyer, A. M. *et al.* Pars plana Baerveldt tube insertion with pars plana vitrectomy for refractory glaucoma. *Oman Journal of Ophthalmology* **5,** 19–27 (2012).

56. Kara, E. & Kutlar, A. I. CFD analysis of the Ahmed glaucoma valve and design of an alternative device. *Computer Methods in Biomechanics and Biomedical Engineering* **13,** 655–662 (2010).

57. Anderson, J. D. *Some Reflections on the History of Fluid Dynamics*. in *Handbook of Fluid dynamics* (ed Johnson, R. W.) 2nd ed., (2–1)–(2–11) (Taylor & Francis Group, Boca Raton, Florida, USA, 2016).

58. Bochmann, F. *et al.* Intraoperative testing of opening and closing pressure predicts risk of low intraocular pressure after Ahmed glaucoma valve implantation. *Eye* **28,** 1184–1189 (2014).

59. Moss, E. B. & Trope, G. E. Assessment of Closing Pressure in Silicone Ahmed FP7 Glaucoma Valves. *Journal of Glaucoma* **17,** 489–493 (2008).

60. Ishida, K. *et al.* Comparison of Polypropylene and Silicone Ahmed Glaucoma Valves. *Ophthalmology* **113,** 1320–1326 (2006).

61. Mosaed, S. & Minckler, D. S. Aqueous shunts in the treatment of glaucoma. *Expert Review of Medical Devices* **7,** 661–666 (2010).

62. Sluch, I. *et al.* Clinical Experience with the M4 Ahmed Glaucoma Drainage Implant. *Journal of Current Glaucoma Practice* **11,** 92–96 (2017).

63. U.S. Food and Drug Administration. *Premarket Studies of Implantable Minimally Invasive Glaucoma Surgical (MIGS) Devices: Draft Guidance for Industry and Food and Drug Administration Staff.* https://www.fda.gov/regulatory-information/search-fda-guidance-documents/premarket-studies-implantable-minimally-invasive-glaucoma-surgical-migs-devices. 2015.

64. U.S. Food and Drug Administration. *510(k) Premarket Notification - AHMED® ClearPath Glaucoma Drainage Device* https://www.accessdata.fda.gov/cdrh_docs/pdf18/K182518.pdf. 2021.

65. Agrawal, P. & Bhardwaj, P. Glaucoma drainage implants. *International Journal of Ophthalmology* **13,** 1318–1328 (2020).

66. Dahan, E. & Mermoud, A. *The Ex-press™ Miniature Glaucoma Implant*. in *Glaucoma* (eds Shaarawy, T. M., Sherwood, M. B., Hitchings, R. A. & Crowston, J. G.) 2nd ed., 1176–1182 (W.B. Saunders, London, England, UK, 2015).

67. Chan, J. E. & Netland, P. A. EX-PRESS glaucoma filtration device: Efficacy, safety, and predictability. *Medical Devices: Evidence and Research* **8,** 381–388 (2015).

68. Patel, H. Y., Wagschal, L. D., Trope, G. E. & Buys, Y. M. Economic Analysis of the Ex-PRESS Miniature Glaucoma Device Versus Trabeculectomy. *Journal of Glaucoma* **23,** 385–390 (2014).

69. Gedde, S. J. *et al.* Treatment Outcomes in the Primary Tube Versus Trabeculectomy Study after 3 Years of Follow-up. *Ophthalmology* **127,** 333–345 (2020).

70. Budenz, D. L. *et al.* Five-year treatment outcomes in the ahmed baerveldt comparison study. *Ophthalmology* **122,** 308–316 (2015).

71. Wang, Y. W., Wang, P. B., Zeng, C. & Xia, X. B. Comparison of the Ahmed glaucoma valve with the Baerveldt glaucoma implant: a meta-analysis. *BMC Ophthalmology* **15,** 132 (2015).

72. Schehlein, E. M., Kaleem, M. A., Swamy, R. & Saeedi, O. J. Microinvasive glaucoma surgery: an evidence-based assessment. *Expert Review of Ophthalmology* **12,** 331–343 (2017).

73. Saheb, H. & Ahmed, I. I. K. Micro-invasive glaucoma surgery: current prespectives and future directions. *Current Opinion in Ophthalmology* **23,** 96–104 (2012).

74. European Glaucoma Society. European Glaucoma Society Terminology and Guidelines for Glaucoma, 5th Edition. *British Journal of Ophthalmology* **105,** 1–169 (2021).

75. Shah, M. Micro-invasive glaucoma surgery – an interventional glaucoma revolution. *Eye and Vision* **6,** 29 (2019).

76. Dick, H. B., Schultz, T. & Gerste, R. D. Miniaturization in Glaucoma Monitoring and Treatment: A Review of New Technologies That Require a Minimal Surgical Approach. *Ophthalmology and Therapy* **8,** 19–30 (2019).

77. Glaukos. *iStent Surgery | Glaukos.* https://www.glaukos.com/healthcare-professionals/istent-inject/. 2020.

78. Shaarawy, T. M., Moschos, M. M. & Sherwood, M. B. *New Glaucoma Surgical Alternatives*. in *Glaucoma* (eds Shaarawy, T. M., Sherwood, M. B., Hitchings, R. A. & Crowston, J. G.) 2nd ed., 1188–1201 (W.B. Saunders, London, England, UK, 2015).

79. Brandão, L. M. & Grieshaber, M. C. Update on minimally invasive glaucoma surgery (MIGS) and new implants. *Journal of Ophthalmology* **2013,** 705915 (2013).

80. Glaukos. *Glaukos - iStent inject® W* https://www.glaukos.com/en-uk/healthcare-professionals/istent-inject-w/. 2021.

81. Chen, D. Z. & Sng, C. C. Safety and Efficacy of Microinvasive Glaucoma Surgery. *Journal of Ophthalmology* **2017,** 3182935 (2017).

82. Kaplowitz, K., Schuman, J. S. & Loewen, N. A. Techniques and outcomes of minimally invasive trabecular ablation and bypass surgery. *The British journal of ophthalmology* **98,** 579–585 (2014).

83. Samet, S., Ong, J. A. & Ahmed, I. I. K. Hydrus microstent implantation for surgical management of glaucoma: a review of design, efficacy and safety. *Eye and Vision* **6,** 32 (2019).

84. *Glaucoma Surgery: Treatment and Techniques* (eds Caretti, L. & Buratto, L.) (Springer International Publishing, Cham, Switzerland, 2018).

85. Kammer, J. A. & Mundy, K. M. Suprachoroidal Devices in Glaucoma Surgery. *Middle East African Journal of Ophthalmology* **22,** 45–52 (2015).

86. Fili, S., Wölfelschneider, P. & Kohlhaas, M. The STARflo glaucoma implant: preliminary 12 months results. *Graefe's Archive for Clinical and Experimental Ophthalmology* **256,** 773–781 (2018).

87. García-Feijoo, J. *et al.* Supraciliary micro-stent implantation for open-angle glaucoma failing topical therapy: 1-year results of a multicenter study. *American Journal of Ophthalmology* **159,** 1075–1081.e1 (2015).

88. Hoeh, H. *et al.* Initial clinical experience with the CyPass micro-stent: Safety and surgical outcomes of a novel supraciliary microstent. *Journal of Glaucoma* **25,** 106–112 (2016).

89. Tam, D. Y. & Ahmed, I. I. K. *New Glaucoma Surgical Devices*. in *Glaucoma. Essentials in Ophthalmology* (eds Grehn, F. & Stamper, R.) 75–98 (Springer-Verlag, Berlin and Heidelberg, 2009).

90. Figus, M. *et al.* The supraciliary space as a suitable pathway for glaucoma surgery: Ho-hum or home run? *Survey of Ophthalmology* **62,** 828–837 (2017).

91. Gigon, A. & Shaarawy, T. The Suprachoroidal Route in Glaucoma Surgery. *Journal of Current* **10,** 13–20 (2016).

92. Oatts, J. T. *et al.* In vitro and in vivo comparison of two suprachoroidal shunts. *Investigative Ophthalmology & Visual Science* **54,** 5416–5423 (2013).

93. Agnifili, L. *et al.* Histological findings of failed gold micro shunts in primary open-angle glaucoma. *Graefe's Archive for Clinical and Experimental Ophthalmology* **250,** 143–149 (2012).

94. Rękas, M., Pawlik, B., Grala, B. & Kozłowski, W. Clinical and morphological evaluation of gold micro shunt after unsuccessful surgical treatment of patients with primary open-angle glaucoma. *Eye* **27,** 1214–1217 (2013).

95. Hueber, A., Roters, S., Jordan, J. F. & Konen, W. Retrospective analysis of the success and safety of Gold Micro Shunt Implantation in glaucoma. *BMC Ophthalmology* **13,** 35 (2013).

96. Allergan. *What is the XEN® Gel Stent?.* https : / / www . xengelstent . com / XENGelStent. 2020.

97. Sadruddin, O., Pinchuk, L., Angeles, R. & Palmberg, P. Ab externo implantation of the MicroShunt, a poly (styrene-block-isobutylene-block-styrene) surgical device for the treatment of primary open-angle glaucoma: a review. *Eye and Vision* **6,** 36 (2019).

98. Dervenis, N., Mikropoulou, A. M., Dervenis, P. & Lewis, A. Dislocation of a previously successful XEN glaucoma implant into the anterior chamber: A case report. *BMC Ophthalmology* **17,** 4–6 (2017).

99. Ali, Z. C., Khoo, D. I., Stringa, F. & Shankar, V. Migration of XEN45 implant: Findings, mechanism, and management. *Journal of Current Glaucoma Practice* **13,** 79–81 (2019).

100. Scheres, L. M. J. *et al.* XEN® Gel Stent compared to PRESERFLO™ MicroShunt implantation for primary open-angle glaucoma: two-year results. *Acta Ophthalmologica* **99,** e433–e440 (2021).

101. Post, M., Lubiński, W., Śliwiak, D., Podborączyńska-Jodko, K. & Mularczyk, M. XEN Gel Stent in the management of primary open-angle glaucoma. *Documenta Ophthalmologica* **141,** 65–76 (2020).

102. Fernández-García, A. *et al.* Medium-term clinical outcomes following Xen45 device implantation. *International Ophthalmology* **40,** 709–715 (2020).

103. Kalina, A. G., Kalina, P. H. & Brown, M. M. XEN® Gel Stent in Medically Refractory Open-Angle Glaucoma: Results and Observations After One Year of Use in the United States. *Ophthalmology and Therapy* **8,** 435–446 (2019).

104. Pinchuk, L., Riss, I., Batlle, J. F., Beckers, H. J. & Stalmans, I. *An ab-externo minimally invasive aqueous shunt comprised of a novel biomaterial.* in *New Concepts in Glaucoma Surgery Series - Volume 1* (eds Ahmed, I. & Samples, J.) 181–193 (Kugler Publications, Amsterdam, The Netherlands, 2020).

105. Acosta, A. C. *et al.* A Newly Designed Glaucoma Drainage Implant Made of Poly(styrene-b-isobutylene-b-styrene). *Archives of Ophthalmology* **124,** 1742–1749 (2006).

106. Gedde, S. J., Panarelli, J. F., Banitt, M. R. & Lee, R. K. Evidenced-based comparison of aqueous shunts. *Current Opinion in Ophthalmology* **24,** 87–95 (2013).

107. Green, W., Lind, J. T. & Sheybani, A. Review of the Xen Gel Stent and InnFocus MicroShunt. *Current Opinion in Ophthalmology* **29,** 162–170 (2018).

108. Beckers, H. J. & Pinchuk, L. Minimally Invasive Glaucoma Surgery with a New Ab-externo Subconjunctival Bypass – Current Status and Review of Literature. *European Ophthalmic Review* **13,** 27–30 (2019).

109. Patel, S. & Pasquale, L. R. Glaucoma drainage devices: A review of the past, present, and future. *Seminars in Ophthalmology* **25,** 265–270 (2010).

110. Schwartz, K. S., Lee, R. K. & Gedde, S. J. Glaucoma drainage implants: A critical comparison of types. *Current Opinion in Ophthalmology* **17,** 181–189 (2006).

111. Fingeret, M. & Dickerson, J. E. The role of minimally invasive glaucoma surgery devices in the management of glaucoma. *Optometry and Vision Science* **95,** 155–162 (2018).

112. Beltran-Agullo, L. *et al.* Comparison of Visual Recovery Following Ex-PRESS Versus Trabeculectomy: Results of a Prospective Randomized Controlled Trial. *Journal of Glaucoma* **24,** 181–186 (2015).

113. Schlenker, M. B., Durr, G. M., Michaelov, E. & Ahmed, I. I. K. Intermediate Outcomes of a Novel Standalone Ab Externo SIBS Microshunt With Mitomycin C. *American Journal of Ophthalmology* **215,** 141–153 (2020).

114. Durr, G. M., Schlenker, M. B., Samet, S. & Ahmed, I. I. K. One-Year Outcomes of Stand-Alone Ab Externo SIBS Microshunt Implantation in Refractory Glaucoma. *British Journal of Ophthalmology* **106,** 71–79 (2022).

115. Schlenker, M. B. *et al.* Efficacy, Safety, and Risk Factors for Failure of Standalone Ab Interno Gelatin Microstent Implantation versus Standalone Trabeculectomy. *Ophthalmology* **124,** 1579–1588 (2017).

116. Pinchuk, L. *et al.* The development of a micro-shunt made from poly(styrene-block-isobutylene-block-styrene) to treat glaucoma. *Journal of Biomedical Materials Research - Part B Applied Biomaterials* **105,** 211–221 (2017).

117. Pillunat, L. E., Erb, C., Jünemann, A. G. & Kimmich, F. Micro-invasive glaucoma surgery (MIGS): A review of surgical procedures using stents. *Clinical Ophthalmology* **11,** 1583–1600 (2017).

118. Ittoop, S. M., Seibold, L. K. & Kahook, M. Y. Current opinion in ophthalmology: Novel glaucoma devices in the pipeline. *Current Opinion in Ophthalmology* **30,** 117–124 (2019).

119. Bettin, P. & Di Matteo, F. Glaucoma: Present challenges and future trends. *Ophthalmic Research* **50,** 197–208 (2013).

120. Mathew, D. J. *et al.* Adherence to World Glaucoma Association Guidelines for Surgical Trials in the Era of Microinvasive Glaucoma Surgeries. *Ophthalmology Glaucoma* **2,** 78–85 (2019).

121. Mathew, D. J. & Buys, Y. M. Minimally Invasive Glaucoma Surgery: A Critical Appraisal of the Literature. *Annual Review of Vision Science* **6,** 47–89 (2020).

122. Agrawal, P. & Bradshaw, S. E. Systematic Literature Review of Clinical and Economic Outcomes of Micro-Invasive Glaucoma Surgery (MIGS) in Primary Open-Angle Glaucoma. *Ophthalmology and Therapy* **7,** 49–73 (2018).

123. Vinod, K. & Gedde, S. J. Clinical investigation of new glaucoma procedures. *Current Opinion in Ophthalmology* **28,** 187–193 (2017).

124. Lim, K. S., Allan, B. D. S., Lloyd, A. W., Muir, A. & Khaw, P. T. Glaucoma drainage devices: past, present, and future. *The British journal of ophthalmology* **82,** 1083–1089 (1998).

125. Park, C. J., Yang, D. S., Cha, J. J. & Lee, J. H. Polymeric check valve with an elevated pedestal for precise cracking pressure in a glaucoma drainage device. *Biomedical Microdevices* **18,** 20 (2016).

126. Siewert, S. *et al.* Development of a micro-mechanical valve in a novel glaucoma implant. *Biomedical Microdevices* **14,** 907–920 (2012).

127. Paschalis, E. I., Chodosh, J., Sperling, R. A., Salvador-Culla, B. & Dohlman, C. A Novel Implantable Glaucoma Valve Using Ferrofluid. *PLoS ONE* **8,** e67404 (2013).

128. Villamarin, A., Roy, S., Bigler, S. & Stergiopulos, N. A new adjustable glaucoma drainage device. *Investigative Ophthalmology & Visual Science* **55,** 1848–1852 (2014).

129. Rheon Medical. *eyeWatch implant | Rheon Medical.* https://www.rheonmedical.com/eyewatch. 2020.

130. Moon, S. *et al.* Selectively bonded polymeric glaucoma drainage device for reliable regulation of intraocular pressure. *Biomedical Microdevices* **14,** 325–335 (2012).

131. Lin, J. C. H., Chen, P. J., Yu, B., Humayun, M. & Tail, Y. C. *Minimally invasive parylene dual-valved flow drainage shunt for glaucoma implant*. in *Proceedings of the 2009 IEEE 22nd International Conference on Micro Electro Mechanical Systems* (Sorrento, Italy, 2009), 196–199.

132. Villamarin, A. *et al.* In vivo testing of a novel adjustable glaucoma drainage device. *Investigative Ophthalmology & Visual Science* **55,** 7520–7524 (2014).

133. Roy, S. *et al.* Comparison between the eyeWatch Device and the Ahmed Valve in Refractory Glaucoma. *Journal of Glaucoma* **29,** 401–405 (2020).

134. Roy, S. *et al.* Initial Clinical Results of the eyeWatch: a New Adjustable Glaucoma Drainage Device Used in Refractory Glaucoma Surgery. *Journal of Glaucoma* **28,** 452–458 (2019).

135. Siewert, S. *et al.* Development of a biodegradable flow resisting polymer membrane for a novel glaucoma microstent. *Biomedical Microdevices* **19,** 78 (2017).

136. Olson, J. L., Bhandari, R., Groman-Lupa, S., Santos-Cantu, D. & Velez-Montoya, R. Development of a laser controlled device to modulate intraocular pressure. *Expert Review of Medical Devices* **14,** 229–236 (2017).

137. Olson, J. L., Velez-Montoya, R. & Bhandari, R. Laser Activated Flow Regulator for Glaucoma Drainage Devices. *Translational Vision Science & Technology* **3,** 3 (2014).

138. Jacob, J. T., LaCour, O. J. & Burgoyne, C. F. Slow release of the antimetabolite 5-fluorouracil (5-FU) from modified Baerveldt glaucoma drains to prolong drain function. *Biomaterials* **22,** 3329–3335 (2001).

139. Wolters, J. *et al.* History, presence and future of mitomycin C in glaucoma filtration surgery. *Current Opinion in Ophthalmology* **32,** 148–159 (2021).

140. Szigiato, A. A., Podbielski, D. W. & Ahmed, I. I. K. Sustained drug delivery for the management of glaucoma. *Expert Review of Ophthalmology* **12,** 173–186 (2017).

141. Choritz, L. *et al.* Surface topographies of glaucoma drainage devices and their influence on human tenon fibroblast adhesion. *Investigative Ophthalmology & Visual Science* **51,** 4047–4053 (2010).

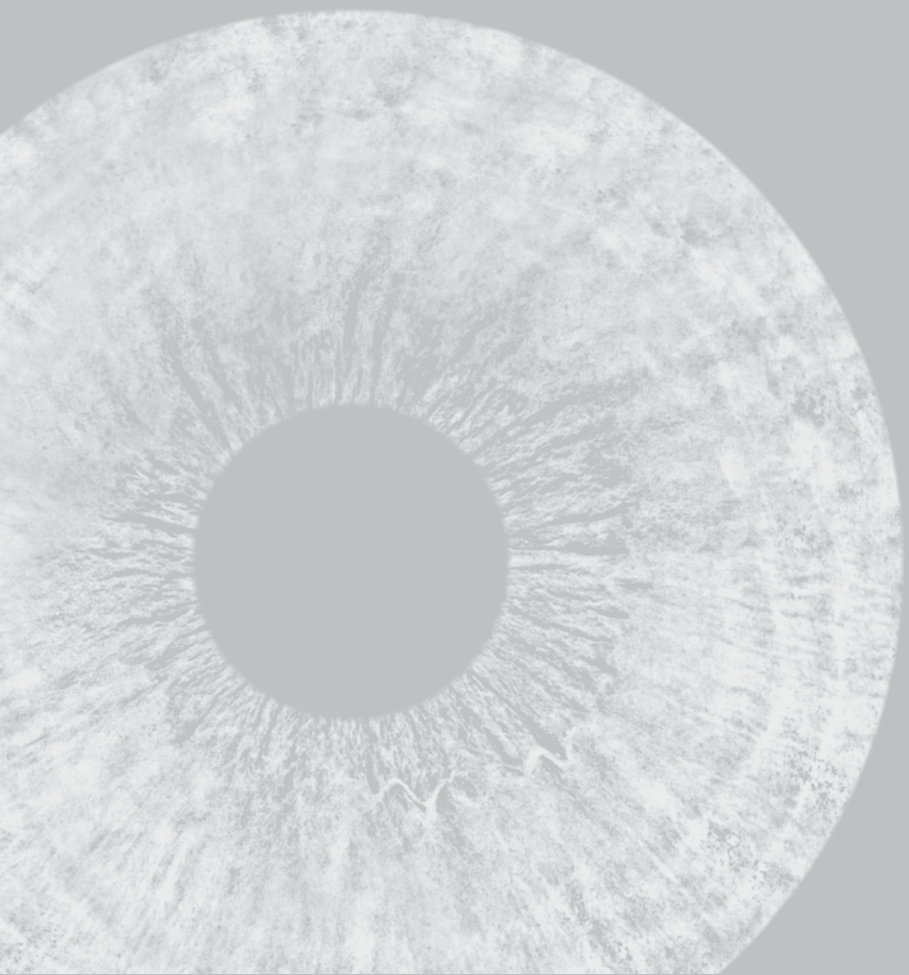

CHAPTER 3

A model for designing intraocular pressure-regulating glaucoma implants

In the previous Chapter we explored the existing glaucoma drainage devices, provided an evidence-based comparison between devices, and surveyed the recent scientific and technological developments that aim to address prevailing unmet needs and unsolved problems. From this literature review, we concluded that a common drawback of most glaucoma implants currently used in clinical practice is that they are passive and do not allow for postsurgical intraocular pressure (IOP) control, which may result in serious complications such as persistent hypotony (too low IOP). This clearly indicates that there is a need for glaucoma implants with a hydrodynamic resistance that can be adjusted after implantation. In this Chapter, the feasibility of using a glaucoma implant with an adjustable hydrodynamic resistance to regulate IOP in glaucoma patients will be explored. To this end, we developed a mathematical model that describes the fluid drainage from the eye through a glaucoma drainage device, its flow into a filtering bleb, and absorption by the subconjunctival vasculature. To obtain insight into the adjustments in the implant's hydrodynamic resistance that are required for IOP control when the two most common postoperative complications following glaucoma filtration surgery take place – hypotony or bleb scarring due to tissue fibrosis –, we simulated the flow through a microshunt with an adjustable lumen diameter. Our findings show that increasing the hydrodynamic resistance of the microshunt by reducing the lumen diameter, can effectively help to prevent hypotony. However, decreasing the hydrodynamic resistance of the implant will not sufficiently decrease the IOP to acceptable levels when the bleb is encapsulated due to tissue fibrosis. Therefore, to effectively reduce IOP, the adjustable glaucoma implant should be combined with a means of reducing fibrosis. The results reported herein may provide guidelines to support the design of future glaucoma implants with adjustable hydrodynamic resistances.

This Chapter is based on:
A model for designing intraocular pressure-regulating glaucoma implants, **Inês C.F. Pereira**, Hans M. Wyss, Leonard Pinchuk, Henny J.M. Beckers, Jaap M.J. den Toonder, *PLoS ONE*, **17**, 2022.

3.1 Introduction

Glaucoma is the second leading cause of preventable blindness worldwide, with over 100 million people expected to suffer from the disease by 2040 [1]. Elevated intraocular pressure (IOP, above 21 mmHg) remains the most important known risk factor for the development and progression of glaucoma. IOP is determined by the balance between the production of aqueous humor within the eye and its drainage out of it through two distinct pathways – the trabecular and the non-trabecular pathway. In patients with primary open-angle glaucoma, there is an abnormal increase of resistance to aqueous outflow through the trabecular outflow pathway, which leads to a build-up of fluid in the eye that results in high IOP [2]. Hence, current treatment options aim to lower the IOP with the goal of preventing additional glaucomatous optic nerve damage [3]. The application of topical ocular hypotensive drug agents is often chosen as the first-line treatment, but fundamental challenges to pharmacological therapy continue to exist, including local and systemic adverse effects and poor patient adherence [3, 4]. Laser-therapy is considered when the visual field continues to deteriorate despite maximum use of topical medication, and if unsuccessful, incisional surgery is considered. Conventional filtration surgeries include trabeculectomy and implantation of glaucoma drainage devices, and both procedures are based upon the same principle: creating an alternative drainage route that allows the aqueous humor to escape from the anterior chamber of the eye as a means of lowering IOP [5]. Conventional aqueous shunts and some of the new minimally invasive glaucoma surgery (MIGS) devices [6], drain the aqueous humor via a shunt into the subconjunctival/sub-Tenon's space, where a fluid reservoir known as filtering bleb is formed, as shown in Figure 3.1. The aqueous humor can then traverse the bleb into the surrounding conjunctival tissue and can be absorbed by the subconjunctival or episcleral vasculature, or, if the bleb is thin-walled, passes directly across the conjunctiva into the tear layer [7, 8].

The bleb and the overlying conjunctiva are considered to be the cornerstone of IOP control following glaucoma filtration surgery [9]. The favorable outcome of filtration surgery is dictated by the proper functioning of the bleb, which is highly dependent upon postoperative modifications in the conjunctival tissue resulting from the healing response [10]. Conjunctival wound healing is a complex multifactorial process consisting of a cascade of overlapping events, including hemostasis, inflammation, cell proliferation and tissue remodeling [11]. During this process, there is a high propensity of subconjunctival fibrous tissue formation, i.e. scarring, resulting in bleb encapsulation (formation of a bleb capsule), which may increase the resistance to aqueous outflow through the bleb wall, thus reducing subconjunctival absorption of aqueous humor. This leads to an elevation of the IOP to preoperative or even higher values, and consequently failure of the glaucoma filtration surgery [8]. There are various mechanisms postulated to contribute to subconjunctival scarring. These mechanisms include previous surgical procedures breaching the conjunctiva, a long history of topical medication, predisposition to conjunctival inflammation, aqueous humor composition, subconjunctival flow rate and direction, as well as hydrostatic pressure acting on the bleb [12]. Antifibrotic agents such as mitomycin C (MMC) and 5-fluorouracil have been increasingly used to control the wound healing process and increase surgical success, however they are often

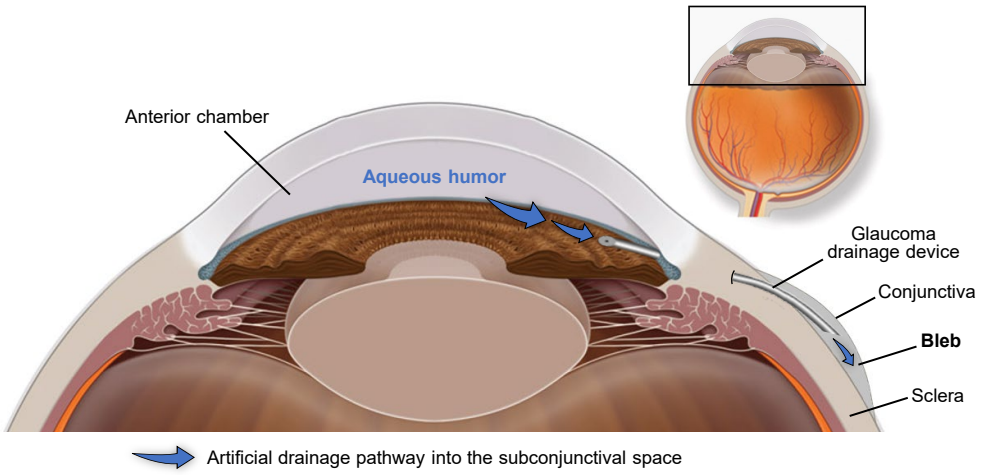

Figure 3.1: Aqueous humor artificial drainage pathway. Schematic representation of the artificial drainage pathway of aqueous humor into the subconjunctival space, where a filtering bleb is formed, following glaucoma drainage device insertion.

associated with serious complications such as bleb leak and hypotony [13, 14]. Besides subconjunctival scarring that leads to increased IOP, hypotony is one of the most common complications following glaucoma surgery. It is defined as very low IOP of 5 mmHg or less, and it may lead to vision loss in up to 20% of the patients who experience hypotony [15]. The acute inflammatory response that naturally follows incisional surgery may also contribute to hypotony – more permeable/leaky subconjunctival capillaries may absorb the aqueous humor at a faster rate than it is produced, thus leading to overfiltration [16].

Although better designed glaucoma implants have emerged in recent years, made from superior materials that evoke minimal tissue inflammation, excessive fibrosis with scar tissue formation and hypotony-related complications are still frequently reported. One reason behind this is that such devices are totally passive, i.e., the drainage of aqueous humor depends upon a fixed hydrodynamic resistance of the shunt [17]. In many cases, however, the hydrodynamic resistance of the shunt may not be optimal which may lead to high IOP, when the resistance in the subconjunctival space is too high (due to the presence of a scar layer), or to overdrainage, if the resistance is too low (resulting in hypotony) [18]. To determine the ideal hydrodynamic resistance that a glaucoma implant must have to overcome these two most common postoperative complications – bleb scarring and hypotony – we developed a model that calculates the pressure in the bleb under these conditions. A porous media model was used to model aqueous humor flow through the bleb and subconjunctival tissue, and its absorption by the subconjunctival vasculature. The model accounts for the bleb size and shape, hydraulic conductivity of the subconjunctival tissue, as well as its fluid absorptive capacity, among other parameters. According to the calculated bleb pressure, the implant design and dimensions, and consequently its hydrodynamic resistance was tuned to achieve a healthy IOP of approximately 10 mmHg.

3.2 Material and methods

The mathematical model used for the calculation of bleb pressure, describing the fluid removal from the anterior chamber of the eye through a glaucoma drainage device, its drainage into the filtering bleb and absorption by the subconjunctival tissue, is based on the work of Gardiner and co-workers [16]. Using this model, Gardiner and co-workers investigated how the IOP is influenced by several factors, including the aqueous humor production and outflow rates, bleb geometry, subconjunctival tissue conductivity and tissue absorptive capacity. We, on the other hand, applied an adapted version of the model to study the possibility to control IOP in glaucoma patients by using a glaucoma implant with adjustable hydrodynamic resistance. To the best of our knowledge, this is the first time that such a model was used to obtain insight into the adjustments in the implant's hydrodynamic resistance that are required for IOP control when the two most common postoperative complications following glaucoma filtration surgery take place, hypotony and bleb scarring.

The commercial finite element method (FEM) package COMSOL Multiphysics was used to numerically solve the mathematical model. The default solver settings were used, and a total of 767,912 triangular mesh elements were created. The maximum element size was set to 0.005 mm and local mesh refinements were not needed, since the average quality of the mesh was 95.98%, and the minimum quality obtained was 55.59%.

3.2.1 Geometry

The model is comprised of two domains: one representing the bleb and subconjunctival tissue, and the other representing the glaucoma drainage device. A tube-like shunt with the same length and lumen diameter as the PRESERFLO™ MicroShunt (Santen, Osaka, Japan) was used to represent the glaucoma drainage device. Its design and dimensions are shown in Figure 3.2 [19]. The sclera was not included in our model. Although it is reported in the literature that some aqueous humor flowing into the bleb after glaucoma filtration surgery is reabsorbed by the episcleral vasculature, tracer-based studies have proved that the conjunctival blood vessels and conjunctival lymphatic system are the main structures involved in removing the excess interstitial subconjunctival fluid (aqueous humor) [9, 20–22]. Taking this into account, we have decided to not include the absorption of aqueous humor by the episcleral vasculature in our model and only consider the conjunctival route of absorption.

The extent and elevation of a filtering bleb vary widely among patients and are important indicators of bleb function. The dimensions of a healthy bleb and overlying conjunctiva/Tenon's capsule are shown in Figure 3.3a and are based on an optical coherence tomography (OCT) image of a functioning bleb, in a patient with a healthy IOP of 10 mmHg. These dimensions were used to simulate the normal case-scenario (healthy/well-functioning bleb) and hypotony cases. To simulate the fibrotic case we have chosen a lower bleb height, as it is commonly reported that scar tissue formation leads to progressive flattening of the bleb, and in some cases even to its disappearance [9]. Additionally, for this scenario a new domain representing the scar layer was added at the interface between the bleb and the subconjunctival tissue, as shown in Figure 3.3b. The thickness of the

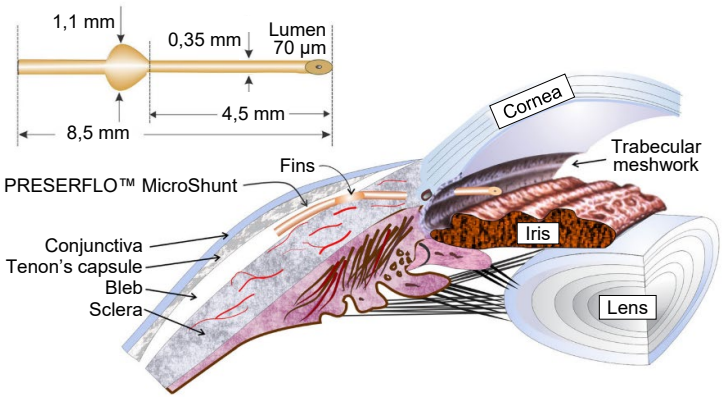

Figure 3.2: The PRESERFLO™ MicroShunt. Schematics showing the PRESERFLO™ Microshunt dimensions and placement in the eye.

scar tissue is dependent upon the natural healing response of each individual after the glaucoma filtration surgery and may vary over time. Nevertheless, in our simulations we have used a constant thickness and only varied the hydraulic conductivity of the tissue to evaluate its impact on the bleb pressure and IOP. It is also generally reported that more fibrosis occurs directly above the center of the bleb, which is where the aqueous humor exits the glaucoma drainage device [8]. Therefore, the thickness of the scar layer used in this model is 100 µm larger at the center than on the lateral sides.

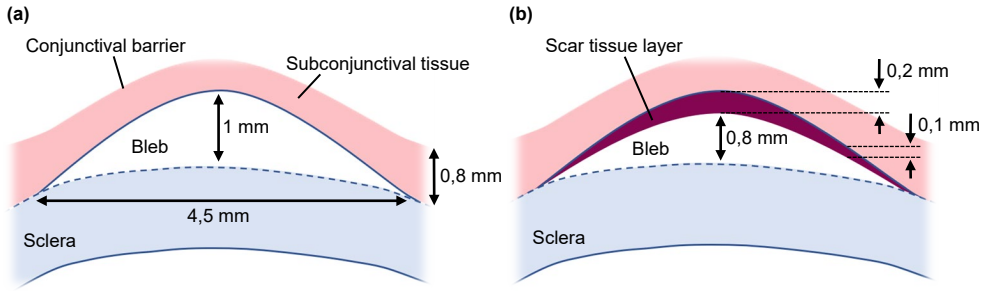

Figure 3.3: Two-dimensional geometry of the filtering bleb. (**a**) Shape and dimensions of a healthy bleb and overlying conjunctival/Tenon's tissue based on a cross-sectional optical coherence tomography (OCT) image (patient with an IOP of 10 mmHg); these dimensions were used to simulate the normal (healthy/well-functioning bleb) and hypotony cases. (**b**) Shape and dimensions of the bleb, scar tissue layer, and subconjunctival tissue used to simulate the bleb scarring scenario.

We assume that the bleb is axisymmetric. Thus, a 2D-axisymmetric model is adopted in which we consider a circular region of the subconjunctival tissue centered on the bleb, as depicted in Figure 3.4. Although not shown, a layer of scar tissue optionally covers the surface of the bleb, depending upon the case study to simulate, as explained above (see Figure 3.3).

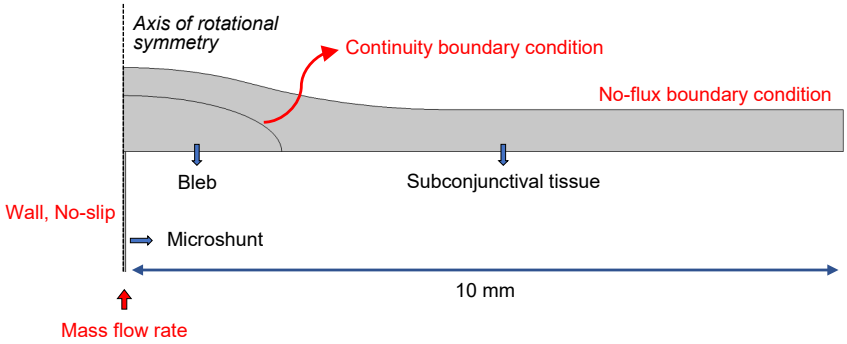

Figure 3.4: 2D-axisymmetric computational domain of the subconjunctival drainage of aqueous humor through a hollow tube-like microshunt. The bleb dimensions are as in Figure 3.3 and a scar tissue layer may be included as in Figure 3.3b. The applied boundary conditions are indicated in red.

3.2.2 Governing equations

The aqueous humor is mainly composed of water (99%), so we describe its behavior by the well-known incompressible Navier-Stokes equation in the shunt domain, coupled with Darcy's law, describing flow in porous media, in the bleb/subconjunctiva domain [23]. Neglecting the gravitational acceleration and assuming steady state, the Navier-Stokes and mass conservation equations describing the fluid flow in the shunt are given as [24]

$$\nabla \cdot \mathbf{v} = 0 \tag{3.1}$$

$$\rho(\mathbf{v} \cdot \nabla \mathbf{v}) = -\nabla p + \mu \nabla^2 \mathbf{v}, \tag{3.2}$$

where ρ[kg m^{-3}] and μ[Pa s] are the density and dynamic viscosity of aqueous humor, respectively, $\mathbf{v}$[m s^{-1}] is the velocity vector, and p[Pa] is the pressure. For the boundary conditions, a mass flow rate calculated from a volumetric flow rate (Q_{in}) of 2.5 µL min^{-1} was assumed at the inlet of the shunt. The value of 2.5 µL min^{-1} was chosen as an approximated average value of aqueous humor production rate during a period of 24 hours. The choice of this value was supported from the literature [25]. For simplification, we did not consider the outflow of aqueous humor through the natural outflow pathways (trabecular and non-trabecular/uveoscleral) in our simulations as was considered by Gardiner and co-workers [16]. The reason for this is that, in a glaucomatous eye and when a glaucoma drainage device is implanted, most aqueous humor drains through the glaucoma implant into the bleb, which represents the easiest fluidic pathway [20]. It is hypothesized in the literature that only 10% of the aqueous humor drains through the natural outflow pathways after trabeculectomy is performed [21].

The average pressure in the bleb p_{bleb} calculated using Darcy's law is applied on the outflow surface of the shunt. Since the wall of the shunt is impermeable, it was modeled with stationary rigid boundaries at which a no-slip boundary condition was imposed.

To describe the movement of fluid into the bleb, through the subconjunctival tissue and its removal by the microvasculature, Darcy's law for flow in porous media was used. Besides the subconjunctival tissue, we considered the bleb as a porous medium since it has numerous microcysts (clear spaces) filled with aqueous humor, lined by epithelium containing goblet cells, and surrounded by a superficial stroma that is composed of loosely arranged connective tissue of irregular collagen with a slight or absent subepithelial inflammatory response of lymphocytes, macrophages, and fibroblasts [12, 22, 26–30]. To couple the equations for the fluid in the shunt domain with Darcy's equation in the bleb, we applied the normal inflow velocity of the fluid leaving the tube as the inlet boundary condition of the bleb, and as mentioned above, we have attributed the average pressure calculated in the bleb as the outlet boundary condition of the tube.

Darcy's empirical observations demonstrated that the fluid velocity in porous media is proportional to the pressure gradient; therefore, fluid transport in the porous media can be described by [31]

$$\mathbf{v}_\mathrm{i} = -K\nabla p_\mathrm{i}, \tag{3.3}$$

where $\mathbf{v}_\mathrm{i}$[m s^{-1}] is the interstitial fluid velocity (often referred to as the Darcy velocity), K[m^2 s^{-1} Pa^{-1}] is the hydraulic conductivity of the tissue, and p_i[Pa] is the hydrostatic pressure in the tissue interstitium. The hydraulic conductivity is the proportionality constant in Darcy's law, and we note here that its value will vary spatially in our model to represent the properties of different tissues, such as scar tissue and subconjunctiva. Additionally, the hydraulic conductivity may vary over time, as a result of the healing response following surgery [16].

The mass balance equation for a steady state incompressible fluid shows that the divergence of the velocity is zero,

$$\nabla \cdot \mathbf{v}_\mathbf{i} = 0. \tag{3.4}$$

This equation is adequate for porous media when there is no fluid source or sink in the medium. However, in biological tissues fluid is exchanged between the interstitial space and the capillaries, which in our model acts as a sink for the fluid. Thus, the steady state incompressible form of the continuity equation becomes

$$\nabla \cdot \mathbf{v}_\mathbf{i} = \phi_\mathrm{v}, \tag{3.5}$$

where ϕ_v is the rate of fluid flow per unit volume from the vasculature into the interstitial space, or vice versa, and can be evaluated through Starling's law as [32, 33]

$$\phi_v = L_p \frac{S_A}{V}(p_v - p_i - \sigma[\pi_v - \pi_i]), \tag{3.6}$$

where L_p[m s^{-1} Pa^{-1}] is the hydraulic permeability of the blood vessel wall, $\frac{S_A}{V}$[m^{-1}] is the surface area of blood vessel walls per volume of tissue for transport in the interstitium, p_v[Pa] is the microvasculature pressure, π_v and π_i [Pa] are the plasma and interstitial fluid oncotic pressures (the osmotic pressure induced by plasma proteins), respectively, and σ is the average reflection coefficient for the plasma proteins (a measure of protein permeability). A reflection coefficient equal to 1 means that the vessel wall is impermeable to plasma proteins, whereas a coefficient equal to 0 means that there is no transport restriction [34]. Because most capillaries in the body are fairly impermeable to high molecular weight proteins, and based on literature research, we have decided to use a reflection coefficient of 0.91 in our simulations. The values of the remaining parameters used in the numerical simulations are listed in Table 3.1, along with references to the experimental studies they are based on.

Table 3.1: Parameter values used in the simulations.

Parameter	Assumed value		Reference
μ, dynamic viscosity of aqueous humor	$7,5 \times 10^{-4}$ Pa s		[24]
ρ, density of aqueous humor	998,7 kg m^{-3}		[24]
L_p, hydraulic permeability of blood vessel wall	Hypotony	1×10^{-8} m s^{-1} Pa^{-1}	[35]
	Normal and Bleb scarring	1×10^{-10} m s^{-1} Pa^{-1}	
$\frac{S_A}{V}$, vessel wall area per tissue volume	$6,7 \times 10^{3}$ m^{-1}		[36]
p_v, vasculature pressure	$1,3 \times 10^{3}$ Pa		[16]
π_v, vessel oncotic pressure	$2,6 \times 10^{3}$ Pa		[16, 37]
π_i, interstitium oncotic pressure	$1,3 \times 10^{3}$ Pa		[16, 37]
σ, reflection coefficient	0,91		[38]
K, hydraulic conductivity	Bleb	$1,5 \times 10^{-8}$ m^2 s^{-1} Pa^{-1}	[16, 39–41]
	Subconjunctival tissue	$1,5 \times 10^{-11}$ m^2 s^{-1} Pa^{-1}	
	Scar tissue	3×10^{-13} m^2 s^{-1} Pa^{-1}	
		2×10^{-13} m^2 s^{-1} Pa^{-1}	
		1×10^{-13} m^2 s^{-1} Pa^{-1}	

We assume that the bleb does not contain vessels, which means that there is no fluid exchange in this domain. Hence, the values attributed to the variables of Starling's equation are only applicable to the subconjunctival tissue. Additionally, due to the extensive hydration of the bleb we assume that it offers little resistance to fluid flow,

and therefore we give it a hydraulic conductivity that is 1000 times higher than that of the subconjunctiva. To investigate the influence of the extent of fibrosis on the aqueous filtration capacity and, consequently, on the IOP, the hydraulic conductivity of the scar tissue layer was varied between $1\times10^{-13} - 3\times10^{-13}$ $m^2\ s^{-1}\ Pa^{-1}$. Regarding the hydraulic permeability of the blood vessel wall in the subconjunctival tissue, we have chosen a lower value to simulate the hypotony case. We have decided to use this value, which is generally reported for tumorous tissues, because in the early postoperative period the tissue is undergoing swelling and acute inflammatory response, which typically results in increased vasculature permeability (leaky vessels) [33, 38, 42].

For the boundary conditions in the bleb/subconjunctiva domain, a no-flux boundary condition was applied on all external boundaries, including the surface in contact with the sclera and except for a central circle at the bottom center of the bleb where the microshunt is positioned. A continuity of flux and pressure was assumed at the interface between the bleb and the subconjunctiva (or between the bleb, scar tissue, and subconjunctiva for the bleb scarring scenario).

The boundary conditions used in the simulations for the shunt and bleb/scar layer/subconjunctival tissue domains are shown in Table 3.2.

Table 3.2: Boundary conditions used in the simulations for the shunt and bleb/scar layer/subconjunctival tissue domains.

Domain	Surface	Boundary conditions	Mathematical expression
Tube	Inlet	Mass flow rate	$\dot{m} = \rho \cdot Q_{in}$, ρ is the aqueous humor density; Q_{in} is the volume flow rate (2.5 µL min^{-1}).
	Outlet	Pressure	$p_{out} = p_i = p_{bleb}$, p_{bleb} is the average pressure calculated in the bleb domain.
	Side walls	No-slip	$\mathbf{v} = 0$, $\mathbf{v}$ is the velocity vector.
Bleb/Subconjunctival tissue	Inlet	Normal inflow velocity (from the tube domain)	$\mathbf{v} = -\mathbf{n}u_0$, $\mathbf{n}$ is the boundary normal pointing out of the domain; u_0 is the normal inflow speed, calculated as follows $u_0 = \mathbf{n} \cdot (\mathbf{v}_r + \mathbf{v}_z)$, $\mathbf{v}_r$ and $\mathbf{v}_z$ being the velocity components in the r and z directions, respectively.
	Side walls	No flux	$-\mathbf{n} \cdot \rho\mathbf{v} = 0$
	Interface bleb/scar layer/subconjunctival tissue	Continuity	$\mathbf{v}_{bleb} = \mathbf{v}_{scar\ layer} = \mathbf{v}_{subconjunctival\ tissue}$ $p_{bleb} = p_{scar\ layer} = p_{subconjunctival\ tissue}$

3.2.3 Model validation based on literature evidence

The validation of the developed model makes use of the available evidence on IOP outcomes after the implantation of the PRESERFLO MicroShunt. Cases of hypotony are rare with this device, especially due to its small lumen diameter of 70 µm [19, 43]. However, there are still patients suffering from this vision-threatening condition. Similarly, and although the material that this implant is made of – poly(styrene-*block*-isobutylene-*block*-styrene), or "SIBS" – is proven to be highly inert and biocompatible, bleb encapsulation cases are still frequently reported [44, 45]. These conditions are associated with extreme, unhealthy IOPs. We compared these values typically reported in clinical trials with those calculated in our simulations to validate the model.

3.2.4 Adjustable glaucoma implant

To obtain insight into the adjustments in the implant's hydrodynamic resistance that are required for IOP control, we have simulated the flow through a microshunt with an adjustable lumen diameter (adjustable hydrodynamic resistance) and its drainage into the subconjunctival space for the different scenarios. In the hypotony case, the simulation was performed with lumen diameters varying between 40 and 70 µm, and for the bleb scarring scenario the lumen diameter was changed from 70 to 370 µm. The hydrodynamic resistance of the microshunt with different lumen diameters was determined, and the resultant IOP was calculated. The hydrodynamic resistance was calculated as

$$r\,(\text{mmHg}/\mu\text{L min}^{-1}) = \frac{IOP - p_{\text{bleb}}}{Q_{\text{in}}}, \tag{3.7}$$

where the IOP is the pressure calculated at the inlet of the glaucoma drainage device, p_{bleb} is the pressure calculated in the bleb, and Q_{in} is the flow rate (2.5 µL min^{-1}). Ideally, an adjustable glaucoma implant must be able to switch between fluidic resistances in order to control and maintain the IOP within healthy values (5–15 mmHg), irrespective of the condition of the bleb/subconjunctival tissue.

3.2.5 Experimental validation

The calculated IOP for the two case scenarios studied with varying shunt lumen diameters was validated experimentally by performing microfluidic tests. For this, two different microchips were fabricated: one for the hypotony model validation, and the other for the encapsulated model validation. In each device, four square cross-section channels were implemented, as shown in Figure 3.5.

All channels have the same length as the PRESERFLO MicroShunt, i.e., 8.5 mm. The height and width of the channels in the hypotony device are, respectively: 37x37, 46x46, 55x55 and 64x64 µm, and in the encapsulated bleb device these are: 64x64, 155x155, 247x247 and 338x338 µm. These dimensions correspond to different circular tube diameters as can be seen in Table 3.3.

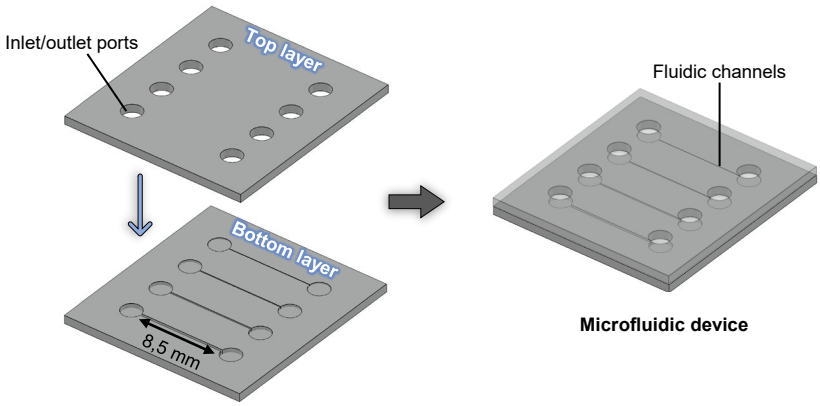

Figure 3.5: Design of the microfluidic devices. Schematic illustration of the design of the microfluidic devices used for the model validation (right side). The bottom and top layers the microdevice is made of are shown on the left side.

Table 3.3: Dimension of the channels of the microfluidic chips and corresponding tube diameters.

Case scenario	Channel dimensions (height x width)	Corresponding circular tube diameter
Hypotony	37 × 37 µm	40 µm
	46 × 46 µm	50 µm
	55 × 55 µm	60 µm
Hypotony and Encapsulated bleb	64 × 64 µm	70 µm
Encapsulated bleb	155 × 155 µm	170 µm
	247 × 247 µm	270 µm
	338 × 338 µm	370 µm

The chosen tube diameters are within the range of diameters also used in the simulations (see previous section 3.2.4). To determine the height and width (h) of a square channel with the same hydraulic resistance (r) of a circular channel, the following formula was applied:

$$r_{\text{square channel}} = r_{\text{circular channel}} \tag{3.8}$$

$$\frac{12\mu L}{1 - 0.917 \times 0.63}\frac{1}{h^4} = \frac{8}{\pi}\mu L\frac{1}{a^4}, \tag{3.9}$$

where μ[Pa s] is the dynamic viscosity of the fluid, L is the length of the channel/tube, h is the height/width of the square channel, and a is the radius of the circular tube.

The microfluidic chips were made from SIBS, the same highly bioinert and biocompatible material that the PRESERFLO MicroShunt is made of. The SIBS pellets with a 25% styrene content were generously provided by InnFocus Inc., a Santen Company (Santen, Osaka, Japan). The devices were fabricated by replica molding with hot embossing, using femtosecond laser machined fused silica glass molds. Femtosecond laser-assisted chemical wet etching has been investigated as an alternative process to fabricate microdevices [46]. It is based on a two-step process of ultrashort-pulsed laser radiation in transparent materials, followed by chemical wet etching to selectively remove the exposed material. The laser beam, focused inside the glass, locally modifies its refractive index and chemical properties, and creates patterns that can be used to, by chemical etching, generate three-dimensional structures with high precision, aspect ratio and complexity [46, 47]. Using this technique, different channel heights can be easily fabricated within one microfluidic chip. This would be extremely cumbersome using other classical manufacturing techniques, such as photolithography, due to the need of multiple photolithography steps with precise alignment, which is very difficult to achieve even when using a mask aligner [48].

The design of the mold for the microfluidic chips was prepared using the dedicated Alphacam software, where the laser scanning path (tool-path) to be fed to the FEMTOprinter f200 aHead (FEMTOprint SA, Switzerland) for exposing the fused silica glass, is also generated. The mold was fabricated on 75x25x1 mm fused silica glass slides. The pulse energy and repetition rate used were 230 nJ and 1000 kHz, respectively. The laser was focused with a Thorlabs 20x microscope objective with a numerical aperture (NA) of 0.4. When the machining program was finished, the glass slide was immersed in a concentrated solution of 45% potassium hydroxide (KOH, Sigma-Aldrich) diluted in water to remove the exposed material. Finally, the mold was rinsed thoroughly with acetone and de-ionized (DI) water to remove all debris. To facilitate the release (demolding) of the patterned SIBS after the hot embossing step (described next), the femtosecond laser-machined glass mold was first coated with a superhydrophobic layer of fluorosilane (Trichloro(1H,1H,2H,2H-perfluorooctyl)silane, Sigma-Aldrich). To improve the adhesion of this coating, the mold underwent an oxygen plasma treatment performed immediately before the fluorosilane vapor deposition. After the silanization treatment, the mold was ready to be used in the hot embossing machine (Specac limited) together with SIBS pellets to fabricate the microfluidic chips. Hot embossing is a microfabrication technique in which micron-scale structures present in a mold are replicated on to a polymer substrate by application of pressure and temperature. We used 150 °C to melt the SIBS and 5 tons of pressure to transfer the features in the mold to the SIBS film. The demolding took place after the hot embossing had cooled down to 80 °C. The patterned SIBS film was then cut into a smaller 16.5x15 mm rectangular film, with the channels centered in the middle, forming the bottom layer of the microfluidic device. The top layer of the device was made of another SIBS rectangular film, but without any imprinted features, and containing the inlet and outlet connections. A biopsy punch was used to create the connection holes. To obtain a closed microfluidic device, bottom and top layers were thermally bonded on a hot plate at 90 °C for 10 min, while applying pressure with a weight placed on top of the device.

The setup used for the microfluidic experiments is illustrated in Figure 3.6 and was comprised of: 1) a syringe pump (Fusion 200, Chemyx Inc.), pumping DI water at a constant flow rate of 2.5 µL min^{-1} – rate of aqueous humor production in the eye; 2) a pressure transducer (Omega Engineering), connected to the syringe pump and to the inlet of the device, thus constantly measuring the pressure upstream the device (in mmHg); and 3) a column of water connected to the outlet of the device, mimicking the pressure in the bleb.

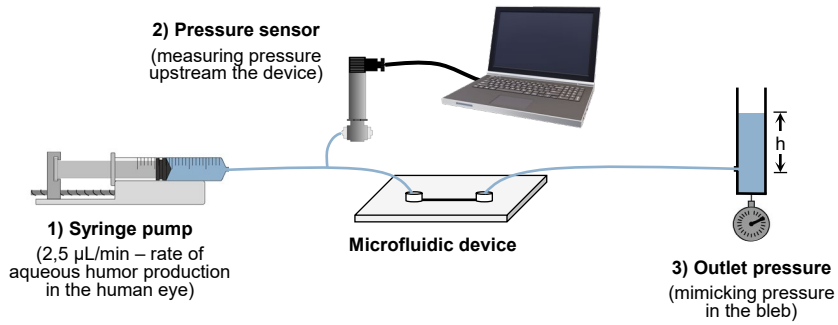

Figure 3.6: Setup used for the microfluidic experiments.

The height of the column of water was adjusted to match the calculated bleb pressures for the different situations studied. The pressure measured at the inlet of the device would correspond to the IOP in a real case scenario. This pressure was measured in four separate samples for each type of microfluidic chip. Then, the measured pressure was finally compared with the calculated IOPs for the different bleb conditions with varying shunt lumen diameters.

3.3 Results

In this section, numerical results obtained for bleb pressure in each of three simulated postoperative conditions – hypotony case, healthy/well-functioning bleb, and encapsulated bleb – are presented. Next, the IOP values calculated when the PRESERFLO MicroShunt is used as the glaucoma drainage device, are compared with the IOP values that are generally reported in the literature following implantation of this device. Finally, we explore the different hydrodynamic resistances that a future adjustable, patient-specific glaucoma implant needs to be able to cover to maintain a healthy IOP. The IOPs calculated using our model are compared to pressures experimentally measured upstream of microfluidic devices that contain channels with different dimensions (thus, different hydrodynamic resistances) when applying constant flow rate while setting the outlet pressure, as a basic *in vitro* model of the implanted glaucoma drainage device.

3.3.1 Bleb pressure and IOP

Figure 3.7 shows the model predictions of the interstitial pressure in the subconjunctival space for three different scenarios: (1) when the subconjunctival space is inflamed in the early period after surgery, which is likely to result in hypotony; (2) in the presence of a healthy or well/functioning bleb; and (3) when excessive fibrosis leads to bleb encapsulation. First, it is possible to verify that for all the investigated situations the interstitial pressure reaches its maximum at the center of the bleb, directly above the distal end of the glaucoma drainage device. The mechanical stresses imposed by the aqueous humor outflow at this location may lead to more vigorous scarring, which explains the commonly observed thicker capsule at this central area. This also suggests that the scar tissue forms first above the bleb, and then grows until covering it completely [8, 10, 49]. In implants where a mechanism to restrict flow is applied in an early period after surgery, a lower incidence of bleb encapsulation is reported on the long-term [50, 51]. This delayed aqueous outflow allows for a maturated bleb to form, which can then more efficiently resist to elevated hydrostatic pressures.

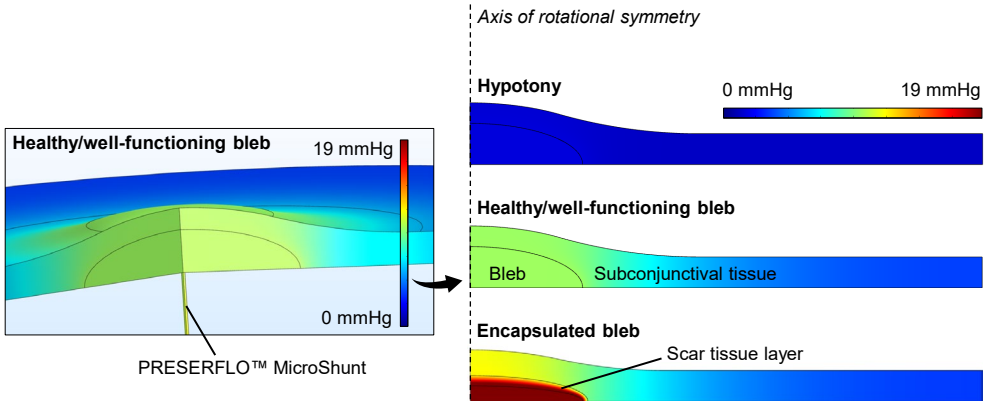

Figure 3.7: Interstitial pressure distribution in the subconjunctival space. Model prediction of the interstitial pressure distribution in the subconjunctival space in the presence of hypotony, healthy/well-functioning bleb, and encapsulated bleb (scar layer with hydraulic conductivity of 2×10^{-13} m^2 s^{-1} Pa^{-1}). In all cases, the PRESERFLO MicroShunt is used as the glaucoma drainage device. Color scale indicates interstitial fluid pressure in mmHg.

The graph in Figure 3.8 shows the values of interstitial bleb pressure and IOP calculated for each of the investigated case-scenarios. For a well-functioning bleb and when the PRESERFLO MicroShunt is used as the glaucoma drainage device, the calculated IOP is 10.42 mmHg, which is consistent with the values generally reported in the literature [43]. The presence of the scar tissue encapsulating the bleb leads to a higher bleb pressure, and consequently to an increase in the IOP, as can be inferred from Figure 3.8. The fibrotic tissue is a vascularized, entangled network of collagen fibers, which along with deposition of glycosaminoglycans and proteoglycan core proteins are associated with low tissue hydraulic conductivity [41]. This hydraulic conductivity is dependent on the extent of the fibrotic reaction. The more severe the fibrotic response is, the lower is the hydraulic

conductivity of the scar tissue and the higher will be the IOP. A decrease in the hydraulic conductivity effectively blocks the flow of aqueous into the subconjunctival tissue, thus decreasing its absorption by the microvasculature. This leads to the accumulation of fluid in the anterior chamber which results in a high IOP. In an extreme case, fluid will not be able to flow out of the bleb anymore and the bleb is no longer an alternative outflow pathway of aqueous humor, bringing the IOP back to values of an unoperated eye. Although we have considered the presence of vasculature in the scar tissue in our simulations, which also plays a role in the absorption of fluid, this seems not to be enough to compensate for the decreased hydraulic conductivity of the tissue. This result is consistent with the uncontrolled IOP that is usually seen in thick-walled blebs, even though they appear to be well vascularized [52].

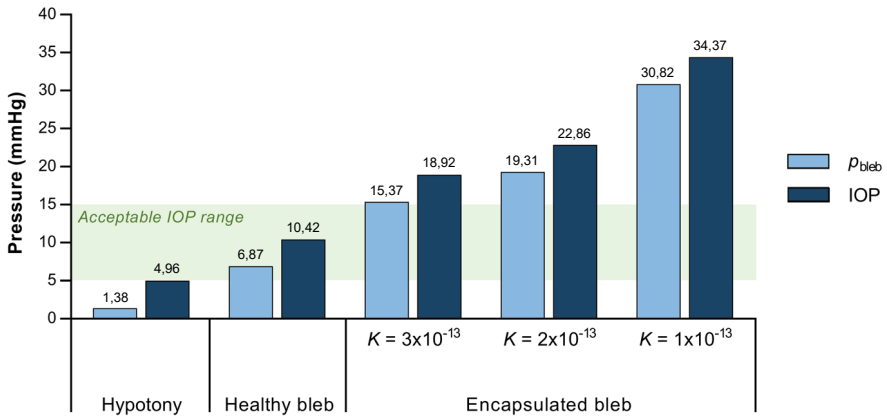

Figure 3.8: Bleb pressure (p_{bleb}) and IOP calculated for each of the case-scenarios studied: hypotony, healthy bleb, and encapsulated bleb. For the latter case, the hydraulic conductivity of the scar layer varies from $1 - 3 \times 10^{-13}$ m^2 s^{-1} Pa^{-1}. In all cases, the PRESERFLO MicroShunt is used as the glaucoma drainage device. The shaded green area represents an acceptable IOP range of 5-15 mmHg.

The IOP value calculated when a high permeability of the microvasculature is considered (hypotony case) is very close to the IOP upper limit used to define hypotony (5 mmHg). This is in line with the literature published on the PRESERFLO MicroShunt, where no cases of severe hypotony (IOP much lower than 5 mmHg) are reported. Only a very small percentage of patients suffer from mild transient hypotony, which usually resolves within a few days [43]. Hypotony can be aggravated if a lower rate of aqueous humor production is considered. Although we have used a constant, average value of aqueous inflow rate in our simulations, this value varies significantly between the waking and sleeping hours. In a healthy person, the aqueous humor production rate is approximately 3 µL min^{-1} in the morning, 2.5 µL min^{-1} in the afternoon, and 1.5 µL min^{-1} during the night [53]. This varies not only with the circadian rhythm, but also among individuals. If the lower value of aqueous flow rate (1.5 µL min^{-1}) is considered when simulating the hypotony case, then the IOP predicted by our model decreases from 4.96 mmHg to 3.43 mmHg. This value can be even lower in the presence of bleb leakage, for example due to the application of antimetabolites (antifibrotic agents) such as MMC in the site of implantation [54, 55].

Furthermore, if we simulate overdrainage using, for instance, the 305 µm lumen diameter of the Baerveldt implant (Johnson & Johnson Vision, California, USA) and considering a normal aqueous flow rate of 2.5 µL min^{-1}, then the resultant IOP is even more vision-threatening – 1.39 mmHg from our model. This is the reason why techniques to restrict early fluid flow through these big-lumen implants, or conventional aqueous shunts, were soon established, including ligating the tube externally with an absorbable ligature or placing an intraluminal suture in the tube [6, 56]. However, ligature/intraluminal suture mispositioning may occur, which then often still leads to early hypotony. Additionally, wound healing time varies widely among patients, and delayed hypotony may still occur in some cases when the temporary outflow restriction is gone [57].

3.3.2 Adjustable glaucoma implant

Considering the complications associated with current (passive) glaucoma implants discussed so far, it becomes clear that an individualized surgical treatment for glaucoma patients is needed. A patient-specific glaucoma drainage device with an adjustable hydrodynamic resistance would be ideal, especially when the outflow of aqueous humor through such a device could be fine-tuned during the postoperative follow-up visits according to the IOP measured in the patient's eyes. In order to identify the hydrodynamic resistance adjustments that are necessary for achieving a healthy IOP when hypotony is most likely to occur, or when bleb scarring takes place, we varied the lumen diameter of the PRESERFLO MicroShunt to evaluate its influence in the IOP. The results are shown in Figure 3.9.

As shown in Figure 3.9a, in case of hypotony, changing the effective lumen diameter of the tube from 70 to 55 µm raises the IOP to an acceptable, healthy value of 10 mmHg. On the other hand, in the case of high IOP due to bleb scarring as shown in Figure 3.9b, enlarging the lumen diameter even to very high values, does not result in the IOP decreasing sufficiently to reach acceptable values. For instance, when a scar layer with hydraulic conductivity of 3×10^{-13} m^2 s^{-1} Pa^{-1} is considered, the IOP of 18.92 mmHg, which occurs for a 70 µm diameter, does not become lower than 15 mmHg by enlarging the effective tube diameter even beyond 370 µm. This means that the fibrotic tissue encapsulating the bleb will always be the limiting factor, as it blocks the fluid flow into the subconjunctival tissue thus hampering its absorption by the microvasculature. Therefore, we can conclude that the adjustable glaucoma implant should be always combined with a means to reduce/limit fibrosis.

The calculated hydrodynamic resistances can be translated into different implant designs than the straightforward tube with constant circular cross-section such as the MicroShunt simulated here. Figure 3.9c shows that to maintain the IOP within healthy levels in the likely case of hypotony, no matter the implant design (with one or multiple channels, with microvalves integrated, etc.), its hydrodynamic resistance needs to be at least approximately 1.4 mmHg/µL min^{-1} to avoid lowering of IOP below 5 mmHg, and it must be increased to 3.4 mmHg/µL min^{-1} to level the IOP to a healthy value of 10 mmHg. For the encapsulated bleb case, the hydrodynamic resistance can also be decreased to the minimum resistance acceptable in terms of device dimensions (bigger channels will result

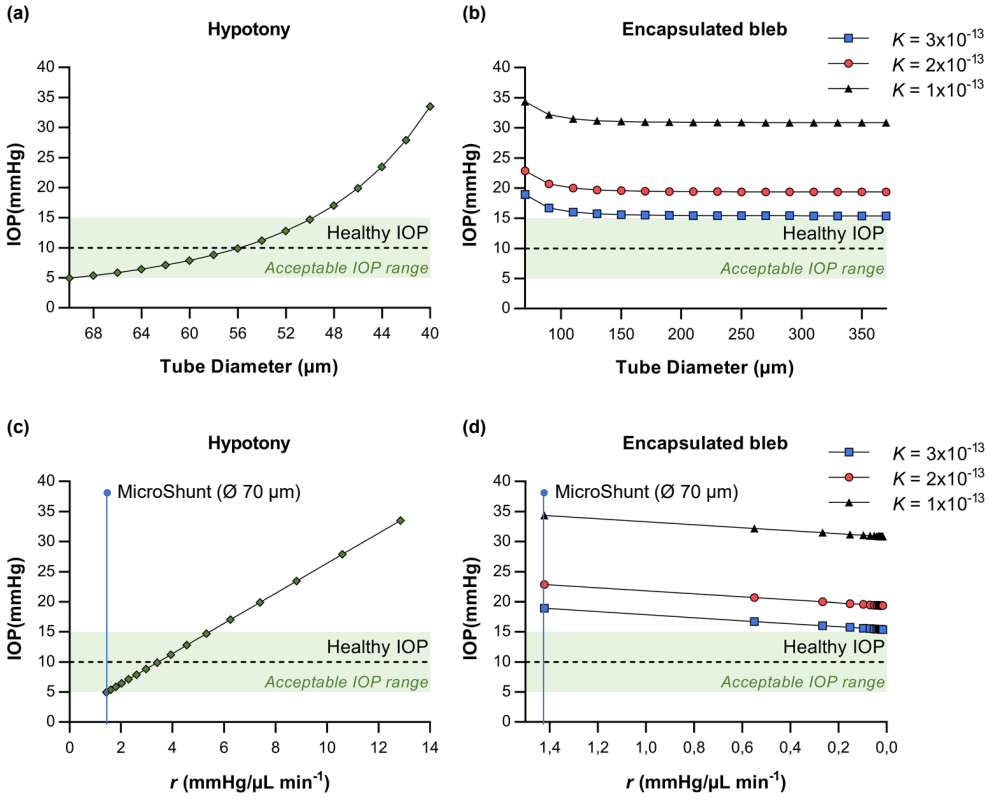

Figure 3.9: Model prediction of the IOP with varying MicroShunt lumen diameters. (**a**) and (**b**) – IOP variation with varying MicroShunt lumen diameter in case of hypotony and encapsulated bleb, respectively. (**c**) and (**d**) – Hydrodynamic resistance (r) of the different lumen-diameter MicroShunts and its impact on the final IOP. The shaded green area represents an acceptable IOP range of 5–15 mmHg.

in bigger outer device dimensions), but only a maximum IOP decrease of around 3 mmHg will be achieved, as shown in Figure 3.9d.

3.3.3 Experimental validation results

To confirm the IOP values calculated for different bleb pressures (resulting from different bleb conditions) and for different shunt lumen diameters with distinct hydrodynamic resistances, we have performed microfluidic experiments. For this, two microchips with four channels each were fabricated. One device was used for the hypotony model validation, whilst the other was used for the encapsulated bleb model validation. Figure 3.10a shows a picture of the FEMTOprint glass mold used in the hot embossing machine for the fabrication of these devices. Figure 3.10b shows a microscopic image of a replica molded bottom SIBS device layer, and Figure 3.10c shows a closed, bonded device used in the microfluidic experiments.

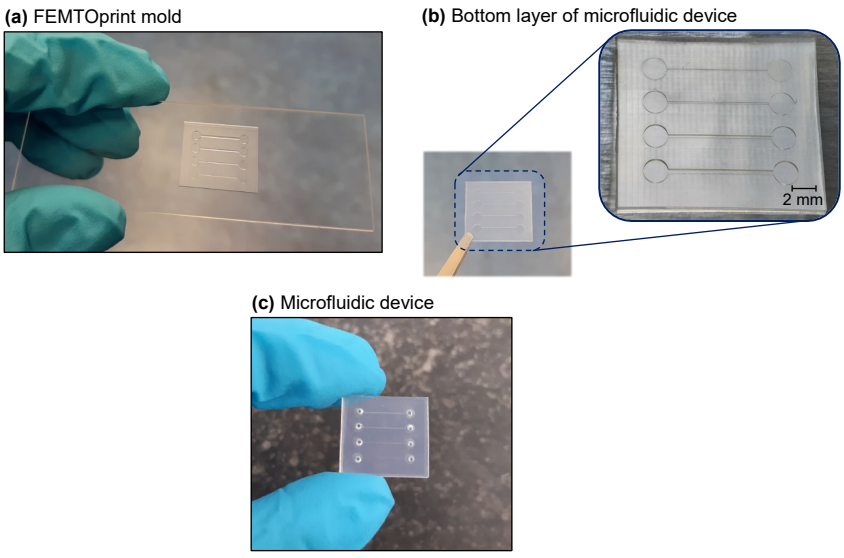

Figure 3.10: Fabricated microfluidic devices. (**a**) FEMTOprint glass mold used for the fabrication of the bottom layers of the microfluidic chips (in this case, for the encapsulated model validation devices). (**b**) SIBS bottom layer of the encapsulated model validation device replicated from the mold. (**c**) Final microdevice used in the microfluidic experiments.

The graphs presented in Figure 3.11 show a comparison between the IOPs calculated using our model and the IOPs measured in the microfluidic experiments. The simulations were performed using the geometry/dimensions of the channels present in the microfluidic devices and using the dynamic viscosity of water at 20 °C (0.001 Pa s) instead of aqueous humor, since DI water was the fluid used in the experiments. From Figure 3.11 we can conclude that there are no significant differences between the calculated and measured pressures, which indicates that our model correctly calculates the inlet pressure (IOP) given a certain outlet pressure (bleb pressure) and device hydrodynamic resistance. In the hypotony case (Figure 3.11a), it is possible to verify that a healthy IOP is achieved when decreasing the channel dimensions from 64x64 µm to 55x55 µm (equivalent to a 70 to 60 µm circular lumen diameter). For the encapsulated bleb scenario (Figure 3.11b, c and d), we can confirm that increasing the channel dimensions from 64x64 µm to 338x338 µm (equivalent to 70 to 370 µm circular lumen diameter) only results in a pressure drop up to 3 mmHg. This is verified for all the hydraulic conductivities of the scar tissue layer considered. These results are in line with the simulation results presented in Figure 3.9.

3.4 Discussion

We studied the possibility to control IOP in glaucoma patients by using an adjustable implanted glaucoma drainage device, for different postoperative conditions. To this end, we developed a model describing the fluid removal from the anterior chamber of the eye through the glaucoma drainage device, its drainage into the filtering bleb and

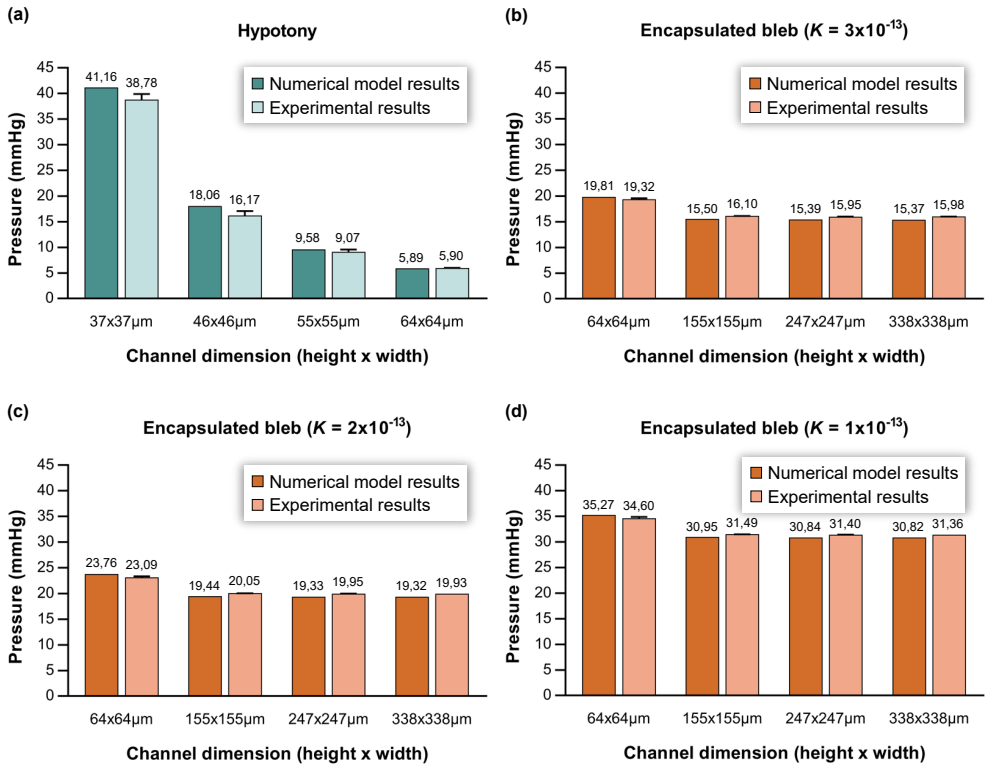

Figure 3.11: Calculated IOP vs. experimental IOP. Comparison between the IOPs calculated with the model and the IOPs measured in the microfluidic experiments in case of (**a**) hypotony, and (**b**), (**c**) and (**d**) bleb encapsulation, for different shunt lumen diameters/channel dimensions.

absorption by the subconjunctival tissue. In the model, the fluid transport in the bleb and subconjunctival tissue is simulated using Darcy's law for fluid flow inside a porous media. To account for the aqueous humor absorption by the subconjunctival vasculature, Darcy's equation is modified by employing Starling's law. The model was numerically solved using the commercial FEM package COMSOL. We simulated three postoperative conditions following glaucoma drainage device implantation – hypotony, healthy/well-functioning bleb, and encapsulated bleb due to tissue fibrosis. A tube-like shunt with the same dimensions as the PRESERFLO MicroShunt was used to represent the glaucoma drainage device in our simulations. The predicted results of IOP are consistent with the evidence available in the literature on the PRESERFLO MicroShunt, where only a few cases of (mild) hypotony are reported, and the IOP is reported to be approximately 10 mmHg (healthy IOP) when a well-functioning bleb is present. When bleb encapsulation takes place, the scar tissue covering the bleb hinders the flow of aqueous humor into the subconjunctival tissue where it should be absorbed by the microvasculature. As a result, the IOP increases. Our findings suggest, as expected, that the lower the hydraulic conductivity of the scar tissue layer becomes (thus, the more severe the fibrotic reaction is), the higher the pressure in the bleb will be and, consequently, the IOP. Our results

also indicate that decreasing the hydrodynamic resistance of the glaucoma drainage device by enlarging its lumen diameter will not decrease the IOP sufficiently to reach acceptable values when the bleb is already encapsulated – only a 3-mmHg pressure drop is achieved. In contrast, in a hypotony situation, increasing the hydrodynamic resistance of the implant by decreasing its lumen diameter does effectively increase the IOP from the hypotonic values to a healthy IOP range. These results were confirmed and validated by performing microfluidic experiments using microdevices containing channels with distinct hydrodynamic resistances. In conclusion, our model, as well as the numerical results, may provide guidelines to help designing future (patient-specific) glaucoma implants with adjustable hydrodynamic resistances, where the outflow of aqueous humor through such devices could be fine-tuned postoperatively according to the IOP measured in the patient's eyes. This way, common postoperative complications, such as hypotony, can be avoided.

Bibliography

1. Tham, Y. C. *et al.* Global Prevalence of Glaucoma and Projections of Glaucoma Burden through 2040: A Systematic Review and Meta-Analysis. *Ophthalmology* **121,** 2081–2090 (2014).
2. Weinreb, R. N., Aung, T. & Medeiros, F. A. The Pathophysiology and Treatment of Glaucoma: A Review. *JAMA* **311,** 1901–1911 (2014).
3. Richter, G. M. & Coleman, A. L. Minimally invasive glaucoma surgery: Current status and future prospects. *Clinical Ophthalmology* **10,** 189–206 (2016).
4. Shah, M. Micro-invasive glaucoma surgery – an interventional glaucoma revolution. *Eye and Vision* **6,** 29 (2019).
5. Gedde, S. J., Parrish, R. K., Budenz, D. L. & Heuer, D. K. Update on aqueous shunts. *Experimental Eye Research* **93,** 284–290 (2011).
6. Pereira, I. C., van de Wijdeven, R., Wyss, H. M., Beckers, H. J. & den Toonder, J. M. Conventional glaucoma implants and the new MIGS devices: a comprehensive review of current options and future directions. *Eye* **35,** 3202–3221 (2021).
7. Stamper, R., Lieberman, M. & Drake, M. *Glaucoma outflow procedures*. in *Becker-Shaffer's Diagnosis and Therapy of the Glaucomas* 8th ed., 466–490 (Elsevier Inc., Edinburgh, Scotland, UK, 2009).
8. Nguyen, D. Q. *et al.* A model to measure fluid outflow in rabbit capsules post glaucoma implant surgery. *Investigative Ophthalmology & Visual Science* **53,** 6914–6919 (2012).
9. Yu, D. Y. *et al.* The critical role of the conjunctiva in glaucoma filtration surgery. *Progress in Retinal and Eye Research* **28,** 303–328 (2009).
10. Kasaragod, D. *et al.* Objective Evaluation of Functionality of Filtering Bleb Based on Polarization-Sensitive Optical Coherence Tomography. *Investigative ophthalmology & visual science* **57,** 2305–2310 (2016).
11. Yu-Wai-Man, C. & Khaw, P. T. Developing novel anti-fibrotic therapeutics to modulate post-surgical wound healing in glaucoma: big potential for small molecules. *Expert Review of Ophthalmology* **10,** 65–76 (2015).
12. Schlunck, G., Meyer-ter-Vehn, T., Klink, T. & Grehn, F. Conjunctival fibrosis following filtering glaucoma surgery. *Experimental Eye Research* **142,** 76–82 (2016).
13. Seibold, L. K., Sherwood, M. B. & Kahook, M. Y. Wound Modulation After Filtration Surgery. *Survey of Ophthalmology* **57,** 530–550 (2012).
14. Bouhenni, R. A. *et al.* Lymphatic and blood vessel density in human conjunctiva after glaucoma filtration surgery. *Journal of Glaucoma* **25,** e35–e38 (2016).
15. Sousa, D. C. & Pinto, L. A. Trabeculectomy - Prevention and Management of Complications. *European Ophthalmic Review* **12,** 98–101 (2018).
16. Gardiner, B. S., Smith, D. W., Coote, M. & Crowston, J. G. Computational modeling of fluid flow and intra-ocular pressure following glaucoma surgery. *PLoS ONE* **5,** e13178 (2010).

17. Lim, K. S. Control and optimisation of fluid flow in glaucoma drainage device surgery. *Eye* **32,** 230–234 (2018).

18. Barberá, M. I. *et al.* Evaluation of the Ultrastructural and In Vitro Flow Properties of the PRESERFLO MicroShunt. *Translational Vision Science and Technology* **10,** 26 (2021).

19. Sadruddin, O., Pinchuk, L., Angeles, R. & Palmberg, P. Ab externo implantation of the MicroShunt, a poly (styrene-block-isobutylene-block-styrene) surgical device for the treatment of primary open-angle glaucoma: a review. *Eye and Vision* **6,** 36 (2019).

20. Lee, J. Y. *et al.* Structural Confirmation of Lymphatic Outflow from Subconjunctival Blebs of Live Humans. *Ophthalmology Science* **1,** 100080 (2021).

21. Kotliar, K. E., Kozlova, T. V. & Lanzl, I. M. Postoperative aqueous outflow in the human eye after glaucoma filtration surgery: biofluidmechanical considerations. *Biomedizinische Technik* **54,** 14–22 (2009).

22. Lee, J. Y. *et al.* Aqueous humour outflow imaging: seeing is believing. *Eye* **35,** 202–215 (2021).

23. Ferreira, J. A., De Oliveira, P., Da Silva, P. M. & Murta, J. N. Numerical simulation of aqueous humor flow: From healthy to pathologic situations. *Applied Mathematics and Computation* **226,** 777–792 (2014).

24. Martínez Sánchez, G. J., Escobar del Pozo, C. & Rocha Medina, J. A. Numerical model of aqueous humor drainage: effects of collector channel position. *Medical Engineering and Physics* **65,** 24–30 (2019).

25. Thygesen, J. *Late Hypotony*. in *Glaucoma* (eds Shaarawy, T. M., Sherwood, M. B., Hitchings, R. A. & Crowston, J. G.) 2nd ed., 863–881 (W.B. Saunders, London, England, UK, 2015).

26. Mastropasqua, R. *et al.* In Vivo Confocal Imaging of the Conjunctiva as a Predictive Tool for the Glaucoma Filtration Surgery Outcome. *Investigative ophthalmology & visual science* **58,** BIO114–BIO120 (2017).

27. Yılmaz, S. G., Değirmenci, C., Palamar, M. & Yağcı, A. Evaluation of filtering bleb function after trabeculectomy with mitomycin C using biomicroscopy, anterior segment optical coherence tomography and in vivo confocal microscopy. *Turkish Journal of Ophthalmology* **45,** 132–137 (2015).

28. Amar, N., Labbé, A., Hamard, P., Dupas, B. & Baudouin, C. Filtering Blebs and Aqueous Pathway. An Immunocytological and In Vivo Confocal Microscopy Study. *Ophthalmology* **115,** 1154–1161.e4 (2008).

29. Guthoff, R., Schlunck, G., Klink, T. & Grehn, F. *Filtering Bleb Imaging with Confocal Laser Technology (Rostock Cornea Module).* in *Glaucoma* (eds Grehn, F. & Stamper, R.) 157–169 (Springer-Verlag, Berlin and Heidelberg, 2006).

30. Jung, K. I., Lee, S.-b., Kim, J. H. & Park, C. K. Foreign Body Reaction in Glaucoma Drainage Implant Surgery. *Investigative Ophthalmology & Visual Science (IOVS)* **54,** 3957–3964 (2013).

31. Soltani, M. & Chen, P. Numerical Modeling of Interstitial Fluid Flow Coupled with Blood Flow through a Remodeled Solid Tumor Microvascular Network. *PLoS ONE* **8,** e67025 (2013).

32. Sefidgar, M., Soltani, M., Raahemifar, K. & Bazmara, H. Effect of fluid friction on interstitial fluid flow coupled with blood flow through solid tumor microvascular network. *Computational and Mathematical Methods in Medicine* **2015,** 673426 (2015).

33. Shojaee, P. & Niroomand-Oscuii, H. CFD analysis of drug uptake and elimination through vascularized cancerous tissue. *Biomedical Physics and Engineering Express* **5,** 035032 (2019).

34. Anderson, J. D. *Some Reflections on the History of Fluid Dynamics*. in *Handbook of Fluid dynamics* (ed Johnson, R. W.) 2nd ed., (2–1)–(2–11) (Taylor & Francis Group, Boca Raton, FL, USA, 2016).

35. Schuff, M. M., Gore, J. P. & Nauman, E. A. A mixture theory model of fluid and solute transport in the microvasculature of normal and malignant tissues. II: Factor sensitivity analysis, calibration, and validation. *Journal of Mathematical Biology* **67,** 1307–1337 (2013).

36. Van Zijderveld, R., Ince, C. & Schlingemann, R. O. Orthogonal polarization spectral imaging of conjunctival microcirculation. *Graefe's Archive for Clinical and Experimental Ophthalmology* **252,** 773–779 (2014).

37. Moghadam, M. C., Deyranlou, A., Shari, A. & Niazmand, H. Numerical simulation of the tumor interstitial fl uid transport : Consideration of drug delivery mechanism. *Microvascular Research* **101,** 62–71 (2015).

38. Sefidgar, M. *et al.* Numerical modeling of drug delivery in a dynamic solid tumor microvasculature. *Microvascular Research* **99,** 43–56 (2015).

39. Loch, C. *et al.* Determination of permeability coefficients of ophthalmic drugs through different layers of porcine, rabbit and bovine eyes. *European Journal of Pharmaceutical Sciences* **47,** 131–138 (2012).

40. Prausnitz, M. R. & Noonan, J. S. Permeability of cornea, sclera, and conjunctiva: A literature analysis for drug delivery to the eye. *Journal of Pharmaceutical Sciences* **87,** 1479–1488 (1998).

41. Pandav, S. S. *et al.* Porosity of bleb capsule declines rapidly with fluid challenge. *Journal of Current Glaucoma Practice* **10,** 91–96 (2016).

42. Mohammadi, M. & Chen, P. Effect of microvascular distribution and its density on interstitial fluid pressure in solid tumors: A computational model. *Microvascular Research* **101,** 26–32 (2015).

43. Batlle, J. F., Corona, A. & Albuquerque, R. Long-term Results of the PRESERFLO MicroShunt in Patients with Primary Open-angle Glaucoma from a Single-center Nonrandomized Study. *Journal of Glaucoma* **30,** 281–286 (2021).

44. Pinchuk, L. *et al.* The development of a micro-shunt made from poly(styrene-block-isobutylene-block-styrene) to treat glaucoma. *Journal of Biomedical Materials Research - Part B Applied Biomaterials* **105,** 211–221 (2017).

45. Acosta, A. C. *et al.* A Newly Designed Glaucoma Drainage Implant Made of Poly(styrene-b-isobutylene-b-styrene). *Archives of Ophthalmology* **124,** 1742–1749 (2006).

46. Suthisomboon, T., Bargiel, S., Rabenorosoa, K. & Pengwang, E. *Design and Simulation of XZ MEMS Micropositioning with 3D-Complex Structure.* in *2020 Symposium on Design, Test, Integration and Packaging of MEMS and MOEMS (DTIP)* (Lyon, France, 2020), 1–5.

47. Steimle, A. 3D Micro-Printing: A new Era for Med-Tech Applications. *Laser Technik Journal* **15,** 32–34 (2018).

48. Tovar, M. *et al.* 3D-glass molds for facile production of complex droplet microfluidic chips. *Biomicrofluidics* **12,** 024115 (2018).

49. Narita, A. *et al.* Characteristics of successful filtering blebs at 1 year after trabeculectomy using swept-source three-dimensional anterior segment optical coherence tomography. *Japanese Journal of Ophthalmology* **61,** 253–259 (2017).

50. Christakis, P. G. *et al.* The Ahmed Versus Baerveldt Study: Five-Year Treatment Outcomes. *Ophthalmology* **123,** 2093–2102 (2016).

51. Budenz, D. L. *et al.* Five-year treatment outcomes in the ahmed baerveldt comparison study. *Ophthalmology* **122,** 308–316 (2015).

52. Ciancaglini, M. *et al.* Filtering bleb functionality: A clinical, anterior segment optical coherence tomography and in vivo confocal microscopy study. *Journal of Glaucoma* **17,** 308–317 (2008).

53. Goel, M., Picciani, R. G., Lee, R. K. & Bhattacharya, S. K. Aqueous Humor Dynamics: A Review. *The Open Ophthalmology Journal* **4,** 52–59 (2010).

54. Matsuo, H., Tomidokoro, A., Suzuki, Y., Shirato, S. & Araie, M. Late-onset transconjunctival oozing and point leak of aqueous humor from filtering bleb after trabeculectomy. *American Journal of Ophthalmology* **133,** 456–462 (2002).

55. Sugimoto, K., Murata, H., Yamashita, T. & Asaoka, R. Bleb plication: a minimally invasive repair method for a leaking ischemic bleb after trabeculectomy. *Scientific Reports* **10,** 14978 (2020).

56. *Surgical innovations in glaucoma* (eds Samples, J. R. & Ahmed, I. I. K.) (Springer New York, NY, New York, NY, USA, 2014).

57. Pollmann, A. S., Mishra, A. V., Campos-Baniak, M. G., Gupta, R. R. & Eadie, B. D. Ab interno suture tube ccclusion of the Baerveldt glaucoma implant for management of postoperative hypotony: A case series. *American Journal of Ophthalmology Case Reports* **19,** 100752 (2020).

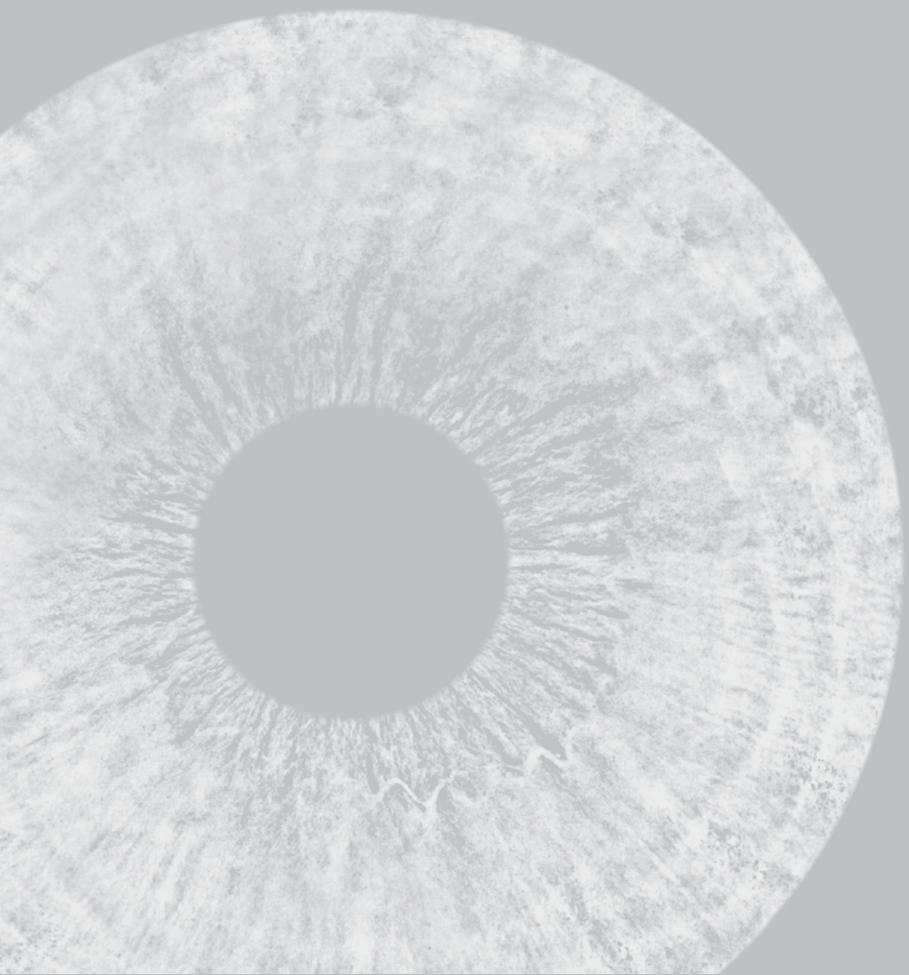

CHAPTER 4

Magnetically actuated glaucoma drainage device for regulating intraocular pressure after implantation

The results from the numerical simulations presented in the previous Chapter provided valuable insights that supported the design of a novel, miniature, magnetically-actuated glaucoma implant, which will be described in this Chapter. This implant will enable the repeated adjustment of the hydrodynamic resistance even after implantation, thus allowing for the intraocular pressure (IOP) to be regulated postoperatively in a non-invasive way. The non-invasive adjustment of the hydrodynamic resistance of the implant is achieved by integrating a magnetic microvalve containing a micro-pencil shaped plug that is moved using an external magnet, thereby opening or closing fluidic channels. The micro-plug is made from the biocompatible poly(styrene-*block*-isobutylene-*block*-styrene) (SIBS) containing iron microparticles. The complete implant consists of a SIBS drainage tube and a housing element containing the microvalve, fabricated with hot embossing using femtosecond laser-machined glass molds. Using *in vitro* and *ex vivo* microfluidic experiments we demonstrate that, when closed, the microvalve can provide sufficient hydrodynamic resistance to overcome hypotony (too low IOP, one of the most common postoperative complications following glaucoma filtration surgery). The valve function is repeatable and stable over time. Due to its small size, our implant provides a promising route towards a safe and easy-to-implant minimally invasive glaucoma surgery device.

This Chapter is based on:
Magnetically actuated glaucoma drainage device for regulating intraocular pressure after implantation, **Inês C.F. Pereira**, Ralph J.S. van Mechelen, Hans M. Wyss, Leonard Pinchuk, Henny J.M. Beckers, Jaap M.J. den Toonder, *Accepted for publication in Microsystems & Nanoengineering*, 2023; and *Implantable ocular drainage device for controlling intraocular pressure*, **Inês C.F. Pereira**, Rosanne van de Wijdeven, Sebastian Fredrich, Albertus P.H.J. Schenning, Hans M. Wyss, Henny J.M. Beckers, Jaap M.J. den Toonder, Patent No. **WO 2022/111892 A1**, filling date October 5, 2021.

4.1 Introduction

Glaucoma is a chronic and progressive eye disease characterized by damage to the optic nerve and visual field loss. With over 70 million people affected worldwide (10% eventually bilaterally blind), glaucoma is the leading cause of irreversible blindness [1, 2]. This number is expected to increase to over 100 million people affected by 2040 [3] The key risk factor for the development and progression of glaucoma is elevated intraocular pressure (IOP), which results from a malfunctioning of the fluidic system of the eye designated to maintain a balanced amount of aqueous humor in the anterior chamber [4–6]. The anatomy of the eye is schematically depicted in Figure 4.1a. The aqueous humor is produced and secreted by the ciliary body and mainly drains out of the eye through the trabecular meshwork and into Schlemm's canal. In patients with primary open-angle glaucoma (POAG), there is an abnormal increase of resistance to aqueous outflow, which leads to a buildup of fluid in the eye that results in elevated IOP. An IOP larger than 21 mmHg is generally considered as abnormally high. Recent clinical trials have designated "success" IOP levels as < 18, < 15, or even < 12 mmHg [7]. In this paper, we consider 15 mmHg as the upper limit of the acceptable IOP range. Currently, IOP is the only risk factor that can be modified to stop the progression of glaucoma. Ophthalmologists use a variety of approaches to lower IOP, including pharmacological medication, laser procedures, and/or incisional surgeries [8]. Surgery is often performed when the maximum tolerated medical/laser treatments do not sufficiently reduce IOP [9]. The standard surgical paradigm involves bypassing the eye's natural outflow pathways by creating an alternative route for the aqueous humor to effectively exit the eye, thereby reducing IOP. Conventional filtration surgeries include trabeculectomy and the implantation of glaucoma drainage devices. Most glaucoma implants, including the conventional aqueous shunts (with tube-plate design) and some of the new less invasive bleb-forming devices, drain the aqueous humor into the subconjunctival/sub-Tenon's space, where a fluid reservoir known as a filtering bleb is formed.

Although better designed glaucoma implants have emerged in recent years, made of superior materials that evoke less tissue inflammation, postoperative complications following glaucoma filtration surgery are still frequently reported, the two most common ones being excessive fibrosis with scar tissue formation and hypotony-related complications [1, 10–14]. Hypotony, commonly defined as an IOP lower than 5 mmHg, is a known complication associated with glaucoma filtration procedures and most often occurs in the initial postoperative phase. Common causes include conjunctival bleb leak and overfiltration of aqueous humor through the implanted device due to the absence of a "maturated" filtering bleb in the early postoperative period [15]. During bleb maturation, the balanced production and degradation of the extracellular matrix and collagen produce a tissue-strengthening effect, which limits the filtration of aqueous humor from the bleb into the subconjunctival tissue [16]. Until this phase is reached, which might take up to a few months, there may be overfiltration of aqueous humor resulting in hypotony [17]. Postoperative hypotony can be further aggravated by the lingering effects of presurgical antiglaucoma medications such as acetazolamide. These medications are designed to reduce the production of aqueous humor in the eye, potentially contributing to a lower postoperative IOP. This vision-threatening condition may lead to vision loss in

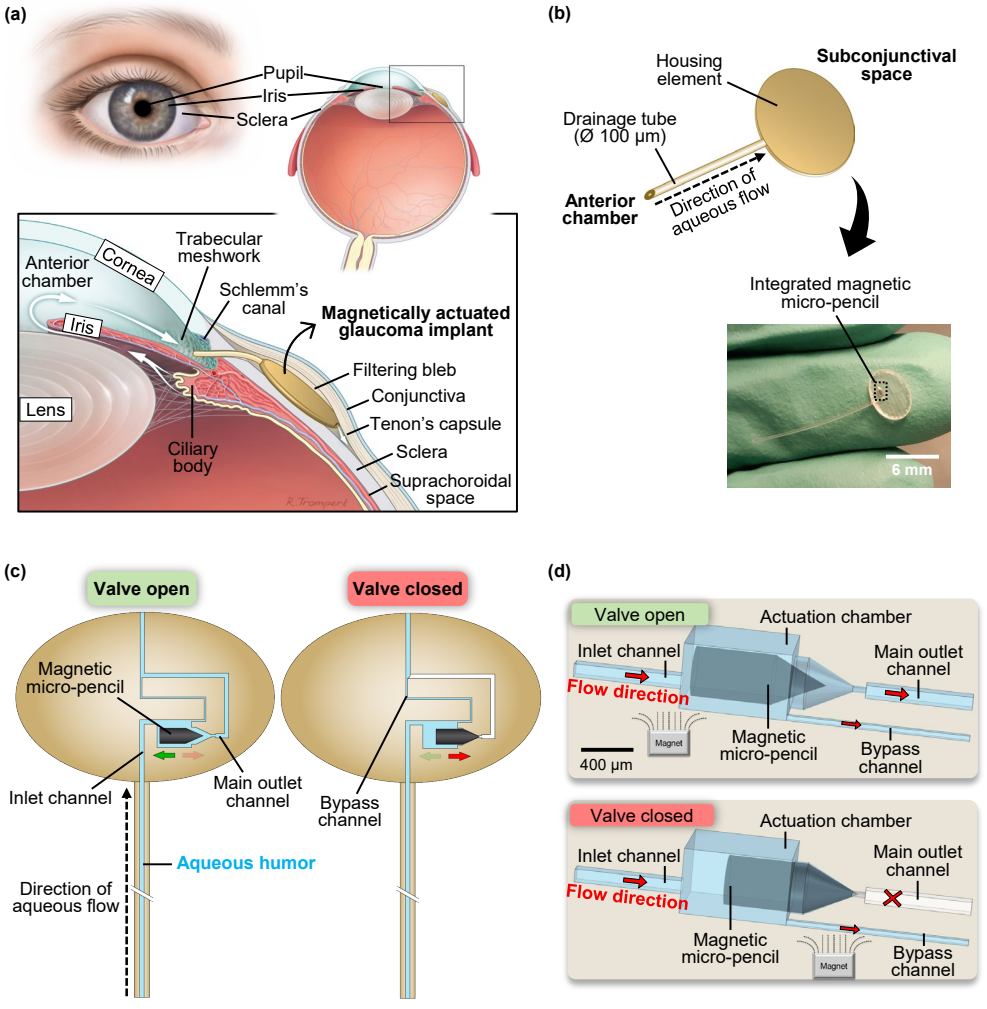

Figure 4.1: Placement of the magnetically actuated glaucoma implant in the eye, and its design and working principle. (**a**) Anatomy of the eye and placement of the implant in the eye (image provided by Rogier Trompert Medical Art). (**b**) Schematic depiction of the magnetically adjustable glaucoma implant design and a photo of the actual device. (**c**) Front view of the implant showing a schematic representation of its channel layout and of the working principle of the integrated valving system. (**d**) Three-dimensional, zoomed view of the microvalve demonstrating the actuation mechanism of the magnetic micro-pencil; the total length and largest diameter of the micro-pencil are 1 mm and 357 µm, respectively.

up to 20% of patients, and it can be accompanied by a shallow anterior chamber, and other complications like choroidal effusions and suprachoroidal haemorrhage [18]. Many flow restricting techniques have been extensively used by ophthalmologists to prevent overdrainage in the early period after surgery, and these include, for instance, placing an intraluminal stent inside the implant's tube and then remove it postoperatively a few months after surgery, or ligating the tube externally with an absorbable ligature that degrades after ∼6 weeks. This reduces flow significantly to enable the formation of a

tissue-capsule over the plate of the implant, which then offers some resistance to aqueous humor outflow [19]. A main drawback to these measures, however, is the lack of precision and predictability in efficiently controlling IOP in the initial postoperative phase, as shown by the regular occurrence of early hypotony [10, 20, 21].

To overcome this lack of postoperative IOP control, some attempts have been made to incorporate valves into glaucoma implants. An example of a valved implant is the Ahmed® Glaucoma Valve (New World Medical, Inc., California, USA), a marketed device that features a built-in Venturi-based flow restrictor. This passive valve is located on the end plate of the device and is comprised of two opposed silicone membranes pinned together along their edges and pretensioned to open at an IOP threshold of 8 mmHg, and to remain closed below this value to reduce the risk of hypotony [22, 23]. Although complications associated with overfiltration and subsequent hypotony appear to occur less frequently with this device, evidence suggests that hypotony continues to affect a significant proportion of patients [10, 13, 14, 24]. Another example of a valved glaucoma implant that has recently been made commercially available, incorporating an active magnetic valve instead, is the eyeWatch™ Implant (Rheon Medical SA, Lausanne, Switzerland). The eyeWatch system features the eyeWatch implant, acting as an adjustable faucet that controls IOP, and the eyeWatch Pen, used to tune the flow resistance of the implant by inducing variable compression of the drainage tube. This compression is achieved by rotating a magnetic disk present inside the implant [25, 26]. Initial clinical results with the eyeWatch suggest that it can prevent hypotony and hypotony-related complications from occurring, and IOP spikes are avoided by fine-tuning the flow resistance of the device when required, thus promoting smooth pressure transitions that may mitigate the tissue response [18, 27]. Nonetheless, further studies involving a significant number of patients and longer follow-up times are necessary to support the long-term safety, efficacy and clinical relevance of this device in comparison with other implants. Apart from the aforementioned valved implants, concepts of temporary valves have also been described, using for example biodegradable materials that allow for a controlled drainage in the early postoperative period and maximized flow capacity when degradation is finished [28].

In this work we have developed a novel miniature magnetically controlled glaucoma drainage device where, unlike the eyeWatch system that requires compression/decompression of a tube to adjust fluidic resistance, we rely on a pencil-tip shaped actuator that selectively opens a larger fluid passageway in the device to lower IOP. A potential advantage of our device is the small size of the integrated magnetic microvalve which enables a smaller overall implant size. Our implant is made from poly(styrene-*block*-isobutylene-*block*-styrene), or "SIBS", which is highly biocompatible due to its inertness, softness and flexibility. It is the thermoplastic elastomer comprising the PRESERFLO™ MicroShunt (Santen, Osaka, Japan) implant, which has been used in humans since 2007 and demonstrates, in the most part, less inflammation and scar tissue formation [29–32]. The movable magnetic micro-plug that is part of our valving system is also fabricated using SIBS mixed with magnetic microparticles. Being only partly comprised of magnetic material, and also due to its small dimensions, the magnetic micro-pencil plug is very light, and as a result, the overall implant might be also lighter and more flexible than other currently available implants. Our approach provides a promising route towards a miniature implant that will enable the ophthalmologist to precisely and actively adjust the

IOP to a desired, healthy range. The outflow of aqueous humor can be kept to a minimum in the immediate postoperative period until the ophthalmologist determines that the bleb is sufficiently mature, thus preventing hypotony, and can be increased to a maximum afterwards to further lower the IOP and stop the glaucoma disease progression.

4.2 Design and working principle of the magnetically actuated glaucoma implant

Our active, magnetically adjustable glaucoma drainage device is comprised of a drainage tube and a housing element, as shown in Figure 4.1b. The housing element is attached to the outlet of the drainage tube and contains an actuation chamber where the magnetic plug with the shape of a "micro-pencil" is integrated. Figure 4.1a shows the implantation site of the glaucoma implant, where the entrance to the drainage tube is in the anterior chamber and the plate is implanted under the conjunctiva and Tenon's capsule. Aqueous humor flows through the tube and into the plate, through the magnetically actuated valve system, and then out the plate to the surrounding tissue. The details of the magnetically actuated valve system are shown in Figure 4.1c and d. The system is implanted with the valve closed so as to minimize the chance of hypotony. In this closed "low-flow, high hydrodynamic resistance" configuration, demonstrated in Figure 4.1c – right and Figure 4.1d – bottom, aqueous humor flows through the tube and into the inlet channel, then to the bypass channel and out of the plate to fill the bleb. Once the bleb is matured, the surgeon can actuate the valve system with an external magnet and move the magnetically-coupled pencil-shaped plug to the left, as shown in Figure 4.1c – left and Figure 4.1d – top, thus opening the "high-flow, low hydrodynamic resistance" main outlet channel to increase flow and decrease IOP. Note that the bypass channel remains open in both low-flow or high-flow modes and has a cross-sectional area smaller than the main outlet channel. The dimensions of this channel were predetermined to achieve a desired minimum pressure in case of hypotony, when the device is in the low-flow mode. According to the numerical model described in the previous Chapter 3 [17], to obtain a healthy IOP of 10 mmHg, the bypass channel must have a cross-sectional area of 50x50 µm (width x height). However, this optimal pressure can only be attained if the micro-pencil totally stops the flow through the main outlet channel. As we anticipated that some fluid leakage might occur around the micro-pencil in the closed state, we fabricated two types of devices with different bypass channel dimensions: 50x50 µm and 40x40 µm. The inlet channel and main outlet channel were designed with a cross-sectional area of 100x100 µm. The actuation chamber in which the micro-pencil is integrated is comprised of a rectangular portion that opens to a channel with the same round tapered shape as the tip of the micro-pencil. As can be seen in Figure 4.1c and d, approximately 200 µm of the micro-pencil tip is already positioned inside the micro-pencil channel of the actuation chamber when the valve is in the open state. This was intentionally designed in this way to ensure that the micro-pencil is always properly aligned with its direction of movement.

4.3 Results

4.3.1 Micro-pencil plug and *in vitro* device fabrication

The magnetic micro-pencil plugs were fabricated by replica molding using hot embossing, as illustrated in Figure 4.2b. The micro-pencils were made of magnetic SIBS, a composite material comprised of SIBS mixed with carbonyl iron powder (CIP) and fabricated upfront using a hot melt extrusion process, as shown in Figure 4.2a. By employing proper mixing parameters, we were able to achieve a good dispersion of the magnetic particles in the SIBS matrix (see Supplementary Figure 4.A1 for microscopic images showing the homogeneity of the particle distribution in SIBS, taken from a 100 µm-thin hot embossed magnetic SIBS film, and captured using varying magnifications in both transmission and reflection modes for imaging the samples).

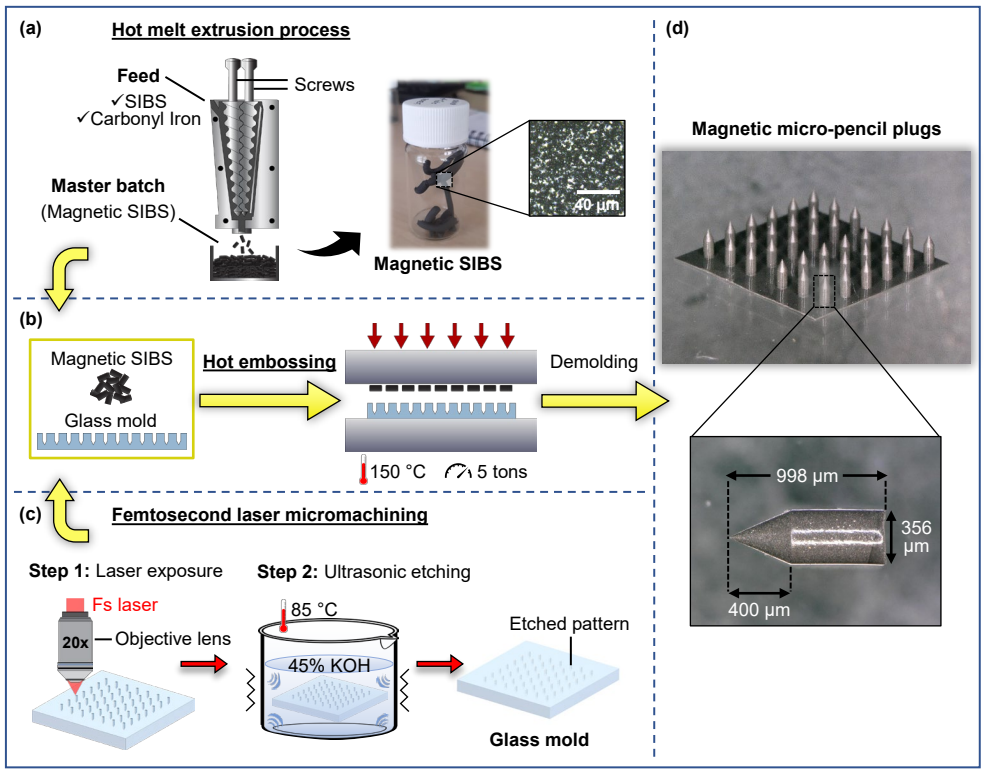

Figure 4.2: Fabrication process of the magnetic micro-pencil plug and its final shape and dimensions. (**a**) Illustration of the hot melt extrusion process used to fabricate the magnetic SIBS pellets, which show a relatively uniform dispersion of the magnetic particles in the SIBS matrix, as seen in the microscopy image on the right. (**b**) Schematic representation of the micro-pencil fabrication by replica molding using hot embossing, with femtosecond laser-machined fused silica glass molds. (**c**) Schematic illustration of the femtosecond laser machining process used to fabricate the glass molds. (**d**) Demolded array of magnetic micro-pencils and shape and dimensions of the micro-pencil plug.

The cytotoxicity of the magnetic SIBS was investigated by means of a resazurin assay on human MG-63 osteosarcoma cells. The magnetic SIBS samples were first immersed into culture medium and then the cells were exposed to the resulting extracts at different concentrations: 100% (undiluted), 50%, 25% and 10%. The experiment confirmed that the magnetic SIBS samples were non-cytotoxic at all the extract concentrations tested (see the Supplementary Information 4.B for more details about this experiment and Figure 4.B1 for the corresponding results).

The mold used to give the magnetic SIBS a micro-pencil shape was fabricated by femtosecond laser micromachining of fused silica glass. Femtosecond laser-assisted chemical wet etching is based on a two-step process of ultrashort-pulsed laser radiation in transparent materials, followed by chemical wet etching to selectively remove the exposed material (Figure 4.2c) [33]. The laser beam, focused inside the glass, locally modifies its refractive index and chemical properties, and creates patterns that can be used to, by chemical etching, generate three-dimensional structures with high precision, aspect ratio and complexity [33, 34]. The complexity of the pencil shape of our micro-plugs would be difficult to achieve using other classical micro-manufacturing techniques, such as photolithography. The glass mold was designed to produce micro-pencils with a total length of 1 mm, a conical tip 400 µm-long and a diameter of 350 µm. As can be seen in Figure 4.2d, the fabricated micro-pencils have tolerances for the length and the diameter of 356 $\pm$ 1 µm and 988.3 $\pm$ 10 µm, respectively. These discrepancies between the designed and measured dimensions are due to the nature of the femtosecond laser machining process, as explained in more detail in the Supplementary Information 4.C. Our experiments indicate that these tolerances do not appear to affect the valve function, provided that the length of the plugs is sufficient to maintain their tips partially inside the micro-pencil opening of the actuation chamber when the valve is in the open state, thus keeping them aligned with the movement direction.

To investigate the actuation of the micro-pencil *in vitro*, we fabricated a microfluidic device with the same channel design and dimensions that will be present in the final implant's housing element (shown in Figure 4.1c and later in Figure 4.6a). Figure 4.3a illustrates the three components – top layer, magnetic micro-pencil and bottom layer – that comprise the device and how they are assembled to obtain a closed device (also shown in Supplementary Figure 4.D1a and b). Both layers contain half of the main outlet and bypass channels and the actuation chamber in which the micro-pencil is positioned, thereby establishing the microvalve. They were fabricated by replica molding using hot embossing and a femtosecond laser-machined fused silica glass mold (Figure 4.3b), following the same procedure used for fabricating the micro-pencil plugs. Figure 4.3c shows a picture of the bonded micro-pencil device filled with ink, identifying the channels and the actuation chamber. The design and dimensions of the microfluidic device and respective channels are represented in Supplementary Figure 4.D1c and d. The height and width of both main outlet and bypass channels were measured, and the results can be found in Supplementary Figure 4.D1e. The measured heights of the channels are very similar to the designed values, whereas the measured widths are slightly smaller than designed. Again, these differences are due to the nature of the femtosecond laser machining process (see the Supplementary Information 4.C).

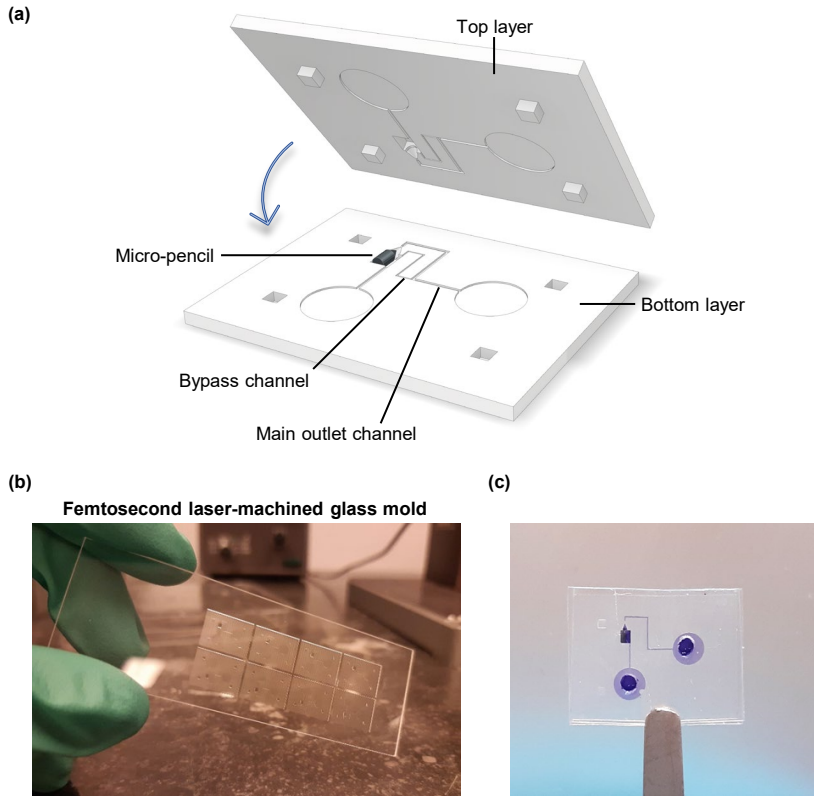

Figure 4.3: Micro-pencil microfluidic device used for the *in vitro* experiments. (**a**) An exploded view of the micro-pencil device with integrated valving system, showing the three components that it is comprised of: top layer, magnetic micro-pencil and bottom layer. The cross-sectional areas of the main outlet channel and bypass channel are 100x100 µm and 50x50 or 40x40 µm, respectively. (**b**) Picture of the glass mold, made using femtosecond laser machining, used for the fabrication of top and bottom layers. (**c**) Picture of the bonded micro-pencil device filled with ink.

4.3.2 *In vitro* performance of the micro-pencil device

The micro-pencil devices were evaluated *in vitro* to determine if the valve function is repeatable, stable over time, and if the devices provide stable pressures under non-static conditions in either open or closed states. The setup used to carry out these experiments is schematically represented in Figure 4.4a. De-ionized (DI) water was pumped into the devices at 2.5 µL min^{-1}, the rate of aqueous humor production in the human eye [35], and the inlet pressure, which would correspond to the IOP, was measured in real time. The value of 2.5 µL min^{-1} was chosen as an approximated average value of aqueous humor production rate during a period of 24 hours [36]. As our glaucoma implant was designed to prevent hypotony from occurring, we simulated a hypotony situation in our *in vitro* experiments to test the performance of our device and integrated microvalve in a real hypotony case-scenario. To simulate this condition, the outlet of the devices was

connected to a column of water mimicking the pressure in the bleb when hypotony is most likely to occur (approximately 1.38 mmHg, or 1.88 cmH_2O). This pressure was calculated in our previous work [17]. Due to the overdrainage of aqueous humor from the bleb into the subconjunctival capillaries, the resultant pressure in the bleb is low, thus leading to a very low IOP. Moreover, this hypotonic situation can be aggravated if bleb leakage occurs, for example due to the application of antimetabolites (antifibrotic agents) such as mitomycin C (MMC) in the site of implantation during the surgical procedure. For simplification, we did not consider the outflow of aqueous humor through the natural outflow pathways (trabecular and non-trabecular/uveoscleral) in our experiments, since in a glaucomatous eye and when a glaucoma drainage device is implanted, most aqueous humor drains through the glaucoma implant into the bleb, which represents the easiest fluidic pathway [37]. It is hypothesized in the literature that only 10% of the aqueous humor drains through the natural outflow pathways after trabeculectomy is performed [38].

First, to evaluate the repeatability of the valving system, we performed a cycle switching test where the microvalve was switched between open and closed states for four times by moving the micro-pencil plug using an external magnet while continuously measuring the pressure upstream from the device. The magnet was placed on either side of the micro-pencil device and the plug was moved to the open or closed positions accordingly (the magnet was not dragged between these two locations). Figure 4.4b shows microscopic images of the microvalve in the open and closed states, and the movement of the micro-pencil between these two states is shown in Supplementary Video 4.F1.

A schematic depiction of the position of the magnet relative to the micro-pencil plug, particularly when the plug is to be moved to the closed state, is shown in Figure 4.4c. The magnetic translational force acting on the plug at this position, i.e., at a distance of 5 mm between the center axis of the magnet and the plug, is approximately 5.67×10^{-5} N (the calculation of the magnetic force is explained in detail in the Supplementary Information 4.E). This force is a combined effect of the magnitude of the magnetic field and the magnetic field gradient experienced by the plug, which, at a 5 mm distance, are $B = 0.27$ T and $\nabla B = 88.77$ T/m, respectively. The calculated magnetic translational force is the resultant force necessary to move the plug, when not considering static and kinetic friction acting on the plug due to the sticky nature of SIBS. Since this stickiness and its effect on the plug's movement is significantly reduced by the constant presence of liquid environment surrounding the plug, we did not consider these forces in our calculations. Indeed, if the device is completely dry, moving the micro-plug seems impossible due to the major role of the friction forces in that scenario. However, once fluid is injected into the device the plug begins to move almost immediately under the influence of the applied magnetic field.

Since the placement of the magnet was done manually, we could never precisely place it at a 5 mm distance from the plug where the maximum magnetic translational force is achieved. Nevertheless, the valve always moved as intended, which confirms that the valving can be controlled robustly, and the exact positioning is not critical. In a final product however, we conceive that the magnet is integrated in a controller device that is placed on the eye, and in which the magnet is easily and robustly translated between two

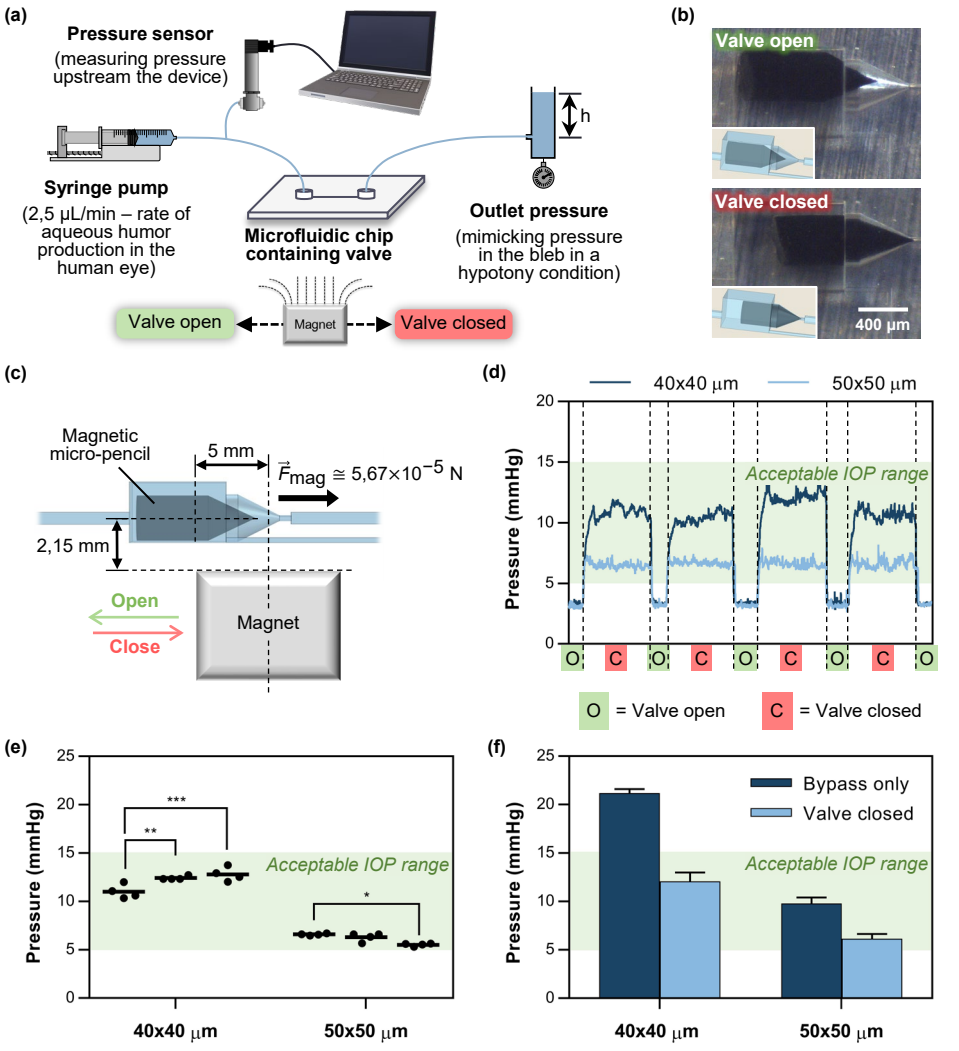

Figure 4.4: *In vitro* microfluidic experiments. (**a**) Schematic depiction of the setup used for the microfluidic experiments. (**b**) Microscopic images showing the microvalve in the open and closed states. (**c**) Magnet placement relative to the micro-pencil plug when the plug is to be moved to the closed state ($\vec{F}_{mag}$ stands for magnetic translational force applied to the plug, calculated as described in the Supplementary Information 4.E). (**d**) *In vitro* measurement of the pressure variation upstream the 40x40 µm and 50x50 µm micro-pencil devices as a result of the valve operation. In this experiment, the pressure was measured for approximately 5 minutes with the valve open, and 30 minutes with the valve closed. (**e**) Overview of the pressures measured in each valve-closed cycle for all individual samples tested. Each data point represents the pressures measured in each valve-closed cycle, and the straight line represents the mean ($n = 4$ cycles per sample). *, ** and *** represent $p \leq 0.05$, $p \leq 0.01$ and $p \leq 0.001$, respectively, as analyzed by two-way ANOVA with Bonferroni multiple comparisons test ($n = 3$ samples per group). (**f**) Comparison between the pressures measured in the devices with the valve in the closed state and the devices containing the bypass channel only, i.e., without the main outlet channel and the integrated microvalve, representing a perfectly closed valve. The data represents the mean ± standard deviation (SD) ($n = 3$). In all graphs, the shaded green areas represent an acceptable IOP range of 5–15 mmHg.

positions (corresponding to open and closed valve positions). Such a controller device could additionally detect the shape of the end plate of the implant under the conjunctiva and precisely position the magnet on either side of the major axis of the ellipse-shaped end plate at a 5 mm distance from the plug.

Two different types of devices were tested in this cycle switching test: one containing the 50x50 µm bypass channel, and the other with the 40x40 µm bypass channel. For both devices, measurements were performed on three different samples. The pressure results of one of the 50x50 µm and 40x40 µm devices tested are presented in Figure 4.4d, and the results for the other devices can be found in Supplementary Figure 4.G1. From these measurements we can confirm that both types of devices are able to increase the pressure when the valve is switched to the closed state, from the very low pressures characteristic from a hypotony situation ($<$ 5mmHg) to a pressure within the acceptable IOP range (5–15 mmHg, shaded green area in the graph of Figure 4.4d). The very low pressure measured when the device is fully open, of approximately 3.6 mmHg, indicates that the device should be implanted in the eye with the valve in the closed state, to effectively prevent hypotony from occurring in the first postoperative weeks, and then switched to the open state when the doctor determines, by measuring the IOP in the follow-up visits, that the bleb is sufficiently mature to offer enough resistance to the outflow of aqueous humor.

Figure 4.4e shows an overview of the pressures measured in each valve-closed cycle for all individual samples tested. These results show that the 50x50 µm micro-pencil device provides pressures in the range of 5–10 mmHg when the valve is closed, whereas the 40x40 µm device offers higher pressures, in the range of 10–15 mmHg. Both devices showed good repeatability, both between cycles and between different samples. This indicates that the different magnetic SIBS valves that we have tested always behaved identically, which is a clear indication that the magnetic particles are homogeneously dispersed within the SIBS polymer. Otherwise, a poorly mixed composite could have negatively affected actuation performance and lead to variations between pressure measurements. When comparing the 50x50 µm and the 40x40 µm devices, the first showed the best repeatability, both between cycles and between different samples. The pressure varied slightly more between measurements in the 40x40 µm device, which may be explained by a possible deformation of channels as a result of the higher fluidic pressures inside this device when the valve is closed. Due to the flexible nature of SIBS, these higher pressures might lead to a slight expansion of the actuation chamber, which can result in a less stable closure of the valve. Besides, the proper function of the valve is highly dependent upon the correct fitting of the micro-pencil into the micro-pencil opening of the actuation chamber. A slight mispositioning could result in different outflow resistances, and therefore, different valve-closed pressures. This alignment might also explain the slight differences between pressures measured in the closed state for all devices tested. However, these differences are not significant and are acceptable for the final application as a glaucoma drainage device.

To investigate if fluid can still leak past the micro-pencil and through the main outlet channel when the valve is closed, we fabricated and tested devices without the main outlet channel and without the microvalve integrated. The pressure measured with these

devices should correspond to the pressure that our microvalve would provide if it would perfectly close and completely stop the flow through the main outlet channel. This pressure was then compared with that measured in the closed-state device. The results are plotted in Figure 4.4f. Our findings show that fluid can still flow through the microvalve, past the micro-pencil and into the main outlet channel when the valve is in the closed state, i.e., the valve is leaky. To avoid leakage, the mechanical properties of the plug could be adjusted; for instance, a more elastic material could (possibly) create a better seal with less leakage. Increasing the elasticity (i.e., lowering the elastic modulus) of the composite could be achieved by two ways: (1) decreasing the amount of magnetic particles in the SIBS matrix, or (2) decrease the styrene content of the SIBS starting material (which, with 25% styrene content as used in this work, has a Young's Modulus of 10 MPa – value provided by InnFocus Inc.). The first option may negatively affect the valve actuation since the magnetic susceptibility of the composite is reduced; this means that the composite would be less responsive to an external magnetic field. The second option, a lower content of styrene, could lead to an increase of adhesion between the plug and the valve chamber, which could also negatively affect actuation. The optimization of the mechanical properties is therefore a delicate balance between various factors and could be a future optimization of the valve.

We theoretically determined the hydrodynamic resistance of both the 40x40 and 50x50 µm devices with the valve in the open and closed states. The hydrodynamic resistance provided by the valve in both devices was also calculated and the obtained values are almost identical, confirming that the functioning of the valve does not depend on the bypass channel dimensions. A detailed description of the equations used for these calculations and corresponding results are provided in the Supplementary Information 4.H and Table 4.H1.

To evaluate the stability of the pressure when the valve is closed, we measured the pressure upstream of the two types of devices for a period of 12 hours. Figure 4.5a shows the results of this experiment, where each column represents one sample, and the error bars indicate the variation of the pressure throughout the experiment. The measured pressures plotted over time can be found in Supplementary Figure 4.I1. Except for one device, the pressure was kept remarkably stable over time, as indicated by the minor size of the error bars. This demonstrates that our micro-pencil is capable of maintaining a steady position in the closed state, thus keeping the pressure barely unchanged over the course of the experiment. The greatest pressure variation (approximately 2 mmHg) in one of the 40x40 µm devices could have been due to a small air bubble that entered into our setup during the experiment and ended up inside the device. Such a trapped bubble will act as an additional fluidic resistance by reducing the diameter of the channels. Apart from the air bubble, an impurity flowing into the device and partially clogging its channels could have also been the reason for this pressure fluctuation. It is reported in the literature that, when implanting glaucoma drainage devices, the lumen of the tubed devices can be obstructed by different particulate matter, including sloughed endothelial cells, pigment from the iris, fibrin from blood clots and lens particulate. From the particulate mentioned, the endothelial cells have the largest diameter of approximately 40–50 µm [39]. This can be an issue, particularly for the micro-pencil device with the larger 50x50 µm bypass channel. When the valve is in the close state, the endothelial cells transported by the

aqueous humor might be able to move into the bypass channel, but they may not be capable of flowing through it and get trapped due to the comparable dimensions of the bypass and the cell, blocking the channel. If the bypass channel is small enough, such as the 40x40 µm, the cell will probably not be able to move into it, thus becoming trapped in the actuation chamber until the valve is opened again. When the valve is open, the cell will flow through the main outlet channel since it has the lower hydrodynamic resistance. Here, clogging is very unlikely to occur due to the bigger dimensions of this channel.

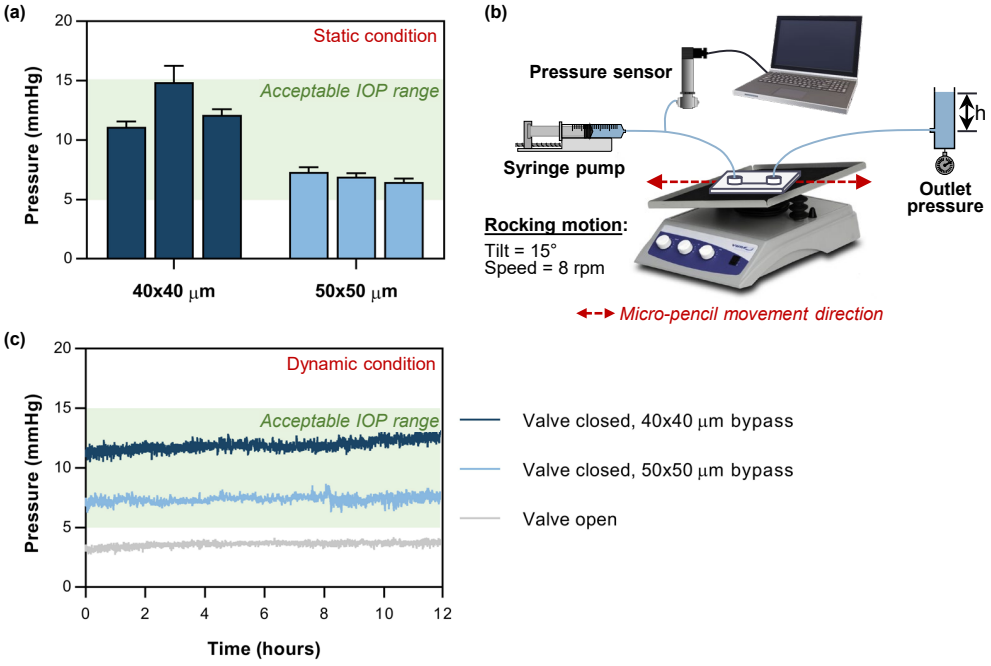

Figure 4.5: ***In vitro*** **12-hour experiments.** (**a**) Overview of the pressures measured upstream the 40x40 µm and 50x50 µm micro-pencil devices for period of 12 hours with the valve in the closed state under static conditions (i.e., the devices did not move over the course of the experiment). Each column represents one sample, and the error bars indicate the variation of the pressure throughout the experiment. (**b**) Schematic depiction of the setup used for the valve stability experiment performed with the devices placed under dynamic conditions, i.e., a rocking motion. (**c**) Pressures measured upstream the 40x40 µm and 50x50 µm micro-pencil devices placed under rocking motion (dynamic condition) for a period of 12 hours with the valve in the closed and open states. In both graphs, the shaded green areas represent an acceptable IOP range of 5–15 mmHg.

The aforementioned experiment was performed under static conditions, i.e., the device did not move throughout the experiment. To investigate if the valve function would be affected by the patient's movements, we repeated the previous experiment but with the devices placed under rocking motion, using a digital platform rocker shaker as illustrated in Figure 4.5b. The rocking, side to side (2D) motion, was performed in the main direction of the micro-pencil movement, and at a tilt of 15° and a speed of 8 rpm, which corresponds to 16 side-to-side movements per minute. Three devices were tested: a 50x50 µm device with the valve in the open state, and 50x50 µm and 40x40 µm devices with the valve in the closed state. The results are represented in Figure 4.5c. Our data confirms that

the valving system is stable under dynamic conditions in both states, open and closed, as indicated by the stable pressure measured over time. This pressure stability suggests that our micro-pencil will not move to the open or closed states just by, for instance, the effect of gravitational forces. This stability is partially achieved due to the sticky nature of SIBS, which makes it very difficult to move the micro-pencil without a stronger external force being applied to induce its movement, in this case, magnetic force. Only when using an external magnet placed close enough to the device, the micro-pencil is able to switch between closed and open states. Another aspect enhancing the stability of the valve, specifically in the closed state, is the special design of the actuation chamber itself. The "pencil" shape of the outlet portion of the actuation chamber is very similar to that of the micro-pencil plug, with very close dimensions in terms of diameter and length of the conical tip. This effectively helps to hold the closed micro-pencil in place.

4.3.3 Valve operation *ex vivo*

We performed *ex vivo* experiments to better understand the performance of our glaucoma device implanted in enucleated porcine eyes. For this experiment, the actual implant comprised of drainage tube and an elliptical-shaped end plate (or housing element) was fabricated. Figure 4.6a schematically depicts the design of the implant, including its dimensions indicated in mm. Figure 4.6b – left shows a picture of the actual magnetically actuated glaucoma device relative to a gloved finger. Figure 4.6b – bottom right shows the area of the plate where a channel was made to accommodate the drainage tube. Other than this connecting channel, the other channels in the end plate have identical design and dimensions as in the microfluidic devices tested above. The main outlet channel extends to the edge of the plate where it opens to the exterior. The size of the bypass channel chosen for this experiment was 40x40 µm.

Prior to implantation, the devices were manually injected with a saline solution by using a simple syringe to eliminate any air bubbles that may be trapped inside the channels. As a result of the fluidic pressure, accumulated bubbles will flow out of the device, and even if this process is not immediate, they gradually decrease in size until they eventually disappear. Thereafter, the devices were implanted in the eyes, and these were injected with a saline solution at a constant flow rate of 20 µL min^{-1}, as experimentally done by Villamarin and co-workers to test the *ex vivo* performance of the eyeWatch device [25]. This specific flow rate was necessary to maintain the physiological ocular rigidity throughout the experiment and keep the anterior chamber inflated, which would otherwise lose its shape at lower flow rates due to the fluid leakage that happens all around the insertion point of the injection needle (through which fluid flows into the eye) and at the back of the enucleated eye. A cannulated eye with the implanted device is shown in Figure 4.6c. This 20 µL min^{-1} of flow rate resulted in an IOP of 21.12 $\pm$ 1.42 mmHg when the implant was in the high-flow mode, i.e., the valve was in the open state. After closing the valve, the IOP was raised to 39.12 $\pm$ 3.60 mmHg, as can be seen in the red-colored datasets of Figure 4.6d. Each red-colored dataset represents the IOP measured in one eye, and each eye was implanted with a different device, meaning that in total five eyes and five implants were used for this experiment. Overall, the results confirm once again the efficacy of our magnetically actuated implant in tuning the IOP as a result of the valve operation. The very similar pressures measured in each ON and

OFF cycles for the different eyes/devices tested further support our conclusions from the previous experiments, proving once more the high reproducibility of our micro-pencil valving system. Furthermore, comparing with the *ex vivo* experiments performed on the eyeWatch implant [25], the pressure difference achieved between open and closed cycles with our device of 18 mmHg is very similar to the 19.3 mmHg pressure difference provided by the eyeWatch between its fully open and fully closed configurations.

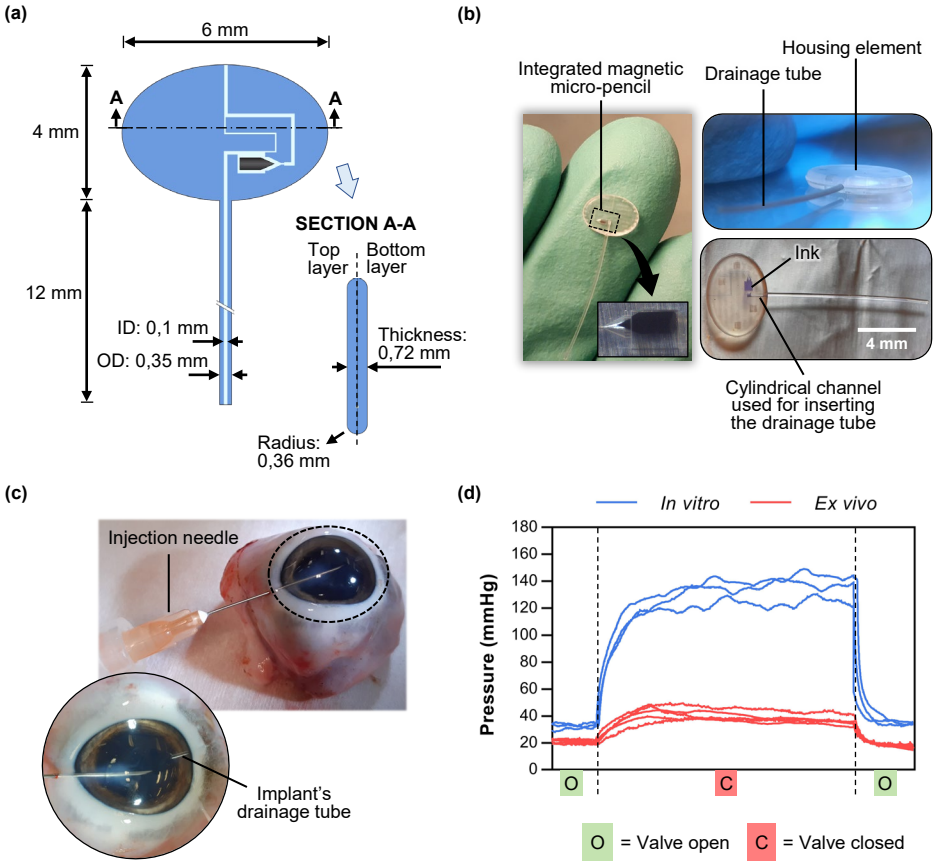

Figure 4.6: ***Ex vivo*** **experiments.** (**a**) Schematic of the magnetically actuated glaucoma implant with dimensions indicated in mm, showing a front view and a cross sectional view. (**b**) Pictures of the fabricated magnetically actuated glaucoma implant with integrated valve containing the micro-pencil. (**c**) Experimental setup used for the *ex vivo* experiments. (**d**) Red-colored lines – pressures measured in the anterior chamber of the porcine eyes as a result of the valve operation. Each dataset represents one device tested in one enucleated porcine eye; Blue-colored lines – pressures measured *in vitro* in the fabricated implants, when applying the same flow rate used for the *ex vivo* experiment. Each dataset represents one device tested. In this experiment, the pressure was measured for approximately 10 minutes with the valve open and 1 hour with the valve closed.

For comparison, *in vitro* experiments were also performed on the fabricated implants, where the same flow rate was applied as in the *ex vivo* experiments (20 µL min^{-1}). The results are shown in blue in the graph of Figure 4.6d, where each dataset represents one

device tested. In the open state, the pressure measured upstream the devices was 32.4 $\pm$ 2.01 mmHg, and this increased to 133.53 $\pm$ 8.12 mmHg when the valve was closed. The large differences observed between pressures measured in the *in vitro* and *ex vivo* experiments (Figure 4.6d, blue- and red-colored lines, respectively) are to be expected, considering that, as mentioned above, in the *ex vivo* experiment fluid leaks all around the insertion point of the needle and at the back of the enucleated eye, thus resulting in lower IOPs. This leakage is aggravated when closing the valve: the higher the hydrodynamic resistance of the implant, the more the fluid leakage around the insertion point of the needle. Leakage at the back of the eye is also likely to increase as a result of the high fluidic pressures that the eye is subjected to when the valve is closed. This leakage is an unavoidable artefact of the *ex vivo* experiment, and should not occur *in vivo*.

4.4 Discussion

We propose herein a novel, miniature, magnetically adjustable glaucoma implant for non-invasively regulating IOP after implantation. Our implant is comprised of a drainage tube and a housing plate in which a microvalve, consisting of an actuation chamber containing a moveable magnetic plug with the shape of a micro-pencil, is integrated. By using an external magnetic stimulus, the micro-pencil can be moved and the microvalve is switched between two states – open and closed – and the hydrodynamic resistance of the implant is changed accordingly. The device is designed to be implanted in the eye with the valve in the closed state to provide a high hydrodynamic resistance to prevent hypotony. When the ophthalmologist determines that the filtering bleb is sufficiently mature to offer resistance to the aqueous outflow, and a lower IOP is desired, the valve can be non-invasively opened with an external magnet to increase flow and decrease IOP.

We introduced a new microfabrication technique for the manufacture of this device and the integrated micro-pencil, based upon replica molding, using hot embossing and femtosecond laser-machined fused silica glass molds. The femtosecond laser machining process has proven to be an effective method to fabricate the molds for both the micro-pencil plug and the glaucoma device. The high geometrical complexity of the micro-pencil shape and differing channel heights were successfully achieved using this technique. Precise machining of this nature would be extremely difficult to accomplish using other conventional micro-manufacturing techniques such as photolithography or micro-milling [40]. The features in the glass molds were successfully transferred via hot embossing to the thermoplastic material SIBS, which comprises the implantable device. Hence, in this study we have demonstrated that the combination of hot embossing of thermoplastic materials with femtosecond laser-machined glass molds is a potentially advantageous process for mass production of microdevices containing three-dimensional structures requiring a few micrometers resolution, high accuracy and complexity [41].

To investigate the performance and function of our micro-pencil valving system, we first performed *in vitro* microfluidic experiments. The results from the cycle switching tests indicated that the pressure difference achieved between open and closed states is sufficient to prevent hypotony, and to maintain the IOP within an acceptable range of 5–15 mmHg. We have also confirmed that the valve function is repeatable, both within and between samples tested. Further experiments additionally demonstrated that our valving system

provides stable pressures over a period of 12 hours in the open and closed states under both static and dynamic conditions, the latter achieved by placing the devices under rocking motion to simulate a patient moving. The valve stability can be explained by two factors: 1) the sticky nature of the SIBS material, which makes it very difficult to move the micro-pencil without an external magnetic force being applied; and 2) the design of the actuation chamber itself. The similarity and close dimensions between the "pencil" shape of the outlet portion of the actuation chamber and the tip of the micro-pencil plug efficiently help to hold the micro-pencil in place when in the closed state. *Ex vivo* experiments performed on enucleated porcine eyes further confirmed the efficacy and reproducibility of our magnetically actuated implant in changing the IOP by the valve operation.

As future work, additional *in vitro* long-term measurements of the pressure over several days or months should be performed in order to further confirm the valve stability over time. Although we have proven that our microvalve is stable under rocking motion with 16 side-to-side movements per minute at 15 degrees, it would be also relevant to investigate if the stability of the valve is maintained under more vigorous agitation, which would better mimic, for instance, a more energetic shaking/nodding of the head, rubbing the eyes, or even after accidents and body impacts. For this, the already performed experiment could be repeated using a higher frequency of side-to-side movements and an increased angle, and to achieve these experimental conditions, a different and more powerful shaker device must be used. Moreover, the performance of our micro-plug may be affected by the application of compressive forces, which could occur if the implant is grasped too tightly with tweezers during the implantation procedure, for instance. To mimic these compressive forces *in vitro*, the device could be placed in a hot embossing machine and compressed using a limited amount of force, and thereafter tested to investigate if the actuation of the microvalve and the overall performance of the device is preserved. Furthermore, as mentioned earlier, occlusion with cells and other particulate matter might also be an issue for this type of small-lumen device, and therefore, more studies (including *in vivo* studies) are needed to check if our implant is at risk of blockage. This potential clogging issue could be explored *in vitro* by injecting fluorescent microparticles into the device and observe if they easily flow out of it or accumulate in the channels. Long-term clogging could also arise from the accumulation of proteins present in the aqueous humor in the small channels of our device. To investigate proteinaceous biofouling over time, an *in vitro* experiment could be performed where a proteinaceous liquid mimicking the aqueous humor, such as fluorescent-tagged bovine serum albumin, is injected into the device. The formation of a proteinaceous film on the inner surface of the channels can then be determined using fluorescence microscopy, as demonstrated by Park et al. [42]. To reduce the risk of blockage, the microchannel design can be further adjusted to feature smoother and curved corners rather than sharp corners, which are more prone to accumulate debris. Moreover, as our device is still in the proof-of-principle stage of development, we did not include a curved end plate to accommodate to the globe curvature. However, if future *in vivo* experiments indicate the importance of this feature, our powerful femtosecond laser machining technique can easily modify the glass mold to create the desired curvature in the end plate. The end plate edges were already designed and fabricated with a rounded shape, as depicted in Figure 4.6a and b, to avoid the potential fibrotic response caused

by sharp edges. This demonstrates our capability to create intricate features in our glass mold, which can be accurately replicated into our devices.

To summarize, in the future we plan to test our implant in an experimental animal model to confirm the laboratory results and to further evaluate the biocompatibility, controllability, and efficacy of our device. These studies would further validate the stability of the valving mechanism when placed in a living eye. Finally, our ultimate goal is to conduct clinical trials in glaucomatous patients with uncontrolled IOPs requiring a filtering procedure. In a first clinical trial, the magnetic resonance imaging (MRI)-compatibility of our device should be also investigated. Patients receiving our device should undergo an MRI-scan, as done by Roy and co-workers in the first clinical study performed on the eyeWatch implant [27]. The results from this study indicated that patients with the eyeWatch implanted experienced no discomfort or pain during MRI, with only minor image artifacts observed. However, the valve's positioning required adjustment following the scan. We anticipate that a similar adjustment may be necessary for our device. Therefore, patients should schedule a follow-up visit with their doctor after undergoing an MRI-scan to ensure proper valve positioning, if needed.

In conclusion, we have successfully developed a new molding technique that enabled the fabrication of a magnetically actuated glaucoma implant capable of switching between two hydrodynamic resistances to prevent hypotony from occurring in the early period after surgery, and to allow for maximum outflow capacity, if warranted, at a later stage, to effectively reduce IOP and stop glaucoma disease progression. By switching between hydrodynamic resistances, in a non-invasive and non-traumatic way, we expect that our magnetically actuated glaucoma implant will be suitable for patients with mild-to-severe glaucoma, ranging from primary open angle glaucoma where large drops in IOP are required, to normal tension glaucoma where fine control of relatively low IOP is required [43]. The new valving system proposed in this study can also be used for other microfluidic applications, such as in lab-on-chip and organ-on-chip systems, and in controlled drug delivery devices, amongst others.

4.5 Material and methods

4.5.1 Micro-pencil plug fabrication

The magnetic micro-pencil plugs were fabricated from SIBS containing homogeneously dispersed magnetic microparticles, carbonyl iron powder (CIP, 99.5%, average diameter of 5 µm, Sigma-Aldrich). The weight ratio between SIBS and CIP was 1:2, and it was predetermined following the critical particle volume concentration (CPVC) principle explained in the Supplementary Information 4.J [44]. The SIBS pellets with a 25% styrene content were generously provided by InnFocus Inc., a Santen Company. To obtain the batch material of magnetic SIBS, a hot melt extrusion process with mixing was used (Figure 4.2a). We ensured a homogeneous dispersion of the particles in the SIBS by thoroughly mixing in a mini twin-screw extruder heated at 150 °C at 100 rpm for 10 min. Microscopic imaging demonstrated that the obtained magnetic SIBS extruded pellets show a uniform dispersion of the particles in the SIBS matrix, see Figure 4.2a and Supplementary Figure 4.A1.

The mold used in the hot embossing machine to give the magnetic SIBS a micro-pencil shape was fabricated using a femtosecond laser machining process (Figure 4.2c). The design of the mold was prepared using the dedicated Alphacam software, where the laser scanning path (tool-path) to be fed to the FEMTOprinter f200 aHead (FEMTOprint SA, Switzerland) for exposing the fused silica glass, was also generated. The mold was fabricated on a 75x25x2 mm fused silica glass slide. The pulse energy and repetition rate used were 230 nJ and 1000 kHz, respectively. The laser was focused with a Thorlabs 20x microscope objective with a numerical aperture (NA) of 0.4. When the machining program was finished, the glass slide was immersed in a concentrated solution of 45% potassium hydroxide (KOH, Sigma-Aldrich) diluted in water to remove the exposed material. Finally, the mold was rinsed thoroughly with acetone and DI water to remove all debris. To facilitate the release (demolding) of the magnetic micro-pencil plugs after the hot embossing step, the femtosecond laser-machined glass mold was first coated with a superhydrophobic layer of fluorosilane (Trichloro(1H,1H,2H,2H-perfluorooctyl)silane, Sigma-Aldrich). To improve the adhesion of this coating, the mold underwent an oxygen plasma treatment performed immediately before the fluorosilane vapor deposition. After the silanization treatment, the mold was ready to be used in the hot embossing machine (Specac limited) together with magnetic SIBS pellets to fabricate the micro-pencil plugs. We used 150 °C to melt the magnetic SIBS and 5 tons of pressure to help the melted polymer to flow into the cavities of the mold (Figure 4.2b). The demolding took place after the hot embossing had cooled down to below 80 °C. After the hot embossing step, the residual layer attached to the micro-pencils was removed by cutting it with a razor blade under microscopic view.

4.5.2 Fabrication of the device with integrated microvalve

The mold used to fabricate the top and bottom layers of the micro-pencil devices was fabricated using the same femtosecond laser machining process as previously described. A fluorosilane coating was also applied. The mold was then used in the hot embossing machine together with the SIBS pellets for the fabrication of the microchip layers, using the same protocol applied for the micro-pencil plugs. After demolding the patterned SIBS film, the microchip layers were cut apart using a razor blade, and a biopsy punch was used to create the inlet and outlet connection holes. To integrate the magnetic micro-pencil into the device, a special coating was needed to prevent the micro-pencil from bonding to the actuation chamber walls during the thermal bonding step (used to make a closed device from the top and bottom layers). For this, a polyvinyl alcohol (PVA, molecular weight = 9000–10000 g mol^{-1}, Sigma-Aldrich) solution (PVA : DI water = 1:10) was prepared, in which the micro-pencil plug was dip coated. For the sacrificial PVA layer to solidify, the coated plug was placed on a hot plate at 90 °C for 5 min. Subsequently, the PVA-coated plug was inserted into the actuation chamber, and bottom and top layers were aligned. To facilitate the alignment process and promote a perfect alignment of the layers, the top layer was designed to have four alignment pins, which fit into the alignment holes of the bottom layer. Due to the stickiness of SIBS, ethanol was used in between the layers to enable moving them while aligning. After the ethanol evaporation, the device was thermally bonded on a hot plate at 90 °C for 10 min, while applying pressure with a

weight placed on top of the device. When the bonding was complete, the PVA was easily removed by flushing the bonded device with DI water.

4.5.3 Micro-pencil plug and device characterization

The shape and morphology, and some key dimensions of the micro-pencil plug and implant's channels were observed and measured using a Keyence VHX-5000 digital microscope.

4.5.4 *In vitro* microfluidic experiments

Microfluidic experiments involving actuating the magnetic micro-pencil with a moving external magnet were carried out to confirm the valving function. The pressure upstream the implant was measured while the microvalve switched between open/closed states. The setup used for this experiment is illustrated in Figure 4.4a and was comprised of: 1) a syringe pump (Fusion 200, Chemyx Inc.), pumping DI water at a constant flow rate of 2.5 μL min^{-1} – equal to the typical rate of aqueous humor production in the eye; 2) a pressure transducer (Omega Engineering), connected to the syringe pump and to the inlet of the device, thus constantly measuring the pressure upstream the device (in mmHg); and 3) a column of water connected to the outlet of the device, mimicking the pressure in the bleb when hypotony is most likely to occur (approximately 1.38 mmHg, or 1.88 cmH_2O). The magnet, with a geometry of 10x10x10 mm^3 and a remnant flux density of 1.3 T, was positioned underneath the device at a distance of 1.75 mm from the device's bottom surface (2.15 mm from the center axis of the integrated micro-pencil plug, as represented in Figure 4.4c). In between the device and the magnet, a 750 μm-thick polycarbonate sheet and a 1 mm-thick glass slide were used to hold the device.

We carried out different microfluidic experiments to fully characterize the valve operation. First, an ON/OFF experiment was performed to check the repeatability of the valve function. In this experiment, the pressure was measured for approximately 5 minutes with the valve open, and 30 minutes with the valve closed. In total, four ON/OFF cycles were performed for each sample. To investigate if fluid can still leak through the main outlet channel when the valve is closed, devices without the main outlet channel and without the microvalve integrated were also fabricated and tested. Second, to evaluate the stability of the pressure when the valve is in the closed state, we measured the pressure upstream the device for period of 12 hours. Third, to investigate if the valve function would be affected by the patient's movements, we measured the pressure for a period of 12 hours with the device placed under rocking motion, using a digital platform rocker shaker (VWR) as illustrated in Figure 4.5b. The rocking, side to side (2D) motion was performed in the main direction of the micro-pencil movement, and a tilt of 15° and a speed of 8 rpm (which corresponds to 16 side to side movements/minute) were used. Except for the non-static experiment, all the aforementioned experiments were performed in three samples/devices of both the 50x50 μm and 40x40 μm bypass channel devices.

4.5.5 *Ex vivo* experiments

Ex vivo experiments were performed on porcine eyes, for which the actual implants comprised of a drainage tube and an elliptical-shaped end plate had to be first fabricated. The fabrication of the plate followed the same procedure that was used for making the microfluidic devices, i.e., the bottom and top layers were fabricated by replica molding using hot embossing and a femtosecond laser-machined glass mold. A home-made punching device with the same elliptical shape as the plate was used to remove the residual layer that was attached to the top and bottom layers after the hot embossing step. A solvent bonding technique was used to attach the drainage tube to the plate. For this, 1.5 mm of a 12 mm-long SIBS tube (100 µm inner diameter, 350 µm outer diameter), kindly provided by InnFocus Inc., was first dip-coated in toluene (98%, VWR Chemicals) and then immediately introduced in the channel of the plate specifically designed for the tube to be connected. Afterwards, the same thermal bonding technique was used as previously explained. Finally, the device was thoroughly flushed with DI water to remove the PVA coating on the micro-pencil and any existing impurity.

Five freshly enucleated porcine eyes, with *post-mortem* time less than 4 hours, were obtained from a local butcher. For the implantation of the devices into the eyes, first a fornix-based conjunctival flap was created, after which a deep scleral pocket was formed. Through the scleral pocket, a needle tract was made with a 25-gauge needle into the anterior chamber. The drainage tube was then implanted through the needle tract. At approximately 180° from the implantation site, the eyes were cannulated with another 25-gauge needle through which a saline solution of sodium chloride (NaCl 0.9%, B Braun) was injected into the anterior chamber at a constant flow rate of 20 µL min^{-1} delivered by a syringe pump – this specific flow rate was necessary to keep the physiological ocular rigidity throughout the experiment. The needle was inserted carefully between the anterior plane of the iris and the posterior surface of the cornea. In between the pump and the needle, a pressure transducer was connected to measure the pressure inside the eye (IOP) in real-time. For each eye, one ON/OFF cycle was performed, and the pressure was measured for approximately 10 minutes with the valve open and 1 hour with the valve closed. For comparison, the same experiment was also performed *in vitro* on the fabricated implants, where the same flow rate was applied.

4.6 Supplementary Information

4.A Magnetic particle dispersion in SIBS

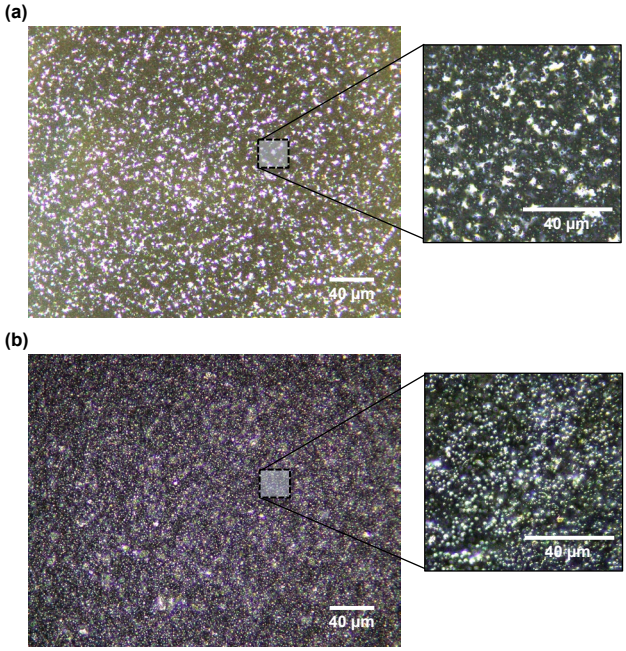

Figure 4.A1: Magnetic particle dispersion in the SIBS matrix. Microscopic images showing the dispersion of the magnetic particles in the SIBS matrix, captured using varying magnifications and using both transmission (**a**) and reflection (**b**) modes for imaging the samples. A 100 µm-thin magnetic SIBS film fabricated upfront using hot embossing was used to take these images.

4.B Magnetic SIBS cytotoxicity

The *in vitro* cytotoxicity of the magnetic SIBS extracts on the human MG-63 osteosarcoma cell line was evaluated according to the ISO 10993-5-2009 standard. The cells were maintained in minimum essential alpha medium supplemented with 10% fetal bovine serum (FBS), 100 U mL^{-1} penicillin and 100 µg streptomycin (now referred to as culture medium). MG-63 cells were cultured and refreshed every 2–3 days. Once the cells reached approximately 80% confluence, they were passaged. One day before the exposure to the extracts, the cells were trypsinized and resuspended in culture medium to create a suspension with a concentration of 1.8×10^4 cells mL^{-1}. Thereafter, 100 µL of the cell suspension was seeded into a 96-well plate, giving a seeding density of 1.8×10^3 cells/well. The cells were incubated for 24 hours at 37 °C with 5% CO_2. The medium was then replaced by different magnetic SIBS extracts. For the preparation of the extracts, first, a 700 µm-thick magnetic SIBS film was fabricated using hot embossing and thereafter cut to small rectangular pieces of 10x5 mm. The samples were sterilized by immersing

in 70% ethanol for 20 minutes. The prepared samples were rinsed in phosphate-buffered saline (PBS) and transferred to culture medium and incubated for 72 hours at 37 °C. The surface area to volume ratio was 3 cm^2 mL^{-1} for all samples (6 cm^2 mL^{-1}, if both top and bottom surfaces of the films are considered), in accordance with the ISO 10993-12-2012 standard. Three technical replicates were used for each sample. Dilutions were prepared to achieve 50%, 25% and 10% extracts. Undiluted, i.e., 100% extracts were also used. After 24-hour of incubation with the extracts, cell metabolic activity was evaluated using a resazurin (PrestoBlue) assay. The treatment medium was aspired and replaced with 90 µL of culture medium and 10 µL of PrestoBlue reagent. After 30 minutes of incubation, fluorescence at 530/590 nm (excitation/emission) was measured. Cytotoxicity of the extracts was depicted as a percentage of metabolic activity of the control, i.e., as relative metabolic activity (RMA) calculated as follows

$$RMA = 100 \times \frac{F_{\text{sample}} - F_{\text{blank}}}{F_{\text{control}} - F_{\text{blank}}}, \tag{4.B1}$$

where F_{sample} stands for the average fluorescence of resorufin produced by the affected cells (i.e., cells incubated with extracts), F_{blank} is the average fluorescence measured in the blank solution (no cells), and F_{control} stands for the average fluorescence of resorufin produced by of the unaffected cells (i.e., negative control cells). Extracts causing the fluorescent signal to decrease below 70% of the activity of the negative control were considered cytotoxic, as described in the standard ISO 10993-5. This experiment confirmed that the magnetic SIBS is non-cytotoxic at all the extract concentrations tested (as indicated in Figure 4.B1).

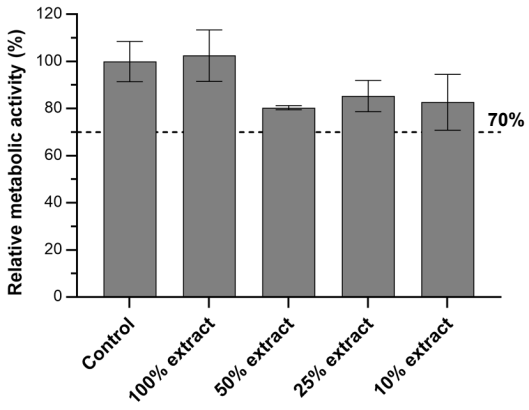

Figure 4.B1: Relative metabolic activity of the human MG-63 osteosarcoma cells (resazurin assay) after 24-hour incubation with 100%, 50%, 25% and 10% extracts of magnetic SIBS. The data represents the mean ± SD ($n = 3$). Sole extraction medium served as a control (unaffected cells which metabolic activity was taken as 100%). The dashed line indicates the normative limit of 70% metabolic activity of the control (ISO 10993-5-2009).

4.C Femtosecond laser machining process and laser affected zone

Although we designed the micro-pencil glass mold to yield micro-pencils with a diameter of 350 µm, following fabrication their diameter was 356 $\pm$ 1 µm, as can be seen in Figure 4.2d. This minor deviation from the desired diameter can be explained by the size of the elliptical-shaped laser affected zone during the femtosecond laser exposure, which, in fused silica glass and when using a 20x objective, is 3 µm-wide and 24 µm-long [45]. This will inevitably enlarge the diameter of the cavity in the glass mold exposed to the KOH by 3 µm, thus resulting in micro-pencil plugs with a larger diameter. Furthermore, after long exposure to KOH etching, the un-exposed parts of the glass also start to be etched. This may explain why the diameter of the plugs was increased even further. The length of the plugs varied quite significantly, with an average length of 988.3 $\pm$ 10 µm. However, these length differences were expected, since the residual layer attached to the cylindrical (bottom) portion of the plugs was manually removed with a razor blade after hot embossing, making it therefore very difficult to guarantee the same length across all the fabricated plugs.

For the channels in the devices, Figure 4.D1e shows that the height appears to have been less affected by the laser affected zone and/or KOH etching than the width. The reason for the height of the channels to be very similar to the initially designed one is that, in the glass mold, not only the top surface of the channel features is machined, but also the bottom surface, all around the channels. Machining the top surface reduces the height of the channels by approximately 12 µm, due to the size of the elliptical-shaped laser affected zone. In contrast, machining around the channel features, on the bottom surface of the mold, leads to a 12 µm-increase in the height of the channels. As the machining is done on both surfaces, the resultant change in the height from the originally designed one is almost negligible. On the other hand, machining both side walls of the channels will decrease their width by at least 3 µm due to the width of the laser affected zone, which can be aggravated by the KOH inadvertently etching the non-machined glass. This explains the smaller width obtained in all channels.

4.D Micro-pencil device design and relevant dimensions

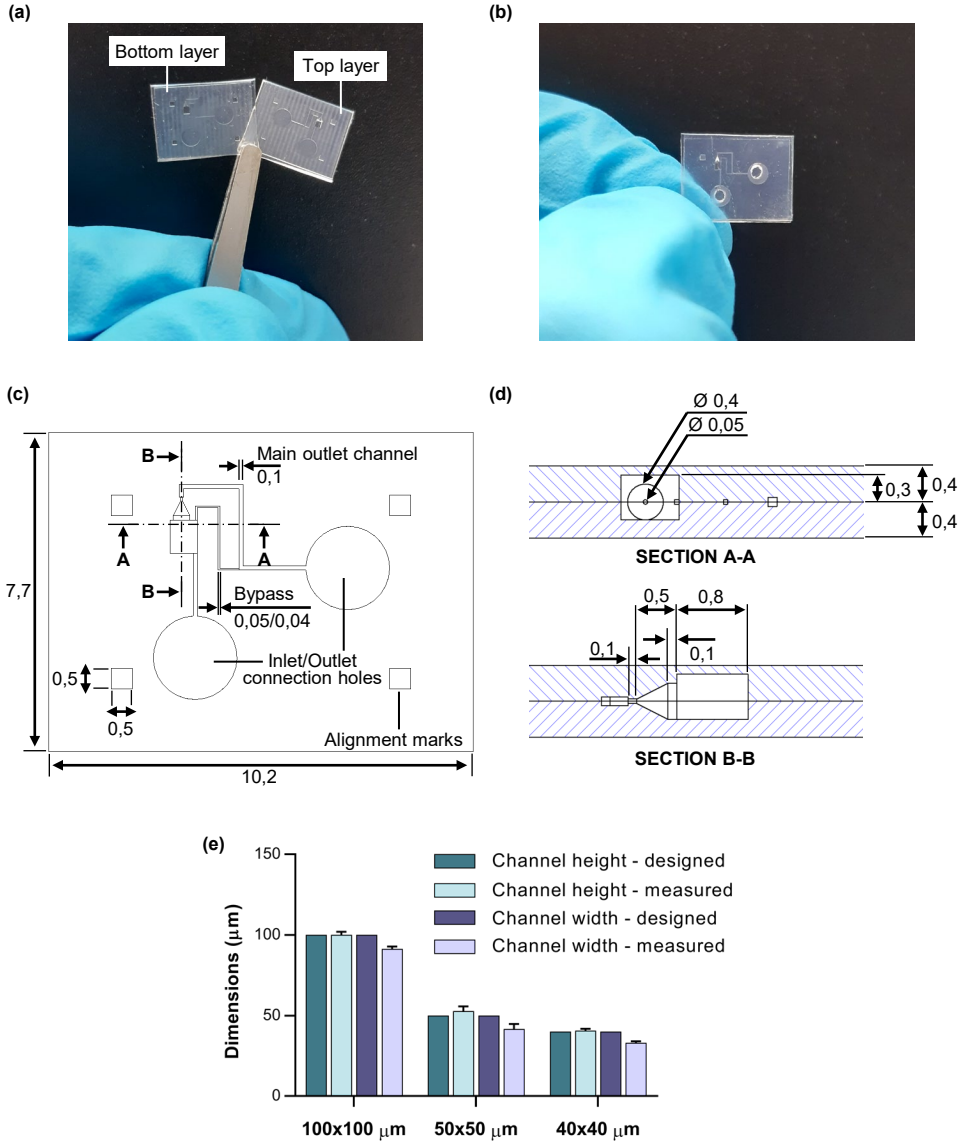

Figure 4.D1: Micro-pencil device design and relevant dimensions. (**a**) Replica-molded top and bottom layers, and (**b**) bonded micro-pencil device used for the *in vitro* experiments. (**c**) Schematic top view of the channel layout and relevant dimensions in mm. (**d**) Cross-sectional views of the device showing the actuation chamber shape and key dimensions in mm. (**e**) Graph indicating the differences between the measured channel dimensions and the initially designed ones. The data represents the mean ± SD ($n = 3$).

4.E Magnetic force calculation

The translational force acting on the magnetic micro-pencil plug is calculated by first computing the magnetic field produced by the permanent magnet, with a geometry of 10x10x10 mm^3 and a remnant flux density of 1.3 T, using the commercially available software COMSOL Multiphysics. The magnetic flux density and its variation (gradient) is extracted from the simulated model to then calculate the net driving force acting on the plug, which is given by

$$\vec{F}_{\text{mag}} = (\vec{m} \cdot \nabla)\vec{B} = \rho V(\vec{M}_0 \cdot \nabla)\vec{B} + \frac{V\chi}{\mu_0}(\vec{B} \cdot \nabla)\vec{B}, \tag{4.E2}$$

where ρ is the density of the magnetic particles (7.86 g/cm^3), V is the volume of magnetic particles in a micro-pencil plug (1.5×10^{-5} cm^3), χ is the magnetic susceptibility of the magnetic particles (here we take $\chi = 0.4$ [46]), μ_0 is the permeability of vacuum, $\vec{M}_0$ is the initial magnetization of the plug and $\vec{B}$ is the applied magnetic field. $\vec{M}_0$ is neglected since it has a value very close to zero. As a result, the above equation becomes

$$\vec{F}_{\text{mag}} = \frac{V\chi}{\mu_0}(\vec{B} \cdot \nabla)\vec{B}. \tag{4.E3}$$

From the above equation, we conclude that the magnetic translational force applied to the micro-pencil plug is a combined effect of the magnitude of the magnetic field and magnetic field gradient experienced by the plug. As the plug has a single degree of freedom (linear translation), we calculated the magnetic translational force applied to the micro-pencil plug along its direction of movement. At a vertical distance of 2.15 mm from the surface of the magnet and horizontal distance varying from 0–8 mm with respect to the center axis of the magnet, we estimated that the magnetic force along the direction of the plug movement varies approximately from 1.97×10^{-6} N (magnitude of the magnetic field B = 0.35 T, magnitude of the magnetic field gradient ∇B = 45.56 T/m), when the center axis of the plug is perfectly aligned with the center axis of the magnet, to a maximum force of 5.67×10^{-5} N (B = 0.27 T, ∇B = 88.77 T/m) when the magnet is at a distance of 5 mm from the plug (corner of the magnet is aligned with the central axis of the plug, as depicted in Figure 4.4c). This force is obtained if we consider that the magnet is positioned with the north-pole facing up (vertical polarity).

4.F Micro-pencil plug actuation

Figure 4.F1: Micro-pencil plug actuation. QR-code for a video demonstrating the microvalve switching between open and closed states by moving the micro-pencil plug using an external magnet.

4.G Additional ON/OFF experiment results

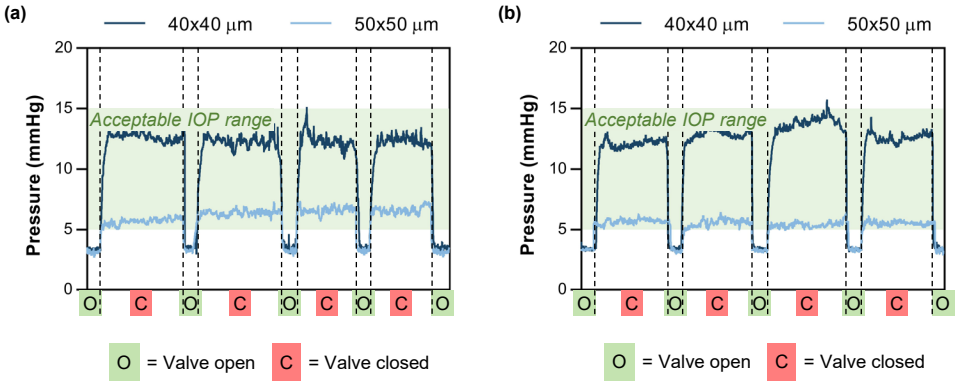

Figure 4.G1: Additional ON/OFF experiment results. *In vitro* measurement of the pressure variation upstream the 40x40 µm and 50x50 µm micro-pencil devices – (**a**) Samples 2 and (**b**) Samples 3 – as a result of the valve operation. The shaded green areas represent an acceptable IOP range of 5–15 mmHg.

4.H Hydrodynamic resistance calculations

We theoretically determined the total hydrodynamic resistance of our micro-pencil devices (r_{total}) by taking the sum of the hydrodynamic resistances of the inlet channel (r_{inlet}), the parallel bypass and main outlet channels (r_{bypass}, $r_{\text{main outlet}}$), and the combined outlet channel ($r_{\text{combined outlet}}$, where the bypass and main outlet channels come together, see Figure 4.3 and Figure 4.D1), as follows

$$r_{\text{total}} = r_{\text{inlet}} + \frac{r_{\text{bypass}} \times r_{\text{main outlet}}}{r_{\text{bypass}} + r_{\text{main outlet}}} + r_{\text{combined outlet}}. \tag{4.H4}$$

To calculate the hydrodynamic resistance of each channel (r_{channel}), the following formula was applied

$$r_{\text{channel}} = \frac{12\mu L}{1 - 0.63(h/w)} \frac{1}{h^3 w}, \tag{4.H5}$$

where μ[Pa s] is the dynamic viscosity of the aqueous humor, L is the length of the channel, and h and w represent, respectively, the average height and width of the channel measured beforehand (see Figure 4.D1e). The r_{total} was determined for the devices with the valve both in the open and in the closed states, as well as for the devices containing only the bypass channel and no main outlet channel. Since r_{total} is the difference between the applied outlet pressure and measured upstream pressure, divided by the applied flow rate, then

$$r_{\text{total}} = \frac{IOP - P_{\text{bleb}}}{Q} = r_{\text{inlet}} + \frac{r_{\text{bypass}} \times r_{\text{main outlet}}}{r_{\text{bypass}} + r_{\text{main outlet}}} + r_{\text{combined outlet}}, \tag{4.H6}$$

where IOP is the pressure measured experimentally, P_{bleb} is the applied outlet pressure, i.e., the pressure in the bleb when hypotony is most likely to occur (approximately 1.38 mmHg), and Q is the flow rate applied (2.5 µL min^{-1}). From equation 4.H7, the $r_{\text{main outlet}}$ for the experiments with the valve closed, which effectively equals the hydrodynamic resistance provided by the valve (r_{valve}), was calculated as follows

$$r_{\text{main outlet}} = \frac{-r_{\text{bypass}} \times \left(\frac{IOP - P_{\text{bleb}}}{Q} - r_{\text{inlet}} - r_{\text{combined outlet}}\right)}{\left(\frac{IOP - P_{\text{bleb}}}{Q} - r_{\text{inlet}} - r_{\text{combined outlet}}\right) - r_{\text{bypass}}}. \tag{4.H7}$$

The results from these calculations are shown in Table 4.H1. Confirming the consistency of the calculations, we find that the estimated hydrodynamic resistance provided by the valve (r_{valve}) is almost identical for the two types of devices. This indicates that the valve behaves in a similar manner and is independent of the bypass channel dimensions. When the valve is open, the total hydrodynamic resistance (r_{total}) is very similar between devices, which is expected since the hydrodynamic resistance is then dominated by the open main outlet channel, which is identical for both devices. On the other hand, and as anticipated, the total hydrodynamic resistance of the 40x40 µm device when the valve is closed is approximately two times higher than that of the 50x50 µm device (4.53 as compared to 2.22 mmHg/µL min^{-1}). When the valve is in the open state, the hydrodynamic resistance of our devices is lower than that theoretically calculated for the PRESERFLO MicroShunt of 1.81 mmHg/µL min^{-1} [47]. This means that our device might possibly produce a more significant IOP-lowering effect compared to that of the PRESERFLO MicroShunt, which has already been proven successful in reducing IOP in glaucoma patients' eyes [30, 48].

Using the calculated hydrodynamic resistance provided by the valve, we estimated the pressure that would be experimentally measured if different inflow rates were used. As mentioned earlier, the *in vitro* experiments were performed using an average inflow rate

Table 4.H1: Hydrodynamic resistance of microfluidic devices used in the *in vitro* experiments.

Bypass channel size (height x width)	Condition	r_{total}	r_{valve}	Units
50x50 µm	Only bypass channel	2.50	15.18	mmHg/µL min^{-1}
	Valve open	0.45		
	Valve closed	2.22		
40x40 µm	Only bypass channel	6.24	14.89	
	Valve open	0.46		
	Valve closed	4.53		

of 2.5 µL min^{-1}. However, the aqueous humor production rate varies slightly between the waking and sleeping hours. In a healthy person, aqueous humor is produced at approximately 3 µL min^{-1} in the morning, 2.5 µL min^{-1} in the afternoon, and 1.5 µL min^{-1} during the night [35]. Based on our calculations, if the valve is in the closed state and the lower value of aqueous flow rate (1.5 µL min^{-1}) is considered, the IOP would be 4.70 mmHg for the 50x50 µm device and 8.18 mmHg for the 40x40 µm device. On the other hand, if the higher flow rate (3 µL min^{-1}) is considered and the valve is closed, the IOP would be 8.03 mmHg and 14.98 mmHg for the 50x50 µm and 40x40 µm devices, respectively. These values do not significantly deviate from the healthy IOP range of 5–15 mmHg, meaning that if the aqueous humor production rate varies slightly with the circadian rhythm, both types of devices with the valve in the closed state would still provide acceptable IOP values.

4.I Additional 12-hour experiment results

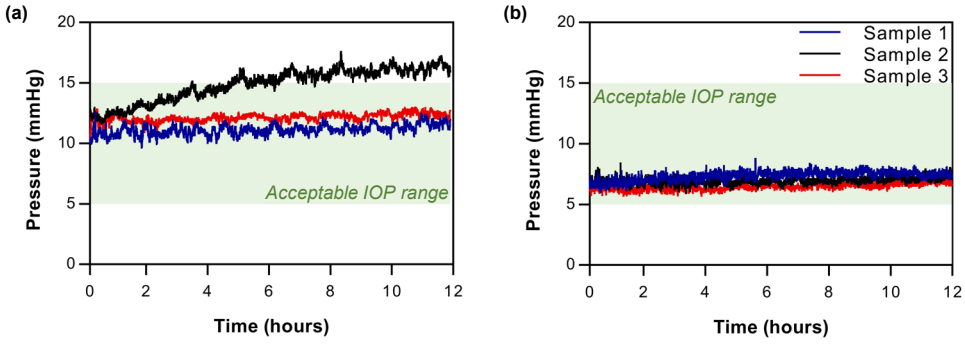

Figure 4.I1: Additional 12-hour experiment results. Overview of the pressures measured *in vitro* upstream the (**a**) 40x40 µm and (**b**) 50x50 µm micro-pencil devices for period of 12 hours with the valve in the closed state, and under static conditions (i.e., the devices did not move over the course of the experiment). Each line represents one of the samples tested. The shaded green areas represent an acceptable IOP range of 5–15 mmHg.

4.J Critical particle volume concentration (CPVC) principle

The amount of magnetic particles, carbonyl iron powder (CIP, 99.5%, average diameter of 5 µm, Sigma-Aldrich), to be mixed with SIBS was pre-determined following the critical particle volume concentration (CPVC) principle [44]. The critical volume concentration of particles in an elastomeric matrix is the concentration at which the particles are in physical contact with each other and the voids between them are completely filled with the elastomer. At concentrations lower than the CPVC, the particles are separated by more elastomer, while for higher concentrations than the CPVC, the amount of elastomer is not sufficient to completely surround the particles. In the latter case, the mechanical properties, such as stress at break, may be deteriorated, and the composite material stiffens due to the increase in filler content. The CPVC for a magnetic powder can be calculated from its apparent/bulk density. When iron particles are stored in a container, there will be a large amount of air in between the particles. This will mean that the "apparent density" is much less than the density of the solid iron particles. If the air is replaced totally by the elastomeric matrix, the result is the elastomer filled with a critical amount of iron. For the CPVC calculation, the following formula can be used

$$CPVC_{\text{CIP}} = 100 \times \frac{\rho_{\text{apparent}}}{\rho_{\text{iron}}}, \tag{4.J8}$$

where ρ_{apparent} is the apparent density of the CIP and ρ_{iron} is equal to 7.86, which is the density of iron (g/cm^3). ρ_{apparent} varies between 3–4 g/cm^3, and we considered the value of 3.50 g/cm^3 in our calculations. According to the formula, the CPVC of CIP in the SIBS matrix is 44.53 vol%. We have decided to fabricate our magnetic SIBS with a weight ratio of 1:2, where the concentration of particles in the SIBS matrix is approximately half of the CPVC ($\approx$ 20 vol%), in order to preserve the mechanical properties of the composite.

Bibliography

1. Pereira, I. C., van de Wijdeven, R., Wyss, H. M., Beckers, H. J. & den Toonder, J. M. Conventional glaucoma implants and the new MIGS devices: a comprehensive review of current options and future directions. *Eye* **35,** 3202–3221 (2021).
2. Lee, R. M., Bouremel, Y., Eames, I., Brocchini, S. & Khaw, P. T. Translating Minimally Invasive Glaucoma Surgery Devices. *Clinical and Translational Science* **13,** 14–25 (2020).
3. Tham, Y. C. *et al.* Global Prevalence of Glaucoma and Projections of Glaucoma Burden through 2040: A Systematic Review and Meta-Analysis. *Ophthalmology* **121,** 2081–2090 (2014).
4. Cardigos, J. *et al.* Nanotechnology-Ocular Devices for Glaucoma Treatment: A Literature Review. *Current Eye Research* **44,** 111–117 (2019).
5. Weinreb, R. N., Aung, T. & Medeiros, F. A. The Pathophysiology and Treatment of Glaucoma: A Review. *JAMA* **311,** 1901–1911 (2014).
6. Guglielmi, P., Carradori, S., Campestre, C. & Poce, G. Novel therapies for glaucoma: a patent review (2013-2019). *Expert Opinion on Therapeutic Patents* **29,** 769–780 (2019).
7. Sihota, R., Angmo, D., Ramaswamy, D. & Dada, T. Simplifying "target" intraocular pressure for different stages of primary open-angle glaucoma and primary angle-closure glaucoma. *Indian Journal of Ophthalmology* **66,** 495–505 (2018).
8. Agrawal, P. & Bradshaw, S. E. Systematic Literature Review of Clinical and Economic Outcomes of Micro-Invasive Glaucoma Surgery (MIGS) in Primary Open-Angle Glaucoma. *Ophthalmology and Therapy* **7,** 49–73 (2018).
9. Conlon, R., Saheb, H. & Ahmed, I. I. K. Glaucoma treatment trends: a review. *Canadian Journal of Ophthalmology* **52,** 114–124 (2017).
10. Christakis, P. G. *et al.* Five-Year Pooled Data Analysis of the Ahmed Baerveldt Comparison Study and the Ahmed Versus Baerveldt Study. *American Journal of Ophthalmology* **176,** 118–126 (2017).
11. Minckler, D. S. *et al.* Aqueous shunts in glaucoma: a report by the American Academy of Ophthalmology. *Ophthalmology* **115,** 1089–1098 (2008).
12. Purtskhvanidze, K., Saeger, M., Treumer, F., Roider, J. & Nölle, B. Long-term results of glaucoma drainage device surgery. *BMC Ophthalmology* **19,** 14 (2019).
13. Christakis, P. G. *et al.* The Ahmed Versus Baerveldt Study: Five-Year Treatment Outcomes. *Ophthalmology* **123,** 2093–2102 (2016).
14. Budenz, D. L. *et al.* Five-year treatment outcomes in the ahmed baerveldt comparison study. *Ophthalmology* **122,** 308–316 (2015).
15. Benson, S. E., Mandal, K., Bunce, C. V. & Fraser, S. G. Is post-trabeculectomy hypotony a risk factor for subsequent failure? A case control study. *BMC Ophthalmology* **5,** 7 (2005).
16. Loewen, N. A. & Tsai, J. C. Managing a failing filtering bleb. *Glaucoma Today,* 39–42 (2009).

17. Pereira, I. C., Wyss, H. M., Pinchuk, L., Beckers, H. J. & den Toonder, J. M. A model for designing intraocular pressure-regulating glaucoma implants. *PLoS ONE* **17,** e0273672 (2022).

18. Roy, S. *et al.* Comparison between the eyeWatch Device and the Ahmed Valve in Refractory Glaucoma. *Journal of Glaucoma* **29,** 401–405 (2020).

19. *Surgical innovations in glaucoma* (eds Samples, J. R. & Ahmed, I. I. K.) (Springer New York, NY, New York, NY, USA, 2014).

20. Tan, M. C. J. *et al.* Two-Year Outcomes of the Paul Glaucoma Implant for Treatment of Glaucoma. *Journal of Glaucoma* **31,** 449–455 (2022).

21. Lim, K. S. Control and optimisation of fluid flow in glaucoma drainage device surgery. *Eye* **32,** 230–234. ISSN: 14765454 (2018).

22. Riva, I., Roberti, G., Oddone, F., Konstas, A. G. & Quaranta, L. Ahmed glaucoma valve implant: Surgical technique and complications. *Clinical Ophthalmology* **11,** 357–367 (2017).

23. Lee, C. K., Ma, K. T., Hong, Y. J. & Kim, C. Y. Long-term clinical outcomes of Ahmed valve implantation in patients with refractory glaucoma. *PLoS ONE* **12,** e0187533 (2017).

24. Nassiri, N. *et al.* Ahmed Glaucoma Valve and Single-Plate Molteno Implants in Treatment of Refractory Glaucoma: A Comparative Study. *American Journal of Ophthalmology* **149,** 893–902. ISSN: 00029394 (2010).

25. Villamarin, A., Roy, S., Bigler, S. & Stergiopulos, N. A new adjustable glaucoma drainage device. *Investigative Ophthalmology and Visual Science* **55,** 1848–1852 (2014).

26. Villamarin, A. *et al.* In vivo testing of a novel adjustable glaucoma drainage device. *Investigative Ophthalmology and Visual Science* **55,** 7520–7524 (2014).

27. Roy, S. *et al.* Initial Clinical Results of the eyeWatch: a New Adjustable Glaucoma Drainage Device Used in Refractory Glaucoma Surgery. *Journal of Glaucoma* **28,** 452–458 (2019).

28. Siewert, S. *et al.* Development of a micro-mechanical valve in a novel glaucoma implant. *Biomedical Microdevices* **14,** 907–920 (2012).

29. Sadruddin, O., Pinchuk, L., Angeles, R. & Palmberg, P. Ab externo implantation of the MicroShunt, a poly (styrene-block-isobutylene-block-styrene) surgical device for the treatment of primary open-angle glaucoma: a review. *Eye and Vision* **6,** 36 (2019).

30. Batlle, J. F., Corona, A. & Albuquerque, R. Long-term Results of the PRESERFLO MicroShunt in Patients with Primary Open-angle Glaucoma from a Single-center Nonrandomized Study. *Journal of Glaucoma* **30,** 281–286 (2021).

31. Acosta, A. C. *et al.* A Newly Designed Glaucoma Drainage Implant Made of Poly(styrene-b-isobutylene-b-styrene). *Archives of Ophthalmology* **124,** 1742–1749 (2006).

32. Shaarawy, T. M., Moschos, M. M. & Sherwood, M. B. *New Glaucoma Surgical Alternatives*. in *Glaucoma* (eds Shaarawy, T. M., Sherwood, M. B., Hitchings, R. A. & Crowston, J. G.) 2nd ed., 1188–1201 (W.B. Saunders, 2015).

33. Suthisomboon, T., Bargiel, S., Rabenorosoa, K. & Pengwang, E. *Design and Simulation of XZ MEMS Micropositioning with 3D-Complex Structure*. in *2020 Symposium on Design, Test, Integration and Packaging of MEMS and MOEMS (DTIP)* (Lyon, France, 2020), 1–5.

34. Steimle, A. 3D Micro-Printing: A new Era for Med-Tech Applications. *Laser Technik Journal* **15,** 32–34 (2018).

35. Goel, M., Picciani, R. G., Lee, R. K. & Bhattacharya, S. K. Aqueous Humor Dynamics: A Review. *The Open Ophthalmology Journal* **4,** 52–59 (2010).

36. Thygesen, J. *Late Hypotony*. in *Glaucoma* (eds Shaarawy, T. M., Sherwood, M. B., Hitchings, R. A. & Crowston, J. G.) 2nd ed., 863–881 (W.B. Saunders, London, England, UK, 2015).

37. Lee, J. Y. *et al.* Structural Confirmation of Lymphatic Outflow from Subconjunctival Blebs of Live Humans. *Ophthalmology Science* **1,** 100080 (2021).

38. Kotliar, K. E., Kozlova, T. V. & Lanzl, I. M. Postoperative aqueous outflow in the human eye after glaucoma filtration surgery: biofluidmechanical considerations. *Biomedizinische Technik* **54,** 14–22 (2009).

39. Pinchuk, L. *et al.* The development of a micro-shunt made from poly(styrene-block-isobutylene-block-styrene) to treat glaucoma. *Journal of Biomedical Materials Research - Part B Applied Biomaterials* **105,** 211–221 (2017).

40. Xu, B. B. *et al.* Fabrication and multifunction integration of microfluidic chips by femtosecond laser direct writing. *Lab on a Chip* **13,** 1677–1690 (2013).

41. Choi, H. W., Bong, S., Farson, D. F., Lu, C. & Lee, L. J. Femtosecond laser micromachining and application of hot embossing molds for microfluid device fabrication. *Journal of Laser Applications* **21,** 196 (2009).

42. Park, H., Raffiee, A. H., John, S. W., Ardekani, A. M. & Lee, H. Towards smart self-clearing glaucoma drainage device. *Microsystems and Nanoengineering* **4,** 35 (2018).

43. Fingeret, M. & Dickerson, J. E. The role of minimally invasive glaucoma surgery devices in the management of glaucoma. *Optometry and Vision Science* **95,** 155–162 (2018).

44. Lokander, M. & Stenberg, B. Performance of isotropic magnetorheological rubber materials. *Polymer Testing* **22,** 245–251 (2003).

45. Rajesh, S. & Bellouard, Y. Towards fast femtosecond laser micromachining of fused silica: The effect of deposited energy. *Optics Express* **18,** 21490–21497 (2010).

46. Shevkoplyas, S. S., Siegel, A. C., Westervelt, R. M., Prentiss, M. G. & Whitesides, G. M. The force acting on a superparamagnetic bead due to an applied magnetic field. *Lab on a Chip* **7,** 1294–1302 (2007).

47. Barberá, M. I. *et al.* Evaluation of the Ultrastructural and In Vitro Flow Properties of the PRESERFLO MicroShunt. *Translational Vision Science and Technology* **10,** 26 (2021).

48. Scheres, L. M. J. *et al.* XEN® Gel Stent compared to PRESERFLO™ MicroShunt implantation for primary open-angle glaucoma: two-year results. *Acta Ophthalmologica* **99,** e433–e440 (2021).

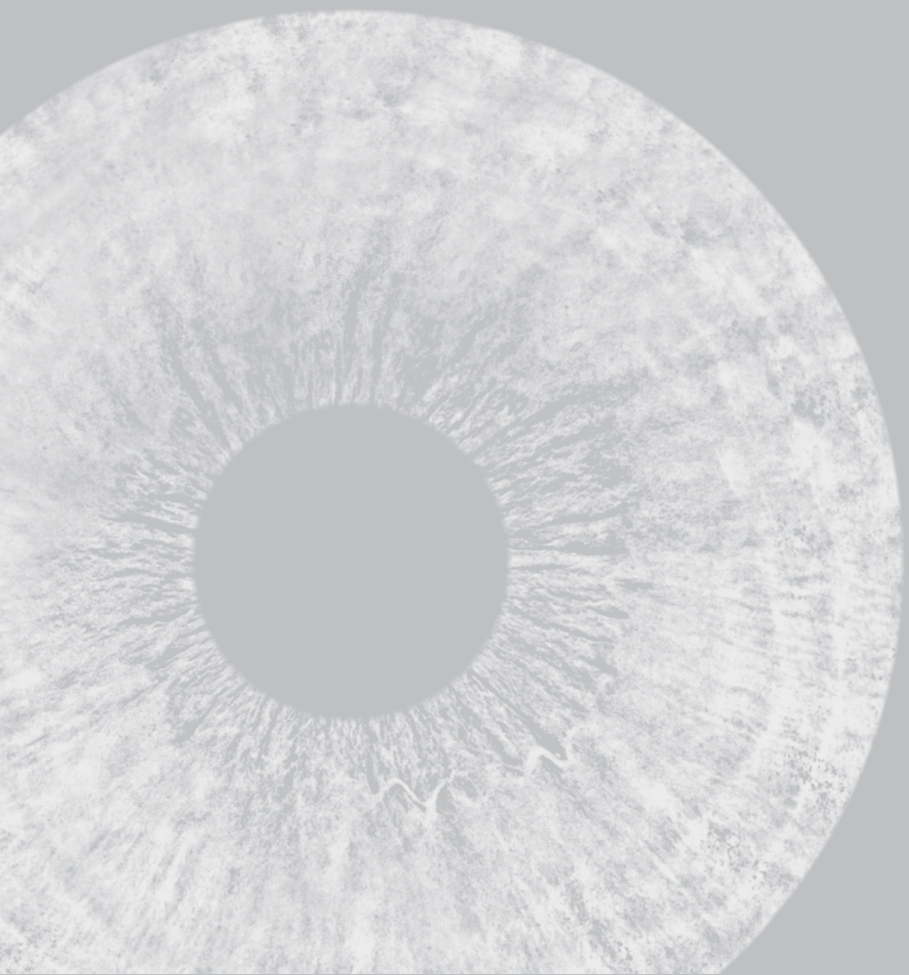

CHAPTER 5

A new polymeric, biodegradable, minimally invasive glaucoma implant

In this Chapter we introduce a novel polymeric, biodegradable, and minimally invasive glaucoma implant. This implant works by increasing the outflow of aqueous humor from the anterior chamber directly into Schlemm's canal, thus bypassing the trabecular meshwork which is considered the major site of aqueous humor outflow resistance in open-angle glaucoma. The implant is made of a unique biodegradable polymer, polycarbonate bisamide (PC-BA), and produced through replica molding using hot embossing and femtosecond laser-machined glass molds. Cytotoxicity tests reveal that the material is not cytotoxic. *Post-mortem* experiments demonstrate successful device implantation into the trabecular meshwork of a rabbit's eye using an injection delivery system, and we have confirmed that the implant remains securely in place. Although the mass loss and changes in molecular weight observed in the *in vitro* degradation experiments were not significant within the tested times and degradation conditions, we hypothesize the PC-BA to be a slow-degradation polymer that degrades mainly through hydrolysis of carbonate and amide groups. Thus, we expect that our implant will also slowly degrade and be absorbed by the body over time, leaving behind a natural outflow pathway. This biodegradable glaucoma implant provides a promising new approach for restoring outflow in a more natural way.

This Chapter is based on:
A new polymeric, biodegradable, minimally invasive glaucoma implant, **Inês C.F. Pereira**, Paul A.A. Bartels, Christian J.F. Bertens, Serge H.M. Söntjens, Hans M. Wyss, Albertus P.H.J. Schenning, Patricia Y.W. Dankers, Henny J.M. Beckers, Jaap M.J. den Toonder, *Manuscript in preparation*.

5.1 Introduction

Glaucoma is a disease of the optic nerve and a leading worldwide cause of irreversible vision loss [1]. In 2020, over 70 million people suffered from glaucoma, and this number is expected to increase to more than 100 million people by 2040 [2]. Elevated intraocular pressure (IOP) is the primary risk factor for the development and progression of glaucoma. The main determinant of IOP is the fine-tuned equilibrium between the production and drainage of aqueous humor (internal eye fluid), and its homeostasis is of vital importance to overall eye health and function. Aqueous humor is produced and secreted by the ciliary body and drains out of the eye mainly through the trabecular meshwork into Schlemm's canal (represented in Figure 5.1). As aqueous humor inflow rate is relatively stable, IOP is mainly regulated by the resistance to aqueous humor outflow [3]. In glaucomatous eyes there is an increased resistance to aqueous humor outflow, which leads to elevated IOP [4]. Currently, lowering IOP remains the only proven treatment for stopping the glaucoma disease progression and related visual field loss [5]. Ophthalmologists use a variety of approaches to lower IOP, including pharmaceutical drugs/medication (usually eye drops), laser procedures, and incisional surgeries. In the traditional paradigm, topical ocular hypotensive drugs and/or laser therapy represent the first-line treatment option for glaucoma. Surgery is often performed when the maximum tolerated medical/laser treatments fail to sufficiently lower IOP and prevent disease progression [6]. More traditional drainage surgeries such as trabeculectomy and implantation of aqueous shunts, although highly effective at lowering IOP, are associated with potentially serious postoperative complications, require substantial postoperative management, and have been reported to have high failure rates [7–10]. In order to provide a safer and less invasive way of reducing IOP, a new class of glaucoma procedures and implants has recently emerged, termed minimally invasive glaucoma surgery (MIGS) [11]. Especially, MIGS devices help to reduce the IOP with minimal tissue manipulation/destruction, and are associated with a relatively high safety profile, short surgery time, and rapid recovery [12]. To date, the available MIGS devices offer a more modest IOP-lowering effect than traditional incisional surgeries, but they have the benefit of a safer risk profile [13]. Thus, these devices are currently targeted at patients with mild-to-moderate glaucoma, whilst trabeculectomy and conventional aqueous shunts are generally preferred for patients with more advanced or severe glaucoma [14].

MIGS devices work by increasing the outflow of aqueous humor from the anterior chamber, either by bypassing the trabecular meshwork and directly accessing Schlemm's canal, or by shunting aqueous humor to the suprachoroidal or subconjunctival spaces (indicated in Figure 5.1a) [15]. As the trabecular meshwork was originally considered the major site of aqueous humor outflow resistance in open-angle glaucoma [16], bypassing this structure and directing the flow from the anterior chamber into Schlemm's canal seems to be the most obvious approach. MIGS devices using this approach to reduce IOP are typically called Schlemm's canal MIGS devices. Currently, the two most commonly used Schlemm's canal MIGS devices are the iStent *inject*® (Glaukos Corporation, California, USA) and the Hydrus® Microstent (Ivantis, Inc., California, USA) [17]. The iStent *inject* (second-generation iStent) is the world's smallest medical device known to be implanted in the human body [18]. It is made of heparin-coated implant-grade titanium and is inserted

ab interno through a microincision made in the anterior chamber using an injection device (injector). This injector is preloaded with two stents, allowing surgeons to implant both stents with a single entry into the eye [19]. This effectively reduces the surgical time and risk of adverse events [15]. Overall, the iStent *inject* has been shown to be a safe and effective procedure in the treatment of different types of open-angle glaucoma in several clinical studies, either as a standalone procedure or combined with cataract surgery; the results showed most patients experienced a clinically significant lowering of IOP and a reduction in reliance on glaucoma medication, with a low incidence of postoperative complications [20–25]. Complications associated with more invasive surgery procedures, such as hypotony (IOP $<$ 5 mmHg), inflammation, endothelial cell loss, or other sight-threatening complications, are avoided using this MIGS device [15, 18, 26, 27]. The most common adverse events reported so far include stent malposition and obstruction, and transient hyphema (collection of blood inside the anterior chamber) [20–25]. Device obstruction can occur due to the excessive wound healing/fibrosis resulting in scarring that might take place in the area of implantation [28]. Previous reports have identified scenarios in which such scarring has resulted in increased IOP and potential need for additional interventions [29–31]. The small lumen diameter characteristic of iStent *inject* (80 µm) might also lead to device obstruction. Smaller lumens are at risk of blockage by sloughed endothelial cells, fibrin, iris pigment, blood, vitreous, and/or lens fragments. Nowadays, stent obstruction is often solved by laser intervention, and ultimately, by implant removal and replacement [32].

Here, we propose a new polymeric Schlemm's canal MIGS implant with design and dimensions similar to the newer version of the iStent *inject*, the iStent *inject*® W. The material we use to fabricate this device is a hydrogen bonding polycarbonate bisamide (PC-BA) polymer. This thermoplastic PC-BA polymer was engineered both to meet the demands of hot embossing used for the implant fabrication and to possess adequate mechanical properties necessary for the implants. The implants need to have sufficient stiffness to prevent permanent deformation when handled. As explained later in this document, they must be loaded into an injector delivery system that allows them to be injected into the trabecular meshwork. Hence, the devices should be able to endure being grasped with tweezers during loading without deforming. Moreover, the injector delivery system exerts a significant amount of force when injecting the device into the trabecular meshwork. Thus, the implant should be tough enough to resist these forces and retain its original shape. However, the implant should not be overly rigid, as this would make it very difficult to demold after the hot embossing process. Also, the polymer should have some flexibility and softness to prevent complications such as endothelial cell loss, which can be caused by harder implants. A polymeric implant is also advantageous in avoiding problems with magnetic resonance imaging (MRI) associated with metallic implants. Also, many patients prefer not to have permanent metal implants in their eyes, and therefore, a polymeric implant could serve as a viable alternative.

The PC-BA polymer comprising our implant was additionally designed to be biodegradable and to degrade slowly, primarily through the hydrolysis of the carbonate and amide groups [33]. For a MIGS implant, we believe that a slow degrading polymer that takes up to a few years to degrade would be ideal. The slow degradation of the PC-BA implant should offer enough time for a proper and sufficient remodeling of the trabecular meshwork to occur

around the implant, and when degradation is completed, the extra outflow site created by the implant may remain patent, thus creating a long-term modification of the trabecular meshwork without the need for a permanent implant. The implant being biodegradable will be additionally advantageous in case it is mispositioned, becomes dislodged, or if the implant is overgrown by membrane-like (fibrotic) material. As the device will degrade over time, there will be no accumulation of "lost" implants inside the eye. Our implant is expected to offer similar positive outcomes as the iStent *inject*® W due to the similar design, but with the possible additional benefit of being a non-metallic and non-permanent implant that will be naturally absorbed by the body over time.

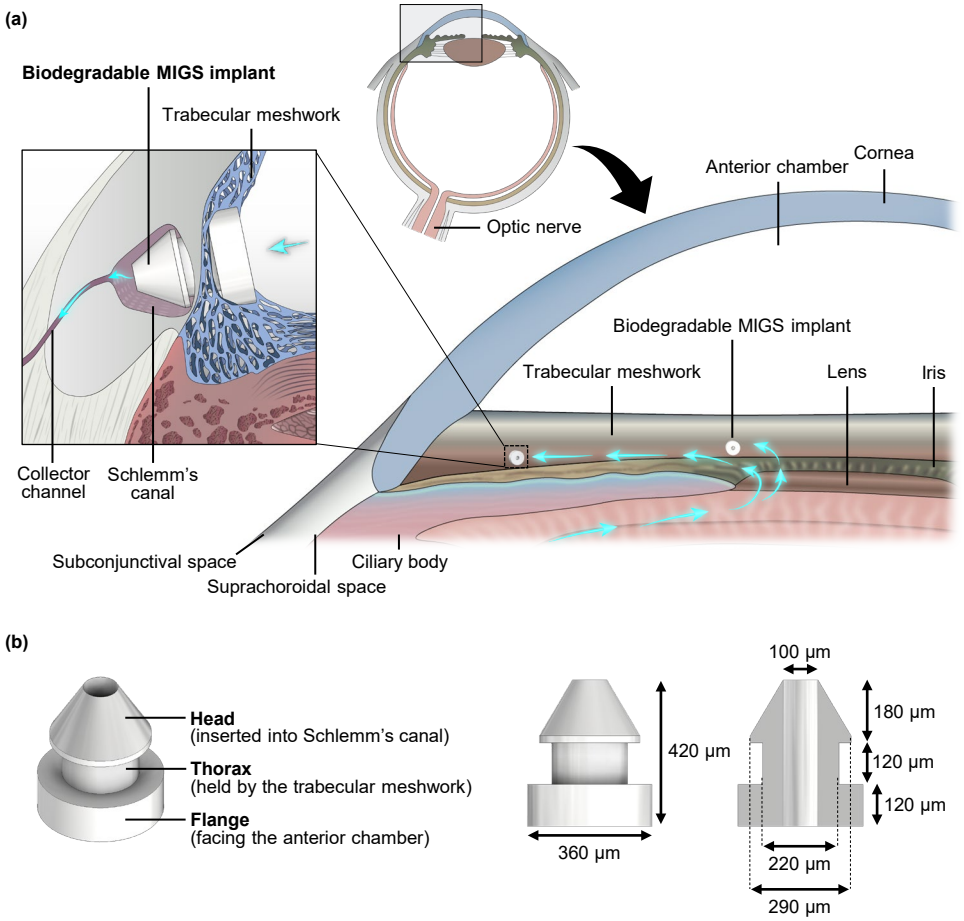

Figure 5.1: Design and dimensions of the polymeric and biodegradable Schlemm's canal MIGS implant and its placement in the eye. (**a**) Illustration showing the implant placement in the eye, with its flange facing the anterior chamber and its head inserted into Schlemm's canal; the blue arrows represent the direction of aqueous humor outflow from the anterior chamber, through the implant and into Schlemm's canal/collector channel. (**b**) Schematic depiction of the implant design and its relevant dimensions.

5.2 Implant design

The design and dimensions of our new Schlemm's canal MIGS implant are shown in Figure 5.1b. It has radial symmetry, and is 420 µm-long and 360 µm-wide, resembling the iStent *inject*® W. It is composed of three parts: a conical-shaped head designed to seat within Schlemm's canal; a wider flange, which faces the anterior chamber; and the thorax, which is retained by the trabecular meshwork, as illustrated in Figure 5.1a. The central lumen of the device through which the aqueous humor will flow has a diameter of 100 µm. With this device, a direct connection between the anterior chamber and the Schlemm's canal/collector channel is made, thus bypassing the trabecular meshwork. Apart from the material that our implant is made of, the main difference from the iStent *inject*® W is that the latter contains four additional side outlets at the head of the stent, whereas our device only contains one central outlet. Also, the 100 µm lumen diameter of our device is larger than the 80 µm lumen diameter of the iStent *inject*® W.

5.3 Results

5.3.1 Synthesis and characterization of polycarbonate bisamide (PC-BA)

The thermoplastic PC-BA polymer used in this study was synthesized by reacting trans-1,4-diaminocyclohexane with the prepolymer poly(hexamethylene carbonate) di-(tetra-fluorophenol active ester), as schematically depicted in Figure 5.2. The activated prepolymer was synthesized by first converting a poly(hexamethylene carbonate) diol to a poly(hexamethylene carbonate) di-carboxylic acid with a yield of 95% and subsequently activating this telechelic di-acid with 2,3,5,6-tetrafluorophenol (80% yield). During the polymerization, the diamine ratio was slowly increased to one equivalent of the prepolymer, and the reaction was monitored with gel permeation chromatography (GPC). The polymer was obtained with a 91% yield. After purification the polymer structure was confirmed with proton nuclear magnetic resonance (^{1}H-NMR) (Supplementary Figure 5.A1).

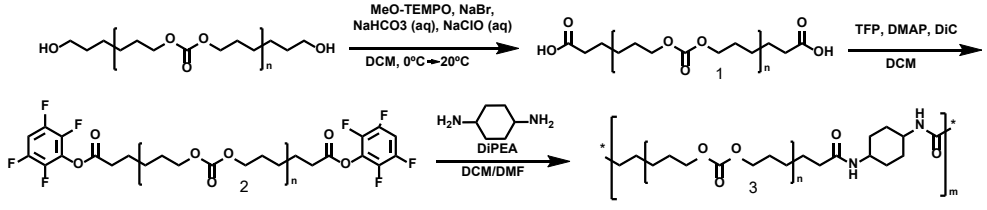

Figure 5.2: Scheme of polycarbonate bisamide (PC-BA) synthesis. This process started with converting poly(hexamethylene carbonate) diol to a poly(hexamethylene carbonate) di-carboxylic acid (95% yield), and then reacting to a poly(hexamethylene carbonate) di-(tetra-fluorophenol active ester) (80% yield), which was reacted with trans-1,4-diaminocyclohexane to obtain the final polymer with a yield of 91%.

The apparent number average molecular weigh (M_n) of the hot embossed PC-BA polymer is 14.0 kg/mol and the weight averaged molecular weigh (M_w) is 27.4 kg/mol, as determined from the GPC measurement (Figure 5.3a, Supplementary Table 5.B1). A

differential scanning calorimetry (DSC) measurement revealed that the polymer has a glass transition temperature for the polycarbonate soft block around -39.6 °C and three different melting transitions around 8.2, 97 and 152.7 °C in the second heating run (Figure 5.3b, Supplementary Table 5.B1). The melting transitions have enthalpies of 5.7, 0.09 and 2.9 J/g, respectively. The first melting peak originates from the soft polycarbonate block and the other two melting peaks originate from the melting of the amide hard block. The hard block has strong hydrogen bonding interactions resulting in a higher melting transition compared to the much weaker dipole interactions of the soft block. The molecular weights, glass transition temperature and melting transitions of the polymer before hot embossing are similar to the values after the polymer has been hot embossed (Supplementary Figure 5.B1a, b and c, and Table 5.B1). Looking into the thermal stability of the polymer with thermogravimetric analysis (TGA) reveals that the PC-BA starts to quickly degrade at a temperature around 270 °C (Supplementary Figure 5.B1d). The mechanical behavior of the hot embossed material was determined with tensile testing and showed a typical curve of a thermoplastic elastomer (Figure 5.3c). The PC-BA has a Young's modulus of 45.8 $\pm$ 3.6 MPa. The cytotoxicity of the embossed PC-BA on primary human tenon fibroblasts was investigated by means of a lactate dehydrogenase (LDH) release assay. LDH is released into the cell culture medium upon damage to the cell's plasma membrane. The percentage of cytotoxicity obtained for all test conditions is shown in Figure 5.3d. The absorbance levels of formazan in the extracted culture medium used to calculate the cytotoxicity percentage are shown in Supplementary Figure 5.C1. This experiment reveals that the PC-BA polymer is non-cytotoxic.

5.3.2 Implant fabrication and characterization

We employed our own innovative microfabrication technique to fabricate the Schlemm's canal MIGS implant. The method involved replica molding using hot embossing and fused silica glass molds created by femtosecond laser micromachining, as demonstrated in Figure 5.4b. The molecular structure of the PC-BA polymer from which the implants are made is represented in Figure 5.4a, which also includes schematic illustration of the stacking of the PC-BA polymer due to hydrogen bonds. As just mentioned, the mold used to give the PC-BA the shape indicated in Figure 5.1b was fabricated by femtosecond laser micromachining of fused silica glass. Femtosecond laser-assisted chemical wet etching is based on a two-step process of ultrashort-pulsed laser radiation in transparent materials, followed by chemical wet etching to selectively remove the exposed material (Figure 5.4c) [34]. The laser beam, focused inside the glass, locally modifies its refractive index and chemical properties, and patterns written by the laser are then chemically etched to form three-dimensional structures with high precision, aspect ratio and complexity [34, 35]. The complexity of the shape of our implant would be extremely difficult to achieve using classical micro-manufacturing techniques, such as photolithography or micro-milling [36]. A picture of the fabricated glass mold is shown in Figure 5.4d, which also includes a zoomed microscopic view of the features in the mold showing the 100 µm-diameter glass pillar used to form the central lumen of the implant. Using this mold, many implants can be fabricated in one single hot embossing step. In the hot embossing, we used 130 °C to melt the PC-BA polymer and 5 tons of pressure to help the melted polymer to flow into the cavities of the mold (Figure 5.4b). The demolding took place after the hot embossing

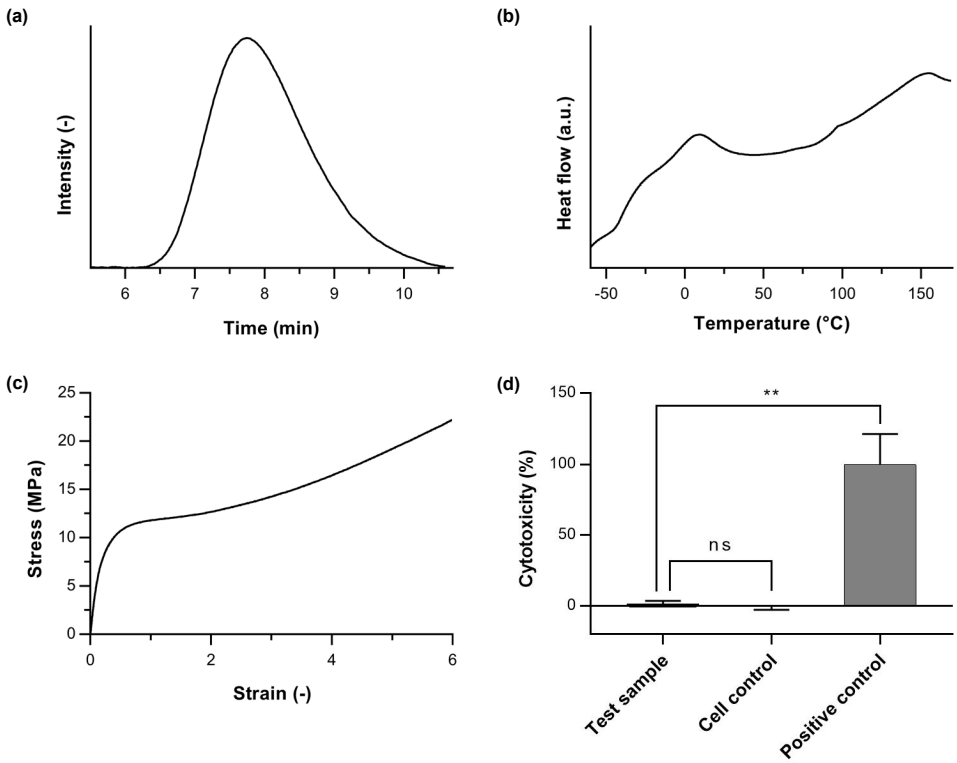

Figure 5.3: Characterization of the hot embossed polycarbonate bisamide (PC-BA). (**a**) Chromatogram measured with gel permeation chromatography (GPC), from which an apparent number averaged molecular weight M_n = 14.0 kg/mol and a weight averaged molecular weight M_w = 27.4 kg/mol are determined. (**b**) Second heating run of the hot embossed polymer measured with differential scanning calorimetry (DSC). (**c**) Stress-strain curve obtained from the average of three measurements in tensile testing (n = 3 samples tested), from which a Young's modulus of 45.8 ± 3.6 MPa can be calculated. (**d**) Calculated percentage of cytotoxicity of the PC-BA on primary human tenon fibroblasts; each bar represents the mean ± standard deviation (SD) (n = 3). ** represents $p \leq 0.01$ and "ns" represents a non-statistically significant difference as analyzed by two-way ANOVA with Tukey's multiple comparisons test.

had cooled down to room temperature. Figure 5.4e shows a microscopic image of the fabricated implants. The glass mold was designed to produce implants with the dimensions shown in Figure 5.1b. After fabrication, the most relevant dimensions of our implants were measured, and the results are shown in Figure 5.4f. Our implants have tolerances for the length of 438 ± 17.93 µm, width of the flange of 362.20 ± 1.64 µm, width of the thorax of 207 ± 6.44 µm, width of the head of 296.60 ± 2.19 µm, and lumen diameter of 93 ± 2.92 µm. The length of the implants varied quite significantly, however, this was expected since the residual layer attached to the flange of the implants was manually removed with a razor blade after the demolding step, making it therefore very difficult to guarantee the same length across all the fabricated implants. Apart from the length, there are some minor deviations between the implant dimensions achieved after fabrication and those

designed, as can be inferred from Figure 5.4f. These deviations can be explained by the size of the elliptical-shaped laser affected zone during the femtosecond laser exposure, which, in fused silica glass and when using a 20x objective, is 3 µm-wide and 24 µm-long [37]. Nevertheless, these differences are not significant for the final application.

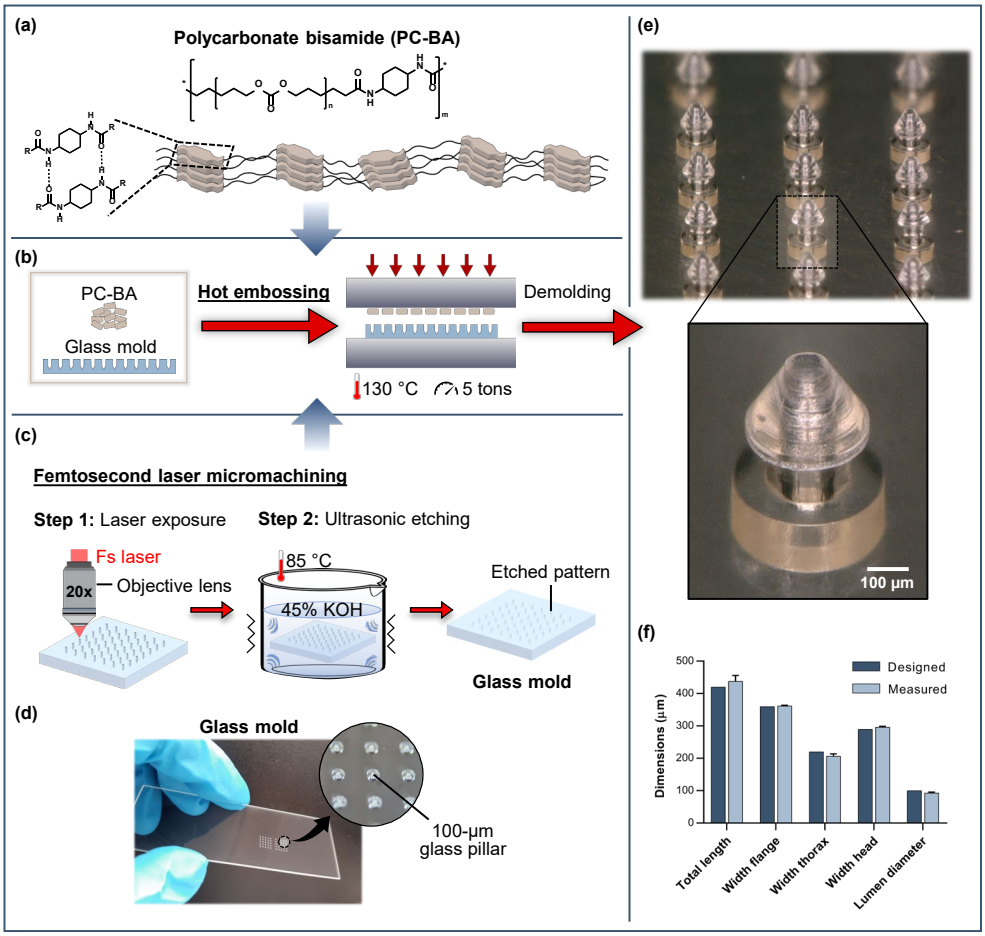

Figure 5.4: Fabrication process of the PC-BA Schlemm's canal MIGS implant and its final shape and dimensions. (**a**) Representation of the PC-BA molecular structure as well as schematic illustration of the stacking of the PC-BA polymer due to hydrogen bonds. (**b**) Schematic representation of the implant fabrication by replica molding using hot embossing, with femtosecond laser-machined fused silica glass molds. (**c**) Schematic illustration of the femtosecond laser machining process used to fabricate the glass molds. (**d**) Picture of the glass mold, made using femtosecond laser machining, used in the hot embossing of the implants. (**e**) Demolded array of implants. (**f**) Graph indicating the differences between the measured dimensions of the implant and the initially designed ones. The data represents the mean $\pm$ SD ($n = 5$).

5.3.3 Adaptation and *in vitro* testing of the iStent *inject*® W injector

Since the dimensions and shape of our implant are very similar to the iStent *inject* W, we used the same injector delivery system to test the implantation of our device. The design and components that comprise the injector device are represented in Figure 5.5a. The working principle of the injector is explained in the patent no. US010271989B2 [38]. The injector is designed to deliver the stents automatically through the trabecular meshwork and into Schlemm's canal when activated by the surgeon. The portion of the injector that enters the anterior chamber is a 23-gauge stainless steel insertion sleeve [39]. When inside the anterior chamber, the sleeve of the injector is retracted using the insertion sleeve retraction button, revealing the micro-insertion tube and the trocar [20]. The surgeon then advances the micro-insertion tube across the anterior chamber to the desired site of implantation, while visualizing the tube through direct gonioscopy (using a gonioprism). After locating the trabecular meshwork and selecting the implant location, the trabecular meshwork is penetrated with the trocar. By pressing the surgeon-activated delivery button on the housing, the stent moves over the small guiding trocar to exit the injector [40]. A single audible click will indicate that the first stent has been delivered [18].

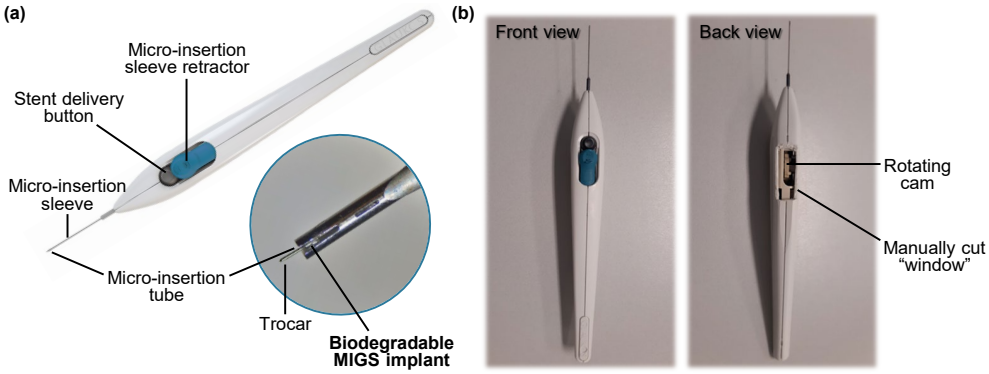

Figure 5.5: Design and components that comprise the injector device of the iStent *inject*® W and its adaptation for ease of reloading. (**a**) Injector design and its components; the zoomed figure shows the injector tip reloaded with one of our PC-BA implants. (**b**) Front and back view of the injector device – the back view reveals the "window" created in the housing of the injector to facilitate manipulating the rotating cam.

Two stents can be implanted with a single entry into the eye, and they should be separated by 2–3 clock hours apart (i.e. separated by an angle of 60 to 90 degrees). A total of four positions are available on the injector to position the two stents. A rotating cam hidden within the housing of the injector rotates in a clockwise manner to deploy the stents when the release button is pressed. After the stent delivery button has been pressed for the fourth time, the rotating cam will no longer rotate, and the injector will no longer function. Therefore, in order to have a functioning injector again, the cam has to be manually rotated counter-clockwise (up to four times). This rotation was possible by releasing the engagement between the trigger stop and the first cam flat, which thereby allows the cam to freely rotate. In order to get a clear view over the cam and to allow manipulating

it easily, a small "opening/window" was created in the housing at the opposite side of the sleeve retractor and stent-release button, as can be seen in Figure 5.5b. This was done before reloading the injector with our implant. The reloading was performed under microscopic view and with the help of sharp and thin-pointed tweezers, as demonstrated in the Supplementary Video 5.D1. In this video we show that the recharged injector successfully injects our implant into a spongy-like substrate, a very simplified *in vitro* model of the trabecular meshwork porous structure. As can be seen in the video, the implant stays fixed and correctly positioned into the sponge, i.e., with the flange at the surface of the sponge and facing the camera used for recording.

5.3.4 *Post-mortem* study

We performed a *post-mortem* experiment on an eye of a dead New-Zealand White rabbit to investigate if the modified injector delivery system is capable of injecting our devices into a real trabecular meshwork as it does for the iStent *inject* W. For this experiment, the injector device was first reloaded with our implant as previously demonstrated in Supplementary Video 5.D1. Subsequently, a corneal incision was made in the eye, and the injector was inserted through it into the anterior chamber to deliver our implant into the trabecular meshwork. A video of the implantation procedure was recorded (Supplementary Video 5.E1), which confirms that our implant was successfully delivered into the trabecular meshwork. The zoomed picture shown in Figure 5.6, also included in the Supplementary Video 5.E1, shows that the flange of our device is visible in the anterior chamber, proving the proper placement of the implant in the trabecular meshwork.

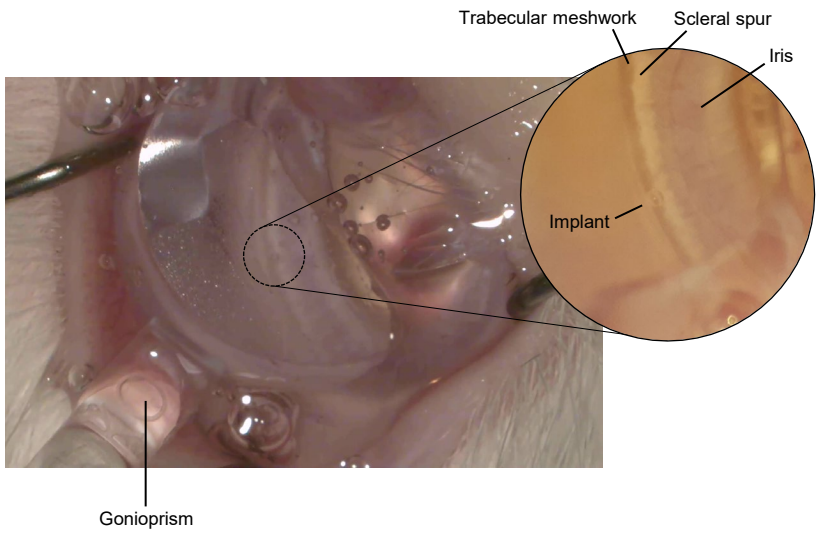

Figure 5.6: *Post-mortem* study. Picture showing the proper placement of our PC-BA Schlemm's canal MIGS implant into the trabecular meshwork, after being delivered by the modified injector device.

5.3.5 *In vitro* degradation

Degradation of the hot embossed PC-BA polymer via hydrolytic or oxidative pathways was studied. The hydrolytic pathway was investigated by incubating the polymeric material in phosphate-buffered saline (PBS, pH 7.4) in an accelerated experiment at 70 °C to study hydrolysis by water for 2, 30 and 60 days. After 60 days, 1% mass loss was observed in the hydrolytic experiment in PBS, as shown in Figure 5.7a. The M_n of the polymer did not change after two days of incubation, but it decreased from 16.7 ± 0.8 kg/mol to 13.8 ± 0.7 kg/mol after 30 days, and after 60 days the molecular weight decreased further to 12.8 ± 0.6 kg/mol (Figure 5.7b, Supplementary Table 5.F2). Enzyme-mediated hydrolysis was studied by incubating the material in lipase at 37 °C for 2, 7 and 14 days. After 14 days, a small decrease in mass of 1–2% was observed (Figure 5.7a). The M_n was 13.2 ± 0.8 kg/mol after two days and it did not decrease further with 7 or 14 days of incubation (Figure 5.7b, Supplementary Table 5.F2). Oxidative degradation was investigated by incubating the polymeric material in a solution of 0.1 M $Co(II)Cl_2{\cdot}6H_2O$ in 20% (w/w) H_2O_2 in de-ionized (DI) water at 37 °C for 2, 7 and 14 days. No mass loss of the material was observed after 14 days (Figure 5.7a). The molecular weight of the polymer under oxidative degradation showed similar behavior to the that under enzymatic degradation. The M_n was 13.5 ± 0.1 kg/mol after two days and it did not decrease any further (Figure 5.7b, Supplementary Table 5.F2).

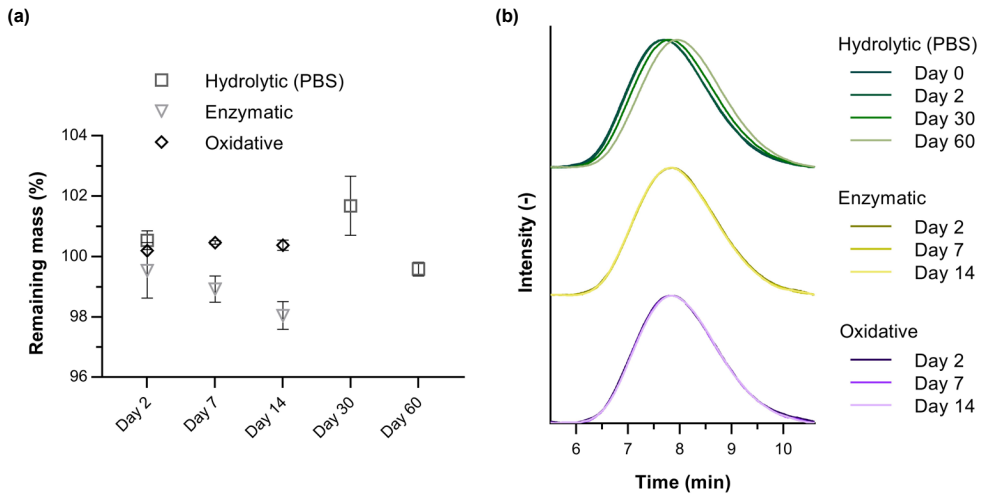

Figure 5.7: Polycarbonate bisamide (PC-BA) characterization after degradation. (**a**) Mass loss measured after 2, 30 and 60 days for the samples exposed to a hydrolytic environment through incubation with a phosphate-buffered saline solution (PBS, pH 7.4) at 70 °C, and after 2, 7 and 14 days for the samples in enzymatic and oxidative environments, both at 37 °C. (**b**) Chromatogram measured with gel permeation chromatography (GPC) of the polymer before and after 2, 30 and 60 days for samples in hydrolytic PBS solution at 70 °C, and after 2, 7 and 14 days for samples in enzymatic and oxidative environments at 37 °C.

These results suggest that the PC-BA polymer favors hydrolytic degradation over oxidative degradation. However, it is necessary to conduct additional long-term degradation studies

to determine whether the observed small changes in mass and molecular weight reported above are indeed indicative of polymer degradation.

5.4 Discussion

This study proposes a new polymeric, biodegradable, and minimally invasive glaucoma drainage device that is designed to be inserted into Schlemm's canal to enhance outflow of aqueous humor from the anterior chamber, thereby reducing IOP. The design of our device was inspired by the currently available iStent *inject*® W, the world's smallest medical device known to be implanted in the human body that has been proven to be generally safe and effective in treating glaucoma. Unlike the iStent *inject* W, which is made of heparin-coated titanium, our device is made of a biodegradable polymeric material called polycarbonate bisamide, or PC-BA. We anticipate that the slow degradation of the PC-BA polymer may provide enough time for proper and sufficient remodeling of the trabecular meshwork to occur around the implant, and, when degradation is completed, this might leave a patent outflow site without the need for a permanent implant that could potentially scar over time and lose effectiveness.

The PC-BA polymer is an ideal polymer for the fabrication of the MIGS devices. The polymer can withstand the hot embossing process used for the implant fabrication without significantly affecting its polymer structure and mechanical properties. The cytotoxicity of the PC-BA on primary human tenon fibroblasts was investigated, proving that the material is non-cytotoxic. In terms of degradation, our *in vitro* degradation experiments did not show significant mass loss or changes in molecular weight within the tested times and degradation conditions. Nevertheless, we expect the PC-BA to be a slow-degradation polymer that mainly degrades through hydrolysis of the carbonate and amide groups, either through interaction with water or from enzymatic reactions [33]. It is known that carbonate and amide groups degrade slower than esters, which are very common in other biodegradable polymers such as polycaprolactone and polylactic acid [41]. We should note that the shape and morphology of the implants can also influence the degradation rate [42]. A non-porous dense material like that of the implants presented in this study degrades slower than a porous scaffold, for example. Moreover, *in vivo* conditions and implantation location also have an influence on the degradation behavior [43, 44].

We have developed a novel microfabrication method for manufacturing our device, which involves replica molding using hot embossing and femtosecond laser-machined fused silica glass molds. The femtosecond laser-machining technique has proven to be highly effective in achieving three-dimensional features with high geometrical complexity in glass, which would have been difficult to achieve using conventional micro-manufacturing methods such as photolithography or micro-milling [36]. We were able to successfully transfer these features from the glass mold to the PC-BA polymer that comprises the implantable device using hot embossing. Hence, in this study we have demonstrated that the combination of hot embossing of thermoplastic materials with femtosecond laser-machined glass molds is a potentially advantageous process for mass production of microdevices containing three-dimensional structures requiring a few micrometers resolution, high accuracy and complexity [45].

Since our implant has a shape and dimensions comparable with the iStent *inject* W, we used the same injector delivery system to test the implantation of our device. With a small adaptation of the injector housing, we were able to repeatedly reload the injector with our implants. Our first *in vitro* implantation test demonstrated that the recharged injector successfully inject the implant into a spongy-like substrate, a very simplified *in vitro* model of the trabecular meshwork porous structure. The implant stays fixed and correctly positioned within the sponge. Furthermore, a *post-mortem* experiment performed on a rabbit eye confirmed that the modified injector device is capable of correctly injecting our implants into a real trabecular meshwork as it does for the iStent *inject* W.

The presented work introduces the concept and shows the proof-of-principle of our biodegradable glaucoma implant, but more research and development need to be done towards the application in clinical practice. As future work, we will further investigate the biocompatibility, biodegradability, and effectiveness of our device in reducing IOP by conducting *in vivo* experiments using an animal model. Given that the degradation rate of the device can be affected by the specific *in vivo* environment, it is essential to perform such long-term animal experiments to gain a better understanding and quantification of its degradation behavior and to investigate how the trabecular meshwork tissue adapts and, as we anticipate, grows around the implant over time. Additionally, these studies will help us verify our initial hypothesis that our new biodegradable implant can create a long-term modification of the trabecular meshwork and leave a permanent extra outflow site that will not be scarred or closed after the device has been fully absorbed into the body.

5.5 Material and methods

5.5.1 Synthesis and characterization of polycarbonate bisamide (PC-BA)

All reagents, chemicals, materials and solvents were obtained from commercial sources and used without further purification, except the poly(hexamethylene carbonate) diol, which was a generously provided by Bayer. Drying of solvents, when necessary, was done using molecular sieves. Reactions were run under an inert atmosphere (Ar) whenever appropriate. ^{1}H-NMR spectroscopy was performed using either a Varian Mercury or a Bruker AVANCE III HD spectrometer at 400 MHz and 298 K. All shifts are reported with respect to TMS at 0 ppm. Infrared spectroscopy was performed using a Perkin Elmer Spectrum One Fourier transform infrared (FT-IR)-attenuated total reflectance (ATR) spectrometer. GPC was performed on Varian/Polymer Laboratories PL-GPC 50 equipment using a Shodex GPC KD-804 column that was operated at 50 °C using dimethylformamide, or DMF (with 10 mM LiBr and 0.3% water), as the eluent or on a Shimadzu LC-10ADVP system with a Shimadzu RID-10A refractive index detector, a Shimadzu SPD-M10AVP UV-Vis detector, and a combination of a PLgel 5-µm mixed-C column and a PLgel 5-µm mixed-D column, using tetrahydrofuran, or THF, as eluent.

Poly(hexamethylene carbonate) di-carboxylic acid (1)

Telechelic poly(hexamethylene carbonate) diol (M_n = 2.0 kg/mol; 32 g, 16 mmol) was dissolved in 150 mL dichloromethane (DCM). MeO-TEMPO (0.1 g, 0.5 mmol) was added to this DCM solution, as well as a solution of NaBr (0.7 g, 7 mmol) in 200 mL 1M $NaHCO_3$. The resulting two-phase system was stirred vigorously and cooled in an ice bath. Aqueous NaOCl (13%, approximately 3.7 M, 60 mL) was added slowly to the reaction mixture, which was allowed to warm to room temperature after addition of the hypochlorite. Stirring was continued for 1 hour, after which ^{1}H-NMR confirmed full conversion of the alcohol end groups. The reaction mixture was subsequently cooled in an ice-bath and adjusted to pH = 1–2 with a concentrated aqueous HCl solution. The organic phase was separated from the aqueous phase, which was subsequently extracted with $CHCl_3$ (2x100 mL). The combined organic phases were washed with water (150 mL), dried with $MgSO_4$, and evaporated to yield the crude product (colorless oil). This oil was stirred vigorously with di-isopropyl ether (iPr_2O; 100 mL), after which the product was allowed to settle at -20 °C overnight. The supernatant was removed, and the resulting white solid was dried in vacuo to yield 30.8 g (95%) of the desired material (**1**).

^{1}H-NMR (400 MHz, $CDCl_3$): δ = 4.1 (t, n*4H), 2.4 (t, 4H, CH_2COOH), 1.8–1.2 (br. m, CH_2) ppm. No CH_2OH protons were detectable by NMR, confirming full conversion. FT-IR (ATR): ν = 2940, 2885, 1740, 1588, 1465, 1404, 1251, 1067, 957, 792, 735 cm^{-1}. ^{1}H-NMR showed n $\approx$ 15.5 (M_n = ca. 2.4 kg/mol). GPC (THF): M_n = 4.7 kg/mol; PDI = 1.75.

Poly(hexamethylene carbonate) di-(tetra-fluorophenol active ester) (2)

Telechelic poly(hexamethylene carbonate) di-carboxylic acid (**1**) (20 g, 8.7 mmol) was dissolved in DCM (75 mL) with 2,3,5,6-tetrafluorophenol (3.6 g, 22 mmol) and 4-dimethylaminopyridine (DMAP) (89 mg). N,N'-diisopropylcarbodiimide (DiC, 3.6 mL, 23 mmol) was added to the reaction mixture, causing almost immediate formation of a crystalline precipitate. After 3 hours, NMR confirmed full conversion of the two carboxylic acid end groups to active ester end groups. The reaction mixture was filtered, evaporated to dryness, stirred with n-pentane and decanted (2x) to afford crude product as a white solid. This solid was redissolved in toluene, stirred with flash silica remove impurities, filtered, and evaporated to dryness. The resulting solid was again dissolved in toluene, stirred with a mixture of flash silica and $MgSO_4$, filtered, and evaporated to dryness. This procedure was repeated twice more with just flash silica and using chloroform as the solvent. The resulting solid was stirred with n-pentane, allowed to settle at -20 °C, decanted, and dried in vacuo to yield 18.2 g (80%) of the prepolymer product (**2**).

^{1}H-NMR (400 MHz, $CDCl_3$): δ = 7.0 (q, 2H), 4.1 (t, n*4H), 2.7 (t, 4H, CH_2COO), 1.8–1.2 (br. m, CH_2) ppm. FT-IR (ATR): ν = 2940, 2870, 1789, 1733, 1645, 1525, 1485, 1466, 1406, 1346, 1329, 1240, 1180, 1083, 1070, 935, 791, 735, 716 cm^{-1}. ^{1}H-NMR showed n $\approx$ 16.1 (M_n = ca. 2.8 kg/mol).

Poly(hexamethylene carbonate) 1,4-cyclohexyl bisamide, P6C-A[6]A (3)

Prepolymer (**2**) (18 g, 6.3 mmol), N,N-diisopropylethylamine (DIPEA, 5.6 mL, 32 mmol) and trans-1,4-diaminocyclohexane (0.686 g, 6.0 mmol, 0.95 eq.) were dissolved in mixture of 50 ml DCM and 20 mL DMF. The reaction mixture was initially turbid but became clear and more viscous over time. After stirring for 16 hours an aliquot was analyzed with NMR and GPC. To improve the chain extension another 0.2 g of the prepolymer (**2**) and, in steps over the next 40 hours while checking with GPC, 25.4, 11.8 and 8.3 mg of the diamine were added, gradually increasing the diamine ratio to 1.0 equivalents with respect to (**2**). The resulting material was precipitated in a mixture of 1.2 L MeOH and 0.2 L water, decanted, stirred with 0.5 L MeOH, decanted, and dried in vacuo at 50 °C. The resulting material was redissolved in 100 mL $CHCl_3$ with 30 mL MeOH and reprecipitated in 1 L MeOH, decanted, and dried in vacuo at 60 °C, yielding 15.3 g of a tan, rubbery solid (91%).

^{1}H-NMR (400 MHz, $CDCl_3$): $\delta = 5.3$ (br. s, 2H), 4.1 (t, n*4H), 3.8 (br. s, 2H), 2.1 (t, 4H), 2.0 (m, 4H), 1.8–1.3 (br. m, CH_2), 1.2 (m, 4H) ppm. FT-IR (ATR): $\nu = 3294$, 2938, 2861, 1737, 1637, 1544, 1464, 1403, 1240, 1062, 960, 904, 792, 731 cm^{-1}.

5.5.2 Differential scanning calorimetry (DSC)

The material was weighed and sealed in Tzero aluminum pans before DSC measurements were done on a DSC Q2000 (TA instruments, United States). The samples were first brought to an isotropic state at 40 °C and then heated to 180 °C at 10 °C/min, which marked the first heating run, and cooled to -70 °C at the same rate. Then the material was further subjected to two heating/cooling cycles from -70 to 180 °C with a heating/cooling rate of 10 °C/min. The data was quantified and analysed using Universal Analysis software (V4.5A, TA Instruments).

5.5.3 Mechanical testing

A mechanical tensile test was performed on PC-BA thin films using a tensile test machine (ZwickRoell Z010) with a crosshead speed of 20 mm/min and a 100 N static load cell. For the preparation of the test specimens, first a 200 µm-thick film was fabricated in a hot embossing machine (Specac limited). We used 130 °C to melt the polymer and 5 tons of pressure press the polymer into the shape of a film. The demolding took place after the hot embossing had cooled down to room temperature. Thereafter, the film obtained was cut into three small rectangular specimens of approximately 30x10x0.2 mm (length x width x thickness). The Young's modulus was determined as the slope of the linear portion of the obtained stress-strain curve.

5.5.4 *In vitro* cytotoxicity

To determine the cytotoxicity of the PC-BA polymer on primary human tenon fibroblasts we used the CyQUANT™ lactate dehydrogenase (LDH) cytotoxicity assay (Invitrogen™, ThermoFisher Scientific) [46, 47]. LDH release into culture medium due to membrane damage of cultured cells was used as an indicator of cytotoxicity. LDH is released into the cell culture medium upon damage to the cell's plasma membrane. The LDH assay protocol

is based on an enzymatic coupling reaction. First, LDH released from the damaged cell into the surrounding medium catalyzes the conversion of lactate to pyruvate via NAD+ reduction to NADH. Oxidation of NADH by diaphorase leads to the reduction of a tetrazolium salt to a red formazan product that can be measured spectrophotometrically. The level of formazan formation is directly proportional to the amount of LDH released into the medium, which is indicative of cytotoxicity.

For making the test samples used in this experiment, a 200 µm-thick film was first fabricated using hot embossing, and thereafter cut to small circular pieces of 7 mm in diameter. The samples were then sterilized by immersing in 70% ethanol for 20 minutes and treated with UV for 15 minutes, after which they were rinsed in PBS (pH 7.4) before transferring to a sterile 96-well plate. The cells were then seeded at 3.2×10^3 cells/well into the well plate containing the test samples (three replicates) using complete Dulbecco's modified eagle medium (DMEM) supplemented with 10% of fetal bovine serum (FBS), 100 U/mL penicillin and streptomycin, and 0.2 mM L-glutamine (now referred to as culture medium). Cells were seeded in triplicate, after which they were incubated at 37 °C in 5% CO_2 for 48 hours along with the positive and negative controls. Untreated cells in culture medium alone served as negative control and used to give the Spontaneous LDH activity. An amount of 10 µL of 10X Lysis Buffer was added to untreated cells (no contact with the test material), and used as the Maximum LDH Activity (positive control). After 45 minutes incubation, 50 µL of the medium from all three conditions was collected and gently mixed with 50 µL of the Reaction Mixture in a new 96-well plate, and thereafter placed on ice for another 45 minutes. The absorbance of each well was then measured at 490 and 680 nm. To determine LDH activity, first the absorbance at 680 nm (background signal from instrument) was subtracted from the absorbance at 490 nm. The percentage of cytotoxicity was then calculated as follows

$$\%\ Cytotoxicity = 100\times\frac{Treatment\ group\ activity\ -\ Negative\ control\ activity}{Positive\ control\ activity\ -\ Negative\ control\ activity}. \tag{5.1}$$

5.5.5 Implant fabrication and characterization

The PC-BA MIGS implants were fabricated by replica molding using a hot embossing machine. The mold used in the hot embossing to give the PC-BA the desired shape of the implant was fabricated using a femtosecond laser machining process (Figure 5.4c). The design of the mold was prepared using the dedicated Alphacam software, where the laser scanning path (tool-path) to be fed to the FEMTOprinter f200 aHead (FEMTOprint SA, Switzerland) for exposing the fused silica glass, was also generated. The mold was fabricated on a 75x25x1 mm fused silica glass slide. The pulse energy and repetition rate used were 230 nJ and 1000 kHz, respectively. The laser was focused with a Thorlabs 20x microscope objective with a numerical aperture (NA) of 0.4. When the machining program was finished, the glass slide was immersed in a concentrated solution of 45% potassium hydroxide (KOH, Sigma-Aldrich) diluted in water to remove the exposed

material. Finally, the mold was rinsed thoroughly with acetone and DI water to remove all debris. To facilitate the release (demolding) of the implants after the hot embossing step, the femtosecond laser-machined glass mold was first coated with a superhydrophobic layer of fluorosilane (Trichloro(1H,1H,2H,2H-perfluorooctyl)silane, Sigma-Aldrich). To improve the adhesion of this coating, the mold underwent an oxygen plasma treatment performed immediately before the fluorosilane vapor deposition. After the silanization treatment, the mold was ready to be used in the hot embossing machine together with the PC-BA pellets to fabricate the implants. We used 130 °C to melt the polymer and 5 tons of pressure to help the melted polymer to flow into the cavities of the mold (Figure 5.4d). The demolding took place after the hot embossing had cooled down to room temperature. Afterwards, the residual layer attached to the flange of the implants was removed by cutting it by hand using a razor blade under microscopic view.

The shape and morphology, and key dimensions of the implant were observed and measured using a Keyence VHX-5000 digital microscope.

5.5.6 Injector

Injectors previously used in iStent *inject* W surgeries were provided by the University Eye Clinic, Maastricht University Medical Center+. After creating the small window in the housing of the injectors using a soldering iron and a scalpel, they were recharged with our implants under microscopic view. To investigate if the injectors successfully deliver our MIGS implants, as they do for the iStent *inject* W, we tested the injection process using a spongy-like substrate, a very simplified *in vitro* model of the trabecular meshwork porous structure. A video showing the reloading of the injector with our implant and its delivery by the injector into the sponge was recorded (see Supplementary Video 5.D1).

5.5.7 *Post-mortem* study

A *post-mortem* experiment was conducted on an eye of a fresh adult New-Zealand White rabbit cadaver kindly provided by the Central Laboratory Facility of Maastricht University. This experiment aimed at investigating whether our devices are successfully delivered into a real trabecular meshwork using the modified injector device. For the implantation procedure, first a clear corneal incision was made with a 1 mm sideport knife (KAI MEDICAL, Japan). Hereafter, a viscoelastic solution (proVisc, Alcon, The Netherlands) was injected to deepen the anterior chamber and for better angle visualization. Gonioscopy was performed to ensure the presence of an open and clear angle suitable for implantation of the device. Thereafter, the recharged injector was inserted through the corneal incision and the implant was delivered into the trabecular meshwork. Upon visual confirmation of the device position in the trabecular meshwork, the delivery system was withdrawn. A video of the implantation procedure was recorded (see Supplementary Video 5.E1).

5.5.8 *In vitro* degradation experiment

The PC-BA polymer was subjected to accelerated hydrolytic degradation by exposition to PBS solution (pH 7.4) at 70 °C according to the international ISO 10993-13-2010 standard. The test samples used in this experiment were prepared as described above for

the cytotoxicity experiment. Shortly, first a 200 µm-thick film was fabricated using hot embossing, and thereafter cut to small circular pieces of 7 mm in diameter. The samples were thoroughly rinsed with 70% ethanol followed by DI water to remove any debris, after which they were individually inserted into 2 mL Eppendorf tubes and placed in a vacuum oven at 50 °C for 2 hours for drying the samples to constant mass. Thereafter, the initial mass of the specimens was measured. PBS was then added to each Eppendorf tube and the samples were inserted into a water bath pre-heated to 70 °C. The sample to PBS ratio was approximately 1 g:40 mL and sampling timepoints were 2, 30 and 60 days. At each time interval the samples were removed from the PBS, washed with DI water and subsequently dried to constant mass in a vacuum oven as previously described. Finally, the mass of the specimens after degradation was measured. The percentage of remaining mass of the test samples after degradation was determined using the following equation

$$\%\ Remaining\ mass = 100 \times \frac{m}{m_i}, \tag{5.2}$$

where m is the mass of the degraded sample measured at each timepoint of the experiment and m_i is the initial mass of the test sample. After measuring the weight loss, the samples were used for GPC measurements by cutting a piece of the samples with appropriate weight (3 mg/mL in DMF).

For the enzymatic and oxidative degradation experiments a similar protocol was followed. However, instead of PBS, a solution of 500 U/mL lipase in PBS was used at 37 °C for the enzymatic degradation experiment, and a solution of 0.1 M $Co(II)Cl_2 \cdot 6H_2O$ in 20% (w/w) H_2O_2 in DI water was used at 37 °C for the oxidative degradation experiment. The sampling time for this experiment was 2, 7 and 14 days. Every 3–4 days the solution was refreshed. The washing of the samples was performed as mentioned above, but they were additionally centrifuged twice in DI water at 4000 rpm for 5 minutes.

5.6 Supplementary Information

5.A ^{1}H-NMR spectrum of PC-BA

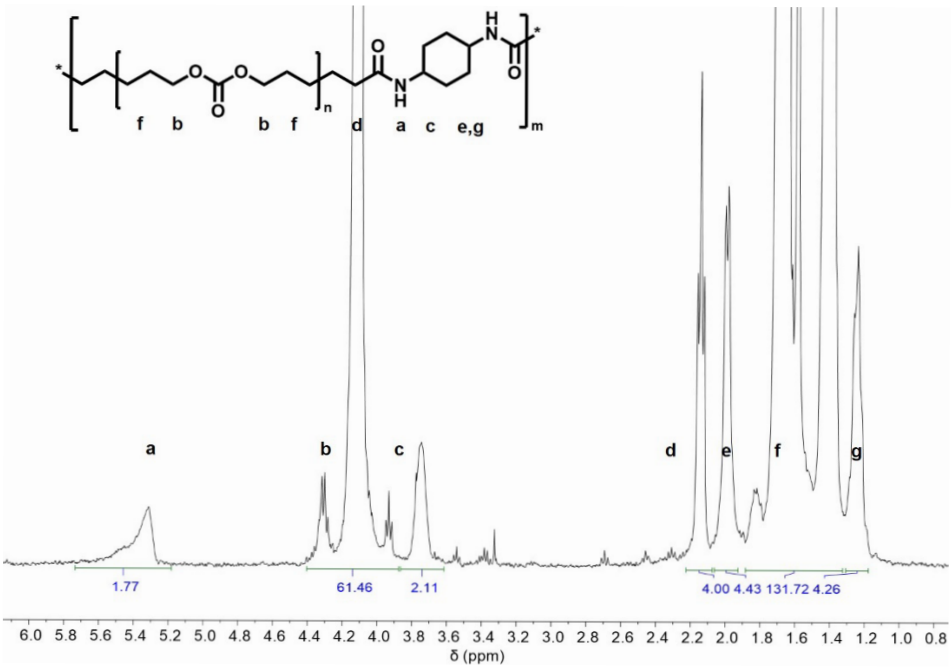

Figure 5.A1: ^{1}H-NMR spectrum of polycarbonate bisamide (PC-BA).

5.B Unprocessed vs. hot embossed PC-BA

The apparent M_n of the unprocessed PC-BA polymer was 16.6 kg/mol and the M_w was 25.6 kg/mol, as determined from the GPC measurement (Supplementary Figure 5.B1a). These molecular weights did not change much after hot embossing (M_n = 14.0 kg/mol, M_w = 27.4 kg/mol). The DSC measurement revealed that the polymer had a glass transition temperature (T_g) for the polycarbonate soft block around -39.7 °C and three different melting transitions (T_m) around 7.5, 97.2 and 151.3 °C in the second heating run (Supplementary Figure 5.B1c). These values were similar to the obtained values after hot embossing the polymer (T_g = -39.6 °C, T_m = 8.2, 97 and 152.7 °C). In the first heating run the melting transitions were similar as well (Supplementary Figure 5.B1b). However, the polymer had a cold crystallization at T_{cc} = 72.6 °C with an enthalpy of 1.3 J/g. This peak disappeared after the first heating run. With hot embossing, the polymer was already melted once, which explained why the cold crystallization peak was not present.

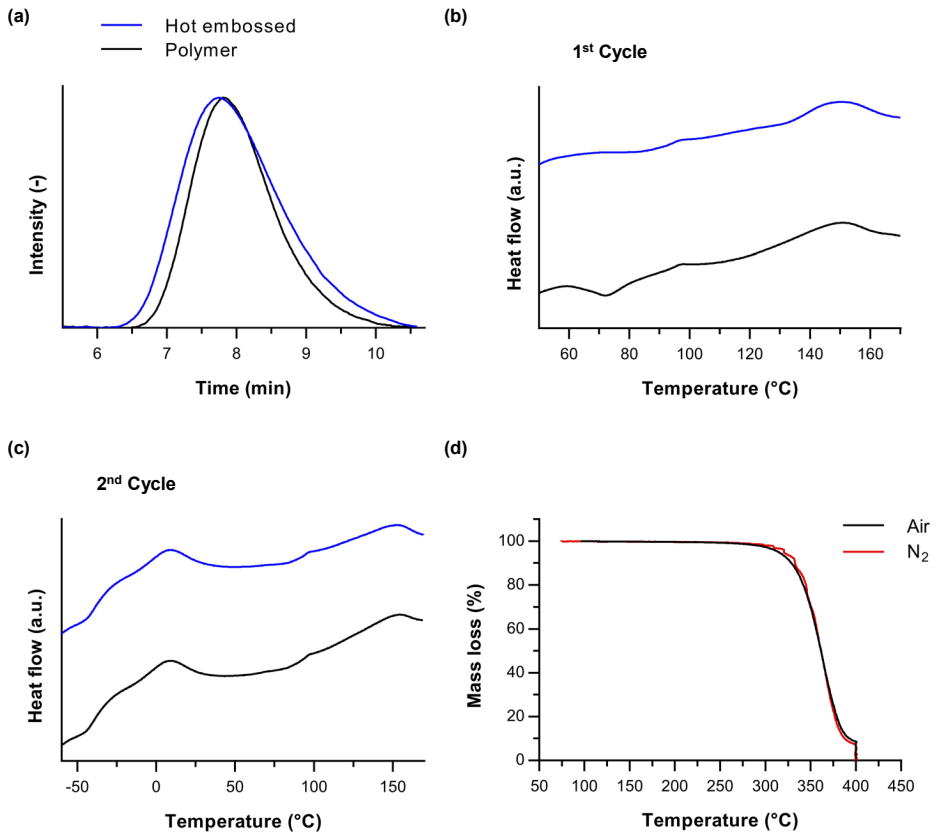

Figure 5.B1: Unprocessed vs. hot embossed polycarbonate bisamide (PC-BA). (**a**) Chromatogram measured with gel permeation chromatography (GPC) of the unprocessed/raw polymer and hot embossed polymer. (**b**) First and (**c**) second heating run of the unprocessed polymer and hot embossed polymer measured with differential scanning calorimetry (DSC). Exothermic reactions are pointing down. (**d**) Polymer mass loss measured upon heating the sample either under air or nitrogen flow.

Table 5.B1: Thermal properties and molecular weight distributions of unprocessed and hot embossed polycarbonate bisamide (PC-BA).

	First heating run						Second heating run							M_n^{GPC} (kg/mol)	M_w^{GPC} (kg/mol)	$Đ_m$
	T_{cc} (°C)	ΔH_{cc} (J/g)	T_{m_1} (°C)	ΔH_{m_1} (J/g)	T_{m_2} (°C)	ΔH_{m_2} (J/g)	T_g (°C)	T_{m_1} (°C)	ΔH_{m_1} (J/g)	T_{m_2} (°C)	ΔH_{m_2} (J/g)	T_{m_3} (°C)	ΔH_{m_3} (J/g)			
Unprocessed PC-BA	72.6	1.3	97.1	0.21	148.9	3.2	-39.7	7.5	5.7	97.2	0.04	151.3	4	16.6	25.6	1.5
Hot embossed PC-BA			96.7	0.11	149.3	3.2	-39.6	8.2	5.7	97	0.09	152.7	2.9	14.0	27.4	2.0

5.C Cytotoxicity of PC-BA - Additional data

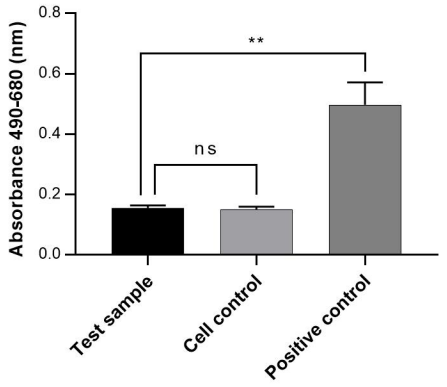

Figure 5.C1: Absorbance levels of formazan used to calculate the cytotoxicity percentage. Absorbance levels of formazan in the extracted culture medium measured for each test condition: test sample – cells directly exposed to the test material (PC-BA); cell control – cells in sole medium; and positive control – intentionally lysed cells. Each bar represents the mean $\pm$ SD ($n = 3$). ** represents $p \leq 0.01$ and "ns" represents a non-statistically significant difference as analyzed by two-way ANOVA with Tukey's multiple comparisons test.

5.D Injector reloading procedure

Figure 5.D1: Injector reloading procedure. QR-code for a video showing the reloading of the injector device with our PC-BA Schlemm's canal MIGS implant and its delivery by the injector into a spongy-like substrate, a very simplified *in vitro* model of the trabecular meshwork porous structure.

5.E *Post-mortem* experiment

Figure 5.E1: *Post-mortem* experiment. QR-code for a video showing the implantation procedure followed to implant our PC-BA Schlemm's canal MIGS implant into the trabecular meshwork of a dead New-Zealand White rabbit eye.

5.F *In vitro* degradation of PC-BA - Additional data

Table 5.F2: Molecular weight distributions of polycarbonate bisamide (PC-BA) after *in vitro* degradation experiments. Molecular weight distributions of hot embossed PC-BA polymer before and after incubating in PBS at 70 °C for 2, 30 or 60 days, and after incubating in an enzymatic or oxidative solution at 37 °C for 2, 7 or 14 days.

	M_n^{GPC} (kg/mol)	M_w^{GPC} (kg/mol)	$Đ_m$
Hydrolytic			
Day 0	16.7 ± 0.8	33.8 ± 0.1	2.05 ± 0.07
Day 2	16.6 ± 0.5	32.8 ± 0.3	2.0 ± 0.1
Day 30	13.8 ± 0.7	29.9 ± 0.2	2.2 ± 0.1
Day 60	12.8 ± 0.6	26.2 ± 0.4	2.1 ± 0.1
Enzymatic			
Day 2	13.2 ± 0.8	29.1 ± 0.8	2.2 ± 0.06
Day 7	13.9 ± 0.7	28.9 ± 0.4	2.1 ± 0.1
Day 14	13.9 ± 0.4	29.0 ± 0.4	2.1 ± 0.1
Oxidative			
Day 2	13.5 ± 0.1	28.7 ± 0.2	2.1 ± 0.0
Day 7	14.1 ± 0.5	28.4 ± 0.4	2.0 ± 0.06
Day 14	14.1 ± 0.5	28.1 ± 0.3	2.0 ± 0.1

Bibliography

1. Parikh, K. S. *et al.* Nano-structured glaucoma drainage implant safely and significantly reduces intraocular pressure in rabbits via post-operative outflow modulation. *Scientific Reports* **10,** 1–12 (2020).
2. Tham, Y. C. *et al.* Global Prevalence of Glaucoma and Projections of Glaucoma Burden through 2040: A Systematic Review and Meta-Analysis. *Ophthalmology* **121,** 2081–2090 (2014).
3. Acott, T. S. *et al.* Intraocular Pressure Homeostasis: Maintaining Balance in a High-Pressure Environment. *Journal of Ocular Pharmacology and Therapeutics* **30,** 94–101 (2014).
4. Andrew, N. H., Akkach, S. & Casson, R. J. A review of aqueous outflow resistance and its relevance to microinvasive glaucoma surgery. *Survey of Ophthalmology* **65,** 18–31 (2020).
5. Konopińska, J., Lewczuk, K., Jabłońska, J., Mariak, Z. & Rękas, M. Microinvasive glaucoma surgery: A review of schlemm's canal-based procedures. *Clinical Ophthalmology* **15,** 1109–1118 (2021).
6. Kerr, N. M., Wang, J. & Barton, K. Minimally invasive glaucoma surgery as primary stand-alone surgery for glaucoma. *Clinical and Experimental Ophthalmology* **45,** 393–400 (2017).
7. Gedde, S. J. *et al.* Treatment Outcomes in the Tube Versus Trabeculectomy (TVT) Study After Five Years of Follow-up. *American Journal of Ophthalmology* **153,** 789–803.e2 (2012).
8. Christakis, P. G. *et al.* The Ahmed Versus Baerveldt Study: Five-Year Treatment Outcomes. *Ophthalmology* **123,** 2093–2102 (2016).
9. Budenz, D. L. *et al.* Five-year treatment outcomes in the ahmed baerveldt comparison study. *Ophthalmology* **122,** 308–316 (2015).
10. Christakis, P. G. *et al.* Five-Year Pooled Data Analysis of the Ahmed Baerveldt Comparison Study and the Ahmed Versus Baerveldt Study. *American Journal of Ophthalmology* **176,** 118–126 (2017).
11. Bloom, P. & Au, L. "Minimally Invasive Glaucoma Surgery (MIGS) Is a Poor Substitute for Trabeculectomy"—The Great Debate. *Ophthalmology and Therapy* **7,** 203–210 (2018).
12. Bar-David, L. & Blumenthal, E. Z. Evolution of Glaucoma Surgery in the Last 25 Years. *Rambam Maimonides Medical Journal* **9,** e0024 (2018).
13. Richter, G. M. & Coleman, A. L. Minimally invasive glaucoma surgery: Current status and future prospects. *Clinical Ophthalmology* **10,** 189–206 (2016).
14. Ansari, E. An Update on Implants for Minimally Invasive Glaucoma Surgery (MIGS). *Ophthalmology and Therapy* **6,** 233–241 (2017).
15. Pillunat, L. E., Erb, C., Jünemann, A. G. & Kimmich, F. Micro-invasive glaucoma surgery (MIGS): A review of surgical procedures using stents. *Clinical Ophthalmology* **11,** 1583–1600 (2017).

16. Grant, W. M. Experimental aqueous perfusion in enucleated human eyes. *Archives of Ophthalmology* **69,** 783–801 (1963).
17. Pereira, I. C., van de Wijdeven, R., Wyss, H. M., Beckers, H. J. & den Toonder, J. M. Conventional glaucoma implants and the new MIGS devices: a comprehensive review of current options and future directions. *Eye* **35,** 3202–3221 (2021).
18. *Minimally invasive glaucoma surgery* (eds Sng, C. C. A. & Barton, K.) 21–50 (Springer, Singapore, 2017).
19. Gonnermann, J. *et al.* Contralateral eye comparison study in MICS & MIGS: Trabectome® vs. iStent inject®. *Graefe's Archive for Clinical and Experimental Ophthalmology* **255,** 359–365 (2017).
20. Shalaby, W. S., Jia, J., Katz, L. J. & Lee, D. IStent inject: Comprehensive review. *Journal of Cataract and Refractive Surgery* **47,** 385–399 (2021).
21. Hengerer, F. H., Auffarth, G. U. & Conrad-Hengerer, I. iStent inject Trabecular Micro-Bypass with or Without Cataract Surgery Yields Sustained 5-Year Glaucoma Control. *Advances in Therapy* **39,** 1417–1431 (2022).
22. Samuelson, T. W. *et al.* Prospective, Randomized, Controlled Pivotal Trial of an Ab Interno Implanted Trabecular Micro-Bypass in Primary Open-Angle Glaucoma and Cataract: Two-Year Results. *Ophthalmology* **126,** 811–821 (2019).
23. Chen, Y. Y. *et al.* Use of iStent as a Standalone Operation in Patients with Open-Angle Glaucoma. *Journal of Ophthalmology* **2020,** 8754730 (2020).
24. Healey, P. R., Clement, C. I., Kerr, N. M., Tilden, D. & Aghajanian, L. Standalone iStent Trabecular Micro-bypass Glaucoma Surgery: A Systematic Review and Meta-Analysis. *Journal of Glaucoma* **30,** 606–620 (2021).
25. Arriola-Villalobos, P. *et al.* Glaukos iStent inject® Trabecular Micro-Bypass Implantation Associated with Cataract Surgery in Patients with Coexisting Cataract and Open-Angle Glaucoma or Ocular Hypertension: A Long-Term Study. *Journal of Ophthalmology* **2016,** 1056573 (2016).
26. Fingeret, M. & Dickerson, J. E. The role of minimally invasive glaucoma surgery devices in the management of glaucoma. *Optometry and Vision Science* **95,** 155–162 (2018).
27. Konopińska, J. *et al.* Evaluation of the effect of the first generation istent on corneal endothelial cell loss—a match case-control study. *Journal of Clinical Medicine* **10,** 4410 (2021).
28. Ang, B. C. H. *et al.* Prospective 12-month outcomes of combined iStent inject implantation and phacoemulsification in Asian eyes with normal tension glaucoma. *Eye and Vision* **9,** 1–11 (2022).
29. Young, C. E. *et al.* Histopathologic Examination of Trabecular Meshwork Changes after Trabecular Bypass Stent Implantation. *Journal of Glaucoma* **27,** 606–609 (2018).
30. Shah, M., Campos-Möller, X., Werner, L., Mamalis, N. & Ahmed, I. I. K. Midterm failure of combined phacoemulsification with trabecular microbypass stenting: Clinicopathological analysis. *Journal of Cataract and Refractive Surgery* **44,** 654–657 (2018).

31. Shah, M. Micro-invasive glaucoma surgery – an interventional glaucoma revolution. *Eye and Vision* **6,** 29 (2019).

32. Schehlein, E. M., Kaleem, M. A., Swamy, R. & Saeedi, O. J. Microinvasive glaucoma surgery: an evidence-based assessment. *Expert Review of Ophthalmology* **12,** 331–343 (2017).

33. Bourke, S. L. & Kohn, J. Polymers derived from the amino acid L-tyrosine: Polycarbonates, polyarylates and copolymers with poly(ethylene glycol). *Advanced Drug Delivery Reviews* **55,** 447–466 (2003).

34. Suthisomboon, T., Bargiel, S., Rabenorosoa, K. & Pengwang, E. *Design and Simulation of XZ MEMS Micropositioning with 3D-Complex Structure.* in *2020 Symposium on Design, Test, Integration and Packaging of MEMS and MOEMS (DTIP)* (Lyon, France, 2020), 1–5.

35. Steimle, A. 3D Micro-Printing: A new Era for Med-Tech Applications. *Laser Technik Journal* **15,** 32–34 (2018).

36. Xu, B. B. *et al.* Fabrication and multifunction integration of microfluidic chips by femtosecond laser direct writing. *Lab on a Chip* **13,** 1677–1690 (2013).

37. Rajesh, S. & Bellouard, Y. Towards fast femtosecond laser micromachining of fused silica: The effect of deposited energy. *Optics Express* **18,** 21490–21497 (2010).

38. Haffner, D. S., Gille, H. K., Kalina Jr., C. R. & Cogger, J. J. *System and method for delivering multiple ocular implants.* US Patent US11197780B2. San Clemente, California, USA, 2019.

39. Fea, A. M. *et al.* Prospective unmasked randomized evaluation of the iStent inject® versus two ocular hypotensive agents in patients with primary open-angle glaucoma. *Clinical Ophthalmology* **8,** 875–882 (2014).

40. Bahler, C. K. *et al.* Second-generation trabecular meshwork bypass stent (istent inject) increases outflow facility in cultured human anterior segments. *American Journal of Ophthalmology* **153,** 1206–1213 (2012).

41. Prakasam, M. *et al.* Biodegradable materials and metallic implants-A review. *Journal of Functional Biomaterials* **8,** 1–15 (2017).

42. Dong, Y., Liao, S., Ngiam, M., Chan, C. K. & Ramakrishna, S. Degradation behaviors of electrospun resorbable polyester nanofibers. *Tissue Engineering - Part B: Reviews* **15,** 333–351 (2009).

43. Bartnikowski, M., Dargaville, T. R., Ivanovski, S. & Hutmacher, D. W. Degradation mechanisms of polycaprolactone in the context of chemistry, geometry and environment. *Progress in Polymer Science* **96,** 1–20 (2019).

44. Tille, J. C. *et al.* Histologic assessment of drug-eluting grafts related to implantation site. *Journal of Developmental Biology* **4,** 11 (2016).

45. Choi, H. W., Bong, S., Farson, D. F., Lu, C. & Lee, L. J. Femtosecond laser micromachining and application of hot embossing molds for microfluid device fabrication. *Journal of Laser Applications* **21,** 196 (2009).

46. Espíndola, C. *et al.* Single -and Multi-Walled Carbon Nanotubes as Nanocarriers for the Delivery of 7-Hydroxyflavone. *Pharmaceutics* **14,** 2806 (2022).

47. Gopalakrishnan, S. *et al.* Ultrasound-Enhanced Antibacterial Activity of Polymeric Nanoparticles for Eradicating Bacterial Biofilm. *Advanced Healthcare Materials* **11,** e2201060 (2022).

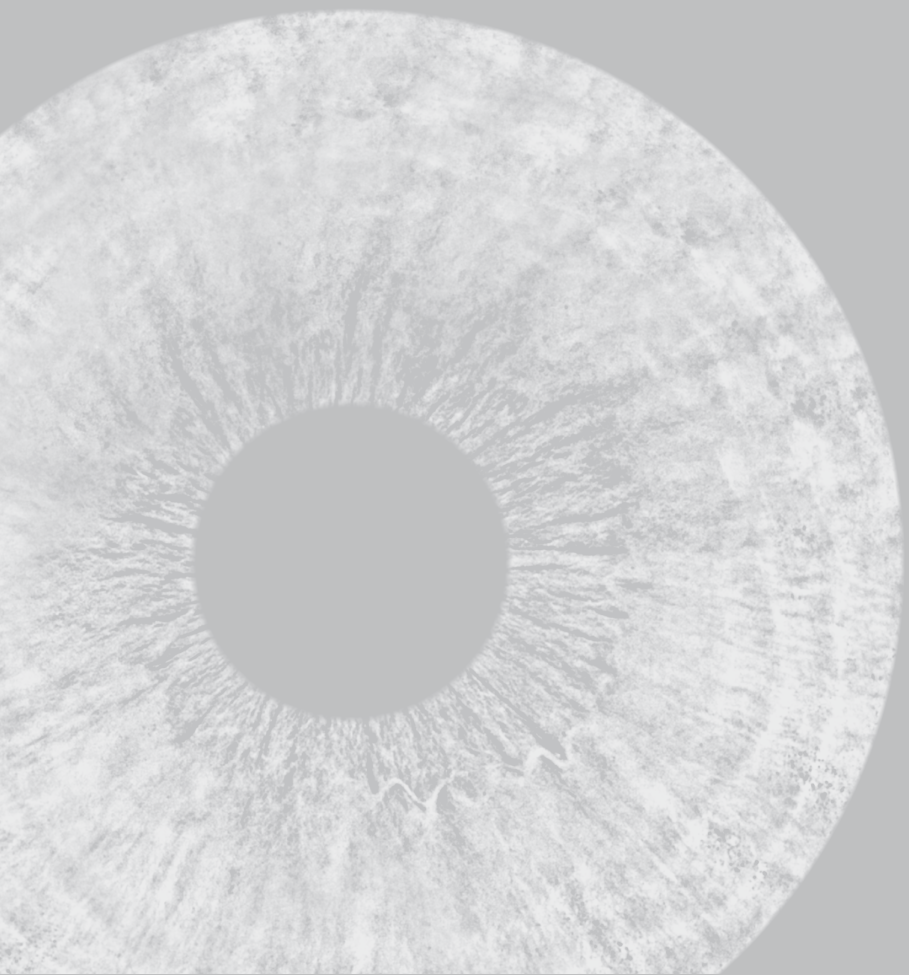

CHAPTER 6

Conclusions and outlook

6.1 Summary of the results and main conclusions

Glaucoma drainage devices are implants used in the treatment of glaucoma, a group of eye diseases that cause progressive damage to the optic nerve and consequently may lead to blindness. These devices are designed to reduce intraocular pressure (IOP), which is a major risk factor for the development and progression of glaucoma. They work by creating a new pathway for the drainage of aqueous humor, the fluid that circulates inside the eye, thereby lowering the IOP. There are different types of glaucoma implants, including the traditional tube shunts and the new minimally invasive glaucoma surgery (MIGS) devices. While current devices have been shown to be effective in reducing IOP and improving visual outcomes in some cases, they also carry risks and potential complications. The aim of this thesis was to develop innovative minimally invasive and smart glaucoma implants that have the potential to improve the outcomes of glaucoma filtration surgery, by enhancing the IOP-lowering efficacy and reducing the risk of postoperative complications.

To begin this search for better glaucoma implants, we found it essential to start by reviewing the glaucoma drainage devices that are currently available on the market. Our comprehensive review, presented in **Chapter 2**, includes a detailed description of each device, along with an evidence-based comparison of their efficacy in stopping disease progression and safety profile. Additionally, we surveyed recent scientific and technological developments that aim to address the prevailing unmet needs and unsolved problems. Our findings suggest that a common limitation of most aqueous shunts currently used in clinical practice is their passive nature, which does not allow for postsurgical IOP control, leading to serious complications such as hypotony (too low IOP). This drawback can only be partially mitigated by invasive procedures, emphasizing the need for glaucoma implants with an adjustable hydrodynamic resistance. A patient-specific, minimally invasive glaucoma drainage device with an adjustable hydrodynamic resistance would be ideal, especially when the outflow of aqueous humor through such a device could be fine-tuned according to the IOP measured in the patient's eyes during the postoperative follow-up visits.

In **Chapter 3**, the feasibility of using a glaucoma implant with an adjustable hydrodynamic resistance to regulate IOP in glaucoma patients was explored. To this end, we developed a numerical model that describes the fluid drainage from the eye through a glaucoma drainage device, its flow into a filtering bleb, and absorption by the subconjunctival vasculature. In this model, the fluid transport in the bleb and subconjunctival tissue is simulated using Darcy's law for fluid flow inside a porous media. To account for the aqueous humor absorption by the subconjunctival vasculature, Darcy's equation is modified by employing

Starling's law. The model was numerically solved using the commercial finite element method (FEM) package COMSOL. We investigated the adjustments needed in the implant's hydrodynamic resistance for IOP control when the two common postoperative complications of glaucoma filtration surgery occur – hypotony and bleb scarring. For this, we simulated the flow through a microshunt with an adjustable lumen diameter. Our findings indicate that reducing the lumen diameter to increase the hydrodynamic resistance of the microshunt can effectively help to prevent hypotony. However, reducing the hydrodynamic resistance by enlarging the lumen diameter of the implant does not sufficiently decrease the IOP to acceptable levels when an encapsulated bleb develops due to excessive tissue fibrosis. This means that the fibrotic tissue surrounding the bleb will always be the limiting factor, as it blocks the fluid flow into the subconjunctival tissue thus hampering its absorption by the subconjunctival microvasculature. These numerical results were confirmed and validated by performing microfluidic experiments using microdevices containing channels with distinct hydrodynamic resistances. Overall, our findings provide guidelines to help designing future (patient-specific) glaucoma implants with adjustable hydrodynamic resistances, where the outflow of aqueous humor through such devices could be fine-tuned postoperatively according to the IOP measured in the patient's eyes. This way, common postoperative complications, such as hypotony, can be avoided.

Using the numerical model described above, we developed a novel miniature magnetically adjustable glaucoma implant, which is described in **Chapter 4**. This implant was designed to allow for non-invasively regulating IOP after implantation, achieved by integrating a microvalve containing a magnetic micro-pencil shaped plug into the implant which opens or closes fluidic channels using an external magnetic stimulus. The device is meant to be implanted in the eye with the valve in the closed state to provide a high hydrodynamic resistance to prevent postoperative hypotony. When the ophthalmologist determines that the filtering bleb is sufficiently mature to offer resistance to the aqueous outflow, and a lower IOP is desired, the valve can be non-invasively opened with an external magnet to increase flow and decrease IOP. Due to its small size, our implant consisting of a drainage tube and a housing element containing the microvalve provides a promising route towards a minimally invasive glaucoma surgery device with less postoperative complications and an easier surgical procedure. Moreover, the implant is comprised of a material, poly(styrene-*block*-isobutylene-*block*-styrene) (SIBS), that evokes minimal tissue reaction, which in combination with the small size might reduce inflammation and the resultant incidence of postoperative complications. The movable magnetic micro-plug that is part of the valving system was also fabricated using SIBS mixed with magnetic microparticles. Being only partly comprised of magnetic material, and also due to its small dimensions, the magnetic micro-pencil plug is very light, and as a result, the overall implant is also lighter and more flexible than other currently available implants. *In vitro* and *ex vivo* microfluidic experiments performed on the fabricated implant show that, when closed, the microvalve can provide sufficient hydrodynamic resistance to overcome hypotony. Furthermore, we demonstrated that our valve function is repeatable and stable over time, under both static and dynamic conditions. The pressure difference achieved between open and closed cycles with our device is very close to the one provided by the eyeWatch implant between its fully open and fully closed configurations. The eyeWatch (Rheon Medical SA,

Lausanne, Switzerland) is currently the only commercially available glaucoma drainage device featuring an active magnetic valve. Initial clinical results with the eyeWatch indicate that it can prevent hypotony and hypotony-related complications, and our results suggest that our device may have similar capabilities but with the benefit of being a more minimally invasive device, which may improve safety and ease of implantation.

In summary, compared to the eyeWatch, our device might present a few advantages: (1) being a minimally invasive device due to its uniquely small size, it requires less operating time and a reduced learning curve, thus making it more suitable for less experienced surgeons; (2) it contains a much simpler valving system where, unlike the eyeWatch system that requires compression/decompression of a tube to adjust fluidic resistance, we rely on a pencil-tip shaped actuator that selectively opens or closes fluid passageways in the device to control IOP; and (3) it is comprised of the unique material SIBS that evokes minimal tissue reaction, thus reducing inflammation and the resultant incidence of bleb encapsulation and related complications. Nonetheless, the eyeWatch implant has a potential advantage over our implant in that it can switch between six different hydrodynamic resistances, as opposed to just two. This feature could be beneficial in achieving more gradual pressure changes during the early postoperative period, particularly when transitioning from an immature bleb where hypotony is a risk and the device should be set to a fully closed state, to a mature bleb where the device should be set to a fully open state. When comparing to the passive flow-control concepts based on flaps, membranes, or ferromagnetic substances presented in Chapter 2 (section 2.6), our microvalve, being active, offers the advantage of allowing the ophthalmologist to precisely and actively adjust the resistance to the aqueous humor outflow to achieve the desired IOP in a non-invasive and patient-specific manner. However, the main advantage of these passive valve mechanisms is that they might provide a simpler way to regulate fluid flow without external control and energy consumption needed.

In this study we have additionally introduced a new microfabrication technique based upon replica molding, using hot embossing and femtosecond laser-machined fused silica glass molds. The complete implant and the integrated micro-plug were fabricated using this technique. This represents a potentially advantageous process for mass production of micro-devices containing three-dimensional structures requiring a few micrometers resolution, high accuracy and complexity. Furthermore, the new valving system proposed in this study can be also suitable for other microfluidic applications, such as in lab-on-chip and organ-on-chip systems, and in controlled drug delivery devices, amongst others.

In **Chapter 5**, we turn our attention towards even less invasive drainage devices for glaucoma and we introduce a new biodegradable, minimally invasive glaucoma implant with approximately the same design and dimensions of the world's smallest medical device known to be implanted in the human body, the iStent *inject*® W (Glaukos Corporation, California, USA). The creation of such a complex and micron-sized implant was only possible by using the femtosecond laser micromachining technique mentioned above to fabricate a glass mold for the subsequent replica molding via hot embossing. Our new MIGS implant is designed to be inserted into the Schlemm's canal to enhance outflow of aqueous humor from the anterior chamber, thereby helping to reduce IOP and stop the progression of glaucoma. Unlike the iStent *inject* W, which is made of heparin-

coated titanium, our device is made of a novel biodegradable polymeric material called polycarbonate bisamide, or PC-BA. Based on our findings, it appears that this newly developed polymer is well-suited for creating the implants, as it demonstrated the ability to withstand the hot embossing process utilized during fabrication without compromising its polymer structure or mechanical properties. The cytotoxicity of the PC-BA on primary human tenon fibroblasts was also investigated, which confirmed that it is a non-cytotoxic material. We believe that our implant can offer similar positive outcomes as the iStent *inject* W, but with the benefit of being a non-metallic and non-permanent implant that will be naturally absorbed into the body. Although the mass loss and changes in molecular weight observed in our preliminary degradation study were not significant within the tested times and degradation conditions, we hypothesize the PC-BA to be a slowly degrading polymer that mainly degrades through hydrolysis of the carbonate and amide groups, either through interaction with water or from enzymatic reactions. This slow degradation should provide enough time for proper and sufficient remodeling of the trabecular meshwork to occur around the implant, and when degradation is finished, the extra outflow site created by the implant should remain patent, thus creating a long-term modification of the trabecular meshwork without the need for a permanent implant that may further scar and lose effectiveness. *In vitro* and *post-mortem* studies indicate that, after reloading our implants into the injector delivery system of the iStent *inject* W, our devices could be successfully implanted *in vitro* into a spongy-like substrate and *post-mortem* into the trabecular meshwork of a real rabbit eye. We confirmed that the implant stays fixed and correctly positioned.

6.2 Recommendations for future work

This thesis proposes two distinct glaucoma drainage devices that are intended to increase the success rate of glaucoma filtration surgery, improve the IOP-lowering effect, and minimize the occurrence of postoperative complications. However, more research needs to be carried out to fully assess the effectiveness of these devices in reducing IOP and stopping disease progression, as well as their safety profile.

Chapter 3 of this thesis describes a numerical model that was developed to investigate the potential of using a glaucoma implant with an adjustable hydrodynamic resistance to regulate the IOP in glaucoma patients. While the study offered valuable information regarding the necessary adjustments to the implant's hydrodynamic resistance to prevent postoperative complications, there is room for improvement in the model to account for additional variables that could impact the outcomes. These include, for instance, the outflow of aqueous humor through the natural drainage pathways (conventional/trabecular and unconventional/uveoscleral drainage pathways). Although it is hypothesized in the literature that only 10% of the aqueous humor drains through these natural outflow pathways after glaucoma filtration surgery is performed, it would still be noteworthy to investigate to which extent this small percentage would influence the results obtained. Additionally, in our study we only focused on the absorption of aqueous humor by the conjunctival vasculature. This is because previous literature suggests that although some aqueous humor flowing into the bleb after glaucoma filtration surgery is also reabsorbed by the episcleral vasculature, the conjunctival blood vessels and lymphatic system play a

major role in removing excess fluid. However, it would still be worthwhile to investigate the potential impact of aqueous humor absorption through the episcleral route on the numerical results.

For the magnetically adjustable glaucoma implant presented in **Chapter 4**, additional *in vitro* long-term measurements of the pressure over several days or months should be performed in order to further confirm the valve stability over time. Although we have proven that our microvalve is stable under dynamic conditions, by placing the devices under rocking motion while doing measurements, it would be also relevant to investigate if the stability of the valve is maintained under more vigorous agitation as well as under the application of compressive forces. This would mimic, for instance, a surgeon grasping the implant too tightly with tweezers during the implantation procedure. Furthermore, occlusion with cells and other particulate matter might also be an issue for this type of small-lumen device, and therefore, more studies (particularly *in vivo* studies) are needed to check if our implant is at risk of blockage. To reduce this risk of blockage, the microchannel design can be further adjusted to feature smoother and curved corners rather than sharp corners, which are more prone to accumulate debris. While we have not encountered any channel clogging during the *in vitro* and *ex vivo* experiments, the risk of blockage may be aggravated over time *in vivo* due the presence of cells, proteins, and other matter. Overall, in the future our implant should be tested in an experimental animal model to confirm the laboratory results and to further evaluate the biocompatibility, controllability, and efficacy of our device. These studies would further validate the stability of the valving mechanism when placed in a living eye. Finally, the ultimate goal is to conduct clinical trials in glaucomatous patients with uncontrolled IOPs requiring a filtering procedure.

As already mentioned, our magnetically actuated implant is limited to two hydrodynamic resistances due to the microvalve's binary ON/OFF states. While a two-state microvalve can provide a significant improvement over traditional glaucoma implants by allowing for active adjustment of the resistance to the aqueous humor outflow, having more than two states can offer greater flexibility and precision in managing the patient's IOP. With multiple resistance states, the ophthalmologist can fine-tune the IOP to meet the specific requirements of each patient, allowing for more precise and personalized management for patients with varying degrees of glaucoma severity. Most importantly, this would allow for smoother pressure transitions during the bleb maturation phase occurring in the early postoperative period. Integrating multiple resistance states in our implant could potentially be achieved by incorporating multiple magnetic microvalves with different orientations in the housing element. By moving the external magnet in different directions, different valves could be activated individually, thereby affecting the overall resistance of the implant. Integrating light-actuated microvalves in addition to magnetic microvalves could provide another possible solution to achieve multiple resistances in our device. By using a combination of magnet and light sources, different valves could be activated, allowing for more than two resistance states. Certainly, this approach would require additional engineering and development work to ensure the proper integration and coordination of the two types of microvalves. Another potential drawback of integrating both magnetic and light actuated microvalves in our device is that ophthalmologists would

need to have access to both a magnet and a light source to adjust the IOP, which may not be practical in certain clinical settings.

In **Chapter 5** we introduce a new biodegradable and polymeric MIGS implant intended to be inserted into the Schlemm's canal to enhance aqueous humor outflow and reduce IOP. Even though we conducted some preliminary studies on the material and device fabricated, additional *in vivo* experiments using an animal model are needed to verify the biocompatibility, biodegradability, and efficacy of our device in reducing IOP. In this work, accelerated *in vitro* degradation experiments were performed on the PC-BA material comprising the implant, from which we concluded that it is a slow-degradation polymer. However, the degradation rate of the material/device can be greatly affected by the *in vivo* environment. Therefore, it is essential to perform long-term animal experiments to gain a better understanding of the device degradation behavior and to investigate how the trabecular meshwork tissue adapts and, like we anticipate, grows around the implant over time. These studies will help us validate our initial hypothesis that our new biodegradable implant can create a long-term modification of the trabecular meshwork and leave a permanent extra outflow site that will not be scarred or closed after the device has been fully reabsorbed into the body. If degradation time is not optimal, other biodegradable materials or formulations with the current PC-BA material might be worth considering in the future. Exploring the potential benefits of a heparin coating for our implant, similar to the iStent *inject* W device, also warrants further investigation through future *in vivo* experiments. The iStent *inject* W is heparin-coated to facilitate lubrication and enable self-priming, allowing for the establishment of initial flow (heparin coating promotes wetting of the titanium surface of the stent). As a result, this coating also helps preventing blood reflux into the anterior chamber, particularly when the episcleral venous pressure exceeds the IOP, which can lead to fluid flow in the opposite direction. Assessing whether our implant would benefit from a similar coating to prevent blood reflux or other sources of hyphema (blood accumulation in the anterior chamber) is an important aspect to consider for future research.

Scientific Output

Journal articles

A new polymeric, biodegradable, minimally invasive glaucoma implant, **Inês C.F. Pereira**, Paul A.A. Bartels, Christian J.F. Bertens, Serge H.M. Söntjes, Hans M. Wyss, Albertus P.H.J. Schenning, Patricia Y.W. Dankers, Henny J.M. Beckers, Jaap M.J. den Toonder, *Manuscript in preparation*.

Magnetically actuated glaucoma drainage device for regulating intraocular pressure after implantation, **Inês C.F. Pereira**, Ralph J.S. van Mechelen, Hans M. Wyss, Leonard Pinchuk, Henny J.M. Beckers, Jaap M.J. den Toonder, *Accepted for publication in Microsystems & Nanoengineering*, 2023.

A model for designing intraocular pressure-regulating glaucoma implants, **Inês C.F. Pereira**, Hans M. Wyss, Leonard Pinchuk, Henny J.M. Beckers, Jaap M.J. den Toonder, *PLoS ONE*, **17**, e0273672, 2022.

Conventional glaucoma implants and the new MIGS devices: a comprehensive review of current options and future directions, **Inês C.F. Pereira**, Rosanne van de Wijdeven, Hans M. Wyss, Henny J.M. Beckers, Jaap M.J. den Toonder, *Eye*, **35**, 3202–3221, 2021.

Patents

Implantable ocular drainage device for controlling intraocular pressure, **Inês C.F. Pereira**, Sebastian Fredrich, Jaap M.J. den Toonder, Albertus P.H.J. Schenning, Henny J.M. Beckers, **Publication No. WO 2022/111891 A1**, filling date October 5, 2021.

Implantable ocular drainage device for controlling intraocular pressure, **Inês C.F. Pereira**, Rosanne van de Wijdeven, Sebastian Fredrich, Albertus P.H.J. Schenning, Hans M. Wyss, Henny J.M. Beckers, Jaap M.J. den Toonder, **Publication No. WO 2022/111892 A1**, filling date October 5, 2021.

Conference contributions

Magnetically actuated glaucoma drainage device for regulating intraocular pressure after implantation, **Inês C.F. Pereira**, Hans M. Wyss, Henny J.M. Beckers, Jaap M.J. den Toonder, **The 26th International Conference on Miniaturized Systems for Chemistry and Life Sciences (µTAS 2022)**, October 23-27 2022, Online, oral presentation.

Magnetically actuated glaucoma drainage device for regulating intraocular pressure after implantation, **Inês C.F. Pereira**, Hans M. Wyss, Henny J.M. Beckers, Jaap M.J. den Toonder, **Micro and Nano Engineering Conference 2022 (MNE 2022)**, September 19-23 2022, Leuven, Belgium, oral presentation.

Magnetically actuated glaucoma drainage device for regulating intraocular pressure after implantation, **Inês C.F. Pereira**, Hans M. Wyss, Henny J.M. Beckers, Jaap M.J. den Toonder, **The Association for Research in Vision and Ophthalmology (ARVO) Annual Meeting 2022**, May 11-12 2022, Online, oral presentation.

Magnetically actuated glaucoma drainage device with adjustable flow properties after implantation, **Inês C.F. Pereira**, Hans M. Wyss, Henny J.M. Beckers, Jaap M.J. den Toonder, **The 25th International Conference on Miniaturized Systems for Chemistry and Life Sciences (µTAS 2021)**, October 10-14 2021, Online, poster presentation.

Magnetically actuated glaucoma drainage device with adjustable flow properties after implantation, **Inês C.F. Pereira**, Hans M. Wyss, Henny J.M. Beckers, Jaap M.J. den Toonder, **1st International Conference on Micromachines and Applications (ICMA 2021)**, April 15-30 2021, Online, oral presentation.

Conference proceedings

Magnetically actuated glaucoma drainage device for regulating intraocular pressure after implantation, **Inês C.F. Pereira**, Hans M. Wyss, Henny J.M. Beckers, Jaap M.J. den Toonder, *Investigative Ophthalmology & Visual Science*, **63**, 443, 2022.

Magnetically Actuated Glaucoma Drainage Device with Adjustable Flow Properties after Implantation, **Inês C.F. Pereira**, Hans M. Wyss, Henny J.M. Beckers, Jaap M.J. den Toonder, *Engineering Proceedings*, **4**, 3, 2021.

Awards

Best Oral Presentation Award sponsored by Microsystems & Nanoengineering/Springer Nature at the 26th International Conference on Miniaturized Systems for Chemistry and Life Sciences (µTAS 2022).

Additional scientific contributions unrelated to this thesis

Journal articles

On-demand microfluidic mixing by actuating integrated magnetic microwalls, Stef Broeren, **Inês C.F. Pereira**, Tongsheng Wang, Jaap M.J. den Toonder, Ye Wang, *Lab Chip*, **23**, 1524-1530, 2023.

Polydopamine-Based All Solid-State Flexible Organic Neuromorphic Devices for Access Device-Free Artificial Neural Networks, Setareh Kazemzadeh, Lloyd Dodsworth, **Inês C.F. Pereira**, Yoeri van de Burgt, *Advanced Electronic Materials*, **9**, 2200427, 2022.

Chitosan and polyethylene glycol based membranes with antibacterial properties for tissue regeneration, **Inês C.F. Pereira**, Ana S. Duarte, Ana S. Neto, José M.F. Ferreira, *Materials Science and Engineering C*, **96**, 606–615, 2019.

Impact of transition metal ions on the structure and bioactivity of alkali-free bioactive glasses, Saurabh Kapoor, Daniela Brazete, **Inês C.F. Pereira**, Gaurav Bhatia, Manpreet Kaur, Luis F. Santos, Dipanjan Banerjee, Ashutosh Goel, José M.F. Ferreira, *Journal of Non-Crystalline Solids*, **506**, 98–108, 2019.

Doping β-TCP as a Strategy for Enhancing the Regenerative Potential of Composite β-TCP–Alkali-Free Bioactive Glass Bone Grafts. Experimental Study in Rats, Manuel M. Ferreira, Ana F. Brito, Daniela Brazete, **Inês C.F. Pereira**, Eunice Carrilho, Ana M. Abrantes, Ana S. Pires, Maria J. Aguiar, Lina Carvalho, Maria F. Botelho, José M.F. Ferreira, *Materials*, **12**, 4, 2018.

Curriculum Vitae

Inês Pereira was born in Viseu, Portugal on the 17th of December 1994. She graduated in 2015 from University of Beira Interior with a BSc in Biomedical Sciences. During her final bachelor project, she performed a literature review on the topic of optical biosensors for the detection of urea in the human body. In 2017, she obtained her MSc in Biomedical Materials and Devices from University of Aveiro in CICECO – Aveiro Institute of Materials. Her master's thesis, under the supervision of Prof. José Ferreira, involved the design, fabrication and characterization of a composite polymeric membrane incorporating nanoparticles of calcium phosphate, zinc oxide and copper oxide, intended to be applied as a biocompatible, osteogenic and antibacterial coating material for dental implants. After finishing her master studies, Inês worked for one year as a research fellow in the project titled "Synaptic networks and personalized medicine approaches to understand neurobehavioral diseases across the lifespan" in the Coimbra Institute for Biomedical Imaging and Translational Research (CIBIT), at University of Coimbra. In this very broad project, Inês was mostly focused on investigating neurodevelopmental disorders, particularly the autism spectrum disorder. She was responsible for programming the tasks used in electroencephalogram acquisitions that were performed on healthy and autistic individuals, as well as for processing and analyzing the obtained bio-signals.

Inês' passion for biomedical devices led her to move to the Netherlands, to join the Microsystems research section headed by prof.dr.ir. Jaap den Toonder at Eindhoven University of Technology, where she started her PhD project in 2019. This PhD project was part of SEAMS, which stands for "Smart, Easy and Accurate Minimally invasive glaucoma Surgery". The results of her research are presented in this thesis.

Public Summary

Glaucoma, an eye disease that can cause irreversible blindness, is a major concern worldwide. The most important risk factor is increased intraocular pressure (IOP) which is caused by an accumulation of fluid in the eye, the aqueous humor. When lowering IOP with eye drops and/or laser treatment is not sufficiently successful, surgical intervention is often performed. Current standard surgical techniques aim at draining the excess fluid from the eye, but they can have severe complications and often fail as a result of excessive scarring and hypotony (i.e., too low IOP). The aim of this PhD thesis was to develop innovative minimally invasive and smart glaucoma implants that have the potential to decrease the incidence of these serious postoperative complications and improve the outcomes of glaucoma filtration surgery. To begin this search for better implants, we started by reviewing the glaucoma drainage devices that are currently available on the market, and surveying the recent scientific and technological developments in this field. A main conclusion from this study was that complications often arise from the fact that current implants do not allow for postsurgical control of the IOP – these implants are often passive and have a fixed resistance to fluid outflow. Therefore, we performed numerical simulations in order to investigate the feasibility of using a glaucoma implant with an adjustable hydrodynamic resistance to regulate IOP in glaucoma patients. The results from these simulations provided valuable insights that allowed the development of a magnetically actuated glaucoma implant that will allow for non-invasively and repeatedly adjusting IOP after implantation. This adjustment is achieved by integrating a magnetic microvalve into the implant, which can open or close fluidic channels and thus change the hydrodynamic resistance of the implant on demand, by using a simple external magnet. With this valving system, the IOP can be effectively tuned according to each patient's needs. Next to our magnetically actuated glaucoma drainage device, we have also developed a new biodegradable and minimally invasive glaucoma implant, with approximately the same size as the world's smallest medical device known to be implanted in the human body. We anticipate that our implant will slowly degrade and be absorbed by the body over time, leaving behind a natural pathway for fluid drainage. This biodegradable glaucoma implant provides a promising new approach for restoring outflow in a more natural way. Both implants proposed in this thesis have the potential to be safer and more effective in reducing IOP than current solutions, and in halting glaucoma disease progression and related visual field loss, and enhancing the quality of life of glaucoma patients.

Publieke Samenvatting

Glaucoom is een oogziekte waardoor mensen onomkeerbaar blind kunnen worden, en dit probleem komt wereldwijd voor. De belangrijkste risicofactor van glaucoom is een verhoogde oogdruk, veroorzaakt door ophoping van de vloeistof die in het oog wordt geproduceerd, het kamerwater. Als oogdruppels of laserbehandelingen niet voldoende helpen om de oogdruk te verlagen, wordt er vaak een oogoperatie uitgevoerd. Bestaande operatieve methodes hebben als doel om de oogdruk te verlagen door overtollig kamerwater uit het oog te laten vloeien via een oogimplantaat, maar de huidige methodes kunnen serieuze complicaties veroorzaken en mislukken vaak door de overmatige vorming van littekenweefsel of door hypotonie (d.w.z. te lage oogdruk). Het doel van het onderzoek dat tot dit proefschrift heeft geleid, was om innovatieve, mimimaal invasieve, slimme glaucoom-implantaten te ontwikkelen waarmee deze complicaties vermeden kunnen worden en die kunnen resulteren in betere resultaten van de chirurgische ingreep. Als startpunt voor deze zoektocht naar betere implantaten hebben we uitgebreid literatuuronderzoek gedaan naar bestaande commerciële glaucoom-implantaten en recente wetenschappelijke en technologische ontwikkelingen. Een hoofdconclusie hiervan was dat de complicaties vaak ontstaan omdat het met de huidige implantaten onmogelijk is om na de operatie de oogdruk in te stellen, want de implantaten zijn meestal passief en hebben een vaste hydrodynamische weerstand. We hebben vervolgens numerieke simulaties uitgevoerd om te onderzoeken of het mogelijk is om postoperatief de oogdruk van glaucoom-patiënten in te stellen met slimme implantaten met een variabele hydrodynamische weerstand. Op basis van de waardevolle inzichten verkregen door de numerieke resultaten, hebben we een magnetisch schakelbaar glaucoom-implantaat ontwikkeld waarmee het mogelijk is om de oogdruk postoperatief, herhaaldelijk, en op een niet-invasieve manier aan te passen. Dit hebben we gerealiseerd door een magnetische micro-schakelaar te integreren in het implantaat. Door deze schakelaar te activeren met een simpele externe magneet, kunnen minimale vloeistofkanalen in het implantaat worden geopend of afgesloten waardoor, on-demand, de hydrodynamische weerstand van het implantaat verandert. De oogdruk kan met deze micro-schakelaar voor elke patiënt naar behoefte door de oogarts worden ingesteld. Naast het magnetisch schakelbare glaucoom-implantaat, hebben we ook een nieuw biodegradeerbaar en minimaal invasief glaucoma-implantaat ontwikkeld, met ongeveer dezelfde afmetingen als het kleinste medische implantaat dat vandaag de dag in het menselijk lichaam wordt geïmplanteerd. Onze hypothese is dat dit implantaat na inbrengen langzaam zal degraderen en opgenomen zal worden door het lichaam, en dat er een natuurlijk pad voor het uitstromen van het kamerwater zal achterblijven. Dit biodegradeerbaar implantaat zorgt er mogelijk voor dat het afvloeien van kamerwater op een natuurlijke manier wordt hersteld. Beide nieuwe implantaten die we in dit proefschrift presenteren zijn mogelijk veiliger en effectiever dan huidige oplossingen, en vormen daarom veelbelovende nieuwe benaderingen om de progressie van glaucoom en het ermee gepaard gaande verlies van gezichtsveld te stoppen, en daarmee de levens van glaucoom-patiënten te verbeteren.

Sumário Público

Glaucoma é uma doença ocular que pode causar cegueira irreversível, sendo, portanto, uma grande fonte de preocupação a nível mundial. Um dos principais fatores de risco para o desenvolvimento desta doença é o aumento da pressão intraocular (PIO) que resulta de uma acumulação excessiva de fluido no interior do olho, o humor aquoso. Quando a redução da PIO com o uso de medicação na forma de gotas oculares (ou colírios) e/ou tratamento a laser não é totalmente bem-sucedida, a intervenção cirúrgica é muitas vezes aconselhada. Técnicas cirúrgicas tradicionais visam drenar o excesso de fluido do olho para reduzir a PIO, no entanto, estas estão frequentemente associadas a complicações graves e muitas vezes não são eficazes devido à ocorrência de cicatrização excessiva e hipotonia (isto é, PIO muito baixa) após a cirurgia. O objetivo deste doutoramento foi desenvolver implantes de drenagem inovadores, minimamente invasivos e inteligentes para o glaucoma, capazes de reduzir efetivamente a incidência dessas graves complicações pós-operatórias e melhorar os resultados da cirurgia de filtração do glaucoma. Nesta busca por melhores implantes, começamos por realizar uma revisão da literatura sobre os dispositivos de drenagem atualmente disponíveis no mercado e explorar os mais recentes avanços científicos e tecnológicos nesta área. Uma das principais conclusões deste estudo foi que muitas das complicações pós-cirúrgicas, incluindo aquelas acima mencionadas, surgem devido ao facto dos implantes de drenagem atuais não permitirem o controlo pós-cirúrgico da PIO – tais implantes são maioritariamente passivos e portanto possuem uma resistência fixa ao escoamento de fluido. Para investigar a viabilidade do uso de um implante com resistência hidrodinâmica ajustável para regular a PIO em pacientes com glaucoma, procedemos em primeiro lugar à realização de simulações numéricas. Os resultados dessas simulações forneceram informações valiosas que possibilitaram o desenvolvimento de um novo implante de drenagem para o glaucoma. Esse implante, controlado magneticamente, permite o ajuste da PIO de forma repetida e completamente não invasiva após a cirurgia. Este ajuste é obtido através da integração de uma microválvula magnética que possibilita a abertura ou o fechamento de canais fluídicos específicos dentro do implante, permitindo assim alterar a sua resistência hidrodinâmica utilizando apenas um magneto externo posicionado sobre o olho. Com esta válvula, a PIO pode ser efetivamente ajustada para atender às necessidades específicas de cada paciente. Para além deste dispositivo de drenagem controlado magneticamente, desenvolvemos ainda um novo implante para o glaucoma que é biodegradável e minimamente invasivo, possuindo um tamanho aproximado ao do menor implante alguma vez implantado no corpo humano. Antecipamos que o nosso implante se irá degradar lentamente e será absorvido pelo corpo ao longo do tempo, deixando para trás um percurso natural para a drenagem de humor aquoso. Este implante biodegradável oferece uma nova e promissora abordagem para restaurar o escoamento de fluido do olho de uma forma mais natural. Ambos os implantes propostos nesta tese de doutoramento têm o potencial de oferecer maior segurança e eficácia na redução da PIO, retardando a progressão do glaucoma e a consequente perda de visão, além de melhorar a qualidade de vida dos pacientes em comparação com as soluções atuais.

Acknowledgements

It is difficult to put into words the immense gratitude and appreciation I feel towards the many individuals who have contributed to the successful completion of this PhD thesis. This thesis represents the culmination of years of hard work, dedication, and perseverance; it has been a challenging yet rewarding experience, and I am honored to have had the support and encouragement of so many remarkable people along the way. I would like to take this opportunity to express my sincerest thanks to all those who have made this achievement possible.

First and foremost, my deepest gratitude goes to my supervisor **Jaap den Toonder**. Professor Jaap, thank you for the encouragement, patience and guidance that you have been providing me continuously over the past 4 years! I deeply appreciate how you have always been so friendly and supportive in all my efforts and struggles. Your trust in me has given me the autonomy to be creative, take initiative, explore my own ideas, and take full "ownership" of the projects that I was involved (as you consistently emphasized in all my annual reviews). Despite your very busy schedule, I am very thankful that you always answered my emails promptly and revised my manuscripts in no time! Thank you also for always showing your appreciation and positive feedback on the work done, which kept me motivated even during times of self-doubt. This is the mirror of the awesome leader you are! This great leadership is also reflected in the way you maintain a healthy and happy research environment within the Microsystems group, and how you extend help to other PhD students with their struggles, students who are not even under your main supervision. I truly admire that in you – the kind and easy-going person you are with everyone. In short, working under your supervision has been a great pleasure and I have learned and grown a lot, as a researcher and mentor, but also as a person! I sincerely hope that we can keep collaborating in the future!

Next to Jaap, a massive thanks to **Henny Beckers** for coming up with the exciting projects that I've been working on during my PhD. Henny, I admire you for your innovative approach to glaucoma surgery, and medicine in general! In a world where many medical professionals are conservative in their practices, your willingness to explore new techniques and methods sets you apart as a progressive and forward-thinking doctor. Thank you for your dedication to pushing the boundaries of what is possible in the field of glaucoma surgery and for constantly seeking to improve quality of life of your patients. Also, thank you for the vast knowledge you have shared with me about glaucoma disease and surgery, and for giving me the opportunity to bring to life the glaucoma implants that you have envisioned!

A special thanks also to **Hans Wyss**! Hans, thank you for sharing with me your outside-the-box and innovative ideas. Your unique perspective has challenged me to step out of my comfort zone – this PhD bubble that we sometimes get trapped in – and look at my work from a different angle. Also, I am very grateful for the opportunity you gave me in the first year of my PhD to be a teaching assistant for the Experimental and Numerical

Skills course, which was actually my first experience in this role. Overall, thank you for your guidance and support, it has been great working with you!

I also want to thank **Albert Schenning** with whom I really enjoy collaborating with! Albert, thank you for introducing me to the light-responsive liquid crystal polymers. It turned out to be more difficult than we expected to integrate such a light-actuated microvalve into a glaucoma implant, but I still hope that this can work out in the future. It would be great! Also, thanks **Sebastian Friedrich** for working so hard on tuning the characteristics of this material to meet the demands of the final application as a glaucoma valve. Thank you also **Lansong Yue**, for the nice collaboration that we have just started on liquid crystal thermoplastics! I really enjoyed the few times we worked together in the lab. I have no doubt that you will achieve great things in your PhD!

Jan de Boer, thank you for being part of my committee and for being a great SEAMS partner. I really enjoyed the discussions we had at the beginning of my PhD about the shape and morphology of the bleb, the mechanism of conjunctival fibrosis, and so on. I've learned a lot from those discussions! In fact, these discussions greatly influenced my decision regarding the shape of the magnetically actuated implant presented in this thesis. I'm very grateful to you for that! And to **Phani Sudarsanam**, of course! Phani, you were one of the first people who helped me get started in the lab at the beginning of my PhD. Thank you for introducing me to SIBS and for sharing with me the techniques you used to imprint features in SIBS. Thank you also for all our brainstorm sessions, most of the times not planned and often starting from casual conversations in the hallway. Those are the brainstorms that I enjoy the most!

Also, I would like to acknowledge **Leonard Pinchuk**. Dear Len, thank you for the warm welcome and hospitality that you and the InnFocus team provided me and other SEAMS partners during our visit to Miami! At that time I was just starting my PhD, and I've learned a lot about how the SIBS is made, the techniques used to fabricate the PRESERFLO MicroShunt out of SIBS, and the tests performed to guarantee the quality of the implants fabricated. It was indeed a very fruitful visit! And of course, I can never forget the amazing dinner you arranged for us at a lovely restaurant with a stunning view of the Miami city and its skyscrapers. Thank you very much for this memory! Thank you also for your always nice comments and very valuable suggestions on the manuscripts that we published together.

I would also like to thank **Patrick Anderson**, for chairing my defense, and **Ronald Dekker** and **Séverine Le Gac** for reading my thesis and being part of my committee.

As already mentioned, this PhD was a part of the SEAMS project, and I would like to express my gratitude to all partners that make this a wonderful team. **Ralph van Mechelen**, thank you for receiving me so many times in Maastricht for the animal experiments. It was never easy for me, as you know, and I think I never got (or will get) used to see the poor rabbits being used to test our devices... they are so cute... but, anyway, I know it's all in the name of science! Thank you also **Anke Schoenmakers** and **Floortje Welten** for your assistance in these experiments. **Jarno Wolters**, thanks for always making the SEAMS meetings more interesting by presenting your results on the

drug delivery devices called "Hamburger", "Macaron", and "Bagel". You definitely made me feel very hungry after those meetings! Also thank you **Theo Gorgels**, **Johan Lub**, and **Filip Maes**, I really enjoyed working with you! **Stephan Peters** and **George Seezink**, many thanks for your help with filing the patents of the magnetically- and light-actuated glaucoma implants. And of course, I must thank **Chemelot Institute for Science & Technology (InSciTe)** for having financially supported the SEAMS project!

I also have to thank the amazing InnFocus team, who were also part of SEAMS. Thank you, **Alessandra Proietti**, **Yongmoon Kwon**, and **Anh Le**, for always promptly sending the SIBS pellets and tubing whenever the "Netherlanders" requested them. Also, thank you for your willingness to answer any questions we had about the SIBS properties. **Yasushi Kato**, thank you for talking to me in Portuguese when I visited InnFocus. Even in Miami, you made me feel like I was home!

From a sister project, the ISEA project, I also want to express my special gratitude to **Christian Bertens**, **Roos van de Wijdeven**, and **Lanhui Li**. Christian, I regret that we didn't work together earlier in my PhD! Thank you for traveling to Eindhoven to teach me how to work with the injector devices used for the biodegradable implant we developed, and for receiving me in Maastricht for the *post-mortem* experiments. You show a unique enthusiasm and passion about the work you do, and that motivates others around you as well. Roos, it was great having you in the Microsystems group! Finally, I had someone to talk to who was also working on a glaucoma implant and facing similar challenges as I was, and specially, with whom I could complain about SIBS and the tight deadlines for the *in vivo* experiments. Lanhui, thank you for always spreading your happiness and positivity to those around you!

I would also like to thank the biodegradable glaucoma implant team! **Patricia Dankers**, you are a role model of a successful woman in science! Thank you for being an inspiration to me and many other young female researchers. It was a pleasure collaborating with you! And with **Paul Bartels**, of course! Paul, thank you for your valuable contribution to this project and for the great manuscript we wrote together. Your relaxed and cooperative attitude made working with you a very nice and productive experience. Thank you also to **Serge Söntjens** for all the data on the raw PC-BA polymer and for the feedback on the manuscript. Finally, many thanks to **Henk Janssen** and **Masaoki Ishiguro** for the help with filing the patent of the biodegradable implant.

A special and huge thanks to my dear paranymphs, **Mohammad Khorsand** and **Setareh Kazemzadeh**, for taking your time to help me in these final steps of my PhD. Mohammad, I still have fresh in my mind the memory of the first day I met you. I came to the Netherlands to sign my contract and Jaap walked with me through the offices to meet everyone in the Microsystems group. There were not many people working at that time since it was carnival break, but there was you, all alone in the last and most faraway office. You and your funny mustache!! I still remember how strange I found your very first questions to me, like what does my name mean or what my zodiac sign says about me, etc. etc. With time, I got used to these not-so-usual questions and now I do enjoy quite a lot our meaningless and absolutely nonscientific conversations! Thank you for always bringing up the most unexpected and interesting facts to discuss in the most

diverse topics, ranging from philosophy to psychology, which so many times helped me take my mind off my work and my problems. You always managed to make me laugh even during the most tormenting times of my PhD, and I am forever grateful to you for that. Thanks for the great friendship we have built! A massive thanks also to you, Setareh! I really admire you, for not only being a great researcher, but for being a great researcher that values self-care and takes the time to do what women usually like to do, like shopping, applying make-up, styling your hair, dressing well, painting your nails, and other things that usually bring us joy and happiness. I can't forget how you kindly paid for my first meal at TU/e when I didn't have yet a Dutch bank account and only had cash with me, which I later learned that wasn't accepted on campus. You saved my life that day! Thank you also for teaching me how to dance to the rhythm of Iranian music, and for all the fun we had together when we went out for dinner or partying, like when we celebrated King's Day during my first month in the Netherlands! Thank you also for our fruitful collaboration and for including me as a co-author in your paper. I am deeply grateful to have you as my friend and hope we can stay in touch even if our paths lead us in different directions in the future.

Many thanks as well to my former and current office mates. **Jiajing Yang**, I truly miss you! You, me and Mohammad came to the Netherlands around the same time and together we were the "best office mates", remember? I miss the first year of our PhDs when we often travelled around in the Netherlands to get to know the most popular cities together, when we went to Keukenhof, and so many other great memories that we shared! I miss you and Mohammad constantly teasing each other, and me just laughing at you and calling you "Tom & Jerry". I hope one day we meet again! **Gülden Akçay** it was a pleasure to be your "buddy" and have helped you find your way and get settled in the Netherlands when you first arrived. I must say, you weren't too much work at all! You were very independent and proactive, which made my buddy task quite easy. It was great sharing the office with you for a while. And also with you, **Rahman Sabahi**! Thank you for always giving me nice compliments about my oral presentations, but also constructive suggestions. It's always nice when someone shows admiration on the work you do. Many thanks for that! **Yiqing Sun**, thank you for sharing the delicious Chinese sweets with us in the office, and for reminding us that it's okay to take a short nap every now and then! Thanks **Roel Koi** for helping with the *in vitro* cytotoxicity experiments on the magnetic SIBS and for patiently answering all my questions about these experiments. **Imke Krauhausen**, thanks for being such a great office mate! It's really nice to have someone else to share a laugh with about the funny things that Mohammad says in the office when we are all focused and working hard. Thanks also for your always kind compliments about the sweaters I knit. That gift card you and Mohammad offered me to buy more yarn and keep knitting was so thoughtful, I will never forget that! Also, thank you for giving me feuerzangenbowle to try for the first time, it was surprisingly delicious, and for introducing me to spinning as well! Finally, welcome to our office, **Bob Huisman**! It was great helping you as a master's student, and now I wish you all the best in your PhD journey.

I want to also express my heartfelt gratitude to many other current and former members of the Microsystems group for creating such a pleasant and enjoyable working environment! **Tanveer Islam**, you are the kind of person who is always willing to help others. You have been there for me in so many ways: from helping me in the lab, to unraveling

the mysteries of strange experiment results, to designing complex things in Alphacam and troubleshooting Alphacam problems, to helping me getting started with the FEMTOprint, to calculating magnetic forces, and so on. You have not only helped me with my work, but you have also been there for me as a friend when I needed someone to talk to or trust secrets with. I'm also very grateful for the memories we shared together, such as going out for snacks or dinner, partying, and travelling around, within the Netherlands but also outside, like we recently did to Kuala Lumpur. Also, thank you for those delicious Kashmiri recipes that you cooked for me and Rui at your place, they were really good! You are an exceptional friend, a hard-working and knowledgeable person, and a great researcher. I genuinely hope that the future holds great things for you and that all your dreams come true, as you deserve nothing but the best! **Eveline van Doremaele**, I admire you for being such a hard-working person, but also for being so caring and kind towards others. Also, it is good to know that I'm not the only one who gets extremely anxious and stressed out before giving oral presentations! **Emma Moonen**, thank you for having invited me over to spend that lovely day in Hilvarenbeek. It was very kind of you to take the time to show me around the village and introduce me to your adorable sheep. I always love seeing the videos of the newborn lambs that you share with me; they're just too cute! Thank you also for all the help in the lab, for helping me supervise students in the courses that we were both TAs, and for the good moments we have shared at conferences. It was also great to have someone like you in the group who understands the challenges of creating a real medical device. **Wei Liu**, **Zhiwei Cui** and **Pan Zuo**, thank you for making our time in Kuala Lumpur so enjoyable, we had so much fun together! Zhiwei, thanks for your contagious laugh, positive attitude, and happiness. Wei, thank you for being able to fall asleep anywhere and everywhere – you always made it possible for us to take some fun pictures while you were napping! And Pan, "lunch?". **Mohammad Jouy Bar**, we definitely shouldn't look at each other when others are presenting in a meeting! I'm afraid one day we won't be able to stop ourselves from laughing! Now seriously, thanks for calling me Inês the cute, and for considering me and Rui as "the most reasonable couple". **Jia-Jun Yeh**, I always love to hear your nice compliments about my outfits. Furthermore, I really appreciate how hard you try to motivate me go to the gym more often to do body pump, cardio core, etc. etc., but I'm very lazy when it comes to sports you know? But thanks for very patiently keep on trying, anyway! **Sevda Malek**, I really admire how you always look so calm and relaxed, and how you always keep yourself neutral and apart from intrigues. Thank you for organizing that lovely party at your place where we all played games and danced to Iranian music until late in the night. Thank you for being such a great host! **Charles-Théophile Coen**, you always do your best to keep the lab organized and clean and to motivate others to follow your steps. Thank you for that! And for frequently hosting such nice parties at your place! **Sofia Gomez**, thank you also for all the effort you put in to ensure that the lab equipment is used correctly, and everything is kept clean. This is why I entrusted you with my "instructor" duties of the FEMTOprint and KOH etching, because I have complete confidence in you! Also, I admire your genuine Latin nature – you're always so direct, honest, and straightforward. Some people might not understand it, mistake it for rudeness even, but I do understand because I come from a country where people are more like that too! **Kalpit Bakal**, you are very proactive, always eager to collaborate with others, and a very good researcher. And I must say, I had a lot of fun listening to you practice your Spanish phrases like "una cerveza, por favor" or

"una paella, por favor" while we were working together in Da Vinci. It was a guaranteed laugh every time, so thank you for that! My gratitude also goes to: **Chris Li**, for having surprised the whole microsystems group with your awesome dancing skills at the MaTe party; **Simone Spolaor**, for also being part of the Woensel crew; **Yangyu Duan**, for making me practice FEMTOprint and hot embossing introductions; **Tongsheng Wang**, for sharing the same love for cats; **Bhavana Venkataramanachar**, for being always so nice and kind; and also, thanks **Jing**, **Hossein**, **Emiel**, **Oscar**, **Suzanne**, **Guillem**, **Alexandra**, **Martha**, and anyone I have forgotten to mention (my apologies!).

Many thanks to **Andreas Pollet**; Olá Andreas! Thank you for listening so patiently to my struggles and for brainstorming solutions with me for creating a functional microvalve. Also, thanks for always being willing to help others in the lab, and for your efforts to keep things running smoothly. **James Marvelous Muganda**, it was a pleasure having you as my "buddy" when I started my PhD. Whenever we meet, you always remember to ask how Feddy is doing, and because I love my cat (as you well know), that means a lot to me. We miss you, James! **Jelle Sleeboom**, thank you for sharing those hilarious stickers with Microsystems people's faces in our whatsapp group, and for always zooming in on the funniest expressions in people's photos (I was a victim of that as well!). **Eriola-Sophia Shanko** thank you for considering my PhD project for the FameLab competition. A big thanks also to many other former colleagues: **Sha Lou**, for your kindness and all the help in organizing Microsystems social activities; **Giorgio Scordo**, for the pleasure of listening to some Italian every now and then; **Alex Bastiaens**, for hosting that awesome and super fun barbecue at your place; **Yanxi Zhang**, for our conversations about settling down and building a family; and **Shuaizhong Zhang**, for the nice memories we shared from the JMBC course at TU Delft. Thank you also **Sertan Sukas** and **Yagmur Demircan Yalçin**.

Irene Dobbelaer, **Jaap de Hullu**, **Erik Homburg**, **Sjoukje Lubach**, and **Katherine Pacheco Morillo**, thank you for trying your best to keep things running smoothly in the lab. Your help in fixing equipment, ordering supplies, and ensuring our safety when working with chemicals is greatly appreciated. Thank you also **Willie ter Elst**; I was just starting my PhD when you left us to enjoy your well-deserved retirement, but I still had the chance to attend the farewell party and barbecue that the Microsystems group and your family prepared for you. It was a really nice event! **Ye Wang**, a big thank you for all of your help and support during these past 4 years, particularly during that time of my PhD when I was struggling so much to get my magnetic microvalve working properly. Our brief discussions have helped me a lot! Also, I am very grateful for having invited me to co-supervise the MSc student **Stef Broeren** with you; it was a very successful collaboration that resulted in a nice publication! A special thanks to Stef as well for all his hard work. **Yoeri van de Burgt** and **Regina Luttge** thank you for contributing to the diversity of research areas within the Microsystems group, and of course, for all your help and support. **Eduard Pelssers**, I really enjoyed the nice talks we had back in the days in the tiny (but cozy) Microsystems lunch room! **Liesbeth van Ballegooij**, you have been exceptionally thoughtful and caring towards us all, just like a mom! When I arrived, you had everything prepared for me, from office supplies to meetings, which helped me to quickly settle in and integrate easily. Thank you for everything that you have done for the Microsystems group, including arranging all those wonderful social events we used

to have. Thank you also for often coming to my office with one specific purpose and ending up sharing all those lovely pictures and videos of your dog! **Joceline Niemarkt**, you recently joined the Microsystems group and I find impressive how so quickly you have adapted to the dynamics of the group. It feels like you've been with us for much longer than you actually have. Thank you so much for all your help so far!

I am also very grateful to the Equipment and Prototype Center (EPC) team at the Eindhoven University of Technology, **Erwin Dekkers**, **Gerrit Fimerius** and **Mariëlle Dirks Smit**, for creating so many different and complicated tools that I needed throughout my PhD. Thank you for your patience, advice, and persistence in problem-solving!

Many thanks also to **Rogier Trompert** for partially drawing Figure 1a of Chapter 4 exactly as requested.

Finally, I want to express a special, heartfelt gratitude to my family. **Mom** and **Dad**, thank you for your endless and unconditional support. Your encouragement, guidance, and love have been the foundation of my success throughout my life. Your belief in me, even when I doubted myself, has been invaluable. Thank you for always being there to listen, to offer advice, to cheer me on. But also, for many times calling me to (solely) share your own struggles, which you always make seem like the end of the world! Anyway, this actually helped me focus on something else than my own struggles and forget about my problems for a while, so I'm very grateful to you for that! Thank you also for always showing great pride in my achievements, even when you didn't fully understand their significance. Finally, I am sorry if sometimes I was grumpy, impatient, and failed to support you enough in return. I love you both so much, and I am grateful for everything you have done for me. I could not have accomplished this without you! And also not without the support and love from my three dear siblings **Mauro**, **Pedro** and **Beatriz**. You mean the world to me, and I always miss you so much! A special thanks also to my **aunties** and **uncles**, and **cousins**, for always showing how proud they are of my courage to leave the country in search for a better life. And a heartfelt thank you goes to heaven, to my beloved **grandparents**, who may no longer be among us, but their memory continues to inspire and comfort me, giving me the strength to carry on and never feel alone.

A very big thank you to **Rui's family** as well, for your kindness, constant support, and understanding, and for having visited us in the Netherlands!

Last, but definitely not least, thank you **Rui**, my love! We are together for a little more than 9 years now, and we have been through and endured so much already! I am so proud of us, how we embrace every challenge together, are adventurous together, have so much fun together, enjoy the moment but also look forward together. You have been providing me unconditional support and guidance in every decision in my life, every step in the way. Thank you for helping me bring out the best in myself, listening to me, offering me the best advice, correcting me when necessary, and for challenging me to do better and better, and to give my utmost best in everything, while also reminding me when I need to slow down and take a rest. As you said, and I sign below, in my PhD you were kind of my unofficial supervisor! Thank you for every time you patiently tried to cheer me up when I was grumpy, upset with my failed experiments, feeling hopeless, and many

times mentally absent. Thank you for coming home, completely exhausted from work, with your own problems in mind, but still willing to brainstorm with me for hours about potential solutions to my problems, new valve designs, different experiments to perform, etc. etc. Thank you for all that and so much more! Only we know how difficult these past 4 years have been for us, being away from our adored country, family, and so many people that we care about, but especially for having lost so many people that were so dear and important to us... But I am very glad that at least we had each other to hold on to, as always! I can't wait to see what the future will bring us! You are my everything, and together with **Feddy**, we make the perfect "small happy family". Amo-te para sempre!